MICROWAVE SPECTROSCOPIC AND COMPUTATIONAL STUDIES ON HYDROGEN-BONDED COMPLEXES

A Thesis

Submitted for the Degree of

Doctor of Philosophy

in the Faculty of Science

by

Surabhi Gupta

Department of Inorganic and Physical Chemistry

INDIAN INSTITUTE OF SCIENCE

Bangalore – 560012, India

May 2024

Dedicated to my grandfather and father.

DECLARATION

I hereby declare that the work presented in this Thesis titled **"Microwave Spectroscopic and Computational Studies on Hydrogen-Bonded Complexes"** has been carried out by me at the Department of Inorganic and Physical Chemistry, Indian Institute of Science, Bangalore, India, under the supervision of Prof. E. Arunan.

February 2024 Surabhi Gupta

CERTIFICATE

I hereby certify that the work presented in this Thesis entitled **"Microwave Spectroscopic and Computational Studies on Hydrogen-Bonded Complexes"** has been carried out by Miss Surabhi Gupta at the Department of Inorganic and Physical Chemistry, Indian Institute of Science, Bangalore, India, under my supervision.

February 2024 Prof. E. Arunan

ACKNOWLEDGEMENTS

First and foremost, I would like to thank my supervisor, Prof Arunan, whose unwavering support, guidance, and encouragement have proven to be invaluable throughout my research journey. I consider myself fortunate to have had a supervisor who values a healthy work-life balance. He ensures that I focus more on the process instead of results, which has significantly influenced my ability to engage in effective learning and function independently as a researcher. His calmness and brilliance have valued each minute of my research discussions with him, which always results in productive thoughts. Thank you for giving me the opportunity to work with you. His constant support, encouragement and enthusiasm for my research work have helped me keep going. I express my deepest gratitude to him for actively encouraging my participation in various conferences and for providing assistance at multiple levels to ensure my active involvement. I thank you for letting me not worry about work during the time I was facing personal issues. I express my sincere gratitude for being a source of positivity amidst these uncertain times.

I would like to extend my heartfelt gratitude to Dr Nicholas R. Walker for granting me the opportunity to conduct research in his laboratory at Newcastle University, UK and for providing accommodation in his home for a period of nearly a month. Moreover, I would like to express my sincere appreciation to Prof Arunan and Dr Susy for their invaluable assistance during my visit to Newcastle.

I wish to express my sincerest thanks to Miss Charlotte Cummings for her exceptional instruction on the intricacies of operating the chirped-pulse Fourier transform microwave spectrometer. I am immensely grateful to Charlotte for her assistance in conducting experiments as well as the subsequent data analysis. I am indebted to her for diligently proofreading section 2.3 of the thesis. She has proven to be an exceptional colleague to work with, and I greatly value her kind friendship. Additionally, I extend my thanks for her support during my stay in Newcastle.

I would like to extend my gratitude to Dr Tryggvi Emilsson and his family for graciously hosting us during our visit to Urbana, Illinois.

I would like to express my appreciation to all the members of the Chemical Dynamics Group for their invaluable contributions. The group meetings have provided me with an enriching opportunity to broaden my knowledge in various scientific fields.

I extend my sincere thanks to the present chair, Prof E. Arunan, as well as the past chair, Prof S. Umapathy, of our department for their unwavering support and the resources allocated to the IPC department.

I am grateful to my esteemed course instructors, Prof E. Arunan, Prof Sai G. Ramesh, Dr Atanu Bhattacharya, Prof Anshu Pandey, Prof S. Ramasesha, and Prof Prabal K. Maiti, for their outstanding teaching and guidance, which have greatly enhanced my understanding of different aspects of the subject matter.

I would like to acknowledge and express my gratitude to Prof Sai G. Ramesh for overseeing the maintenance of the computational facilities within the department.

I am deeply appreciative of Dr Atanu Bhattacharya and Dr Govinda Raj for providing me with the opportunity to serve as a teaching assistant in the UC101 lab. I extend my thanks to all the members of the UC101 lab for their cooperation and support.

I extend my sincere thanks to Prof P. Balram for introducing us to the acetylene-ammonia-18-crown-6 crystal structure.

I would like to express my gratitude to Dr Jayashree Nagesh for engaging in insightful discussions regarding ammonia tunnelling through the 18-crown-6 problem.

I gratefully acknowledge DST-INSPIRE and IISc for the fellowship. I express my appreciation to DST, GARP and SPARC for providing funding to attend various conferences. I acknowledge Newcastle University for the funds to conduct experiments there.

I extend my sincere appreciation to all the staff members of IPC, Ms Roopa, Mr Vishal, Ms Jyothishree, and Mr Murthy. I am deeply grateful to Ms Roopa and Mr Vishal for their diligent handling of all the official paperwork. Their invaluable assistance has been of great help to me.

I would like to specifically express my thanks to Mr Arul Nambi for his invaluable guidance in fulfilling the electrical, plumbing, and gas line requirements.

I am deeply indebted to Mr Arul Nambi, Mr Nanjappa, Mr Shankar, and Mr Shiju for their invaluable support in relocating the spectrometer from the old IPC building to the New Chemical Sciences Building.

I would like to extend my heartfelt gratitude to Mrs Arunan for her kindness and the numerous invitations to her home for lunch/dinner. I am immensely thankful for her support during the challenging phase of my life.

I would like to express my gratitude to my fellow lab mates, Dr Sharon, Dr Arijit, Kabir, Govinda, Amresh, Deepak, Sumaiya, Dr Kunal, Kiran, Dr Subharaj, Chaitanya, and Dr Sarvesh K Pandey, for their continuous assistance and support. I am also thankful to all the undergraduate students and project students who visited our lab. I extend my thanks to Dr Sharon and Dr Arijit for their thorough teachings on the spectrometer and their guidance in various aspects of my PhD. In particular, I am grateful to Dr Arijit for his guidance when I first started my experiments. I also thank Dr Arijit for his invaluable assistance during the relocation of the spectrometer from the old IPC department to the Chemical Sciences building.

I would like to acknowledge my fellow PhD batchmates, Dipangkali, Nishant, Vipin, Saibalendu, Vidyalaxmi, Mita, Arpitha, Sambit, Munthasir, Sekhar, and Chesta, for the enjoyable moments we shared during birthdays. I would especially like to thank Dipangkali, Nishant, Vipin and Saibalendu for their friendship.

I would like to express my gratitude to all the members of the '2018' Al(l)chemists' club.

I extend my heartfelt gratitude to my cherished friends from both my bachelor’s and master’s courses, Ankita, Surabhi, Parth, Rajib, Pratibha, and Khyati, for their unwavering friendship.

To my extended family here at IISc-Uttam, Dipangkali, Simran, Neetu, Sanjna, Adersh, Himanshu, and Amit, I owe an immense debt of gratitude. You guys made my time during my PhD really special. I especially thank Uttam for his constant support during all the ups and downs of my life. You have always been an inspiration and motivation to

push myself a step further. Thank you for being part of this. His encouragement has been a constant source of strength. I thank Uttam for his help and assistance during formatting my Thesis. I thank Dipangkali for her kind friendship. I thank her for bringing homemade food for me. I thank her for always being available for me whenever I needed her. I thank Simran for teaching me different lessons in biology. I express my gratitude to Simran, Sanjna, and Neetu for their unwavering love and support and for making me feel at home during my stay in the hostel. I extend my thanks to Adersh, Himanshu, and Amit for their friendship, which I thoroughly cherish.

I consider myself incredibly fortunate to have had the privilege of growing up alongside a loving and supportive individual. The impact my family has had on my life is indescribable. I would like to express my gratitude to my late grandfather, Mr Jamuna Prasad, for continually motivating me to pursue science and explore the world. His incredible spirit and positive energy have left a lasting impression on me. Moreover, I am deeply thankful to my late father, Mr Kailash Prasad, for his unwavering support and encouragement from the very beginning. His faith in me has been a source of motivation, particularly in moments of failure.

To my mother, I owe an immeasurable debt of gratitude for her constant love and support. Her patience throughout the years has been truly remarkable. I would also like to express my appreciation to my elder brothers, Mr Sneh Gupta and Mr Saurabh Gupta, as well as my sisters-in-law, Mrs Babita Gupta and Mrs Shalu Gupta, for their love and support. Special mention must be made of my nieces, Prisha and Veda, whose presence has brought immense joy and love to our family. It is with deep gratitude that I acknowledge my family for the strength and freedom they have provided me.

I apologise for any names I may have missed.

Surabhi Gupta

Contents

SYNOPSIS

Hydrogen bonding is a unique interaction that has a profound impact on the structures and properties of molecules, as well as chemical and biochemical reactions, including life processes. The work presented in this Thesis details results from investigations on some hydrogen-bonded intermolecular interactions. Experimental tools such as the home-built Balle Flygare Fourier Transform Microwave (BF-FTMW) spectrometer at IISc Bangalore, India and the Chirped Pulse Fourier Transform Microwave Spectrometer (CP-FTMW) at Newcastle University, United Kingdom, were employed to study the molecules/complexes. The obtained experimental results were further complemented by computational studies, including Atoms in Molecules (AIM), Non-covalent Interactions (NCI) index, Natural Bond Orbital (NBO), and Symmetry-Adapted Perturbation Theory (SAPT) analyses. Both spectrometers mentioned above are equipped with a pulsed nozzle, which enables the production of a molecular beam where the molecules and complexes are free from interactions with other molecules, thereby providing information about the isolated molecule/complex. The experimental geometry obtained from microwave spectroscopy can be utilised to evaluate the performance of various *ab-initio* and DFT methods.

This Thesis comprises of six chapters. *Chapter 1* provides a concise introduction to intermolecular interactions and the theoretical aspects of microwave spectroscopy.

Chapter 2 presents an overview of the BF-FTMW and CP-FTMW spectrometers. Additionally, this chapter briefly discusses computational methods such as AIM, NCI, NBO, and SAPT analyses.

Chapter 3 focuses on the microwave spectra of the phenylacetylene···methanol complex. *Ab-initio* (MP2) and DFT (B3LYP-D3) calculations for the complex resulted in three optimised hydrogen-bonded structures. In the first and second structures, CH_3OH donates a hydrogen bond to the phenyl-π and acetylenic-π systems, respectively. In the third structure, phenylacetylene acts as a hydrogen bond donor through an acetylenic C-H bond. Interestingly, the MP2/aug-cc-pVDZ level of theory identifies the acetylenic bound structure as the global minimum. Conversely, the B3LYP-D3/aug-cc-pVDZ level

gives the acetylenic bound structure as the global minimum. The acetylenic bound structure also exhibits distinct interactions at both levels of theory. The phenylacetylene···methanol complex demonstrates contrasting results in two experimental studies. IR-UV double resonance spectroscopic results indicate that CH_3OH donates a hydrogen bond to the phenyl-π system, while FTIR spectroscopy suggests that CH_3OH donates a hydrogen bond to the acetylenic-π system. We investigated this complex using both BF-FTMW and CP-FTMW spectrometers. Our study using the rotational spectroscopy on this complex confirms the preference for the acetylenic structure, consistent with the arrangement where CH_3OH donates the H-bond to the acetylenic π-system, and CH_3OH accepts a weak H-bond through the ortho hydrogen of phenylacetylene. The observed rotational transitions show splitting, indicating the internal motion of the CH_3 group in CH_3OH. The barrier to internal rotation of the CH_3 group is determined to be 353.4 cm^{-1}. The obtained global minimum structure is compared with several CH_3OH-containing complexes to gain insights into the internal rotation of the CH_3 group and its impact on the V_3 barrier. The SAPT analysis suggests that electrostatics play a significant role in stabilising the acetylenic-bound structure.

Chapter 4 presents a re-examination of the structure of 1-fluoronaphthalene (1FN). Previous research that employed microwave spectroscopy did not include any investigation of isotopes, which is essential for accurate structure determination. A CP-FTMW spectrometer was employed to record the spectrum of 1FN. All singly substituted ^{13}C isotopologues of 1FN were assigned based in their natural abundance. The rotational constants of the parent 1FN, as reported in previous studies, closely align with our investigation. The precise atomic coordinates of all carbon atoms in the 1FN ring were determined. The inertial defect remained uniform (-0.14 amu $Å^2$) for all isotopologues, suggesting that isotopic substitution had little effect on the structure. Furthermore, this chapter also discusses the observed negative inertial defect, which is also attributed to the low out-of-plane bending mode of the 1FN ring.

Chapter 5 explores the monohydrate and dihydrate complexes of 1FN. The CP-FTMW spectrometer was employed to examine these complexes. The rotational spectrum of the $1FN···H_2O$ complex revealed the presence of an O-H···F hydrogen bond, with H_2O acting as an H-bond donor, alongside a C-H···O weak interaction, where H_2O acts as a weak H-bond acceptor. The experimentally obtained inertial defect (-1.30 amu $Å^2$) of the

1FN···H_2O complex indicates an effective planar geometry. The presence of hydrogen bonds was supported by analyses such as Atoms in Molecules (AIM), Natural Bond Orbital (NBO), and Non-covalent Interactions (NCI). Energy decomposition analysis emphasised the dominant role of electrostatic interactions in stabilising the 1FN···H_2O complex. Preliminary results of the dihydrate complex of 1FN confirmed a structure in which the water dimer forms O-H···F and O-H···C hydrogen bonds while interacting from above the 1FN plane. The energy decomposition analysis indicates that dispersion significantly contributes to stabilising the configuration mentioned above in the 1FN···$(H_2O)_2$ complex.

In *Chapter 6* of this Thesis, an investigation was conducted on the hydrogen bonding, inversion, and tunnelling phenomena displayed by the NH_3 molecule when complexed with 18-crown-6. One crystal structure was reported in which NH_3 molecules are connected by N-H...O intermolecular hydrogen bonds above and below the crown ether plane. The occurrence of NH_3 molecules donating hydrogen bonds is exceedingly rare, not only in the gas phase but also in crystal structures. The NH_3 molecule and its barrier for inversion, specifically the v_2 normal mode, have been extensively studied through numerous calculations. The inversion and tunnelling of NH_3 in the complex with 18-crown-6 were examined. N-H···O hydrogen bonding interactions have a significant influence on the barriers for NH_3 inversion. The barrier for this inversion is 51.5 kJ/mol, compared to 22.2 kJ/mol for free NH_3. To explore the tunnelling of NH_3 through the CE ring, both 1D and 2D potential energy scans were conducted.

Appendix A provides a summary of the *ab-initio* and DFT calculations conducted, as well as the initial fit acquired for the 1FN-Neon complex. The fit implies that the Neon atom is situated atop the 1FN ring and interacts with the π electron cloud. A preliminary investigation of the Ar-$(H_2S)_2(H_2O)$ cluster is showcased and summarised in *Appendix B*. *Appendix C* presents the *ab-initio* and DFT calculations, along with AIM analyses, on the hexafluorobenzene-methanol complex. A broadband rotational spectrum was recorded for this complex. The spectrum has not been assigned yet, and the obtained signal frequencies are listed in this *Appendix*.

List of Tables:

List of Figures

List of Abbreviations and Symbols

Symbol	Abbreviation
PhAc	Phenylacetylene
1FN	1-Fluoronaphthalene
CE	18-crown-6
HFB	Hexafluorobenzene
FID	Free Induction Decay
AWG	Arbitrary Waveform Generator
TWT	Travelling Wave Tube
BSSE	Basis Set Super Position Error
AIM	Atoms in Molecules
NBO	Natural Bond Orbital
NCI	Non-covalent Interactions
SAPT	Symmetry Adapted Perturbation Theory
PN-FTMW	Pulsed Nozzle Fourier Transform Microwave
BF-FTMW	Balle Flygare Fourier Transform Microwave
CP-FTMW	Chirped Pulse Fourier Transform Microwave
RF	Radio Frequency
MW	Microwave
BCP	Bond Critical Point
RCP	Ring Critical Point
A, B, C	Rotational constants
$D_J, D_{JK}, D_K, d_1, d_2$	Distortion constants
I_a, I_b, I_c	Moments of inertia in the abc principal axes system
P_{aa}, P_{bb}, P_{cc}	Planar moments in the abc principal axes system
μ_a, μ_b, μ_c	Dipole moment component along the abc principal axes system
Δ	Inertial defect
J	Total angular momentum
K	Projection of the total angular momentum on the body-fixed axis

K_a	Projection of J onto the a-rotational axis of the molecule
K_c	Projection of J onto the c-rotational axis of the molecule
M	Projection of the total angular momentum on the space-fixed axis
κ	Ray's asymmetry parameter
r_e	Equilibrium structure
r_s	Substitution structure
r_0	Effective or ground-state structure
ρ	Electron density
$\nabla^2\rho$	Laplacian of electron desnity
$\lambda_1, \lambda_2, \lambda_3$	Eigenvalues of the Hessian Matrix of electron density
υ	Torsional levels
V_3	internal rotation barrier
F	Rotational constant of the internally rotating methyl top
δ	Angle between the principal axis x and the principal axis z
ε	Angle between the principal axis x and the projection of the internal rotation axis onto the xy-plane
s	Reduced dimensionless barrier height

Properties of Nuclides

Properties of relevant nuclides reproduced from the NIST database:[1]

Element Symbol	Atomic number	Atomic Mass	Isotopic Abundance	Nuclear Spin[2]
H	1	1.007 825 032 23(9)	99.9885(70)	1/2
	2	2.014 101 778 12(12)	0.0115(70)	1
	3	3.016 049 2779(24)	Unstable nuclide	1/2
C	12	12.0000000(00)	98.93(8)	0
	13	13.003 354 835 07(23)	1.07(8)	1/2
	14	14.003 241 9884(40)	Unstable nuclide	0
O	16	15.99491461956(16)	99.757(16)	0
	17	16.99913170(12)	0.038(1)	5/2
	18	17.9991610(7)	0.205(14)	0
S	32	31.972 071 1744(14)	94.99(26)	0
	33	32.971 458 9098(15)	0.75(2)	3/2
	34	33.967 867 004(47)	4.25(24)	(0)
	36	35.967 080 71(20)	0.01(1)	(0)
F	19	18.998 403 162 73(92)	100	½
Ne	20	19.992 440 1762(17)	90.48(3)	(0)
	21	20.993 846 685(41)	0.27(1)	3/2
	22	21.991 385 114(18)	9.25(3)	(0)

The zero spins enclosed by parentheses are based on the absence of observable hyperfine structure.

References:

(1) Atomic Weights and Isotopic Compositions with Relative Atomic Masses. *NIST* **2009**.
(2) Gordy, W.; Cook, R. L. *Microwave Molecular Spectra*.

CHAPTER 1

Introduction

CHAPTER 1 | Introduction |

1.1 Intermolecular Interactions:

Interactions between molecules, which are commonly known as non-covalent interactions, assume a crucial function in determining the physical and chemical characteristics of substances. These intermolecular interactions encompass the forces that exist between molecules and are accountable for maintaining their cohesion in different phases of matter, ranging from solid to liquid, as well as gaseous states. The significance of these intermolecular interactions is immense in various scientific domains such as chemistry, physics, biology, and materials science, where these interactions are the building blocks in understanding the behaviour and properties of matter. van der Waals interactions, halogen bonding and hydrogen bonding, are important for many biological phenomena, such as the double-stranded structure of DNA, protein folding and many biological reactions. These interactions are also important in designing macromolecules in the domain of crystal engineering and supramolecular chemistry.[1–3]

Johannes Diderik van der Waals, a Dutch physicist, made a noteworthy contribution to comprehending intermolecular forces. In his thesis titled "*The Continuity of the Gaseous and Liquid States*", his contributions encompassed the formulation of the van der Waals equation of state.[4] He was awarded the Nobel Prize in Physics in 1910 for his pioneering work.[5] van der Waals addressed the limitations of the ideal gas law, as initially postulated by Clapeyron (*Equation 1*).[6] Clapeyron's gas law presumed gas molecules to be point masses with no discernible interactions between them.[6] In contrast, van der Waals introduced the concept of finite molecular masses and intermolecular interactions, recognising the non-ideal gas behaviour.

$$\frac{d\ ln\ P}{dT} = \frac{\Delta H_{vap}}{RT^2} \qquad (1)$$

The van der Waals equation of state is:

$$\left(P + \frac{a}{n^2V^2}\right)(V - nb) = nRT \qquad (2)$$

The van der Waals equation of state (*Equation 2*) provides a more comprehensive description of real gases, accounting for intermolecular forces and molecular volumes, which are factors not considered in the ideal gas law. Here, P, V, T, and n denote pressure, volume, temperature, and the number of moles of the gas, respectively. The parameters a and b in the van der Waals equation are the coefficients that correct for intermolecular forces and molecular volume, respectively. The van der Waals equation is particularly valuable when dealing with real gases under conditions where intermolecular forces and molecular size play significant roles, such as at high pressure or low temperature. The ideal gas law cannot accurately explain liquefaction and phase transitions. The "*a*" coefficients of water vapour and the hydrogen sulphide are 5.536 and 4.490 L^2bar/mol^2, respectively.[7] The "*a*" coefficient, which corrects the intermolecular forces, has a major role in describing the strength of the interactions. The higher value of "*a*" tends to the stronger attraction between molecules. Therefore, in the case of H_2O and H_2S, the difference in the value displays the change in the state; water is liquid at room temperature, whereas H_2S remains gas.

The nature of interactions present in the molecules is not given by van der Waals equation. Initially, all types of intermolecular interactions were called van der Waals interactions. However, the difference between the physical states of H_2O and H_2S highlighted the need for understanding the nature of interactions present between these molecules. In the early 20th century, a new classification called "Hydrogen Bonding" was introduced. Hydrogen bonding is considered a class of van der Waals interactions.[8–10] The hydrogen bond has been redefined recently.[11]

Interaction energy for a molecular complex can be decomposed into five terms: electrostatic, exchange repulsion, induction, dispersion, and charge transfer.

$$\Delta E_{total} = \Delta E_{elec} + \Delta E_{ex} + \Delta E_{ind} + \Delta E_{disp} + \Delta E_{ct}$$

Electrostatic Component (ΔE_{elec}): Arising from charge interactions, this component reflects the attractive or repulsive nature of electrostatic forces.

Exchange Energy (ΔE_{ex}): It is a repulsion term which arises due to the repulsion between the electrons and is based on Pauli's exclusion principle, according to which the electrons from the two monomers cannot be present in the same region of space.

Induction Energy (ΔE_{ind}): Also known as polarisation energy, this term reflects the impact of polarisation interactions on the total energy. The ions and multipoles can polarise a non-polar molecule, leading to the induced dipole moment. The induction terms are responsible for these interactions. The induction energy plays a significant role in stabilising the rare gas-molecule complexes.[12,13]

Dispersion Energy (ΔE_{disp}): Quantifying the contributions from dispersion forces, this term results from fluctuating electron distributions. Dispersion forces are the dominant forces between non-polar units and are akin to induced-dipole-induced-dipole interactions. The complexes formed between the rare gases are mainly stabilised by dispersion interaction.[14,15]

Charge Transfer Energy (ΔE_{ct}): Accounting for electron exchange between molecules, this component becomes more significant at close distances and contributes to the covalent character.

These various weak interactions encompass hydrogen bonding, as well as additional categories such as aerogen bonding,[16–18] halogen bonding,[2,19–21] chalcogen bonding,[22–24] pnictogen bonding,[25–29] tetrel bonding,[30–33] and triel bonding[34]. A comprehensive understanding of these diverse weak intermolecular interactions is fundamental to chemistry, given their impact on molecular behaviour in contexts ranging from biomolecular structures to material design and pharmaceutical development.

1.2 Rotational Spectroscopy:

Rotational spectroscopy is a powerful analytical technique used in physical chemistry, physics, and astronomy to investigate the rotational motion of molecules. This branch of spectroscopy provides valuable insights into the structure, composition, and dynamics of molecules. Rotational spectroscopy primarily focuses on the rotational transitions of molecules, which occur when molecules absorb or emit electromagnetic radiation in the microwave region of the electromagnetic spectrum. The fundamental principle that underlies rotational spectroscopy is the quantisation of angular momentum within molecules. Similar to the discrete energy levels that electrons can occupy in atoms, molecular rotation is also quantised, indicating that it can only occur at certain energy levels. When a molecule absorbs a photon possessing energy that matches the rotational

transition, it experiences a modification in its rotational state. This modification leads to the molecule transitioning from one rotational level to another, and the absorption or emission of microwave radiation accompanies this transition. One of the key advantages of rotational spectroscopy is its high precision. It allows scientists to determine molecular structures with remarkable accuracy. The obtained rotational constants from the observed rotational spectra exhibit an inverse relationship with the moments of inertia. The moments of inertia are linked to the bond lengths, hence enabling the determination of experimental structure. Modifications in the moments of inertia due to isotopic substitutions can be readily determined and assist in the determination of the exact structure. As a result, rotational spectroscopy serves as an exceedingly precise and responsive approach for the determination of molecular structure. This level of precision has made rotational spectroscopy an invaluable tool for investigating complex molecular systems and unravelling their structural details. This chapter deals with the fundamental concepts of rotational spectroscopy This chapter is based on the books, Microwave Molecular Spectra by Gordy and Cook, and Microwave Spectroscopy by Townes and Schawlow.[35,36]

1.2.1 Types of Molecules:

The molecules are classified based on the three moments of inertia based on the principal axis system (*a*, *b*, *c*). This classification is given in *Table 1-1*.

Table 1-1: Classification of molecules based on their principal moments of inertia.

Class	Moments of inertia
Spherical Tops	$I_a=I_b=I_c$
Linear Rotors	$I_a=0$, $I_b=I_c$
Symmetric Tops	*Prolate:* $I_a<I_b=I_c$ *Oblate:* $I_a=I_b<I_c$
Asymmetric Tops	$I_a<I_b<I_c$

1.2.1.1 Spherical Tops:

The spherical tops have zero dipole moment because this class of molecules possess moments of inertia that are equivalent along each principal axis. Microwave spectroscopy can only be conducted on molecules that possess a non-zero dipole moment. However, the presence of centrifugal distortion constants can induce a dipole moment, leading to the possibility of recording the Microwave spectrum for higher *J* values. The rotational energy equation for a spherical top is given below:

$$E = 2B(J+1)$$

The expression mentioned above corresponds to the transitions from *J* to *J*+1.

1.2.1.2 Linear Rotors:

For a linear polyatomic molecule, the spectral properties closely resemble those of diatomic molecules, except for the added complexity arising from a greater number of vibrational modes and therefore, potential functions of polyatomic molecules are more complicated compared to diatomic molecules. In the linear molecule, the angular momentum about the figure axis a is zero and therefore,

$$I_b = I_c = I$$

The Hamiltonian can be expressed as,

$$\hat{H}_0 = \frac{P^2}{2I}$$

Where *I* is the moment of inertia and P^2 is the operator conjugate to the square of the total angular momentum.

The energy eigenvalues become,

$$E_J^0 = \langle J|\hat{H}_0|J\rangle = \left(\frac{1}{2I}\right)\langle J|P^2|J\rangle = \frac{h^2J(J+1)}{8\pi^2 I}$$

$$B = \frac{h}{8\pi^2 I}$$

$$E_J^0 = hBJ(J+1)$$

Since P^2 and P_Z commute, where P_Z is the component of angular momentum in spaced fixed coordinates. Therefore, P^2 and P_Z have common eigenfunctions,

$$P^2\psi_{J,M} = \hbar^2 J(J+1)\Psi_{J,M}$$

$$P_Z\psi_{J,M} = \hbar M_J \Psi_{J,M}$$

The J is the angular momentum quantum number can take integral values,

$$J = 0,1,2,3, \ldots$$

And M is the projection of J on space fixed axis (Z), and it also take integral values such that, $|M_J| \leq J$.

$$M_J = J, J-1, J-2, \ldots, -J$$

Based on the selection rules for dipole absorption of radiation, $J' = J \pm 1$ and $M_{J'} = M_J \; or \; M_J \pm 1$

In the case of a linear rotor, the transition $J \rightarrow J+1$ correspond to absorption of radiation, hence the absorption line frequencies are given by,

$$E = 2B(J+1)$$

Therefore, the rotational frequencies of the rigid, linear, polyatomic molecule, like those of the diatomic molecule, form a series of *2B*, *4B*, *6B* and so on.

1.2.1.3 Symmetric Tops:

A symmetric top is characterised by the presence of an axis of symmetry, denoted as C_n, where the value of n is equal to or greater than three ($n \geq 3$). In this type of molecules two of the principal moments of inertia are equal. Within the category of symmetric tops, further distinctions can be made based on the relationship between the principal moments of inertia. In the prolate symmetric top molecule, the principal moments of inertia are ordered such that $I_a < I_b = I_c$. In this case, the axis of least moment of inertia lies along the symmetry axis. The term "prolate" refers to the elongated shape of the molecule along its symmetry axis. One example of a prolate symmetric top molecule is CH_3F. In this molecule, the distribution of principal moments of inertia satisfies the condition $I_a < I_b =$

I_c, with the '*a*' axis serving as the symmetry axis. Conversely, an oblate symmetric top, the principal moments of inertia satisfy the condition $I_a = I_b < I_c$. In these kinds of molecules, the axis of greatest moment of inertia lies along the symmetry axis. The term "oblate" is used to describe the flattened or disc-like shape of the molecule along its symmetry axis. An example of an oblate symmetric top molecule is BCl_3.

The rigid rotor Hamiltonian is given by:

$$\widehat{H}_0 = \frac{\hat{P}_a^2}{2I_A} + \frac{\hat{P}_b^2}{2I_B} + \frac{\hat{P}_c^2}{2I_C}$$

The Hamiltonian for a rigid rotor prolate top is given by:

$$\hat{P}^2 = \hat{P}_a^2 + \hat{P}_b^2 + \hat{P}_c^2$$
$$\hat{P}_b^2 + \hat{P}_c^2 = \hat{P}^2 - \hat{P}_a^2$$

For a Prolate top:

$$\widehat{H}_0 = \left[\frac{\hat{P}_a^2}{2I_A} + \frac{1}{2I_B}\left(\hat{P}_b^2 + \hat{P}_c^2\right)\right]$$

$$\widehat{H}_0 = \left[\frac{\hat{P}^2}{2I_B} + (\frac{1}{2I_A} - \frac{1}{2I_B})\hat{P}_a^2\right]$$

The eigenvalues for the angular momentum operators P^2, P_z, P_Z for the symmetric top molecules are given by,

$$\langle J, K, M|P^2|J, K, M\rangle = \hbar^2 J(J+1)$$

$$\langle J, K, M|P_z|J, K, M\rangle = \hbar K$$

$$\langle J, K, M|P_Z|J, K, M\rangle = \hbar M$$

Where, J is the angular momentum quantum number, K is the projection of J on body fixed axis (a/c) and M is the projection of J on space fixed axis (Z).

$$J = 0, 1, 2, 3, \ldots$$

$$K = 0, \pm 1, \pm 2, \pm 3, \ldots, \pm J$$

$$M = 0, \pm 1, \pm 2, \pm 3, \ldots, \pm J$$

In the *x*, *y*, *z* system, *z* is chosen as the symmetry axis and in the *a*, *b*, *c* system, *z* becomes *a* for the prolate top, and *z* becomes *c* for the oblate top.

By solving the Hamiltonian, the energy of a prolate top obtained is given by:

$$E_{JK} = BJ(J+1) + (A-B)K^2 \quad (For\ a\ prolate\ top)$$

Similarly, for an oblate top, the Hamiltonian becomes,

$$\hat{H}_0 = \left[\frac{\hat{P}^2}{2I_B} + (\frac{1}{2I_C} - \frac{1}{2I_B})\hat{P}_c^2\right]$$

And the energy corresponding to an oblate top is given by solving above Hamiltonian:

$$E_{JK} = BJ(J+1) + (C-B)K^2 \quad (For\ a\ prolate\ top)$$

Due to K^2 term in the energy expression for prolate and oblate tops, all the *K* levels except those for *K=0* are doubly degenerate.

In symmetric tops, a permanent dipole moment must lie along the symmetry axis. The selection rules for the symmetric top molecules are therefore:

$$\Delta J = 0, \pm \ and \ \Delta K = 0$$

1.2.1.4 Asymmetric Tops:

Most molecules are asymmetric tops and in this type of molecules, all principal moments of inertia are not equal.

$$I_a \neq I_b \neq I_c$$

The pure rotational spectrum becomes very complex for asymmetric rotors and the rotational frequencies can no longer be expressed in simple equations as previously shown for linear and symmetric top molecules.

For prolate near-symmetric tops, the three moments of inertia has the following relation,

$$I_c \approx I_b > I_a$$

And the majority of the asymmetric top molecules are prolate near-symmetric tops. For oblate-near symmetric tops:

$$I_c > I_b \approx I_a$$

In asymmetric tops, P_z no longer commutes with the Hamiltonian as there is no internal component of the angular momentum that is a constant of motion in the asymmetric rotors. Therefore, K is no longer good quantum number and only J and M remain good quantum numbers. However, the asymmetric rotor energy levels could be labelled in terms of the limiting K values in prolate and oblate limit, as the moments of inertia for every molecule must lie within this limit. Hence the rotational transitions are labelled as:

$$J'_{K'_{-1}K'_{+1}} \rightarrow J''_{K''_{-1}K''_{+1}}$$

The single prime (') indicates the upper state and double prime (") the lower state. K_{-1} and K_{+1} are the limiting cases of prolate and oblate tops. The K levels are no longer degenerate for asymmetric tops.

The allowed changes in J for dipole absorption of radiation are:

$$\Delta J = 0, \pm 1$$

For an asymmetric top molecule, there are three dipole moment components, μ_a, μ_b, and μ_c along the principal axes. Each of the three changes in the dipole component might give rise to an absorption line. The selection rules are given in the *Table 1-2*.

Table 1-2: Selection rules for ΔK_{-1} and ΔK_{+1}.

Dipole Component	$\Delta K_{-1}=0$	$\Delta K_{+1}=0$
$\mu_a \neq 0$ (along axis of least moment of inertia)	0, ±2, …	±1, ±3, …
$\mu_b \neq 0$ (along axis of intermediate moment of inertia)	±1, ±3, …	±1, ±3, ...
$\mu_c \neq 0$ (along axis of greatest moment of inertia)	±1, ±3, …	0, ±2, …

The Ray's asymmetry parameter,[37] κ, is used to define the asymmetry of the molecules quantitatively and it is given by;

$$\kappa = \frac{2B - A - C}{A - C}$$

Here, A, B, and C represent the rotational constants. The limiting value of κ is -1 and +1 which correspond to the prolate and oblate symmetric tops, respectively. If $\kappa = 0$, then molecule shows the highest degree of asymmetry. The energy levels of an asymmetric tops can also be expressed as a function of κ. Notably, higher K_{-1} values correspond to higher energy levels for prolate tops, whereas, for oblate tops, higher K_{-1} levels are associated with lower energies. The correlation diagram for asymmetric top energy level is shown in

Figure 1-1.

For a rigid asymmetric top molecule the Hamiltonian is given by,

$$\hat{H} = AP_a^2 + BP_b^2 + CP_c^2$$

The above Hamiltonian can be rearranged as a function of κ,

$$\hat{H} = \frac{1}{2}(A + C)P^2 + \frac{1}{2}(A - C)\hat{H}(\kappa)$$

Where $\hat{H}(\kappa)$ is the reduced Hamiltonian,

$$\hat{H}(\kappa) = P_a^2 + \kappa P_b^2 - P_c^2$$

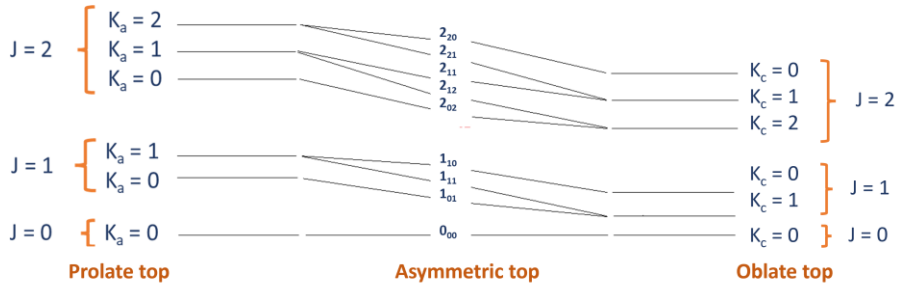

Figure 1-1: Correlation diagram of the energy levels of an asymmetric top.

1.2.2 Centrifugal Distortion Constants:

The initial formulation discussed in the previous sections of this chapter assume that the molecules are rigid. However, in reality the nuclei are held together by finite restoring forces. Therefore, when a molecule experiences a centrifugal force due to rotation, the

bond length and angles will vary, and this effect will give rise to a centrifugal distortion. For example, in the CH_3F molecule, the rotation about the symmetry axis will lead to the lengthening of the C-H bond and increase of $\angle FCH$ angle, because of the rotation about its C_3 axis. However, the end-over-end rotation would give rise to the closing of the methyl group umbrella and a stretching of the *C-F* bond. Centrifugal distortion is more important in microwave spectra of asymmetric rotor than symmetric tops. In case of symmetric rotor, the shifts in rotational frequencies of 1 megacycle or less is produced whereas in the case of asymmetric top molecules, many hundreds of megacycle change are rotational frequencies is observed. These large shifts in asymmetric top molecules can be attributed to the fact that, in asymmetric rotors, the rotational transitions may occur between the states of rather large angular momentum and of very large rotational energy.

For asymmetric rotors, the expression for first order energy can be represented as follows:

$$E = E_r + E_d$$

In this equation, E_r signifies the energy of a rigid rotor. The definition of E_d incorporates five distortion constants, namely Δ_J, Δ_{JK}, Δ_K, δ_J, and δ_K.

$$E_d = -\Delta_J J^2(J+1)^2 - \Delta_{JK} J(J+1)\langle P_z^2\rangle - \Delta_K\langle P_z^4\rangle - 2\delta_J J(J+1)\langle P_x^2 - P_y^2\rangle - \delta_K\langle P_z^2(P_x^2 - P_y^2) + (P_x^2 - P_y^2)P_z^2\rangle$$

To fit the experimental data for asymmetric tops, Watson's reduced Hamiltonian is employed.[39] Watson developed two distinct reductions for asymmetric top molecules, known as *A*-reduction and *S*-reduction. While *A*-reduction, or asymmetric reduction, yields imprecise outcomes for nearly symmetric asymmetric molecules, *S*-reduction, also referred to as symmetric reduction, should be employed in such cases.

1.2.3 Large Amplitude Motions:

Large amplitude motion entails significant changes in structure, such as torsional rotations, inversions, and puckering. These dynamic movements have the potential to induce conformational changes, thereby influencing the physical and chemical properties of a molecule. It is imperative to acknowledge that molecules are not characterized by

rigidity; rather, they possess the capability to undergo a multitude of internal motions, which in turn affect their moments of inertia. All these large amplitude motions affect the rotational energy levels and hence the rotational spectrum observed. Analysis of rotational spectrum can give information about frequency of these large amplitude motions and potential barriers between conformers. In this section, the various large amplitude motions in a molecule/complex that affect the rotational transitions are discussed.

1.2.3.1 Internal Rotation of Methyl Group:

In molecules containing two groups connected by a single bond, there exists the potential for these groups to rotate relative to one another around this bond. For example, in CH_3-CF_3 molecule, the rotation may take place between two planes, first plane is defined by the C-C bond and a specifically chosen C-H bond, and the other plane is defined by the C-C bond and one of the C-F bonds of the CF_3 group.

The barrier height plays a significant role in this internal motion of the methyl groups about the C-C bond. When the barrier is high, the motion involves simple harmonic torsional oscillation, while a low barrier allows nearly free rotation around the C-C bond. These internal motions, however, impact the overall rotational behaviour, leading to the observed transitions being split. The fine structure observed in spectra is directly influenced by the potential barrier's height, which impedes such motions. The information obtained from rotational spectra is valuable in understanding the height of barriers associated with these internal motions.

The internal rotation of two parts of a molecule relative to each other can be characterized by the parameter α, referred to as the internal rotation angle or torsional angle. The potential energy surface associated with the internal rotation of a CH_3 group can be mathematically represented as a periodic function of α. This function exhibits periodicity at 120-degree intervals, corresponding to $2\pi/N$, where N denotes the rotational group's N-fold symmetry. For CH_3 rotation, N equals 3, and the potential energy surface can be mathematically expressed as follows:

$$V(\alpha) = \frac{V_3}{2}(1 - cos3\alpha) + \frac{V_6}{2}(1 - cos6\alpha) + \cdots$$

Generally, only first term of the cosine expansion is retained:

$$V(\alpha) = \frac{V_3}{2}(1 - cos3\alpha)$$

To illustrate this further, the V_3 barrier to internal rotation was calculated for methanol at the MP2/aug-cc-pVDZ level and the sinusoidal shape of this periodic hindering potential is shown in *Figure 1-2*. This has a minimum value of zero at α = 0, ±2π/3, ±4π/3, …, and a maximum value of V_3 at α = ±π/3, ±π, ±5π/3, … and so on.

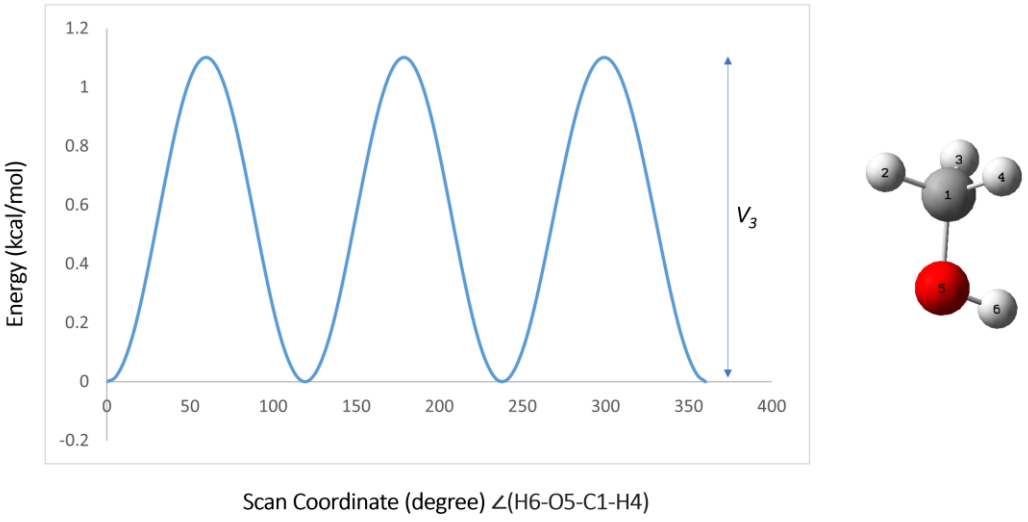

Figure 1-2: Calculated representation of the V_3 hindering potential in methanol. Identical minima are repeated over 120˚ rotations of the (H_6-O_5-C_1-H_4) dihedral angle.

If the variation of the potential is α, the torsional energy levels for a system with internal rotation of a three-fold group are given by,

$$-F\frac{d^2U(\alpha)}{d\alpha} + \left[\frac{V_3}{2}(1 - cos3\alpha) - E\right]U(\alpha)$$

Where, α is the angle of internal rotation, V_3 is the height of the barrier having threefold symmetry which hinders the internal rotation, and F is the rotational constant which is given by the equation: $F = \frac{\hbar^2}{2I_r}$, in which, I_r is the reduced moment of inertia for the relative motion of the two groups, $\left(I_r = \frac{I_\alpha I_\beta}{I_\alpha + I_\beta}\right)$.

In case of CH_3-CF_3 molecule, the I_α and I_β are the moments of inertia of the two tops. The solution of the above differential equation yields the eigen values E and the eigenfunctions $U(\alpha)$.

For deriving the torsional energy expressions, we consider two extremes' conditions: For very small barrier i.e., $V_3 \rightarrow 0$, which will result in free rotation:

$$\frac{d^2U(\alpha)}{d\alpha} + \left(\frac{1}{F}\right)EU(\alpha) = 0$$

The solution for the above equation is given by:

$$U(\alpha) - Ae^{im\alpha} = A\big(cos(m\alpha) + i\, sin(m\alpha)\big)$$

Where A is the normalization factor the energy is given by:

$$E = Fm^2$$

m is the internal rotation quantum number, and which can take values of 0, ±1, ±2, ±3… and so on.

In the case of a very high barrier, $V_3 \rightarrow \infty$, the internal motions will be restricted to small oscillations about the minima of the barrier. For small values of α, the cosine functions are expanded as:

$$cos3\alpha = 1 - \left(\frac{9}{2}\right)\alpha^2 + \left(\frac{27}{8}\right)\alpha^4 + \cdots$$

And therefore,

$$V(\alpha) = \left(\frac{9}{4}\right)V_3\alpha^2 - \left(\frac{27}{16}\right)V_3\alpha^4 + \cdots$$

For a harmonic approximation, the first term of the above expansion retains:

$$\frac{d^2U(\alpha)}{d\alpha^2} + \frac{1}{F}\left[E - \frac{1}{2}\left(\frac{9}{2}V_3\right)\alpha^2\right]U(\alpha) = 0$$

The above expression has the same form as the simple harmonic oscillator wave equation.

The solution is given by:

$$E = 3(V_3F)^{1/2}\left(v + \frac{1}{2}\right)$$

Where, $\vartheta = 0, 1, 2, 3, \ldots$.

The torsional levels approximate those of a harmonic oscillator with frequencies.

$$\vartheta = \frac{3}{2\pi}\left(\frac{V_3}{2I_r}\right)^{1/2}$$

This expression of the frequency of torsional oscillation provides the basis for determination of the barrier by infrared studies or microwave intensity studies.

1.2.3.2 Inversion and Tunnelling:

Based on the principles of quantum mechanics, it has been established that molecules characterized by a pyramidal XY_3 symmetry possess the inherent ability to engage in an inversion motion. This motion is similar to an umbrella that inverts, leading to the terminology inversion. This inversion configuration can be rigorously derived by applying a mathematical operation that changes the sign of the coordinates of all constituent particles, as measured from the centre of mass. *Figure 1-3* provides the inversion potential curve for the NH_3 molecule. When plotting the potential energy as a function of the distance between the N atom and the H_3 plane, two distinct minima become apparent. These minima correspond to the two equilibrium configurations that are entirely equivalent. The molecular wave functions, in turn, can be represented as linear combinations of ϕ_L and ϕ_R of those of the molecule in the equivalent right and left configurations. Their mathematical expressions are as follows:

$$\Psi_+ = \frac{1}{\sqrt{2}}(\phi_L + \phi_R)$$

$$\Psi_- = \frac{1}{\sqrt{2}}(\phi_L - \phi_R)$$

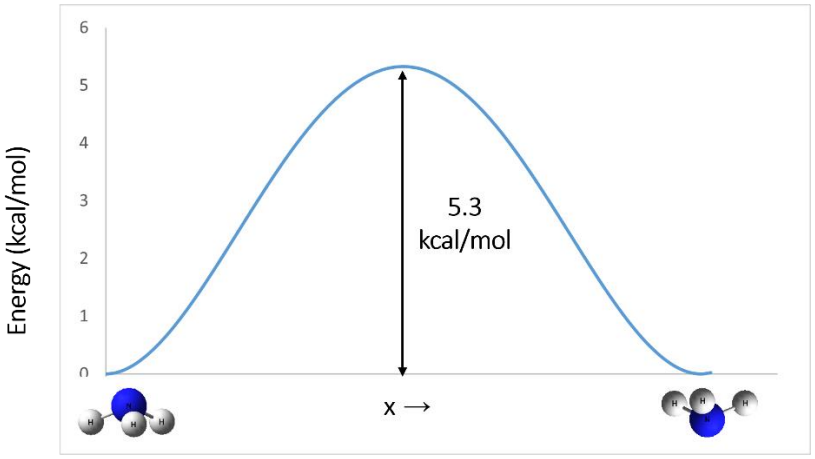

Figure 1-3: Potential energy curve of the NH_3 inversion calculated at M062X-aug-cc-pVDZ level of theory.

In cases where states exhibit an infinite barrier height, these are commonly denoted as degenerate states. However, when the barrier height is notably low, as in the case of NH_3, these two states are separated by a measurable interaction energy. In addition to the inversion motion, the molecule in question also demonstrates a symmetrical vibrational mode, wherein atom X undergoes oscillatory motion along the symmetry axis in contrast to the motion of the Y_3 atoms. In the first and second excited symmetrical modes, the vibrational energy for NH_3 falls below the energy barrier separating the two minima. However, for all other XY_3 molecules, the potential barrier separating vibrational and potential energy is considerably higher than the vibrational energy itself. Consequently, in lower symmetrical vibrational modes, the XY_3 molecule engages in vibrational motions within the potential valley on either side of the barrier. Classically, the molecule is incapable of undergoing inversion when in these vibrational states situated below the maximum potential. Nonetheless, from a quantum mechanical perspective, the molecule has the ability to achieve inversion transitions through a phenomenon known as "barrier tunnelling." The manifestations of barrier tunnelling, particularly with respect to the internal rotation and torsional oscillation of groups within symmetric-top and asymmetric-top molecules, are observable in microwave spectra. A detailed exposition of these phenomena can be found in Chapter XII of the book titled "Microwave Molecular Spectra" by Gordy and Cook.[36]

1.2.4 Structure Determination:

The employment of microwave spectroscopy allows for the determination of a structure that possesses broad applicability and high precision. Through the utilization of experimentally derived rotational constants, the Ray's asymmetry parameter provides a quantitative assessment of the asymmetry of an asymmetric top. The principal moments of inertia, which are inversely proportional to the rotational constants, are used to get the structural information of molecules/complexes.

In order to obtain an accurate structure, it is necessary to carry out spectral measurements and assignments for various isotopologues.

1.2.4.1 Inertial Defects and Planar (Second) Moments:

The inertial defect, denoted as Δ, serves as a valuable parameter for assessing the planarity of a molecule or complex, and it is calculated as follows:

$$\Delta = I_c - I_a - I_b$$

In an ideal scenario, the inertial defect of a planar molecule should be zero. However, it is anticipated that deviations from this will occur for molecules exhibiting low-energy large amplitude vibrations. In a broader context, in-plane molecular vibrations contribute positively to the inertial defect, while out-of-plane molecular vibrations yield negative values. To gain more insights into the structure of a molecule or complex, the planar (or second) moments, P_{aa}, P_{bb}, and P_{cc}, are frequently computed.[40] These moments establish a basis for direct comparisons and are interconnected with the principal moments of inertia through the following expressions:

$$P_{aa} = \sum_i m_i\, a_i^2 = (I_b + I_c - I_a)/2$$

$$P_{bb} = \sum_i m_i\, b_i^2 = (I_a + I_c - I_b)/2$$

$$P_{cc} = \sum_i m_i\, c_i^2 = (I_a + I_b - I_c)/2$$

1.2.4.2 Substitution Structure (rs) and Kraitchman Equations:

Kraitchman introduced a method to accurately determine the location of an atom within a molecule by analysing changes in moments of inertia caused by replacing a single isotope of the atom.[41] This particular approach assumes that the molecular framework remains unaltered by the substitution of the isotope. However, it is important to acknowledge that this assumption does not hold valid in the situation of H/D substitution, as the introduction of deuterium leads to significant change in zero-point vibrations, and the average X-D bond length decreases compared to X-H bond length. In the instance of a non-planar asymmetric top molecule, the coordinate of the substituted atom can be established in the following manner:

$$|a| = \left[\frac{\Delta P_a}{\mu}(1+\frac{\Delta P_b}{I_a - I_b})(1+\frac{\Delta P_c}{I_a - I_c})\right]^{\frac{1}{2}}$$

$$|b| = \left[\frac{\Delta P_b}{\mu}\left(1+\frac{\Delta P_c}{I_b - I_c}\right)\left(1+\frac{\Delta P_x}{I_b - I_a}\right)\right]^{\frac{1}{2}}$$

$$|c| = \left[\frac{\Delta P_c}{\mu}\left(1+\frac{\Delta P_a}{I_c - I_a}\right)\left(1+\frac{\Delta P_b}{I_c - I_b}\right)\right]^{\frac{1}{2}}$$

where, $\Delta P_a = \frac{1}{2}(-\Delta I_a + \Delta I_b + \Delta I_c)$, $\Delta P_b = \frac{1}{2}(-\Delta I_b + \Delta I_c + \Delta I_a)$, and $\Delta P_c = \frac{1}{2}(-\Delta I_c + \Delta I_a + \Delta I_b)$

$\Delta I_a = I_a' - I_a$ and so on. The I_a, I_b, I_c and I_a', I_b', I_c' are the principal moment of inertia of the parent and isotopically substituted molecules respectively.

The above-mentioned equations are implemented in the KRA program[42] which is available on the PROSPE website.

1.2.4.3 Ground State or Effective Structure (r_0):

The effective structures (r_0), also known as ground state structure, are determined by performing a least square fitting of structural parameters to the moments of inertia that are experimentally determined. These moments of inertia are obtained from the rotational constants at zero-point energy level of the available isotopologues. In order to obtain the

structural parameter, a large number of isotopologues are often required. The method does not consider changes that may be induced to the structure by isotopic substitution or large amplitude motions. The STRFIT program[43] has been commonly employed for symmetric and asymmetric top molecules.

1.2.5 Spectral Predictions and Fitting:

To perform spectral prediction in the cavity-based Balle-Flygare Fourier transform microwave spectrometer (BF-FTMW), it is necessary to have a well-estimated structure in order to search for transitions. The rotational constants, centrifugal distortion constants, and dipole moment components along the three principal axes are determined through quantum chemical calculations using DFT and *ab-initio* methods. These parameters are then used to predict the transition frequencies. In the operating range of the spectrometer, a Fortran program called ASROT,[44] which can be found on the PROSPE website[45], is utilized to predict the transition frequencies. Subsequently, the observed rotational transitions are fitted to an appropriate Hamiltonian using the ASFIT program,[46] allowing for the determination of experimentally observed rotational constants and the centrifugal distortion constants.

In the chirped-pulse Fourier transform microwave spectrometer (CP-FTMW), spectral analysis is conducted using the PGOPHER program developed by Watson.[47] This program incorporates Watson's *A*- and *S*-reduced Hamiltonians. PGOPHER enables the interactive visualization of broadband spectra alongside a simulation based on the calculated rotational constants. Neither PGOPHER nor ASFIT is equipped to handle internal motions such as internal rotation. For this purpose, the XIAM program[48] is utilized. XIAM, available on the PROSPE website, allows for the simultaneous fitting of *A*- and *E*-states. The implementation of *A*- and *S*-reduced Hamiltonians in XIAM and the fitting procedure are essentially similar to those of PGOPHER, with the exception of the absence of a graphical interface in XIAM.

1.3 Present Investigations:

This thesis investigates the structure of monomer and weakly bonded complexes through the use of rotational spectroscopy and various theoretical methodologies. CHAPTER 2 provides a comprehensive overview of the experimental techniques employed in rotational spectroscopy, including Balle Flygare Fourier transform microwave spectrometers and chirped pulse Fourier transform microwave spectrometers.

Additionally, this chapter discusses various theoretical methods, for example, Atoms in Molecules (AIM), non-covalent interactions (NCI) index plots, and natural bond orbital (NBO) analyses to understand the nature of interaction present in the complex. The symmetry adapted perturbation theory (SAPT) is also discussed briefly, which has been used to get insights about the forces involves within molecular complexes.

The rotational spectra and dynamics of the phenylacetylene···methanol complex are presented in CHAPTER 3. This chapter confirms that the methanol donates hydrogen bond to the acetylenic π-system and accepts a weak hydrogen bond from the ortho hydrogen of the phenylacetylene. It has also been observed that the structure of the phenylacetylene with methanol is very similar to the structure with water molecule. The rotational transitions were split in the phenylacetylene···methanol complex due to the internal rotation of CH_3 group and the barrier for this rotation has been found to be 353.4 cm^{-1}.

We revisited the rotational spectrum of 1-fluoronaphthalene (1FN) monomer, and it is presented in the CHAPTER 4. We assigned all the singly substituted ^{13}C isotopologues of the 1FN monomer, revealing a nearly uniform inertial defect (-0.14 amu $Å^2$) across all isotopologues. We accurately determined the atomic coordinates of all the carbon atoms of 1FN using the substitution method. The observed negative inertial defect is attributed to the low out-of-plane bending mode of the 1FN ring. A formula based on empirical data was utilised for the computation of the lowest out-of-plane bending mode, which was then compared with the bending mode calculated using the MP2/aug-cc-pVTZ level of theory.

In CHAPTER 5, we studied the monohydrate and dihydrate complexes of 1FN. In the case of 1FN···H_2O, H_2O serves as a proton donor and participates in a C-H···O weak interaction where H_2O acts as a weak proton acceptor. The inertial defect of the 1FN···H_2O complex (measured experimentally as -1.30 amu $Å^2$) suggests a planar geometry. In the case of 1FN···$(H_2O)_2$, the preliminary analysis confirms a structure

where $(H_2O)_2$ interacts from the top of the 1FN plane, forming O-H···F and O-H···C hydrogen bonds.

CHAPTER 6 presents the study of the hydrogen bonding, inversion, and tunnelling of NH_3 in the complex with 18-crown-6 (CE). The NH_3@CE complex is interesting because the NH_3 molecule acts as an H-bond donor, which is rare in both gas phase and crystal structures. N-H···O hydrogen bonding interactions significantly influence the barriers for NH_3 inversion. The barrier for this inversion is 12.1 kcal/mol, compared to 5.3 kcal/mol for free NH_3. The configuration of the CE remains unchanged. A 1D relaxed scan and a 2D rigid scan were conducted to understand the tunnelling motion of NH_3 through the CE ring, yielding a barrier of approximately 11 kcal/mol.

APPENDIX A provides a comprehensive analysis of the preliminary examination of the 1FN···Ne complex. The initial findings pertaining to the $Ar(H_2S)_2(H_2O)$ complex are showcased in APPENDIX B, while APPENDIX C reports the preliminary outcomes obtained for the hexafluorobenzene···methanol complex.

1.4 References:

(1) Desiraju, G. R. Designer Crystals: Intermolecular Interactions, Network Structures and Supramolecular Synthons. *Chem. Commun.* **1997**, No. 16, 1475–1482. https://doi.org/10.1039/a607149j.

(2) Metrangolo, P.; Neukirch, H.; Pilati, T.; Resnati, G. Halogen Bonding Based Recognition Processes: A World Parallel to Hydrogen Bonding. *Acc. Chem. Res.* **2005**, *38* (5), 386–395. https://doi.org/10.1021/ar0400995.

(3) Desiraju, G. R. The C−H···O Hydrogen Bond: Structural Implications and Supramolecular Design. *Acc. Chem. Res.* **1996**, *29* (9), 441–449. https://doi.org/10.1021/ar950135n.

(4) Tang, K.; Toennies, J. P. Johannes Diderik van Der Waals: A Pioneer in the Molecular Sciences and Nobel Prize Winner in 1910. *Angew Chem Int Ed* **2010**, *49* (50), 9574–9579. https://doi.org/10.1002/anie.201002332.

(5) *The Nobel Prize in Physics 1910*. NobelPrize.org. https://www.nobelprize.org/prizes/physics/1910/summary/ (accessed 2024-02-06).

(6) Clapeyron, B. P. E. Memoir on the Driving Power of Heat. *Journal of the Royal Polytechnic School* **1834**, 153–190.

(7) Weast, R. C. *Handbook of Chemistry and Physics*, 53rd ed.; Chemical Rubber Pub, 1972.

(8) Pauling, L. *The Nature of Chemical Bonding*; Cornell University Press: Ithaka, 1960.

(9) Moore, T. S.; Winmill, T. F. CLXXVII.—The State of Amines in Aqueous Solution. *J. Chem. Soc., Trans.* **1912**, *101* (0), 1635–1676. https://doi.org/10.1039/CT9120101635.

(10) Latimer, W. M.; Rodebush, W. H. Polarity and Inonization from the Standpoint of the Lewis Theory of Valence. *Journal of the American Chemical Society* **1920**, *42*, 1419–1433.

(11) Arunan, E.; Desiraju, G. R.; Klein, R. A.; Sadlej, J.; Scheiner, S.; Alkorta, I.; Clary, D. C.; Crabtree, R. H.; Dannenberg, J. J.; Hobza, P.; Kjaergaard, H. G.; Legon, A. C.; Mennucci, B.; Nesbitt, D. J. Defining the Hydrogen Bond: An Account (IUPAC Technical Report). *Pure and Applied Chemistry* **2011**, *83* (8), 1619–1636. https://doi.org/10.1351/PAC-REP-10-01-01.

(12) Gutowsky, H. S.; Emilsson, T.; Arunan, E. Rotational Spectra, Structure, and Internal Dynamics of Ar–H2S Isotopomers. *The Journal of Chemical Physics* **1997**, *106* (13), 5309–5315. https://doi.org/10.1063/1.473066.

(13) Gutowsky, H. S.; Klots, T. D.; Chuang, C.; Keen, J. D.; Schmuttenmaer, C. A.; Emilsson, T. Rotational Spectra and Structures of the Small Clusters Ar3-HF and Ar3-DF. *J. Am. Chem. Soc* **1985**, *107*, 7174.

(14) Xu, Y.; Jäger, W.; Djauhari, J.; Gerry, M. C. L. Rotational Spectra of the Mixed Rare Gas Dimers Ne–Kr and Ar–Kr. *The Journal of Chemical Physics* **1995**, *103* (8), 2827–2833. https://doi.org/10.1063/1.470518.

(15) Grabow, J.-U.; Pine, A. S.; Fraser, G. T.; Lovas, F. J.; Suenram, R. D.; Emilsson, T.; Arunan, E.; Gutowsky, H. S. Rotational Spectra and van Der Waals Potentials of Ne–Ar. *The Journal of Chemical Physics* **1995**, *102* (3), 1181–1187. https://doi.org/10.1063/1.468904.

(16) Bauzá, A.; Frontera, A. Aerogen Bonding Interaction: A New Supramolecular Force? *Angewandte Chemie International Edition* **2015**, *54* (25), 7340–7343. https://doi.org/10.1002/anie.201502571.

(17) *π-Hole aerogen bonding interactions - Physical Chemistry Chemical Physics (RSC Publishing) DOI:10.1039/C5CP03272E*. https://pubs.rsc.org/en/content/articlehtml/2015/cp/c5cp03272e (accessed 2024-02-06).

(18) Bauzá, A.; Alkorta, I.; Elguero, J.; Mooibroek, T. J.; Frontera, A. Spodium Bonds: Noncovalent Interactions Involving Group 12 Elements. *Angewandte Chemie International Edition* **2020**, *59* (40), 17482–17487. https://doi.org/10.1002/anie.202007814.

(19) C. Legon, A. The Halogen Bond: An Interim Perspective. *Physical Chemistry Chemical Physics* **2010**, *12* (28), 7736–7747. https://doi.org/10.1039/C002129F.

(20) Clark, T.; Hennemann, M.; Murray, J. S.; Politzer, P. *Halogen bonding: the σ-hole | Journal of Molecular Modeling*. https://link.springer.com/article/10.1007/s00894-006-0130-2 (accessed 2024-02-06).

(21) Alkorta, I.; Blanco, F.; Solimannejad, M.; Elguero, J. Competition of Hydrogen Bonds and Halogen Bonds in Complexes of Hypohalous Acids with Nitrogenated Bases. *J. Phys. Chem. A* **2008**, *112* (43), 10856–10863. https://doi.org/10.1021/jp806101t.

(22) Wang, W.; Ji, B.; Zhang, Y. Chalcogen Bond: A Sister Noncovalent Bond to Halogen Bond. *J. Phys. Chem. A* **2009**, *113* (28), 8132–8135. https://doi.org/10.1021/jp904128b.

(23) Manna, D.; Mugesh, G. Regioselective Deiodination of Thyroxine by Iodothyronine Deiodinase Mimics: An Unusual Mechanistic Pathway Involving Cooperative Chalcogen and Halogen Bonding. *J. Am. Chem. Soc.* **2012**, *134* (9), 4269–4279. https://doi.org/10.1021/ja210478k.

(24) Bleiholder, C.; Werz, D. B.; Köppel, H.; Gleiter, R. Theoretical Investigations on Chalcogen−Chalcogen Interactions: What Makes These Nonbonded Interactions Bonding? *J. Am. Chem. Soc.* **2006**, *128* (8), 2666–2674. https://doi.org/10.1021/ja056827g.

(25) Scheiner, S. The Pnicogen Bond: Its Relation to Hydrogen, Halogen, and Other Noncovalent Bonds. *Acc. Chem. Res.* **2013**, *46* (2), 280–288. https://doi.org/10.1021/ar3001316.

(26) Del Bene, J. E.; Alkorta, I.; Sanchez-Sanz, G.; Elguero, J. Structures, Energies, Bonding, and NMR Properties of Pnicogen Complexes $H_2XP{:}NXH_2$ (X = H, CH_3, NH_2, OH, F, Cl). *J. Phys. Chem. A* **2011**, *115* (46), 13724–13731. https://doi.org/10.1021/jp2094164.

(27) Zahn, S.; Frank, R.; Hey-Hawkins, E.; Kirchner, B. Pnicogen Bonds: A New Molecular Linker? *Chemistry A European J* **2011**, *17* (22), 6034–6038. https://doi.org/10.1002/chem.201002146.

(28) Moilanen, J.; Ganesamoorthy, C.; Balakrishna, M. S.; Tuononen, H. M. Weak Interactions between Trivalent Pnictogen Centers: Computational Analysis of Bonding in Dimers $X_3E\cdots EX_3$ (E = Pnictogen, X = Halogen). *Inorg. Chem.* **2009**, *48* (14), 6740–6747. https://doi.org/10.1021/ic900635f.

(29) Solimannejad, M.; Gharabaghi, M.; Scheiner, S. SH···N and SH···P Blue-Shifting H-Bonds and N···P Interactions in Complexes Pairing HSN with Amines and Phosphines. *The Journal of Chemical Physics* **2011**, *134* (2), 024312. https://doi.org/10.1063/1.3523580.

(30) Mani, D.; Arunan, E. The X–C···Y (X = O/F, Y = O/S/F/Cl/Br/N/P) 'Carbon Bond' and Hydrophobic Interactions. *Phys. Chem. Chem. Phys.* **2013**, *15* (34), 14377. https://doi.org/10.1039/c3cp51658j.

(31) Thomas, S. P.; Pavan, M. S.; Guru Row, T. N. Experimental Evidence for 'Carbon Bonding' in the Solid State from Charge Density Analysis. *Chem. Commun.* **2014**, *50* (1), 49–51. https://doi.org/10.1039/C3CC47226D.

(32) Bauzá, A.; Mooibroek, T. J.; Frontera, A. Tetrel-Bonding Interaction: Rediscovered Supramolecular Force? *Angew Chem Int Ed* **2013**, *52* (47), 12317–12321. https://doi.org/10.1002/anie.201306501.

(33) Grabowski, S. J. Tetrel Bond–σ-Hole Bond as a Preliminary Stage of the S_N2 Reaction. *Phys. Chem. Chem. Phys.* **2014**, *16* (5), 1824–1834. https://doi.org/10.1039/C3CP53369G.

(34) Grabowski, S. Triel Bonds, π-Hole-π-Electrons Interactions in Complexes of Boron and Aluminium Trihalides and Trihydrides with Acetylene and Ethylene. *Molecules* **2015**, *20* (6), 11297–11316. https://doi.org/10.3390/molecules200611297.

(35) Townes, C. H.; Schawlow, A. L. *Microwave Spectroscopy*; 1984.

(36) Gordy, W.; Cook, R. L. *Microwave Molecular Spectra*.

(37) Ray, B. S. Über Die Eigenwerte Des Asymmetrischen Kreisels. *Zeitschrift für Physik* **1932**, *78* (1–2), 74–91.

(38) Hainer, R. M.; Cross, P. C.; King, G. W. The Asymmetric Rotor. VII. Extension of the Calculation of Energy Levels. *The Journal of Chemical Physics* **1949**, *17* (9), 826–836. https://doi.org/10.1063/1.1747406.

(39) Watson, J. K. G. Determination of Centrifugal Distortion Coefficients of Asymmetric-Top Molecules. III. Sextic Coefficients. *The Journal of Chemical Physics* **1968**, *48* (10), 4517–4524. https://doi.org/10.1063/1.1668020.

(40) Bohn, R. K.; Montgomery, J. A.; Michels, H. H.; Fournier, J. A. Second Moments and Rotational Spectroscopy. *Journal of Molecular Spectroscopy* **2016**, *325*, 42–49. https://doi.org/10.1016/j.jms.2016.06.001.

(41) Kraitchman, J. Determination of Molecular Structure from Microwave Spectroscopic Data. *American Journal of Physics* **1953**, *21* (1), 17–24. https://doi.org/10.1119/1.1933338.

(42) KRA Program. http://info.ifpan.edu.pl/~kisiel/struct/struct.htm#kra.

(43) *STRucture FITting to rotational data (STRFIT)*. http://info.ifpan.edu.pl/~kisiel/struct/struct.htm#strfit (accessed 2023-08-30).

(44) *Asymmetric Rotor Programs*. http://info.ifpan.edu.pl/~kisiel/asym/asym.htm#asrot (accessed 2024-02-06).

(45) *PROSPE - Programs for ROtational SPEctroscopy*. http://info.ifpan.edu.pl/~kisiel/prospe.htm#table_of_programs (accessed 2023-08-30).

(46) *Asymmetric Rotor Programs*. http://info.ifpan.edu.pl/~kisiel/asym/asym.htm#asfit (accessed 2024-02-06).

(47) Western, C. M. PGOPHER: A Program for Simulating Rotational, Vibrational and Electronic Spectra. *Journal of Quantitative Spectroscopy and Radiative Transfer* **2017**, *186*, 221–242. https://doi.org/10.1016/j.jqsrt.2016.04.010.

(48) Hartwig, H.; Dreizler, H. The Microwave Spectrum of Trans-2,3-Dimethyloxirane in Torsional Excited States. *Zeitschrift für Naturforschung A* **1996**, *51* (8), 923–932. https://doi.org/10.1515/zna-1996-0807.

CHAPTER 2

Experimental and Computational Methods

CHAPTER 2 | Experimental and Computational Methods |

2.1 Brief History of Microwave Spectroscopy:

The microwave region of the electromagnetic spectrum is shown in *Figure 2-1*. The microwave region encompasses wavelengths ranging from 30 cm to 0.3 mm, or in terms of frequency, it spans from 1 GHz to 1000 GHz. In the initial stage of microwave spectroscopy, measurements were conducted within the cm wave region utilising oscillators and detectors that were specifically developed for microwave radar (radio detection and ranging) during the Second World War.[1] Microwaves are suitable for radar applications because of their shorter wavelengths, which provide enhanced resolution and accuracy compared to longer radio waves.

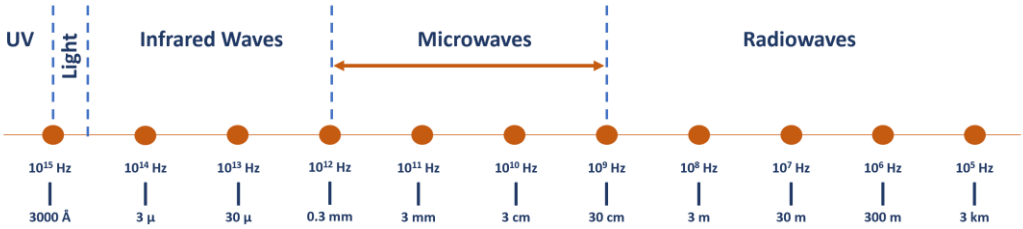

Figure 2-1: Chart showing the extent of the microwave region of the electromagnetic spectrum.

The first spectroscopic experiment involving microwave radiation was conducted in 1934 by Cleeton and Williams.[2] They recorded the microwave spectrum of ammonia in the 1-4 cm wavelength region, probing the inversion vibrational mode of ammonia.[2] To generate microwave radiation, they utilised magnetron-type oscillators as a continuous short-wave radiation source. Later, the advancements and developments of crystal harmonic generators and crystal diode detectors led the MW region to extend throughout mm and sub-mm wavelengths.[1] Post World War II, scientists further refined and expanded the applications of microwave spectroscopy, particularly in the study of molecular structures. This technique proved increasingly valuable in providing insights into bond lengths, bond angles, and other molecular parameters.

During the 1950s, low-intensity spontaneous emission lines were not observable in the microwave or radiofrequency region. However, later, with the invention of the maser, observation of MW spectral lines through stimulated emission became common.[3] For the seminal contributions made in the field of quantum electronics that led to the development of oscillators and amplifiers based on the maser-laser principle, Charles H. Townes was awarded the Nobel Prize in Physics in 1964. In the 1970s, Ekkers and Flygare conducted an experiment using advanced electronics and vacuum technology and developed Fourier transform microwave spectroscopy,[4] like the more popular Fourier transform nuclear magnetic resonance, in the radiowave. This included a Fabry-Perot cavity kept in vacuum with one stationary mirror and a movable mirror. Gaseous sample could be introduced into this cavity, which could be tuned to specific frequencies. If the sample absorbs this frequency, it leads to a free induction decay, which could be detected in time-domain which on Fourier transformation gives the frequency spectrum. Later, in 1981, a spectrometer was introduced that incorporated a molecular beam for supersonic expansion with the Fourier transform microwave spectrometer.[5] This technique offered high resolution and sensitivity by achieving low internal temperatures of a few Kelvins and shifting the population to low-energy rotational states. Consequently, rotational transitions with high intensity were observed. The measurement of molecular emissions in the time domain and subsequent Fourier transformation to the frequency domain significantly improved the spectral resolution and signal-to-noise ratio of the measured spectra. The main limitation of Balle-Flygare type spectrometers is their bandwidth, which is about ~1 MHz only. Hence, recording the microwave spectrum of a molecule involved laborious scanning of several GHz spectral ranges, 1 MHz at a time. In 2008, Pate and coworkers introduced the Chirped Pulse Fourier Transform Microwave (CP-FTMW) spectrometer, marking a breakthrough in the field of rotational spectroscopy.[6] This spectrometer incorporates an arbitrary waveform generator (AWG) and travelling wave tube (TWT) amplifiers. The AWG generates chirped microwave pulses, enabling the scanning of large bandwidths up to 12 GHz in a single spectral acquisition, while the TWT provides sufficient power to polarise the entire bandwidth with minimal losses. In this Thesis, both the Balle-Flygare Fourier transform microwave spectrometer at the Indian Institute of Science Bangalore, India, and the chirped pulse Fourier transform microwave spectrometer at Newcastle University, United Kingdom, were utilised.[7–9] This chapter provides a brief discussion of both spectrometers and their functionalities.

2.2 Belle-Flygare Fourier Transform Microwave Spectrometer:

Belle-Flygare Fourier transform microwave spectrometer (BF-FTMW) is categorised into two parts: mechanical and electrical. A more detailed description of the spectrometer at Bangalore is given elsewhere.[7] A brief description of the spectrometer's design and operation is given below.

2.2.1 Mechanical Design of the BF-FTMW spectrometer:

The mechanical design of the BF-FTMW spectrometer is given in *Figure 2-2*. The vacuum chamber of the spectrometer is made of stainless steel (SS 304), which is 1000 mm long and has a diameter of 850 mm. The chamber contains two identical spherical aluminium mirrors, and these mirrors are coaxially mounted on three rods. These aluminium mirrors are made from 65 mm thick aluminium disks and have a diameter of 500 mm. The radius of curvature of the mirror is 800 mm. These aluminium mirrors are highly polished to ensure that the surface roughness and the radius are good to 1 micron. The lower frequency cutoff of the spectrometer is limited by Fresnel's condition, which is given by the following expression:

$$\frac{a^2}{R\lambda} \geq 1$$

here, a is the mirror radius, and R is the radius of curvature. These two factors determine the lowest wavelength of the spectrometer. The lower cut-off is 3.8 GHz in the current spectrometer. However, transitions as low as 2447.8427 MHz for the Ar···H_2S complex have been observed in the spectrometer.[10] The current operating range of the spectrometer is 2-26 GHz.

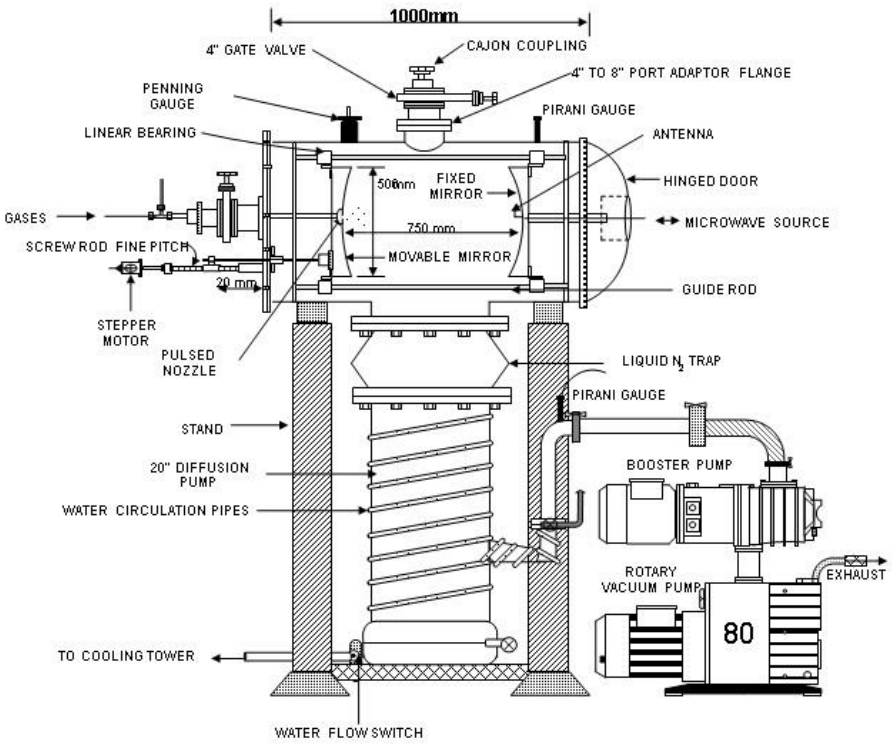

Figure 2-2: The mechanical design of the BF-FTMW spectrometer. Taken with permission from Dr Arijit Das's Thesis.[11]

In the chamber, one of the two mirrors is fixed, and the other is movable. The distance of the movable mirror can be varied from 630 mm to 730 mm. A fine-pitch linear screw rod which has a pitch of 5 mm, holds the movable mirror. The mirror movement is controlled by a stepper motor (*103H8221-5041, Sanyo Denki, Japan)* and a stepper motor driver (*MicroLOGIX Driver MSB-403*). For a complete rotation, the stepper motor takes 4000 steps. Therefore, the mirror moves by 1.25 micron in each step.

The resonant frequencies of the prominent TEM_{mnq} modes are provided by the following relation.

$$\nu = \frac{c}{2d}\left[(q+1) + \left(\frac{1}{\pi}\right)(m+n+1)cos^{-1}\left(1-\frac{d}{R}\right)\right]$$

where R is the mirror's radius of curvature, d is the distance between the two mirrors, m, n, and q are the cavity modes, ν_0=c/2d, and (q+1) denotes the number of half wavelength in the cavity. The TEM_{00q} modes are used in our experiment.

The fixed mirror has a small hole at its centre. An SMA female connector at one end goes through this hole, and an L-shaped antenna is connected to this SMA connector inside the vacuum chamber. A coaxial cable is connected to the other end of the SMA connector, and microwave radiation can be transmitted and received from this antenna. The coaxial cable has a hermetically sealed SMA connector at the other end so that microwave power can be coupled in and out of the cavity at the vacuum chamber. The same antenna is used for both sending and receiving the signal. The working frequency range of the antenna depends on its length,

$$L = \frac{\lambda}{4}$$

A suitable antenna for a specific range can be designed by varying the wire length using the above relationship.

A 20" oil diffusion pump (*Vacuum Techniques, Bangalore, India*) with a 10,000 l s^{-1} pumping speed is used to evacuate the chamber. Water circulation around the diffusion pump is used to cool it since the diffusion pump produces heat while it runs continuously. The diffusion pump is supported by a belt-less rotary pump (*Boc Edwards, E2M80*) and a roots blower (*Boc Edwards, EH 250*). Together, the two pumps have a backing capacity of 4000 l s^{-1}. The chamber can be evacuated by the pumps to 10^{-6} mbar. There are two gauges used to track the cavity's pressure. Pressure may be measured to as low as 10^{-3} mbar with the Pirani gauge and as low as 10^{-6} mbar with the Penning gauge.

2.2.2 Electrical Design of the BF-FTMW spectrometer:

The spectrometer's electrical circuit is composed of two components, as depicted in *Figure 2-3*. The first component is the polarization circuit, while the second component is the detecting circuit. Each component is assigned a model number enclosed in parentheses. The microwave source utilized is a signal generator (*Keysights, MXG, N5183 A*) with a resolution of 0.01 Hz, capable of producing frequencies ranging from 100 kHz to 32 GHz with an accuracy of 0.01 Hz.

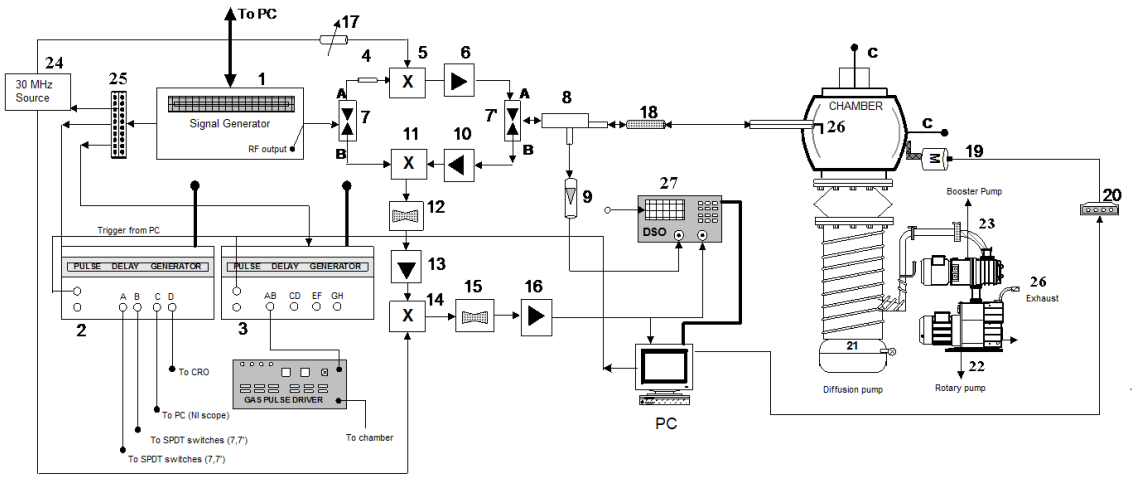

Figure 2-3: Electrical design of the PN-FTMW spectrometer at IISc Bangalore. Taken with permission from Dr Arijit Das's Thesis.[11]

1. Signal generator ***(****Keysights, MXG, N5183 A*), **2.** Delay generator *(BNC-575)*, **3**. Dealy generator *(SRS DG645),* **4**. Attenuator *(HP, 8493C, 3dB);* **5**. *SSBM (Mitteq, SMO-226LC1A),* **6**. Low noise amplifier *(Miteq, JS4-02002600-30-10P),* **7.** SPDT switch *(Sierra Microwave),* **8.** Directional coupler *(Narda, 1.7-26.5-4227-16)*, **9.** Diode detector *(HP, 0.01-26.5 GHz, 8473C)*, **10.** Low noise amplifier *(Miteq, JS4-02002600- 30-10P),* **11.** IRM *(Miteq, IRO-0226LC1A),* **12.** Band pass flier (Mini circuits, BBP-30), **13**. RF amplifier *(Mini circuits, ZFL-500LN),* **14**.RF mixer *(Mini Circuit, ZAD-1)*, **15.** Low pass filter *(Mini circuits, BLP-5),* **16.** RF amplifier *(HD communication corporation, HD 17153BB)*, **17**. Attenuator *(Mini Circuit, ZAFT-51020)*. **18.** Blocking capacitor *(HP, 11742A)*, **19**. Stepper *motor (103H8221-5041, Sanyo Denki, Japan),* **20.** Stepper driver *(*MicroLOGIX Driver MSB-403*)* **21.** Diffusion pump *(Vacuum Techniques, Bangalore, India)* **22**. Rotary pump *(Boc Edwards, E2M80)* **23**. Booster pump *(Boc Edwards, EH 250)* **24**. Distribution amplifier (SRS, FS710), **25**. Antenna (custom made) **26**. Exhaust **27.** Digital storage oscilloscope *(Tektronix TDS 2022)*

The RF output (*v*) generated by the signal generator is received by a 60 dB single-pole-double-throw (SPDT) switch (*Sierra Microwave, 0.5-26.5 SFD0526-00*). This output can be routed either to an image rejection mixer (*Miteq, IRO-0226LC1A*) or a single sideband mixer (SSBM) (*Miteq, SMO-226LC1A*). During a polarization cycle, the output is sent to the SSBM, where it is mixed with a synchronous 30 MHz (intermediate frequency)

signal from a function generator (*SRS, DS345*). The SSBM generates an upper band output of ν+30 MHz. This signal is then amplified by a low noise amplifier (*Miteq, JS4-02002600-30-10P*) with a gain of 30 dB. The amplified signal passes through another identical SPDT switch. Both SPDT switches operate synchronously with the polarization and detection circuits and are controlled by a delay generator (*BNC 575*). The delay generator simultaneously sends two pulses of typically microsecond duration to the SPDT switches, each with different polarities. The switch output then passes through a directional coupler (*Narda, 1.7-26.5-4227-16*), which directs the signal to the antenna via a DC block. The molecules are polarized by the signal, and if they absorb the designated frequency, they emit microwave radiation of frequency ν+30±Δ MHz in a coherent manner, where Δ represents the offset from ν+30 MHz. The signal is detected using the same antenna and directed towards the directional coupler, which redirects 2.5% of the signal to a diode detector (*Hewlett-Packard, 0.01-26.5 GHz, 8473C*), output of which is connected to the oscilloscope *(Tektronix TDS 2022)*. During the experiment at a given frequency, it is crucial to tune the cavity; when the cavity is not tuned, it is an open circuit and the microwave power will be reflected. When the cavity is tuned to a particular frequency, standing waves are generated. This particular adjustment necessitates the precise placement of the two mirrors at a distance equivalent to integral multiples half-wavelength. To accomplish this task, the movable mirror is appropriately calibrated with the aid of a stepper motor, which is controlled by the LabVIEW program. Once the cavity has been correctly tuned, a decrease in reflected microwave power becomes observable. *Figure 2-4* depicts the representation of the oscilloscope's output, which showcases both a tuned and untuned cavity.

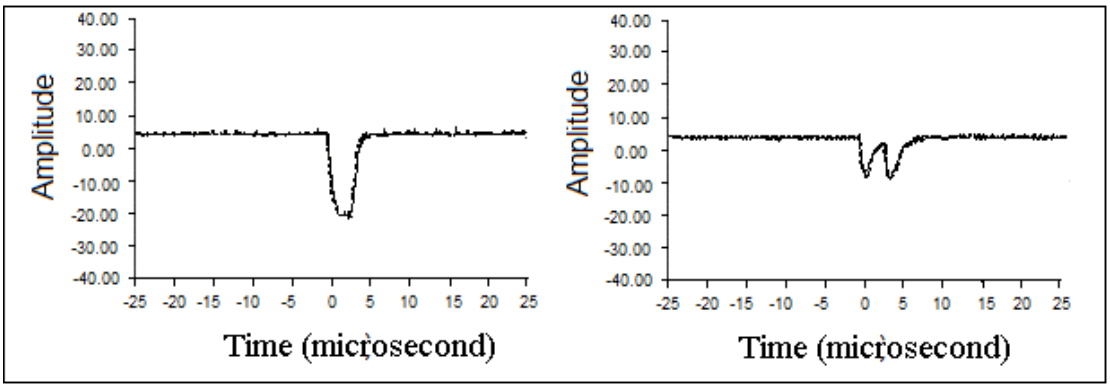

Figure 2-4: Reflected power signal on the oscilloscope in both not tuned (Left) and tuned (Right) states. Taken with permission from Dr Arijit Das's Thesis.[11]

The remaining 97.5% of the power is utilised for the detection of microwave transitions. Initially, the power passes through a low noise amplifier (*Miteq JS4-02002600-30-10P*, with a gain of 30 dB) via the SPDT switch. Subsequently, the amplified signal is mixed with the signal generator's output (ν) using an image rejection mixer (IRM). The IRM effectively removes the ν component from the ν+30±Δ MHz output, resulting in a 30±Δ MHz signal. This signal is then directed to a 30 MHz bandpass filter (*Mini-Circuits, BBP-30*) and a low-noise RF amplifier (*Mini-Circuits, ZFL-500LN*). Lastly, the signal is down-converted to ±Δ MHz by mixing it with the 30 MHz output from the function generator in an RF mixer *(Mini-Circuits, ZAD-1)*. The ±Δ signal is transmitted to the low pass filter (*Mini-Circuits, BLP-5*) and subsequently amplified by an additional RF amplifier (*HD Communications Corp., HD 17153BB*). Afterwards, the resulting signal is digitized using an NI-Scope card (*National Instruments, PCI-5114*, with a maximum sampling speed of 250 MS/s) at a sampling rate of 5 MHz. This specific detection technique is commonly known as "double heterodyne detection". Since digitizers with a range of 2-26 GHz were not available during the development of the Balle-Flygare spectrometer, it was necessary to process the signal within a much lower frequency range. The time-domain signal is transformed into the frequency domain by means of a Fourier transformation. The alignment of the antenna and pulsed nozzle in a coaxial manner leads to the doppler doublet in the frequency domain, as the standing wave is equivalent to a superposition of left and right traveling waves and the molecular beam is moving in one direction.

2.2.3 Time Sequences of the pulses:

The temporal order of the pulses is presented in *Figure 2-5*. The SRS-DG645 delay generator regulates the gas pulse, while the BNC-575 delay generator controls the microwave pulses. The duration of the microwave pulse, ranging from 0.2 to 3.0 µs, is chosen depending on the dipole moment of the molecule/complex being investigated. This microwave pulse is directed towards the cavity, resulting in the formation of a stationary wave within it., After the duration of the microwave pulse, the cavity may have some coherent noise, called ringing, which could last 10s of µs. When the emission from molecules/complexes is recorded, a suitable delay should be introduced for the ringing to end. Subsequently, the resulting digitized signal is stored as noise. Following this, a gas pulse containing the molecular sample of interest is introduced into the cavity. The duration of this gas pulse is 1 ms.

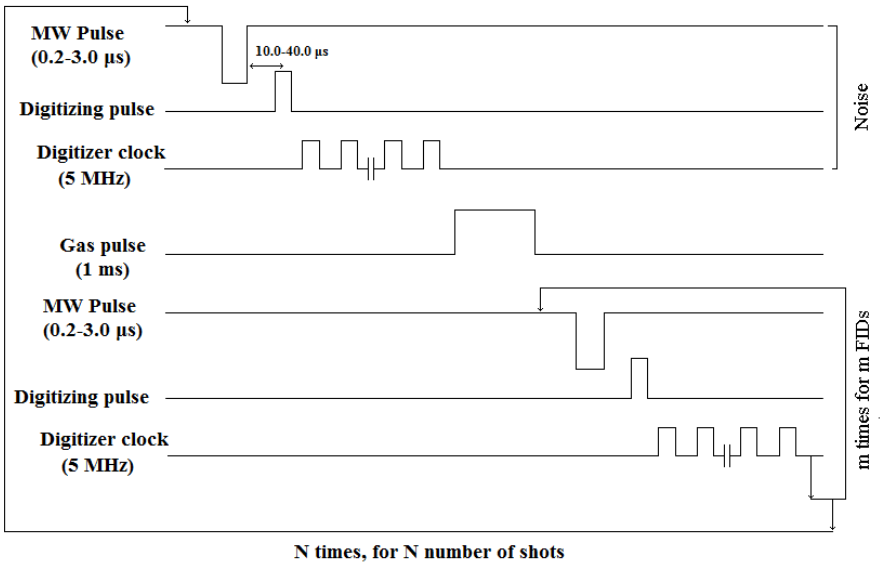

Figure 2-5: The pulse sequence for the PN-FTMW spectrometer. Taken with permission from Dr Arijit Das's Thesis.[11]

Another microwave pulse is then transmitted to the cavity to polarise the gas sample. A delay referred to as the "start delay," which lasts for a few microseconds, occurs between the gas pulse and the microwave pulse. This delay arises from the processing time of the

program. The gas pulse typically requires 2 ms to reach the opposite mirror, while the typical acquisition time is 100 microseconds. Consequently, multiple microwave pulses can be sent in response to a single gas pulse. The signal is acquired through the elimination of the noise that was captured prior to the gas pulse. The entire process is commonly referred to as "one-shot". Multiple shots were recorded to improve the signal-to-noise ratio.

2.2.4 Sample Preparation:

The BF-FTMW spectrometer employs a pulsed nozzle to generate a molecular beam. The introduction of the molecules into the cavity occurs through the supersonic expansion of the carrier gas, which contains the molecules to be investigated. Helium and argon serve as carrier gases. Typically, 1-5% of gas samples are combined with the carrier gases. For complexes involving liquid samples, the carrier gas passes through each sample individually and is subsequently mixed at a four-way junction. The flow of the gases is regulated by three distinct mass flow controllers. A 500 SCCM mass flow controller is utilized for the carrier gas, with helium typically set at 200 SCCM and argon at 150 SCCM. The flow rate of the sample molecule, which depends on the vapour pressure of the molecule, is typically less than 15 SCCM. Therefore, a 20-50 SCCM mass flow controller is typically used. An appropriate backing pressure is required for a complex. Generally, larger complexes require greater backing pressure, while smaller complexes necessitate less backing pressure. In helium, the backing pressure typically ranges from 1.0 to 2.0 bar, whereas in argon, it ranges from 0.6 to 1.2 bar, as argon is more efficient in cooling the molecular beam.

2.2.5 Software for the BF-FTMW spectrometer:

The spectrometer's software is programmed using LabVIEW 7.1. A comprehensive discussion of the software's particulars can be found elsewhere.[12] The codes regulate the frequency synthesizer through the GPIB interface. The gas pulse and microwave pulses are controlled by two distinct delay generators. The delay generator responsible for

controlling the gas pulses is connected to the computer via a parallel port, while the delay generator controlling the microwave pulse is internally triggered. The stepper motor driver is also controlled via the parallel port on the computer.

In the year 2023, the computer system was replaced with a PXIe (*National Instruments, NI PXIe-1071*), and efforts to update the code to LabView 2019 have been underway since then. The research conducted for this thesis employed the code written in LabView 7.1. The PXIe is equipped with a 125 MHz oscilloscope (*National Instruments, NI PXIe-5114*), a GPIB (*National Instruments, NI PXI-GPIB*), and a relay module (*NI PXI-2564 16 SPST*). The GPIB interface is employed to control the frequency synthesizer. The delay generator responsible for controlling the gas pulse is connected to a National Instruments myDAQ, which is capable of producing TTL pulses. The stepper motor is also managed using the same myDAQ. The latest code, developed by VI Solutions in Bangalore, is written for LabView 2019 and is still in progress.

2.3 Chirped-Pulse Fourier Transform Microwave Spectrometer:

The description of the chirped-pulse Fourier transform microwave (CP-FTMW) spectrometer has been provided by Pate and coworkers. Digitizing FIDs with frequencies higher than 1 GHz is now feasible because of the advanced technology employed in the telecom sector. By substituting the limiting microwave pulse with a chirped pulse that sweeps quickly (~ 1 μs) throughout the many GHz of the measurement's frequency bandwidth, the CP-FTMW spectrometer has an advantage over the BF-FTMW spectrometer in terms of measured frequency range. This dissertation makes use of a CP-FTMW spectrometer at Newcastle University, United Kingdom. A brief overview of the CP-FTMW spectrometer is given here, and a detailed description can be found elsewhere.[8,9]

2.3.1 Microwave Circuit:

The CP-FTMW spectrometer at Newcastle University operates within the frequency range of 2.0 to 18.5 GHz. To capture the spectrum within the range of 2.0 to 8.0 GHz,

certain modifications are required in the existing circuit that operates within the range of 7.0 to 18.5 GHz. The subsequent section provides a concise overview of the excitation and detection circuit in both the 7.0 to 18.5 GHz and 2.0 to 8.0 GHz regions. The circuit diagram is shown in *Figure 2-6* and *Figure 2-7* . This chapter gives a brief account of the microwave circuit and sample preparation.

2.3.2 The 7.0-18.5 GHz frequency region:

2.3.2.1 Excitation Circuit:

A chirped pulse, which encompasses a linear frequency sweep ranging from 12.5 to 0.5 GHz, is generated utilising a 20 GS/s arbitrary waveform generator (AWG) (*Tektronix AWG7102*). This AWG is synchronised with a 10 MHz signal produced by a frequency standard. Throughout the course of the experiments conducted in this thesis, either a rubidium frequency standard (*FS725, SRS C*) or an analog signal generator (*Agilent N5183A*) served as the reference source. The chirp pulse (12.5-0.5 GHz) generated by the AWG goes through a low-pass filter (12.2 GHz, Lorch D) and is up-converted by a triple balance mixer (*MITEQ, TBO 440L WI-R*). The chirped pulse is mixed with a 19 GHz signal emanating from a phase-locked dielectric resonant oscillator (PDRO) (*XPDRO-14373, Herley, CTI*). The PDRO is phase-locked to the identical 10 MHz reference as the AWG. An additional undesired sideband is eliminated from the resultant higher frequency sideband (31.0 to 19.5 GHz) by means of a bandpass filter (*K&L Microwave, 3C60-19000/T100-O/O*). Prior to reaching a 300 W Travelling-Wave Tube (TWT) Amplifier, the 7.0-18.5 GHz chirp propagates through a pre-amplifier (*MITEQ, AMF-5F-080018-14-10P-R*). The signal is attenuated prior to its transmission to the TWTA, a measure taken to safeguard the TWTA from excessive input signals. The microwave pulse is then propagated via a horn antenna (*ATM 750-442-C3*) in order to polarize the molecular ensemble formed through supersonic expansion within the vacuum chamber.

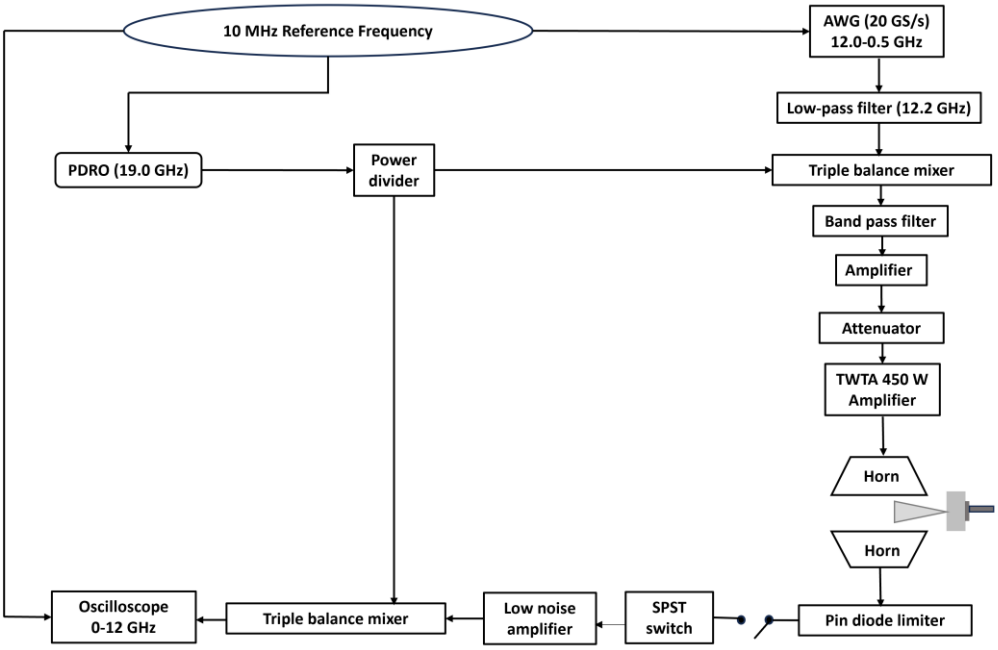

Figure 2-6: The microwave circuit (7.0-18.5 GHz) of the chirped-pulse Fourier transform microwave spectrometer (CP-FTMW) at Newcastle University.

2.3.2.2 Detection Circuit:

Two horn antennas with an identical design are positioned across from each other inside the vacuum chamber. The emission of molecules are observed in the form of a free induction decay, and they are captured by means of the second horn antenna. To safeguard the sensitive components of the detection circuitry from potential damage caused by the high-power microwave excitation pulse, a pin diode limiter (*ACLM-4539C6R1K*) and a single-pole single-throw (SPST) pin diode switch (*Arra H8753-8OD*) are employed. The switch is only activated during the collection of the free induction decay. Subsequently, the signal is amplified by a low noise amplifier (*MITEQ, AMF-5F-08001800-14-10P-R*). Given that the oscilloscope (*Tektronix DPO72304XS,* sampling rate: 100 GS/s) has the maximum sampling frequency range of about 12.0 GHz, mixing is necessary prior to digitisation. Therefore, the signal undergoes down-conversion (high-side conversion) by means of a triple-balanced mixer, which combines it with a 19 GHz signal produced by the same PDRO and derived from the power divider (*P218, ATM*). Afterwards, the down-converted signal is directed through a low pass filter (*K&L Microwave, 11SBL-10-12500/T19000-O/O*) that effectively removes frequencies above 12 GHz. The heterodyned signal is then digitised using the same oscilloscope over a time span of 20

μs. To ensure synchronization with the arbitrary waveform generator (AWG) and the PDRO, the oscilloscope is phase-locked to a 10 MHz signal emitted by the same source.

2.3.3 The 2.0-8.0 GHz frequency region:

2.3.3.1 Excitation Circuit:

In this thesis, the CP-FTMW spectrometer at Newcastle University is utilised to examine the systems within the 2.0-8.0 GHz range. To expand the spectral region to the frequency range of 2.0 to 8.0 GHz, some modifications in the existing circuit of 7.0 to 18.5 GHz are necessary. The circuit diagram for the 2.0-8.0 GHz frequency range is shown in *Figure 2-7*. No mixing is required before transmitting the chirp pulse to the TWTA.

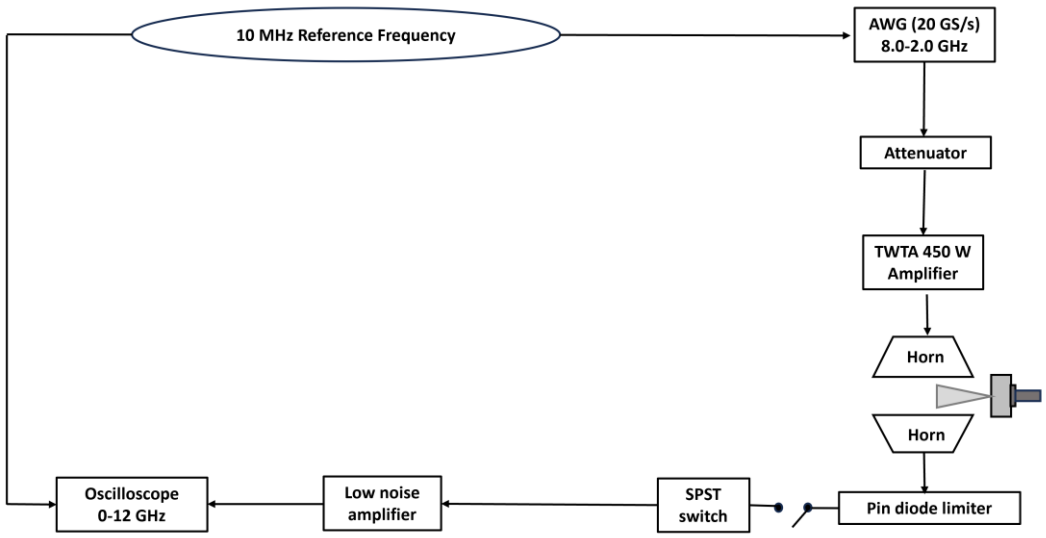

Figure 2-7: The microwave circuit (2.0-8.0 GHz) of the chirped-pulse Fourier transform microwave spectrometer (CP-FTMW) at Newcastle University.

The PDRO and low pass filters are eliminated from the circuit. A chirped pulse that spans the frequency range of 2.0-8.0 GHz is produced by the 20 GS/s AWG and subsequently attenuated and directly sent to the TWT amplifier (*Applied Systems Engineering Inc., 450 W*) for amplification. Finally, the chirp is propagated to the vacuum chamber through the first horn antenna.

2.3.3.2 Detection Circuit:

The detection circuit used for the 2.0-8.0 GHz region is identical to that employed for the 7.0-18.5 GHz range, with the exception of the removal of PDRO and low pass filters from the detection end of the circuit. This modification is undertaken since the oscilloscope's range adequately encompasses the necessary frequency range for digitisation.

2.3.4 Sample Preparation:

The liquid sample was contained within a reservoir that was equipped with a faceplate. The reservoir was filled with glass wool, after which approximately 0.5 ml of the liquid sample was introduced into the glass wool. Details of the reservoir are given elsewhere.[13] The reservoir and faceplate design can be seen in *Figure 2-8*. The reservoir is placed after the nozzle in the spectrometer. Furthermore, this reservoir is equipped with a band heater, which enhances the signal intensity for systems with lower vapour pressure.

Figure 2-8: The faceplate and reservoir assembly.

2.4 Computational Methods:

2.4.1 Geometry Optimization and Binding Energy:

The geometry optimisation of a molecular structure was done using the Gaussian 09 software suite.[14,15] Many different quantum chemical methods have been used to understand the various intermolecular interactions present. Structure optimisation was done utilising density functional theory and *ab-initio* quantum chemical calculations. Two different methods were used in the systems studied in this Thesis: the harmonic hybrid functional of Becke, Lee, Yang, and Parr (B3LYP),[16–18] which was combined with Grimme's dispersion correction effects,[19] and the MP2 functional.[20,21] The optimised structures are required to provide a guess for the rotational constants and dipole moment components along the three principal axes. Centrifugal distortion constant due to the vibrational-rotational coupling can be computed using the *freq=vibrot* keyword. Harmonic frequency calculations are performed to ascertain that the optimised structure is a minimum at the potential energy surface. Many conformations are possible for weakly bound complexes, and therefore, the energy ordering is very important, which is determined by binding energy (ΔE). The bonding energy (ΔE) is calculated by the supermolecule approach. The expression for calculating the binding energy is given below:

$$\Delta \boldsymbol{E} = \boldsymbol{E}(\boldsymbol{Complex}) - \sum \boldsymbol{E}(\boldsymbol{Monomer})$$

where, ΔE is the binding energy for the complex and, E(complex) and E(monomer) are the energies of the complex and the monomer at their optimized states, respectively.

The binding energies were corrected for the basis set superposition error (BSSE) using Boys and Bernardi's counterpoise method,[21] and the zero-point energy (ZPE) corrections were obtained from the harmonic frequency calculations.

2.4.2 Atoms in Molecules (AIM) Analysis:

The Atoms in Molecules (AIM) theory is a prominent tool for characterising chemical bonding and the nature of intermolecular interactions. Central to AIM is the concept of the electron density field, which describes the probability of finding an electron in a given

region of space.[22] A critical point is any point in space where the first derivative of the electron density becomes zero. The topological attributes of the electron density function, denoted as ρ, including maxima, minima, and saddle points, are characterised by examining the signs of its second derivatives along the three principal axes. The determination of eigenvalues (λ) involves the construction and diagonalisation of a Hessian matrix derived from ρ. The Laplacian ($\nabla^2\rho$) is obtained as the sum of the trace of the diagonalised matrix. The trajectory along which the electron density reaches its maximum defines the bond path. Critical points, designated as (r, s), are identified based on the Hessian matrix of the electron density. Here, 'r' signifies the rank (indicating the number of non-zero eigenvalues), while 's' denotes the signature, representing the algebraic sum of the signs of the non-zero eigenvalues. The comprehensive classification of critical points is given in *Table 2-1*, providing a systematic overview of their characteristics.

Table 2-1: The critical points are classified on the basis of the eigenvalues of the rank and signature.

Types of critical points	**λ1**	**λ2**	**λ3**	**(Rank, Signature)**	**Curvature**
Nuclear attractor (NCP)	-	-	-	(3, -3)	All negative, Local maxima
Bond critical point (BCP)	-	-	+	(3, -1)	Two negative, One positive
Ring critical point (RCP)	-	+	+	(3, +1)	One negative, Two positive
Cage critical point (CCP)	+	+	+	(3, +3)	All positive, Local minima

The examination of charge density properties serves as a valuable tool for quantifying and comprehending the nature of interactions between atoms. The specific values of the charge density (ρ) and its Laplacian ($\nabla^2\rho$) at the Bond Critical Point (BCP) play pivotal roles in discerning the type of bond between atoms. The quantities of ρ and $\nabla^2\rho$ at the BCP serve to discern the specific category of bond that is present between the atoms. Substantial high values of ρ and negative values of $\nabla^2\rho$ indicate the existence of shared

interactions, which are properties of a covalent bond. Conversely, low values of ρ and positive values of $\nabla^2\rho$ at the BCP suggest a closed-shell interaction.

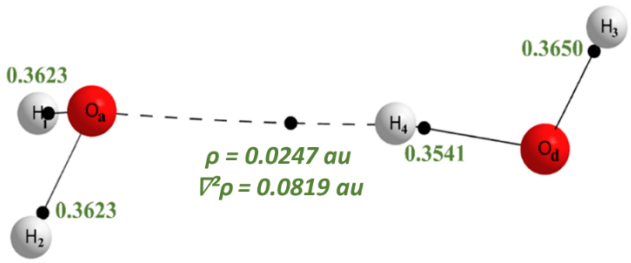

Figure 2-9: Atoms in Molecules topology study for $(H_2O)_2$ showing bond critical points (black). Taken with permission from Dr Arijit Das's Thesis.[11]

Koch and Popelier have defined certain requirements for C-H···O hydrogen bonds.[23] It recommends that the electron density, ρ(r), at the bond critical point (BCP), falls within the range of 0.002-0.034 atomic units (au). Additionally, the recommended range for the Laplacian of the charge density ($\nabla^2\rho$) evaluated at the bond critical point is 0.024-0.139 au (with allowance for minor variations in basis set). The *Figure 2-9* shows the BCPs for the water dimer. At the BCP, the electron density, ρ(r), is measured at 0.0247 au, while the charge density ($\nabla^2\rho$) is found to be 0.0819 au. Notably, these values fall within the suggested range for closed shell interactions.

2.4.3 Non-covalent Interactions (NCI) Index:

The Non-Covalent Interactions (NCI) index plot is another computational tool used to visualise and analyse non-covalent interactions within molecular systems.[24] The NCI index plot provides a visual representation of non-covalent interactions by mapping the electron density of a molecular system. The NCI analysis offers an index that makes it possible to categorise non-covalent interactions. This index is based on the electron density and its derivatives. It is based on a two-dimensional plot of the electron density, ρ, and the reduced density gradient, s, where:

$$s = \frac{1}{2(3\pi^2)^{1/3}} \frac{[\nabla\rho]}{\rho^{4/3}}$$

At the critical point of the bond, where the electron density's first derivative approaches zero [∇ρ(r) = 0], the reduced density gradient also reaches zero. Consequently, the interaction between molecules or within a molecule can be determined by examining the plot of the reduced density gradient and electron density. The second eigenvalue of the Hessian matrix (λ_2) is employed to differentiate between various types of interactions. If $\lambda_2 < 0$, this signifies a bonding interaction like hydrogen bonding and van der Waals interaction, whereas if $\lambda_2 > 0$ indicates a non-bonding interaction, for example steric hindrance. The NCI plot for weakly bound complexes is computed using Multiwfn software.

One instance of the NCI plot is illustrated in *Figure 2-10*, showing the water dimer. Within this NCI plot, the peak on the scatter diagram signifies the presence of a hydrogen bond, particularly in the case of the water dimer, where a strong O-H···O hydrogen bond is formed.

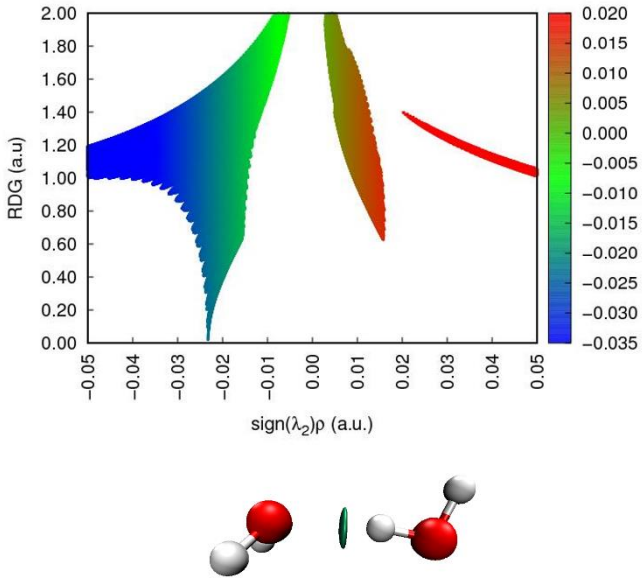

Figure 2-10: Non-covalent interactions (NCI) index plots for $(H_2O)_2$. Taken with permission from Dr Arijit Das's Thesis.[11]

2.4.4 Natural Bond Orbital (NBO) Analysis:

Natural Bond Orbital (NBO) analysis, developed by Frank Weinhold,[25] represents a powerful theoretical framework for understanding chemical bonding within the context of quantum chemistry. The NBO calculations, which employ the NBO 6.0 software[26] integrated into Gaussian 09, are conducted for this purpose. NBO analysis focuses on generating localized orbitals that correspond to specific bonds or lone pairs within a molecule. These localized orbitals enhance the interpretability of molecular structure and bonding. The determination of the degree of perturbative stabilization of natural orbitals resulting from donor-acceptor interaction is also achieved by calculating the second-order perturbation energy. The *Figure 2-11* shows the interaction of a filled orbital sigma of the formal Lewis structure with one of the unfilled antibonding orbitals σ* to give the second-order energy lowering which is given by the equation given below:

$$\Delta E^{(2)}_{\sigma\sigma^*} = -2\frac{\langle \sigma|\hat{F}|\sigma^*\rangle^2}{\epsilon_{\sigma^*} - \epsilon_{\sigma}}$$

In the previous equation, $\hat{F}$ is the Fock operator and ϵ_{σ} and ϵ_{σ^*} are NBO orbital energies. For example, *Figure 2-12* shows the interacting natural orbitals of the dimer. The second order perturbation energy in water dimer for lone pair of oxygen atoms to the σ* antibonding orbitals of the O-H group is 30.5 kJ/mol calculated at MP2/aug-cc-pVTZ level of theory.

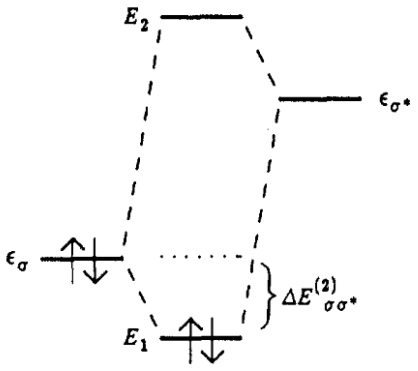

Figure 2-11: Perturbative donor-acceptor interaction, involving a filled orbital σ and an unfilled orbital σ.*[27]

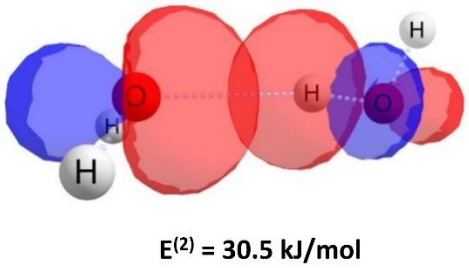

Figure 2-12: Interacting Natural Bond Orbitals in $(H_2O)_2$. The second-order perturbation energy calculated at MP2/aug-cc-pVTZ level of theory. Taken with permission from Dr Arijit Das's Thesis.[11]

2.4.5 Symmetry Adapted Perturbation Theory (SAPT):

The SAPT methodology is commonly utilised for the computation of non-covalent interaction energies in quantum chemistry.[28] In quantum chemistry, there exist two primary approaches for the determination of non-covalent interaction energies, namely supermolecular and perturbative. As outlined in **Section 2.4.1**, by the supermolecular approach, the interaction energy is derived by subtracting the total energy of the molecular complex from the sum of the energies of each individual monomer. The SAPT methodology works on the foundation of the perturbative approach, whereby the interaction energy can be evaluated based on perturbation of the Hamiltonian of the isolated monomers. SAPT offers a means to elucidate the fundamental forces that contribute to the stabilization of the molecular complex. Its significant advantage over the supermolecular approach lies in its ability to break down the overall interaction energy between molecules into distinct physical components, including electrostatic, induction, dispersion, and exchange terms. Each of these components is then analysed individually, allowing for a meticulous examination of the diverse forces that contribute to the overall interaction. A detailed explanation of the theoretical details of the SAPT methodology can be found in other sources. In the present thesis, we employed the SAPT'2+3' and SAPT-DFT variants of the SAPT methodology.[28] The SAPT analysis was conducted using the PSI4 software.[29]

2.5 Summary:

In brief, the rotational spectra of hydrogen bonded complexes were acquired using the Balle-Flygare Fourier transform microwave spectrometer (BF-FTMW) currently available at the Indian Institute of Science Bangalore India and the chirped-pulse Fourier transform microwave spectrometer (CP-FTMW) currently available at Newcastle University, United Kingdom. A concise introduction to these two spectrometers has been provided in this chapter. Given that the microwave spectroscopy is incapable of establishing a connection between two atoms, after obtaining the geometry of the molecule/complex, the quantum chemical calculations were conducted in order to obtain the structure. The Atoms in Molecules (AIM), Natural Bond Orbital (NBO), Non-covalent Interactions (NCI) Index, and Symmetry Adapted Perturbation Theory (SAPT) have been utilized to collect knowledge about the nature of intermolecular interactions.

2.6 References:

(1) Gordy, W.; Cook, R. L. *Microwave Molecular Spectra*.

(2) Cleeton, C. E.; Williams, N. H. Electromagnetic Waves of 1.1 Cm Wave-Length and the Absorption Spectrum of Ammonia. *Phys. Rev.* **1934**, *45* (4), 234–237. https://doi.org/10.1103/PhysRev.45.234.

(3) Gordon, J. P.; Zeiger, H. J.; Townes, C. H. The Maser—New Type of Microwave Amplifier, Frequency Standard, and Spectrometer. *Phys. Rev.* **1955**, *99* (4), 1264–1274. https://doi.org/10.1103/PhysRev.99.1264.

(4) Ekkers, J.; Flygare, W. H. Pulsed Microwave Fourier Transform Spectrometer. *Review of Scientific Instruments* **1976**, *47* (4), 448–454. https://doi.org/10.1063/1.1134647.

(5) Balle, T. J.; Flygare, W. H. Fabry–Perot Cavity Pulsed Fourier Transform Microwave Spectrometer with a Pulsed Nozzle Particle Source. *Review of Scientific Instruments* **1981**, *52* (1), 33–45. https://doi.org/10.1063/1.1136443.

(6) Brown, G. G.; Dian, B. C.; Douglass, K. O.; Geyer, S. M.; Shipman, S. T.; Pate, B. H. A Broadband Fourier Transform Microwave Spectrometer Based on Chirped Pulse Excitation. *Review of Scientific Instruments* **2008**, *79* (5), 053103. https://doi.org/10.1063/1.2919120.

(7) Arunan, E.; Tiwari, A. P.; Mandal, P. K.; Mathias, P. C. Pulsed Nozzle Fourier Transform Microwave Spectrometer: Ideal to Define Hydrogen Bond Radius. *Current Science* **2002**, *82* (5), 533–540.

(8) Zaleski, D. P.; Stephens, S. L.; Walker, N. R. A Perspective on Chemistry in Transient Plasma from Broadband Rotational Spectroscopy. *Phys. Chem. Chem. Phys.* **2014**, *16* (46), 25221–25228. https://doi.org/10.1039/C4CP04108A.

(9) Stephens, S. L.; Walker, N. R. Determination of Nuclear Spin–Rotation Coupling Constants in CF3I by Chirped-Pulse Fourier-Transform Microwave Spectroscopy. *Journal of Molecular Spectroscopy* **2010**, *263* (1), 27–33. https://doi.org/10.1016/j.jms.2010.06.007.

(10) Mandal, P. K. Rotational Spectra of Weakly Bound H2S Complexes and "Hydrogen Bond Radius." Ph.D. Thesis, Indian Institute of Science, Bangalore, 2005.

(11) Das, A. Microwave Rotation-Tunnelling Spectroscopic and Theoretical Studies on Weakly Bound Molecular Complexes: Intermolecular Bonding across the Periodic Table. Ph.D. Thesis, Indian Institute of Science, Bangalore, 2021.

(12) Goswami, M. Rotational Spectroscopic and Ab Initio Studies on the Weakly Bound Complexes Containing O-H•••π and S-H•••π Interactions. Ph.D. Thesis, Indian Institute of Science, Bangalore, 2009.

(13) Loru, D.; Bermúdez, M. A.; Sanz, M. E. Structure of Fenchone by Broadband Rotational Spectroscopy. *The Journal of Chemical Physics* **2016**, *145* (7), 074311. https://doi.org/10.1063/1.4961018.

(14) Gaussian 09, Revision A.02, M. J. Frisch, G. W. Trucks, H. B. Schlegel, G. E. Scuseria, M. A. Robb, J. R. Cheeseman, G. Scalmani, V. Barone, G. A. Petersson, H. Nakatsuji, X. Li, M. Caricato, A. Marenich, J. Bloino, B. G. Janesko, R. Gomperts, B. Mennucci, H. P. Hratchian, J. V. Ortiz, A. F. Izmaylov, J. L. Sonnenberg, D. Williams-Young, F. Ding, F. Lipparini, F. Egidi, J. Goings, B. Peng, A. Petrone, T. Henderson, D. Ranasinghe, V. G. Zakrzewski, J. Gao, N. Rega, G. Zheng, W. Liang, M. Hada, M. Ehara, K. Toyota, R. Fukuda, J. Hasegawa, M. Ishida, T. Nakajima, Y. Honda, O. Kitao, H. Nakai, T. Vreven, K. Throssell, J. A. Montgomery, Jr., J. E. Peralta, F. Ogliaro, M. Bearpark, J. J. Heyd, E. Brothers, K. N. Kudin, V. N. Staroverov, T. Keith, R. Kobayashi, J. Normand, K. Raghavachari, A. Rendell, J. C. Burant, S. S. Iyengar, J. Tomasi, M. Cossi, J. M. Millam, M. Klene, C. Adamo, R. Cammi, J. W. Ochterski, R. L. Martin, K. Morokuma, O. Farkas, J. B. Foresman, and D. J. Fox, Gaussian, Inc., Wallingford CT, 2016.

(15) *Gaussian.com | Expanding the limits of computational chemistry*. https://gaussian.com/ (accessed 2023-08-29).

(16) Miehlich, B.; Savin, A.; Stoll, H.; Preuss, H. Results Obtained with the Correlation Energy Density Functionals of Becke and Lee, Yang and Parr. *Chemical Physics Letters* **1989**, *157* (3), 200–206. https://doi.org/10.1016/0009-2614(89)87234-3.

(17) Vosko, S. H.; Wilk, L.; Nusair, M. Accurate Spin-Dependent Electron Liquid Correlation Energies for Local Spin Density Calculations: A Critical Analysis. *Can. J. Phys.* **1980**, *58* (8), 1200–1211. https://doi.org/10.1139/p80-159.

(18) Becke, A. D. Density-Functional Thermochemistry. I. The Effect of the Exchange-Only Gradient Correction. *The Journal of Chemical Physics* **1992**, *96* (3), 2155–2160. https://doi.org/10.1063/1.462066.

(19) Grimme, S.; Steinmetz, M. Effects of London Dispersion Correction in Density Functional Theory on the Structures of Organic Molecules in the Gas Phase. *Phys. Chem. Chem. Phys.* **2013**, *15* (38), 16031. https://doi.org/10.1039/c3cp52293h.

(20) Binkley, J. S.; Pople, J. A. Møller-Plesset Theory for Atomic Ground State Energies: MØLLER-PLESSET THEORY FOR ATOMIC GROUND STATE ENERGIES. *Int. J. Quantum Chem.* **1975**, *9* (2), 229–236. https://doi.org/10.1002/qua.560090204.

(21) Møller, Chr.; Plesset, M. S. Note on an Approximation Treatment for Many-Electron Systems. *Phys. Rev.* **1934**, *46* (7), 618–622. https://doi.org/10.1103/PhysRev.46.618.

(22) Bader, R. F. W. *Atoms in Molecules: A Quantum Theory*; The International series of monographs on chemistry; Clarendon Press ; Oxford University Press: Oxford [England] : New York, 1994.

(23) Koch, U.; Popelier, P. L. A. Characterization of C-H-O Hydrogen Bonds on the Basis of the Charge Density. *J. Phys. Chem.* **1995**, *99* (24), 9747–9754. https://doi.org/10.1021/j100024a016.

(24) Contreras-García, J.; Johnson, E. R.; Keinan, S.; Chaudret, R.; Piquemal, J.-P.; Beratan, D. N.; Yang, W. NCIPLOT: A Program for Plotting Noncovalent Interaction Regions. *J. Chem. Theory Comput.* **2011**, *7* (3), 625–632. https://doi.org/10.1021/ct100641a.

(25) Weinhold, F.; Landis, C. R.; Glendening, E. D. What Is NBO Analysis and How Is It Useful? *International Reviews in Physical Chemistry* **2016**, *35* (3), 399–440. https://doi.org/10.1080/0144235X.2016.1192262.

(26) Glendening, E. D.; Landis, C. R.; Weinhold, F. *NBO 6.0* : Natural Bond Orbital Analysis Program. *J. Comput. Chem.* **2013**, *34* (16), 1429–1437. https://doi.org/10.1002/jcc.23266.

(27) Reed, A. E.; Curtiss, L. A.; Weinhold, F. Intermolecular Interactions from a Natural Bond Orbital, Donor-Acceptor Viewpoint. *Chem. Rev.* **1988**, *88* (6), 899–926. https://doi.org/10.1021/cr00088a005.

(28) Parker, T. M.; Burns, L. A.; Parrish, R. M.; Ryno, A. G.; Sherrill, C. D. Levels of Symmetry Adapted Perturbation Theory (SAPT). I. Efficiency and Performance for Interaction Energies. *The Journal of Chemical Physics* **2014**, *140* (9), 094106. https://doi.org/10.1063/1.4867135.

(29) Parrish, R. M.; Burns, L. A.; Smith, D. G. A.; Simmonett, A. C.; DePrince, A. E.; Hohenstein, E. G.; Bozkaya, U.; Sokolov, A. Yu.; Di Remigio, R.; Richard, R. M.; Gonthier, J. F.; James, A. M.; McAlexander, H. R.; Kumar, A.; Saitow, M.; Wang, X.; Pritchard, B. P.; Verma, P.; Schaefer, H. F.; Patkowski, K.; King, R. A.; Valeev, E. F.; Evangelista, F. A.; Turney, J. M.; Crawford, T. D.; Sherrill, C. D. PSI4 1.1: An Open-Source Electronic Structure Program Emphasizing Automation, Advanced Libraries, and Interoperability. *J. Chem. Theory Comput.* **2017**, *13* (7), 3185–3197. https://doi.org/10.1021/acs.jctc.7b00174.

CHAPTER 3

Insights into Intermolecular Interactions: Microwave Spectroscopic and Computational Analyses of the Phenylacetylene···Methanol Complex

CHAPTER 3 | Insights into Intermolecular Interactions: Microwave Spectroscopic and Computational Analyses of the Phenylacetylene···Methanol Complex |

3.1 Introduction:

PhAc displays a wide range of binding behaviour, which is characterised by the presence of three potential docking sites. The specific docking sites that are utilised by PhAc are dependent on the type of solvent and the environmental conditions present.[1] One of the ways in which PhAc interacts with other molecules is by acting as a hydrogen bond donor. This is facilitated through the presence of its acetylenic CH group. Additionally, PhAc can accept hydrogen bonds through the π-clouds in acetylene and benzene moieties. In the gas phase, studies have shown that all three binding sites of PhAc can be identified in its interactions with some molecules.[2–13] Furthermore, PhAc has been extensively investigated in complexation studies with various molecules. Some examples of these binding molecules include argon,[11,12] water,[7,10,13] methanol,[2–4] ammonia,[3] methylamine,[3] hydrogen sulphide,[9] trifluoroethanol[1] and itself.[5] In order to investigate these complexes, researchers have utilised techniques such as matrix isolation infrared spectroscopy, low-temperature supersonic jet studies involving IR/UV double resonance and microwave spectroscopy, and high-level quantum chemical calculations. The identification of the higher energy structures alongside the global minima has been made possible using matrix isolation techniques. On the other hand, studies utilizing molecular beam with IR/UV double resonance and microwave techniques have primarily detected the global minima of these complexes.

For the PhAc···H_2O complex, it is evident that there is a clear preference for water to bind with the acetylenic moiety (rather than the phenyl ring) while acting as a hydrogen bond donor.[7,10] This interaction is accompanied by a secondary interaction involving the ortho C-H group of PhAc and the oxygen atom of water. In contrast, in the PhAc···H_2S complex, hydrogen sulphide is located above the phenyl ring and donates a hydrogen bond to the π-cloud of the phenyl ring.[9] In order to obtain a deeper understanding of the effects of replacing water with alcohols as the donor molecule in the complexes formed with PhAc, an IR-UV double resonance spectroscopic method was utilized.[3,4] This method allowed for the investigation of

the interactions between the donor alcohols and PhAc, providing valuable insights into the nature of these complexes.

During their investigations using the IR-UV double resonance spectroscopic technique, Singh *et al*. reported some intriguing differences in hydrogen bonding tendencies exhibited by H_2O and CH_3OH when interacting with PhAc. H_2O showed a preference for forming hydrogen bonds with the acetylenic π-cloud of PhAc, while CH_3OH donated hydrogen bonds to the phenyl π-system. These observations were derived from fluorescence dip infrared (FDIR) spectra obtained for H_2O and CH_3OH complexes with PhAc. To further substantiate the intriguing methyl group-induced hydrogen bond switching phenomenon, they conducted energy decomposition analyses employing symmetry-adapted perturbation theory (SAPT). The SAPT calculations brought to light a disparity in energy contributions between the PhAc···H_2O and PhAc···CH_3OH complexes. In contrast to the predominantly electrostatic energy component characterizing the PhAc···H_2O complex, the PhAc···CH_3OH complex exhibited dispersion as its primary energy-driving force.

It is noteworthy that microwave studies were conducted on the complex formed between PhAc and hydrogen sulphide (H_2S), revealing that H_2S resides above the phenyl ring and donates a hydrogen bond to the phenyl π-system.[9] Given the similarity in mass between CH_3OH and H_2S, it was inferred that dispersion plays a dominant role in both PhAc···CH_3OH and PhAc···H_2S complexes. The interplay of various noncovalent interactions holds immense significance in the realm of chemical and biochemical processes due to its overarching influence on the phenomena of molecular recognition and aggregation. The delicate balance of these interactions, which encompass a range of forces such as electrostatic interactions between permanent multipoles, induction, dispersion, and exchange-repulsion, plays an important role in regulating the intricate molecular recognition events that occur in chemical and biological systems. Consequently, the critical significance lies in the experimental investigation and accurate estimation of the structure at the global minimum.

Surprisingly, nearly a decade later, Karir *et al*. conducted a study utilizing the slit-jet molecular beam with FTIR detection of the PhAc···H_2O complex, which yielded some conflicting results compared to the earlier findings.[2] While the structure of the PhAc···H_2O complex remained consistent with the previous observations, a discrepancy emerged in the structure of the complex formed between PhAc and CH_3OH. Analysis of Fourier-transform infrared (FTIR) spectra obtained from these experiments indicated that methanol also donates hydrogen bonds

to the acetylenic π-cloud, a result supported by density functional theory (DFT) calculations, which identified the acetylene-bound structure as the global minimum.

The discrepancy in results for the PhAc···CH_3OH complex that arises from the combination of molecular beam with IR-UV double resonance spectroscopic and FTIR spectroscopic experimental results can potentially be resolved using microwave spectroscopy. Microwave spectroscopy offers the advantage of providing an unambiguous structure for the complex. A significant amount of research has been carried out on different complexes involving methanol, with microwave spectroscopy being used in many of these studies. Specifically, the barrier height to internal rotation of CH_3OH and CH_3OH-containing complexes, including the CH_3OH dimer, has been a topic of great interest and investigation.[14–34] In the case of CH_3OH, it has been reported that this barrier height is 373 cm^{-1}, and this barrier is believed to be a result of the interactions between the internal rotation of the methyl group and the large amplitude motion of the OH group.[14] Furthermore, there are reports that suggest that the presence of CH_3OH in the complexes can influence the internal rotation of the methyl group in the methanol molecule. Given these findings, it would be of interest to further explore the barrier to internal rotation of the methyl group in the PhAc···CH_3OH complex.

This study presents a comprehensive analysis of the microwave spectrum exhibited by five isotopologues of the PhAc···CH_3OH complex. Furthermore, in order to delve deeper into the intricate nature of the interactions within the complex, the study employs techniques such as atoms in molecules (AIM) theory, natural bond orbital (NBO) analysis and non-covalent interactions (NCI) index analysis. Through these methods, the molecular interactions present in the complex is explored. The results of this analysis provide valuable insights into the intricate and complex nature of the PhAc···CH_3OH compound.

3.2 Methods:

3.2.1 Computational Details:

The Gaussian09 package[35] was employed for the optimization of the PhAc···CH_3OH complex structures, utilizing DFT and *ab initio* quantum chemical calculations. Two alternative methods were used in this study to optimize the structures: the harmonic hybrid functional[36–38] of Becke,

Lee, Yang, and Parr (B3LYP), which was combined with Grimme's dispersion correction effects,[39] and the MP2 functional.[40,41] These methods were used with Dunning's augmented double-ζ aug-cc-pVDZ basis sets.[42–45] The initial guess geometries were taken from the previous reports.[2,4] Harmonic frequency calculations were performed to ascertain that the structures obtained were minima on the potential energy surface. The freq=vibrot keyword was used to calculate the centrifugal distortion constants for all isotopologues. The binding energies for the complexes were calculated using the supermolecule approach. The binding energies were corrected for the basis set superposition error (BSSE) using Boys and Bernardi's counterpoise method.[46] To understand the internal rotation of the methyl group, the relaxed potential energy scan was performed using the opt=modredundant keyword. The barriers obtained from this scan would help to determine the feasible pathways for internal rotation that lead to the splitting of the observed spectra. The electron density topologies for the optimized structures have been calculated to understand the nature of interactions present using the AIMAll software.[47] Noncovalent interactions index (NCI) analysis [48] and natural bond orbital (NBO) analysis[49] were also performed to characterize and visualize the intermolecular interactions. The NCI plots were computed using Multiwfn software[50] and NBO calculations were performed using NBO 6.0 software.[51] The energy decomposition analysis (SAPT'2+3' and SAPT-DFT) was carried out using the PSI4 program.[52,53] The wavefunctions for these calculations were obtained from Gaussian 09 calculations at B3LYP-D3/aug-cc-pVDZ level of theory.

3.2.2 Experimental Details:

The spectrum of the most naturally abundant isotopologue of PhAc···CH_3OH, hereafter referred to as the parent isotopologue, was obtained over a frequency range of 2.0-8.0 GHz using a chirped pulse Fourier transform microwave (CP-FTMW) spectrometer at Newcastle University, and over a range of 8.0-14.0 GHz using a Balle-Flygare type pulsed-nozzle Fourier transform microwave (PN-FTMW) spectrometer at the Indian Institute of Science Bangalore. The PhAc···CH_3OH complex was formed through the pulsed supersonic expansion of a gaseous mixture comprising helium (99.999%) or neon (BOC, CP grade) as carrier gases. A 98% pure sample of phenylacetylene, phenylacetylene-D (99%), methanol (99.9%), methanol-

D (99%), methanol-D4 (99.8%) and methanol-^{13}C (99%) were obtained from Sigma Aldrich and used without further purification.

For the experiments conducted at Newcastle University, the introduction of PhAc into a neon flow was executed under a backing pressure of 5 bar. Owing to the low vapour pressure, the PhAc was heated to 50° C, facilitated by a modified general valve,[54] in order to produce the mixture with the carrier gas. A second reservoir containing CH_3OH (or isotopic variants) was positioned downstream of the modified general valve allowing the introduction of low concentrations of CH_3OH into the neon carrier gas. A detailed description of the spectrometer can be found elsewhere.[55,56] To capture the broadband spectrum, a chirped pulse was generated by an Arbitrary Waveform Generator (Tektronix AWG7102) with a frequency range from 2.0 GHz to 8.0 GHz and a duration of 1 μs, was sent directly to a 450 W traveling-wave tube amplifier (TWTA) (Applied Systems Engineering), before transmission to the vacuum chamber. The polarization of the molecules within the sample was achieved following the introduction of the chirp from the horn antenna to the vacuum chamber. The microwave radiation and the expanding gas jet exhibit a mutually perpendicular orientation. Subsequently, the free induction decay (FID) of a 20 μs duration was recorded using a second horn antenna after the microwave pulse interaction. The FID's were then digitised by employing a 100 GS/s oscilloscope (Tektronix DPO72304XS). The utilization of a gas pulse lasting approximately 200 μs facilitates the acquisition of eight FID's per gas pulse, which was achieved through the implementation of the 'fast frame' operational mode of the oscilloscope. Subsequently, the FID's were co-added in the time domain and then Fourier transformed using either a Kaiser-Bessel or High Resolution Window function. Individual lines in the frequency domain spectrum have a full width at half-maximum of approximately 100 kHz allowing line centres to be measured with an estimated precision of 10 kHz. The arbitrary waveform generator (AWG) and the oscilloscope were referenced to a 10 MHz local oscillator obtained from an Analog Signal Generator (Agilent MXG N5183A) or an Rb-clock (SRS FS725) to guarantee phase coherence within the temporal domain and precision in the transition frequencies.

The pulsed nozzle Fourier transform microwave spectrometer (PN-FTMW) was utilized to acquire experimental data at the Indian Institute of Science Bangalore. A comprehensive description of the spectrometer can be found elsewhere.[57] The PhAc and CH_3OH both were kept in two different bubblers at ambient conditions. The most optimal signal intensity was achieved by allowing helium to flow through the PhAc and CH_3OH bubblers at a rate of approximately 20 SCCM (Standard cubic centimeter per minute) and 2 SCCM, respectively.

At a four-way junction, the samples were mixed with a bath of helium (about 200 SCCM), and the mixture was then sent to the nozzle. The mixture underwent expansion via a 0.8 mm nozzle after being subjected to a backing pressure of 1.5-2.0 bar. A microwave pulse duration of 0.4 μs was found to be optimal for inducing *a* and *c*-dipole transitions, while a duration of 1.0 μs was found to yield the highest intensity signals for *b*-dipole transitions. The Doppler doubling phenomenon observed in the spectra is a consequence of the molecular beam's colinear arrangement relative to the cavity axis. The spectra were recorded utilizing a sampling frequency of 5 MHz, and during the scanning for the transitions, 256 points were collected. To obtain the high-resolution spectra, the observed rotational lines were subsequently averaged at 512 points.

3.3 Results:

3.3.1 Optimized Structures:

The structural elucidation of the PhAc monomer has been well-established through microwave spectroscopy.[58,59] For optimizing the structure of the PhAc···CH_3OH complex, initial structural approximations were drawn from previous IR/UV double resonance and FTIR spectroscopic studies.[2,4] Subsequently, the structures were optimised using *ab initio* and DFT calculations with MP2 and B3LYP-D3 functionals employing aug-cc-pVDZ basis set. The optimized structures of PhAc···CH_3OH complex are shown in *Figure 3-1*. Our nomenclature of the complexes lists the donor molecule acronym (P for PhAc and M for CH_3OH) connected by a dash to the acceptor molecule abbreviation (P for PhAc and M for CH_3OH), adding the acceptor docking site (Ac for acetylenic, Ph for phenyl and OH for hydroxyl preference) as an index. For example, the phenyl-bound complex of CH_3OH with PhAc is denoted as $(M\text{-}P)_{Ph}$. Within the scope of our investigation, two distinct scenarios were considered: one where CH_3OH serves as the hydrogen bond donor and PhAc acts as the hydrogen bond acceptor, and the other where the roles are reversed. Notably, the configuration in which CH_3OH donates a hydrogen bond to the phenyl ring of PhAc is found to have the same interactions at both MP2 and DFT computational levels. However, variations emerge when CH_3OH acts as the hydrogen bond donor to the acetylenic π-bond moiety (*Figure 3-1*). In the $(M\text{-}P)_{Ac}$ configuration optimized using the MP2 method, CH_3OH donates a hydrogen bond to the acetylenic moiety, while the

methyl group interacts with the π-cloud of the phenyl ring. In contrast, in the structure optimized using DFT methods, CH_3OH donates a hydrogen bond to the acetylenic moiety, and the ortho hydrogen of PhAc interacts with the oxygen of CH_3OH.

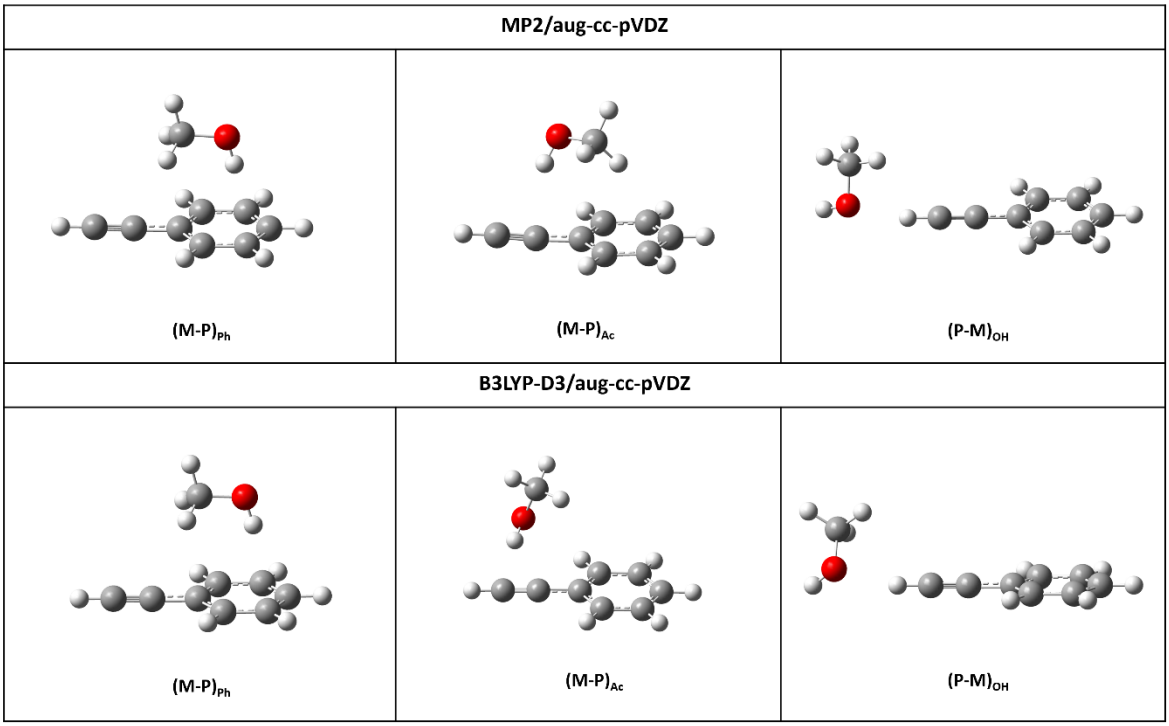

Figure 3-1: Structures of the PhAc···CH_3OH complex optimized at MP2/aug-cc-pVDZ (top panel) and B3LYP-D3/aug-cc-pVDZ (bottom panel) level of theories.

The energy landscape reveals interesting details. At the MP2 level of theory, the $(M\text{-}P)_{Ph}$ structure is the lowest energy configuration, with a marginal 0.4 kJ/mol difference from the $(M\text{-}P)_{Ac}$ structure. Furthermore, their rotational constants exhibit a high degree of similarity. Discrimination between these two configurations based on their rotational spectra becomes feasible by considering their *c*-dipole moments. The $(M\text{-}P)_{Ph}$ configuration possesses a zero *c*-dipole moment, rendering it devoid of *c*-type transitions in its microwave spectrum. In contrast, at the B3LYP-D3/aug-cc-pVDZ level of theory, the $(M\text{-}P)_{Ac}$ is the global minimum, exhibiting a 3.0 kJ/mol energy difference from the $(M\text{-}P)_{Ph}$ configuration. The structures optimized using the B3LYP-D3/aug-cc-pVDZ level of theory exhibit markedly distinct rotational constants and dipole moment components, facilitating their obvious differentiation in rotational spectra analysis. The structure where PhAc acts as the hydrogen bond donor and CH_3OH as the acceptor has higher energy at both MP2 and DFT levels of theory. Detailed molecular

properties such as rotational constants, dipole moment components and binding energies, corrected for basis set superposition error (BSSE) are presented in *Table 3-1*. Calculated atomic coordinates of each structure presented in *Figure 3-1* are provided in the supplementary information *Table 3-15* to *Table 3-20*.

Table 3-1: Rotational constants (MHz), electric dipole moment (Debye), second moments and the binding energy (ΔE) with BSSE corrected binding energy (ΔE_{BSSE}) (kJ/mol) calculated at MP2/aug-cc-pVDZ and B3LYP-D3/aug-cc-pVDZ level of theories.

Parameters	**MP2/aug-cc-pVDZ**			**B3LYP-D3/aug-cc-pVDZ**		
	$(M\text{-}P)_{Ph}$	**$(M\text{-}P)_{Ac}$**	**$(P\text{-}M)_{OH}$**	**$(M\text{-}P)_{Ph}$**	**$(M\text{-}P)_{Ac}$**	**$(P\text{-}M)_{OH}$**
A_e	1469.97	1564.70	4193.61	1380.46	2004.82	4252.43
B_e	1121.38	1041.56	364.67	1136.82	802.76	369.14
C_e	828.30	817.29	348.24	803.93	621.78	347.38
μ_a	-0.8	-1.8	-1.5	-0.6	-1.6	-1.3
μ_b	-1.7	1.0	1.0	-1.7	0.6	1.2
μ_c	0.0	0.8	0.8	-0.0	1.2	0.0
P_{cc} (u Å^2)	92.17	94.92	27.56	91.00	34.42	16.54
ΔE	31.8	30.8	18.3	21.3	23.6	15.9
ΔE_{BSSE}	16.9	16.5	12.9	18.2	21.2	14.0

P_{cc} is the second moment given by: $P_{cc} = \frac{I_b - I_a - I_c}{2}$

3.3.2 Observations and Spectral Analysis:

The broadband rotational spectrum, obtained from a mixture of PhAc and CH_3OH with neon as the carrier gas, is depicted in *Figure 3-2* (upper trace). The spectral data were acquired over the frequency range of 2.0 to 8.0 GHz and the displayed spectrum is an average over 1.11 million FID's (approximately 18.5 hours of data collection).

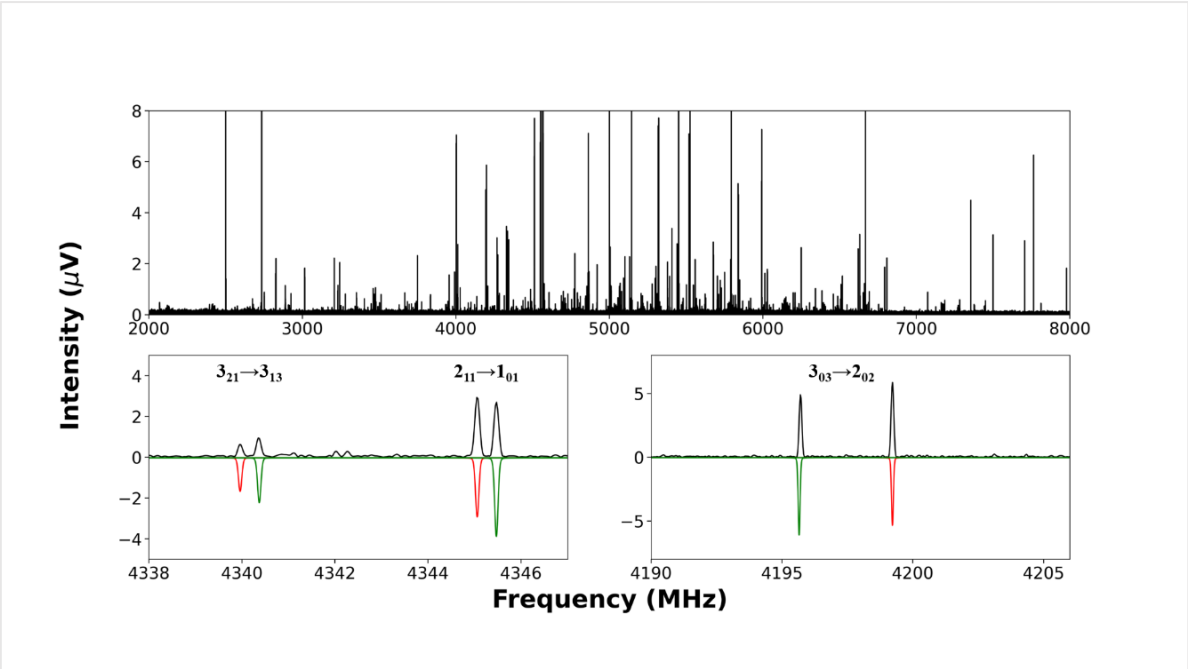

Figure 3-2: (Top panel) The broadband rotational spectrum of PhAc···CH_3OH complex recorded in 2.0-8.0 GHz region using CP-FTMW spectrometer. (Bottom panels) Experimentally observed transitions of the PhAc···CH_3OH complex are shown (black) above the simulated spectrum (red and green for A- and E- states, respectively).

Notably, the spectrum reveals the presence of CH_3OH dimer and parent and six ^{13}C isotopologues of the PhAc monomer, all of these have been subjects of prior investigation.[20,22,59] In particular, the CH_3OH dimer exhibits line splitting attributable to internal motions of the methyl group. Each of the two possible structures of PhAc···CH_3OH (as shown in *Figure 3-1*) displays the feature of a nearly prolate asymmetric top. Computational calculations, as outlined earlier, were employed to anticipate the rotational constants (A_e, B_e, and C_e) as well as five distortion constants (D_J, D_{JK}, D_K, d_1, d_2) for the equilibrium configuration of both isomers. Subsequently, based on these computational predictions, the observed spectral transitions were fitted, and the experimental rotational constants agree with the structure optimised at B3LYP-D3/aug-cc-pVDZ level of theory, in which the CH_3OH donates the hydrogen bond to the acetylenic π-cloud, and there is a secondary interaction between the ortho hydrogen with the oxygen atom of the CH_3OH ($(M\text{-}P)_{Ac}$). This fitted structure of the PhAc···CH_3OH complex is consistent with the structure reported by Karir *et al.*[2] The lower trace of *Figure 3-2* presents a small section of the broadband spectrum, spanning from 4190 to 4206 MHz and from 4338 to 4348 MHz, showing selected transitions.

For the PhAc···CH_3OH parent complex, a total of 59 transitions were successfully fitted to Watson's *S*-reduced asymmetric rotor Hamiltonian[60] within the I^r representation using the Western's PGOPHER[61] program. Notably, most of the assigned transitions in the PhAc···CH_3OH complex were part of a doublet splitting pattern, indicative of a methyl rotor-type large amplitude motion. The complete list of transitions for both states is given in the *Table 3-2*. The assignment includes strong *a*- and *c*-type transitions, alongside weaker *b*-type transitions. The fitted parameters determined by fitting to the frequencies of *A*-state transitions are shown in *Table 3-3*. The experimentally determined rotational constants and distortion constants closely match those calculated for the $(M\text{-}P)_{Ac}$ isomer using DFT methods. Additionally, *E*-state transitions, arising from the internal rotation of the methyl group, were identified in the spectra, and subsequently assigned using the XIAM[14] program to obtain a global fit. The details of the global fit are provided in Section 4.1. Successively, utilizing the fitted rotational constants, the spectral predictions were regenerated within the 8.0 to 14.0 GHz frequency range, and the predicted transitions were searched using a PN-FTMW spectrometer in IISc Bangalore. Both the *A*- and *E*-state transitions were measured. A representative portion of the recorded spectra, displaying *A* and *E*-type transitions, is presented in *Figure 3-3*. All the transitions were further split into Doppler doublets.

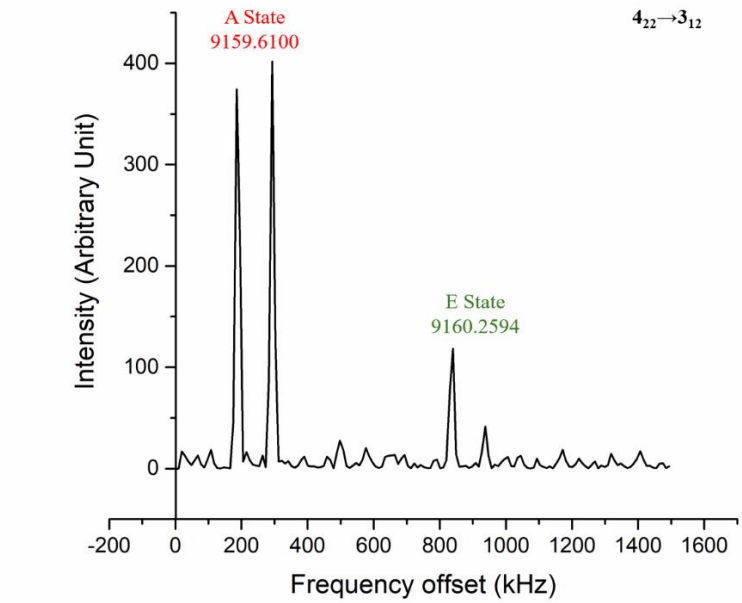

Figure 3-3: The $4_{22}\rightarrow3_{12}$ transition of PhAc···CH_3OH complex (Recorded using PN-FTMW spectrometer) showing A and E-states. The transitions are further split due to the Doppler effect.

The observed *A*-state transitions using PN-FTMW spectrometer were further fitted alongside transitions observed using the CP-FTMW spectrometer, utilizing the ASFIT[25] program (Fitted parameters are given in *Table 3-3*). As previously highlighted, the fitting results consistently support the conclusion that the observed spectra correspond to the isomeric configuration where CH_3OH is bound to the acetylenic moiety of PhAc, and the ortho-hydrogen of PhAc interacts with the oxygen of CH_3OH. It is noteworthy that despite rigorous investigation, spectral data for the complex in which CH_3OH donates a hydrogen bond to the π-cloud of the phenyl ring, as well as the isomer where CH_3OH donates a hydrogen bond to the acetylenic moiety, while the methyl group interacts with the π-cloud of the phenyl ring, remained elusive.

Table 3-2: Experimentally observed rotational transition and their assignments for the $C_6H_5CCH\cdots CH_3OH$ complex.

Transitions	***A*-State**		***E*-State**	
	ν_{obs}	$\nu_{obs-cal}$	ν_{obs}	$\nu_{obs-cal}$
$2_{12} \rightarrow 1_{11}$	2674.8410	0.0081	--	--
$1_{10} \rightarrow 0_{00}$	2751.9090	0.0045	2752.338	-0.0083
$2_{02} \rightarrow 1_{01}$	2827.8380	0.0003	2826.037	0.0086
$4_{23} \rightarrow 4_{13}$	2916.0860	0.0104	2916.819	-0.0168
$2_{11} \rightarrow 1_{10}$	3015.8220	0.0024	3015.006	0.0028
$4_{22} \rightarrow 4_{13}$	3166.7290	-0.006	--	--
$3_{03} \rightarrow 2_{12}$	3193.4780	-0.002	--	--
$3_{22} \rightarrow 3_{12}$	3232.0100	0.0035	3230.366	-0.0063
$2_{21} \rightarrow 2_{11}$	3476.099	0.0031	3467.847	-0.0068
$2_{20} \rightarrow 2_{11}$	3493.5700	0.0097	--	--
$9_{27} \rightarrow 9_{28}$	3503.1760	0.0008	--	--
$4_{04} \rightarrow 3_{12}$	3695.6870	0.0106	--	--
$2_{12} \rightarrow 1_{01}$	3833.5750	-0.0009	3834.746	-0.0066
$3_{13} \rightarrow 2_{12}$	4001.7840	0.0017	4003.048	0.0013
$2_{20} \rightarrow 2_{12}$	4005.0490	0.0051	--	--
$3_{03} \rightarrow 2_{02}$	4199.2200	0.0018	4195.706	0.0044
$3_{22} \rightarrow 3_{13}$	4253.8320	0.0047	4249.064	-0.0089

$3_{22} \rightarrow 2_{21}$	4268.0330	0.0028	4273.546	0.0041
$5_{14} \rightarrow 4_{22}$	4283.6180	0.0062	4278.869	-0.0457
$3_{21} \rightarrow 2_{20}$	4336.6920	-0.0054	4329.521	0.0026
$3_{21} \rightarrow 3_{13}$	4339.9620	0.0031	4340.359	-0.019
$2_{11} \rightarrow 1_{01}$	4345.0610	0.0015	4345.467	-0.0095
$5_{05} \rightarrow 4_{13}$	4510.7770	-0.0068	--	--
$3_{12} \rightarrow 2_{11}$	4512.1230	0.0034	4511.031	0.0077
$4_{04} \rightarrow 3_{13}$	4717.4980	0.0007	--	--
$4_{22} \rightarrow 4_{14}$	4863.7710	0.0013	--	--
$3_{13} \rightarrow 2_{02}$	5007.5220	0.0015	5011.761	-0.0099
$7_{35} \rightarrow 7_{25}$	5043.5670	0.0001	5042.878	-0.015
$4_{14} \rightarrow 3_{13}$	5317.6780	0.0005	5321.644	0.0001
$6_{34} \rightarrow 6_{24}$	5480.4100	0.0033	5476.219	0.0102
$4_{04} \rightarrow 3_{03}$	5525.8000	0.0004	5518.885	-0.0023
$5_{23} \rightarrow 5_{15}$	5621.2100	0.0032	--	--
$4_{23} \rightarrow 3_{22}$	5676.9610	0.0005	5677.705	0.0021
$4_{32} \rightarrow 3_{31}$	5722.6170	-0.0042	5724.548	0.028
$4_{31} \rightarrow 3_{30}$	5729.3230	-0.0018	5725.029	-0.0205
$6_{15} \rightarrow 5_{23}$	5780.0080	0.0114	--	--
$5_{33} \rightarrow 5_{23}$	5808.4970	0.0051	5797.215	0.0104
$4_{22} \rightarrow 3_{21}$	5841.4850	-0.0033	5838.612	0.0047
$4_{13} \rightarrow 3_{12}$	5992.8910	-0.0004	5991.252	0.0125
$4_{32} \rightarrow 4_{22}$	6024.6180	-0.0047	6005.57	-0.0011
$3_{12} \rightarrow 2_{02}$	6029.3430	0.0016	--	--
$10_{010} \rightarrow 9_{18}$	6134.2690	0.002	--	--
$3_{31} \rightarrow 3_{21}$	6143.4910	0.0011	--	--
$3_{30} \rightarrow 3_{21}$	6144.6140	-0.0011	--	--
$3_{30} \rightarrow 3_{22}$	6230.7570	0.0102	--	--
$4_{31} \rightarrow 4_{23}$	6283.0950	-0.016	--	--
$5_{32} \rightarrow 5_{24}$	6394.3790	-0.0171	--	--
$2_{21} \rightarrow 1_{10}$	6491.9150	-0.0005	6482.864	0.007
$2_{20} \rightarrow 1_{10}$	6509.3790	-0.0009	--	--
$5_{15} \rightarrow 4_{14}$	6621.1120	-0.0053	6631.209	-0.0123
$2_{21} \rightarrow 1_{11}$	6662.4140	0.0017	6653.836	-0.0018
$2_{20} \rightarrow 1_{11}$	6679.8850	0.0082	--	--

$5_{05} \rightarrow 4_{04}$	6807.9940	-0.0048	6794.241	-0.0076
$5_{24} \rightarrow 4_{23}$	7074.2460	-0.0044	7073.758	0.0095
$5_{33} \rightarrow 4_{32}$	7162.4200	-0.0034	7168.254	0.0345
$5_{32} \rightarrow 4_{31}$	7185.5250	-0.0104	7176.774	-0.0209
$5_{15} \rightarrow 4_{04}$	7221.2900	-0.0075	--	--
$5_{23} \rightarrow 4_{22}$	7378.5570	0.0027	7376.599	0.0131
$5_{14} \rightarrow 4_{13}$	7450.3480	0.0029	--	--
$4_{22} \rightarrow 3_{12}$	9159.6100	-0.0140	9160.2594	-.0191
$7_{17} \rightarrow 6_{16}$	9192.0197	-0.0029	9224.6726	-.0187
$7_{07} \rightarrow 6_{06}$	9295.2367	0.0014	--	--
$8_{18} \rightarrow 7_{17}$	10462.7660	0.0064	10499.7117	-.0359
$8_{08} \rightarrow 7_{07}$	10529.8465	0.0016	10486.9252	-.0104
$7_{25} \rightarrow 6_{24}$	10478.9344	0.0014	10476.5645	.0089
$7_{16} \rightarrow 6_{25}$	8134.0953	-0.0150	8123.6800	-.0339
$6_{16} \rightarrow 5_{05}$	8325.4246	-0.0103	--	--
$8_{17} \rightarrow 7_{16}$	11587.5759	0.0028	11579.8379	.0160
$6_{16} \rightarrow 5_{15}$	7912.1367	-0.0006	7933.0909	-.0077
$6_{06} \rightarrow 5_{05}$	8058.7148	-0.0057	8033.3655	-.0141
$6_{15} \rightarrow 5_{14}$	8874.9295	-0.0045	8871.5425	.0212
$6_{24} \rightarrow 5_{23}$	8931.4748	-0.0136	8929.4836	.0019
$7_{07} \rightarrow 6_{16}$	9028.5266	0.0058	--	--

Table 3-3: Experimental rotational Constants (MHz), centrifugal distortion constants (kHz) and second moment of A-state, fitted using ASFIT program (fit include the transitions obtained from both the CP-FTMW spectrometer and the PN-FTMW spectrometer) and PGOPHER program (fit includes transitions obtained from the CP-FTMW spectrometer only).

Constants	**ASFIT**	**PGOPHER**	**B3LYP-D3/aug-cc-pVDZ**
A_0'	1955.3333(8)	1955.3330(8)	2004.82
B_0'	796.5837(3)	796.5831(4)	802.76
C_0'	626.0865(2)	626.0852(3)	621.78
D_J	1.2(2)	1.120(6)	0.49
D_{JK}	-6.006(3)	-6.00(2)	-2.37
D_K	17.52(8)	17.54(8)	8.83
d_1	-0.137(1)	-0.144(1)	-0.09

d_2	-0.0060(9)	-0.0002(8)	-0.001
P_{cc} (u Å^2)	42.85	42.85	34.41
N_A	71	59	--
σ (kHz)	5.6	5.2	--

P_{cc} is the second moment given by: $P_{cc} = \frac{I_b - I_a - I_c}{2}$

Rotational constants, distortion constants, and second moment calculated at B3LYP-D3/aug-cc-pVDZ level of theory are taken from *Table 3-1*.

3.3.3 Isotopic Substitution:

The spectra for isotopologues of the PhAc···CH_3OH complex were recorded to ascertain the geometry of the observed structure and to better comprehend the motions that lead to the spectral splitting. The results of the spectroscopic fitting for $(M\text{-}P)_{Ac}$ enabled the identification and fitting of transitions for four more isotopologues, including PhAc···CH_3OD, PhAc···CD_3OD, PhAc-D···CH_3OH, and PhAc···$^{13}CH_3OH$. The CP-FTMW spectrometer at Newcastle University was used to detect and assign transitions for each isotopologue. The spectroscopic parameters were determined by fitting the observed transitions through the utilization of Western's PGOPHER[61] program. Transition frequencies and their assignments for all the isotopologues are given in the *Table 3-4* to *Table 3-7*. Intriguingly, all the isotopologues exhibited distinct spectral splitting in the transition frequencies due to the large amplitude motion of the methyl group. Subsequently, a global fit analysis was conducted for all the isotopologues, excluding the PhAc···CD_3OD complex. In the case of PhAc···CD_3OD, substantial overlap between *A* and *E*-state transitions, coupled with reduced signal intensity precluded the global fit. Additionally, hyperfine structures (caused by the deuterium nucleus which has I=1) could not be resolved for the PhAc···CH_3OD, PhAc···CD_3OD, and PhAc-D···CH_3OH complexes. For each isotopologue, the fitted rotational constants and centrifugal distortion constants of *A*-state transitions are presented in *Table 3-8*. The rotational constants and centrifugal distortion constants determined from the global fit are presented in *Table 3-9*.

Table 3-4: Experimentally observed rotational transition and their assignments for the C_6H_5CCH···CH_3OD complex.

Transitions	***A*-State**	***E*-State**

	ν_{obs}	$\nu_{obs-cal}$	ν_{obs}	$\nu_{obs-cal}$
$1_{1\,1} \rightarrow 0_{0\,0}$	2582.175	0.0124	--	--
$2_{1\,2} \rightarrow 1_{1\,1}$	2644.11	-0.0346	--	--
$1_{1\,0} \rightarrow 0_{0\,0}$	2748.775	-0.0073	2749.012	0.0027
$2_{0\,2} \rightarrow 1_{0\,1}$	2794.261	-0.0058	2793.176	-0.0101
$2_{1\,1} \rightarrow 1_{1\,0}$	2977.379	0.0036	2976.878	0.0134
$2_{1\,2} \rightarrow 1_{0\,1}$	3820.91	-0.0155	3821.489	-0.0045
$3_{1\,3} \rightarrow 2_{1\,2}$	3956.335	0.0034	3956.824	0.0015
$3_{0\,3} \rightarrow 2_{0\,2}$	4151.204	-0.0036	4149.152	-0.0017
$3_{2\,2} \rightarrow 2_{2\,1}$	4216.191	0.0132	4219.458	0.0171
$3_{2\,1} \rightarrow 2_{2\,0}$	4281.025	0.016	4276.589	0.0308
$2_{1\,1} \rightarrow 1_{0\,1}$	4320.778	0.002	4320.977	0.0068
$3_{1\,2} \rightarrow 2_{1\,1}$	4455.117	-0.0152	4454.413	-0.0099
$3_{1\,3} \rightarrow 2_{0\,2}$	4983	0.0097	4985.13	0.0000
$4_{1\,4} \rightarrow 3_{1\,3}$	5258.032	0.002	5259.89	0.0012
$4_{0\,4} \rightarrow 3_{0\,3}$	5465.46	0.0034	5461.531	0.0017
$6_{3\,4} \rightarrow 6_{2\,4}$	5592.913	-0.0001	--	--
$4_{2\,3} \rightarrow 3_{2\,2}$	5608.6	-0.0068	5608.753	-0.0085
$4_{3\,2} \rightarrow 3_{3\,1}$	5651.775	0.0155	--	--
$4_{3\,1} \rightarrow 3_{3\,0}$	5657.863	0.0016	5654.315	-0.0097
$4_{2\,2} \rightarrow 3_{2\,1}$	5764.34	-0.0184	5762.665	-0.0058
$4_{1\,3} \rightarrow 3_{1\,2}$	5918.318	-0.0019	5917.271	0.0014
$3_{1\,2} \rightarrow 2_{0\,2}$	5981.639	-0.0024	5982.201	-0.0061
$4_{1\,4} \rightarrow 3_{0\,3}$	6089.814	0.0012	--	--
$5_{0\,5} \rightarrow 4_{1\,4}$	6112.264	0.0015	6094.56	0.0001
$5_{1\,5} \rightarrow 4_{1\,4}$	6547.833	-0.0025	6552.975	0.0008
$5_{0\,5} \rightarrow 4_{0\,4}$	6736.621	0.0024	6728.896	0.0003
$5_{2\,4} \rightarrow 4_{2\,3}$	6990.037	-0.013	6989.497	-0.0022
$5_{3\,3} \rightarrow 4_{3\,2}$	7073.534	0.0037	7078.131	0.0056
$5_{3\,2} \rightarrow 4_{3\,1}$	7094.59	0.0005	7087.912	-0.0158
$5_{2\,3} \rightarrow 4_{2\,2}$	7279.388	-0.0001	7278.132	-0.003
$5_{1\,4} \rightarrow 4_{1\,3}$	7359.715	0.0168	7358.216	0.0083

Table 3-5: Experimentally observed rotational transition and their assignments for the $C_6H_5CCD\cdots CH_3OH$ complex.

Transitions	*A*-State		*E*-State	
	ν_{obs}	$\nu_{obs-cal}$	ν_{obs}	$\nu_{obs-cal}$
$2_{12} \rightarrow 1_{11}$	2635.172	2635.666	-0.0183	2635.172
$2_{02} \rightarrow 1_{01}$	2790.078	2788.263	0.0102	2790.078
$2_{11} \rightarrow 1_{10}$	2983.027	2982.196	-0.0024	2983.027
$3_{22} \rightarrow 3_{12}$	3057.972	3056.206	0.004	3057.972
$3_{03} \rightarrow 2_{12}$	3191.811	3185.137	-0.0051	3191.811
$2_{12} \rightarrow 1_{01}$	3737.278	3738.49	-0.0012	3737.278
$3_{13} \rightarrow 2_{12}$	3941.414	3942.873	0.0068	3941.414
$3_{03} \rightarrow 2_{02}$	4139.01	4135.382	0.0015	4139.01
$3_{22} \rightarrow 2_{21}$	4213.658	4219.575	-0.0002	4213.658
$2_{11} \rightarrow 1_{01}$	4259.056	4259.475	-0.0115	4259.056
$3_{12} \rightarrow 2_{11}$	4461.871	4460.776	0.0002	4461.871
$3_{13} \rightarrow 2_{02}$	4888.625	4893.103	-0.0017	4888.625
$4_{14} \rightarrow 3_{13}$	5235.776	5240.274	0.0019	5235.776
$4_{04} \rightarrow 3_{03}$	5440.198	5432.862	0.0009	5440.198
$4_{23} \rightarrow 3_{22}$	5603.285	5604.167	-0.0022	5603.285
$4_{31} \rightarrow 3_{30}$	5660.493	5655.775	-0.0231	5660.493
$4_{22} \rightarrow 3_{21}$	5780.984	5778.073	0.0054	5780.984
$4_{13} \rightarrow 3_{12}$	5923.645	5921.996	-0.0006	5923.645
$3_{12} \rightarrow 2_{02}$	5930.859	5932.014	0.0046	5930.859
$4_{14} \rightarrow 3_{03}$	5985.38	5998.002	0.0057	5985.38
$2_{20} \rightarrow 1_{10}$	6308.194	6317.367	-0.0039	6308.194
$7_{34} \rightarrow 7_{26}$	6742.715	--	--	6742.715
$5_{24} \rightarrow 4_{23}$	6980.282	6979.908	0.0007	6980.282
$11_{39} \rightarrow 10_{47}$	6982.021	--	--	6982.021
$5_{33} \rightarrow 4_{32}$	7075.431	7082.079	0.0227	7075.431
$5_{23} \rightarrow 4_{22}$	7306.128	7304.185	0.0006	7306.128
$3_{21} \rightarrow 2_{11}$	7613.412	--	--	7613.412
$6_{16} \rightarrow 5_{15}$	7785.148	7808.21	-0.0052	7785.148
$6_{06} \rightarrow 5_{05}$	7921.241	7893.91	-0.0007	7921.241

Table 3-6: Experimentally observed rotational transition and their assignments for the $C_6H_5CCH\cdots{}^{13}CH_3OH$ complex.

Transitions	*A*-State		*E*-State	
	ν_{obs}	$\nu_{obs-cal}$	ν_{obs}	$\nu_{obs-cal}$
$1_{1\,0} \rightarrow 0_{0\,0}$	2721.48	-0.0031	2721.88	-0.0014
$2_{0\,2} \rightarrow 1_{0\,1}$	2791.584	0.0037	2789.806	-0.0004
$2_{1\,1} \rightarrow 1_{1\,0}$	2975.255	0.0012	2974.473	-0.0009
$3_{2\,2} \rightarrow 3_{1\,2}$	3212.272	-0.0044	3210.961	0.0063
$2_{2\,1} \rightarrow 2_{1\,1}$	3451.221	-0.0021	3443.889	-0.002
$2_{2\,0} \rightarrow 2_{1\,1}$	3468.075	-0.001	3476.825	-0.0009
$4_{0\,4} \rightarrow 3_{1\,2}$	3651.26	0.0034	3640.049	0.0069
$2_{1\,2} \rightarrow 1_{0\,1}$	3792.125	0.0058	3793.274	-0.0044
$3_{1\,3} \rightarrow 2_{1\,2}$	3952.39	0.0032	3953.58	-0.0012
$2_{2\,0} \rightarrow 2_{1\,2}$	3968.472	0.0092	3976.447	-0.0038
$3_{0\,3} \rightarrow 2_{0\,2}$	4146.289	0.0029	4142.857	-0.0014
$3_{2\,2} \rightarrow 3_{1\,3}$	4211.972	0.0138	4207.605	0.0004
$3_{2\,2} \rightarrow 2_{2\,1}$	4212.732	-0.0031	4217.673	0.0031
$3_{2\,1} \rightarrow 2_{2\,0}$	4279.031	0.0034	4272.432	-0.0052
$2_{1\,1} \rightarrow 1_{0\,1}$	4292.506	0.0000	4292.899	-0.0042
$3_{2\,1} \rightarrow 3_{1\,3}$	4295.099	-0.0046	4295.301	-0.0057
$9_{2\,7} \rightarrow 9_{1\,8}$	4332.372	-0.0025	4450.605	-0.0013
$3_{1\,2} \rightarrow 2_{1\,1}$	4451.682	0.0001	4440.807	-0.0092
$5_{0\,5} \rightarrow 4_{1\,3}$	4463.654	0.0053	--	--
$4_{2\,3} \rightarrow 4_{1\,4}$	4563.263	0.0049	--	--
$4_{2\,2} \rightarrow 4_{1\,4}$	4805.41	0.0026	4799.166	0.0053
$3_{1\,3} \rightarrow 2_{0\,2}$	4952.922	-0.0037	4957.094	0.0408
$4_{1\,4} \rightarrow 3_{1\,3}$	5252.411	0.0003	5256.188	-0.0014
$4_{0\,4} \rightarrow 3_{0\,3}$	5457.579	0.0009	5450.886	-0.0008
$4_{2\,3} \rightarrow 3_{2\,2}$	5603.708	-0.0026	5604.249	-0.0054
$4_{3\,2} \rightarrow 3_{3\,1}$	5647.826	-0.001	5649.597	0.0235
$4_{3\,1} \rightarrow 3_{3\,0}$	5654.205	-0.0023	5650.072	-0.0317
$4_{2\,2} \rightarrow 3_{2\,1}$	5762.721	0.0064	5760.047	0.0036
$5_{3\,3} \rightarrow 5_{2\,3}$	5771.138	-0.0091	--	--
$4_{1\,3} \rightarrow 3_{1\,2}$	5913.154	0.0016	5911.526	-0.0012

$3_{1\,2} \rightarrow 2_{0\,2}$	5952.606	-0.0016	5953.695	-0.008
$4_{1\,4} \rightarrow 3_{0\,3}$	6059.039	-0.0113	6070.375	-0.0092
$3_{3\,1} \rightarrow 3_{2\,1}$	6095.394	0.0072	--	--
$2_{2\,0} \rightarrow 1_{1\,0}$	6443.333	0.0032	6451.296	-0.0038
$5_{1\,5} \rightarrow 4_{1\,4}$	6540.351	0.0015	--	--
$2_{2\,1} \rightarrow 1_{1\,1}$	6593.271	-0.0038	--	--
$5_{0\,5} \rightarrow 4_{0\,4}$	6725.546	0.0016	6712.304	0.0027
$5_{2\,4} \rightarrow 4_{2\,3}$	6983.439	-0.007	6982.864	-0.0127
$5_{3\,3} \rightarrow 4_{3\,2}$	7068.684	-0.0006	7074.05	0.0238
$5_{2\,3} \rightarrow 4_{2\,2}$	7278.044	0.0072	7276.145	0.0048
$5_{1\,4} \rightarrow 4_{1\,3}$	7352.188	-0.0027	7349.848	0.0019
$4_{1\,3} \rightarrow 3_{0\,3}$	7719.463	-0.0108	7722.37	-0.0019
$3_{2\,1} \rightarrow 2_{1\,1}$	7747.101	-0.0026	7749.264	0.0009
$6_{1\,6} \rightarrow 5_{1\,5}$	7816.217	0.0036	7836.312	-0.0065

Table 3-7: Experimentally observed rotational transition and their assignments for the $C_6H_5CCH\cdots CD_3OD$ complex.

Transitions	***A*-State**	
	ν_{obs}	**$\nu_{obs-cal}$**
$3_{1\,3} \rightarrow 2_{1\,2}$	3798.176	-0.0114
$3_{0\,3} \rightarrow 2_{0\,2}$	3980.696	0.0098
$3_{2\,2} \rightarrow 2_{2\,1}$	4039.795	-0.0004
$3_{2\,2} \rightarrow 3_{1\,3}$	4090.933	-0.0008
$9_{2\,7} \rightarrow 9_{1\,8}$	4093.134	0.0006
$3_{1\,2} \rightarrow 2_{1\,1}$	4262.493	0.0104
$4_{1\,4} \rightarrow 3_{1\,3}$	5048.69	-0.0091
$4_{0\,4} \rightarrow 3_{0\,3}$	5244.112	0.0042
$4_{2\,3} \rightarrow 3_{2\,2}$	5374.682	0.0093
$6_{3\,4} \rightarrow 6_{2\,4}$	5462.981	0.0079
$4_{2\,2} \rightarrow 3_{2\,1}$	5516.706	-0.0019
$6_{3\,3} \rightarrow 6_{2\,4}$	5535.716	-0.0079
$4_{1\,3} \rightarrow 3_{1\,2}$	5663.559	-0.0122
$10_{0\,10} \rightarrow 9_{1\,8}$	6030.854	0.0001
$5_{1\,5} \rightarrow 4_{1\,4}$	6288.302	0.0008

$5_{05} \rightarrow 4_{04}$	6467.609	0.0054
$5_{24} \rightarrow 4_{23}$	6699.603	-0.0055
$5_{23} \rightarrow 4_{22}$	6964.26	0.002

Table 3-8: Experimental rotational constants (MHz), centrifugal distortion constants (kHz) and second moment of the A-state transitions (fit includes transitions obtained from the CP-FTMW spectrometer only).

Constants	**PhAc···CH_3OD**	**PhAc···CD_3OD**	**PhAc-D···CH_3OH**	**PhAc···$^{13}CH_3OH$**
A_0'	1962.830(4)	1874.216(6)	1891.357	1935.976(1)
B_0'	786.003(1)	750.848(2)	789.244(1)	785.5179(5)
C_0'	619.383(1)	595.748(2)	615.3135(7)	618.7179(4)
D_J	1.051(1)	0.77(3)	1.045(6)	1.153(9)
D_{JK}	-5.462(7)	-5.9(2)	-4.91(8)	-6.25(4)
D_K	53.2(6)	29.6(8)	17.9(7)	18.1(1)
d_1	-0.177(1)	-0.222(9)	-0.131(8)	-0.153(5)
d_2	-0.022(9)	0.002(2)	-0.009(5)	-0.014(3)
P_{cc} (u Å^2)	42.25	47.21	43.10	43.80
N_{lines}	31	23	29	44
σ (kHz)	7.4	12.5	6.8	4.6

P_{cc} is the second moment given by: $P_{cc} = \frac{I_b - I_a - I_c}{2}$

Table 3-9: Experimental rotational constants (MHz), centrifugal distortion constants (kHz) and second moment obtained from the global fit containing A- and E- state transitions (fit includes transitions obtained from the CP-FTMW spectrometer only).

Constants	**PhAc···CH_3OH**	**PhAc···CH_3OD**	**PhAc-D···CH_3OH**	**PhAc···$^{13}CH_3OH$**
A_0	1955.321(2)	1962.819(6)	1891.342(3)	1935.968(2)
B_0	796.5626(8)	785.989(2)	789.2236(9)	785.4967(9)
C_0	626.0065(9)	619.323(2)	615.2373(8)	618.66413(7)
D_J	1.13(1)	1.06(2)	1.040(6)	1.14(1)
D_{JK}	-6.05(3)	-5.49(8)	-4.88(7)	-6.30(5)
D_K	17.5(1)	53.1(7)	16(7)	18.3(2)
d_1	-0.145(2)	-0.18(2)	-0.131(8)	-0.146(7)

d_2	0.001(1)	-0.03(1)	-0.018(6)	-0.017(5)
$D_{\pi 2J}$	-322(4)	-271(1)	-313(4)	-325(2)
$D_{\pi 2K}$	849(6)	760(5)	780(9)	857(6)
V_3 (cm^{-1})	234(8)	253(7)	235(4)	236(1)
F_0 (cm^{-1})	6.15(6)[a]	6(1)[a]	6(1)[a]	6.18(5)[a]
∠(*i*, *a*) (degree)	68(2)	68(7)	68(2)	67(1)
∠(*i*, *b*) (degree)	22.9(2)	22(6)	23(2)	22(1)
∠(*i*, *c*) (degree)	96.156(9)	95.6(0)	96.765(8)	95.747(5)
P_{cc} (u $Å^2$)	42.80	42.22	43.06	43.77
N_A/N_E	59/39	31/26	29/24	44/38
σ (kHz)	10.5	11.9	8.0	8.9

P_{cc} is the second moment given by: $P_{cc} = \frac{I_b - I_a - I_c}{2}$

[a]The corresponding *F* values for PhAc···CH_3OH, PhAc···CH_3OD, PhAc-D···CH_3OH, and PhAc···$^{13}CH_3OH$ are 6.17, 6.11, 6.18, and 6.21 cm^{-1}, while the ρ value is approximately 0.004 for all isotopologues.

3.4 Discussions: Structure and Dynamics

3.4.1 Internal Rotation of Methyl Group:

Observation of both *A*- and *E*-state transitions allows for an analysis of large amplitude motions within the PhAc···CH_3OH complex. It will be shown that it is possible to fit the frequencies of both *A*- and *E*-state transitions to the predictions of a Hamiltonian that includes parameters to describe the internal rotation of the methyl group within the complex. These include V_3, the height of the potential energy barrier to the internal rotation that has three-fold symmetry about the rotor axis; *F*, which is equal to $h / [8\pi^2 I_\alpha(1-\rho_a)]$ where $\rho_a = I_\alpha / I_a$ and I_α is the moment of inertia for rotation of the CH_3 group about the internal rotor axis; ∠(*i*, *a*), ∠(*i*, *b*), and ∠(*i*, *c*) which represent the angles between the rotor axis and each of the principal inertial axes, *a*, *b* and *c* respectively; and $D_{\pi 2J}$, $D_{\pi 2K}$ and $D_{\pi 2-}$ terms which represent the effects of centrifugal distortion. However, it is important first to review the extent to which a Hamiltonian containing these terms is appropriate for modelling the large amplitude motions present within PhAc···CH_3OH.

It is possible to separately determine F and V_3 where a sufficient number of rotational transitions are recorded for multiple torsional states as achieved by De Lucia *et al*. for the CH_3OH monomer.[14] However, in general, studies of CH_3OH-containing complexes performed by microwave spectroscopy tend to probe rotational transitions of only the ground torsional state and this is also true of the present work. It is not possible to separately determine F and V_3 with high precision through fits performed to rotational spectra recorded only for the ground torsional state. An approach often taken by microwave spectroscopists involves fixing F at an assumed value such that a fitted value of V_3 can be obtained. Many studies have sought to explore changes in V_3 as a function of the substitution position of a CH_3 group on a rigid molecular framework (for example, at different substitution positions on an aromatic ring). In such examples, it is well-established that I_α and F_0 (where F_0 is equal to F for the limiting case where $\rho_a = 0$) can respectively be approximated as ~3.2 u Å^2 and ~157.9 GHz and this knowledge was exploited by several authors of the present work during recent analyses of internal rotation within isomers of the monohydrate complexes of methylthiazole and methylimidazole.[62,63] However, the CH_3 group is *not* bound to a rigid molecular framework within CH_3OH so the value of F_0 cannot *a priori* be assumed to be reliable in such cases. In fact, as long ago as the 1980's, papers by Lovas *et al*. and Suenram *et al*. analysed large amplitude motions within hydrogen-bonded complexes containing CH_3OH while highlighting that their analyses would not reliably distinguish the effects of CH_3 internal rotation from vibrational motions of the O–H group.[24,25] Authors were careful to report only "effective" V_3 barriers which they did not intend to be used in direct comparisons with V_3 determined for other molecules and complexes. A recent study of the diphenyl ether···CH_3OH complex highlighted this continuing constraint.[23] The results of two alternative approaches were presented when the spectrum of diphenyl ether···CH_3OH was analysed: (1) a fit was performed to determine both V_3 and F_0 even while it was explained that these parameters are unavoidably correlated in the fit that was performed and (2) a fit was performed to determine V_3 while assuming a fixed value of F_0. To facilitate broad comparisons of data sets which may follow in future works, the same approach will be taken towards the reporting of results for internal rotation parameters herein. The results presented in *Table 3-9* employed the first of the approaches described above while the results obtained by the alternative approach are presented in the Supplementary Data (*Table 3-23)*.

To gain insight into the V_3 barrier within the context of the PhAc···CH_3OH complex, we conduct a relaxed potential energy scan for the rotation of the CH_3 group within the (M-

P)$_{Ac}$ structure. This potential energy scan is carried out at the B3LYP-D3/aug-cc-pVDZ level of theory. The resulting potential energy curve for this relaxed scan is shown in *Figure 3-4*, in which the barrier to CH_3 rotation is found to be 312.8 cm^{-1}. The computed barrier height, when compared to that observed in the methanol monomer, suggests that the methyl (CH_3) group within the (M-P)$_{Ac}$ complex is not significantly engaged in intermolecular interactions with PhAc. Analysis of the experimental spectra is facilitated by the XIAM program, which can be used to perform a "global" fit of both *A*- and *E*-state transitions to determine parameters in a rotational Hamiltonian, which includes terms to describe the effects of centrifugal distortion and internal rotation. The XIAM program utilizes a Hamiltonian that is formulated within the principal axis system. The program uses a "local" approach, treating each torsional state individually without taking into account any interactions between different torsional states. The analysis yields the values shown in *Table 3-9* for the F_0, V_3, $\angle(i, a)$, $\angle(i, b)$, $\angle(i, c)$, $D_{\pi 2J}$ and $D_{\pi 2K}$ parameters (defined within the opening paragraph of this section) for each of four isotopologues of the PhAc···CH_3OH complex.

Table 3-10 presents a comparison of results reported for F and V_3 for the series of CH_3OH-containing complexes studied to date where analyses of internal rotation have been reported. As noted earlier, F_0 and V_3 cannot be independently determined from rotational spectra reported for only a single torsional state. On the other hand, the value of the reduced barrier, $s = 4V_3 / 9F$ (a dimensionless quantity), is also sensitive to the splitting between *A*- and *E*-state transitions and provides an interesting perspective on the results shown. The complexes featured in *Table 3-10* are presented in order of decreasing s. Many previous works assumed a fixed value of F_0 to allow the determination of an "effective" V_3. It is immediately apparent from *Table 3-10* that the results for V_3 cannot easily be rationalised with any trend in molecular properties or geometry across this set of complexes. For example, the V_3 reported for Ar···CH_3OH and HCl···CH_3OH are significantly lower than that for the CH_3OH monomer for reasons that do not obviously connect with any aspect of the properties of these complexes.[14,25,26] In any case, as noted by the authors of the original works, the V_3 of these species almost certainly differ because accurate values of F_0 were not available when the fits to determine V_3 for each of Ar···CH_3OH and HCl···CH_3OH were performed, and unreliable assumptions were therefore made. An alternative and more insightful perspective on the underpinning molecular physics is provided by the trend in s as a function of molecular geometry and bonding across the series of complexes featured in *Table 3-10*.

CH_3OH-containing complexes where the O of CH_3OH acts as hydrogen bond *acceptor* ($HCl\cdots CH_3OH$ or monomer II of $(CH_3OH)_2$) or where the complex is bound by another form of weak interaction (e.g. $SO_2\cdots CH_3OH$, $Ar\cdots CH_3OH$) have values of *s* which are very similar to that determined (*s* = 6.0) for the isolated CH_3OH monomer.[14,21,22,25,27] Those complexes where the O–H of CH_3OH acts as a hydrogen bond donor have significantly higher *s* that range from 14.12 for $CO\cdots CH_3OH$ to 21.95 for phenyl vinyl ether$\cdots CH_3OH$.[30,34] There also appears to be a correlation between the relative strength of the hydrogen bond(s) formed within each complex and the value of *s*. Where a complex contains only a single hydrogen bond, and especially where this bond can be expected to be weak, the *s* for the complex appears to lie at the lower end of the range. Complexes with stronger hydrogen bonds generally associate with higher values of *s* and those at the high end of the range are held together by multiple interactions. For example, formamide$\cdots CH_3OH$ contains multiple intermolecular hydrogen bonds whereas the diphenyl ether and CH_3OH monomers interact via dispersion interactions in addition to the hydrogen bond present within the diphenyl ether$\cdots CH_3OH$ complex. An important confirmation of the described relationship is provided by the *s* values attributed to each of the CH_3OH monomers present within the CH_3OH dimer. This complex is primarily the result of a hydrogen bond formed between the O–H of one monomer and the oxygen atom of the second. That monomer which acts as hydrogen bond donor within the CH_3OH dimer has a value for *s* that is consistent with its role. The other, which acts as the hydrogen bond acceptor, has an *s* value similar to that seen for the isolated CH_3OH monomer.

Table 3-10: Barrier heights V_3 for methyl rotation in the previously studied methanol-containing complexes.

Molecule	V_3 (cm^{-1})	F (cm^{-1})	*s*	Reference
CH_3OH = H-bond donor				
Phenyl vinyl ether$\cdots CH_3OH$	261.8	5.3[a]	21.95	[34]
Diphenyl ether$\cdots CH_3OH$	480	10.16[ab]	21.00	[23]
Diphenyl ether$\cdots CH_3OH$	250.74	5.3[a]	21.03	[23]
Formamide$\cdots CH_3OH$	231.01	5.26[a]	19.52	[24]
Aniline$\cdots CH_3OH$	215	5.28	18.10	[29]
$H_2CO\cdots CH_3OH$	240.5	6.17	17.32	[31]
PhAc$\cdots CH_3OH$	200.1	5.27	16.88	Present work

PhAc···CH_3OH	234	6.17[b]	16.86	Present work
CH_3OH dimer (Mon I)[c]	201	5.4[b]	16.54	[20]
Trimethylamine···CH_3OH	174	5.30	14.59	[28]
CO···CH_3OH	183	5.76	14.12	[30]
Other Molecules and Complexes				
Phenol···CH_3OH	170	5.27	14.34	[64]
CO_2···CH_3OH	174.8	5.45	14.25	[31]
SO_2···CH_3OH	128.7	5.3	10.79	[27]
CH_3OH dimer (Mon II)[c]	118.7	5.16[b]	10.22	[20]
HCl···CH_3OH	74.0	5.3[a]	6.21	[26]
CH_3OH monomer	373	27.63[b]	6.00	[14]
Ar···CH_3OH	68.5	5.3[a]	5.74	[65]

[a]The original works fixed F_0 rather than F, so the value for F_0 is quoted in this table. For the heavier complexes (phenyl vinyl ether…MeOH, diphenyl ether…MeOH), it can reliably be assumed that the value of F_0 will be very similar to (within a few percent of) that of F. This will not necessarily be true for complexes of MeOH with lighter molecules such as HCl, Ar or formamide.

[b]Allowed to float during the fitting procedure.

[c]Mon I and Mon II are the two CH_3OH monomers within the $(CH_3OH)_2$ dimer, where Mon I is the hydrogen bond donor whereas Mon II is hydrogen bond acceptor.

Except as indicated by footnotes (a,b), the original works performed fits to determine V_3 while fixing the values for F at the results shown.

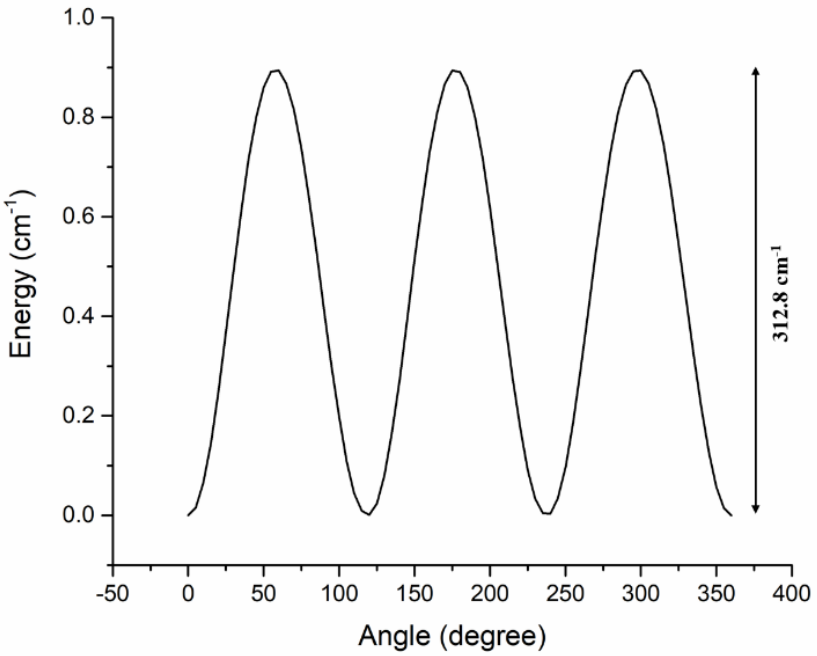

Figure 3-4: The potential energy curve for the internal rotation of CH_3 group in the PhAc···CH_3OH complex.

3.4.2 Structural Analysis:

Analysis of the fitted rotational constants reveals a very close agreement between the experimentally determined values and those computed for the $(M\text{-}P)_{Ac}$ structure using DFT (B3LYP-D3/aug-cc-pVDZ). The structural characteristics observed in the PhAc···CH_3OH complex exhibit similarities to those observed in the PhAc···H_2O complex.[10] In both cases, there is a hydrogen bond donation from the hydroxyl (OH) group of CH_3OH/H_2O to the acetylene moiety of PhAc, accompanied by a secondary interaction involving the ortho hydrogen of PhAc and the oxygen atom of CH_3OH or H_2O.

The findings of the IR/UV double resonance experiments conducted on the PhAc···H_2O and PhAc···CH_3OH complexes have been previously reported, with the determination of their structures relying on the analysis of the fluorescence dip infrared (FDIR) spectra in the O-H and C-H stretching regions.[4] The vibrational frequencies corresponding to the O-H stretch ($\nu_{O\text{-}H}$) of the H_2O and CH_3OH complexes of PhAc, both calculated and experimentally obtained (as cited in reference 2), are given in *Table 3-24* of the Supplementary Information. In the case of the PhAc···H_2O complex, the experimentally recorded $\nu_{O\text{-}H}$ value for the PhAc···H_2O complex was identified at 3629 cm^{-1} for the hydrogen bonded O-H and 3724 cm^{-1} for the free OH. The predicted values for the hydrogen bonded $\nu_{O\text{-}H}$ in acetylenic and phenyl bound structures were 3587 and 3621 cm^{-1}, respectively. Clearly, the observed value of 3629 cm^{-1} is larger than what is predicted for both conformers, though closer to the phenyl-bound structure. Still, the acetylenic bound structure was favoured for the following reasons. The resonant ion-dip infrared spectra of the benzene···H_2O π hydrogen bonded complex in the O-H stretch region exhibit over six transitions, attributed to the large amplitudes tumbling motion of the H_2O molecule.[66] As previously mentioned, the FDIR spectrum of the PhAc···H_2O complex displays two distinctive transitions corresponding to the hydrogen bonded and the free O-H vibrations. Consequently, it was deduced that, unlike benzene···H_2O, the H_2O molecule forms a strong bond with the PhAc in the PhAc···H_2O complex. Given that the acetylenic bound structure involves O-H···π and C-H···O hydrogen bonds leading to a cyclic structure, it suggests the plausibility of the acetylenic bound configuration. More importantly, the FDIR spectra in the C-H stretch region were utilized to gain more comprehensive insights. In the PhAc monomer, peaks at 3325 cm^{-1} and 3343 cm^{-1} were detected, indicating the occurrence of

Fermi resonance. This Fermi resonance entails the vibration of C-H stretching and a combination band of one quantum of C≡C stretch and two quanta of out-of-plane acetylenic C-H bend. Disturbances impacting the C≡C bond stretching vibration, such as intermolecular bonding, lead to the disappearance of Fermi resonance bands and the appearance of a single band corresponding to the free C-H oscillator. The FDIR spectrum of the PhAc···H_2O complex reveals a single band at 3331 cm^{-1}, which further confirms the interaction of the O-H group with the π electron density of the acetylenic group.

As for the PhAc···CH_3OH complex, the experimental ν_{O-H} for the hydrogen bonded O-H was identified at 3615 cm^{-1}. The theoretically predicted ν_{O-H} for the acetylenic (3633 cm^{-1}) and phenyl bound (3637 cm^{-1}) structures of the PhAc···CH_3OH complex were very similar, with a marginal difference of only 4 cm^{-1}. Consequently, these slight infrared band shifts observed in the weak O-H···π complexes do not offer sufficient evidence for definitive structural determinations. In the C-H stretch region of the FDIR spectrum, two bands were observed at 3323 cm^{-1} and 3334 cm^{-1}, indicating the presence of Fermi resonance. Hence, based on the Fermi resonance bands, it was deduced that the PhAc···H_2O complex involves O-H···π interactions through the acetylenic-π, while the PhAc···CH_3OH complex exhibits O-H···π interactions through the phenyl π-system.

The PhAc···H_2O complex has already been previously investigated by microwave spectroscopy and has confirmed the unambiguous structure of the complex to the acetylenic bound conformer.[10]

Karir *et al*. explored the docking preference of CH_3OH in the PhAc and its methylderivative (3-methylphenylacetylene) using FTIR spectroscopy of supersonic jet expansions.[2] The FTIR jet spectra of the 3-methylphenylacetylene···CH_3OH complex displayed two additional peaks at 3620 cm^{-1} and 3639 cm^{-1} in the O-H stretch region (see Figure S7 of reference 1) compared to the spectrum of bare methanol (3686 cm^{-1}), therefore these new bands were attributed to the acetylene and phenyl docking of the CH_3OH. It is well-established that deuteration reduces the hydrogen bond weakening effect of (zero point vibrational energy) ZPVE in more localized and strong interactions. The observed spectrum of 3-methylphenylacetylene···CH_3OD complex was very similar (OD stretch region was scaled to the OH stretch region by using a scaling factor of 1.356) with a reduction in intensity noted for the less shifted band (Figure 4 of reference 1). Thus, the band at 3620 cm^{-1} was assigned to the acetylenic bound whereas the band at 3639 cm^{-1} was assigned to the phenyl bound structure. The observation of both the

phenyl and acetylene bound structure in 3-methylphenylacetylene···CH_3OH complex is possible if the barriers between the docking sites are too high to be overcome. The DFT calculations (refer to Table 1 of reference 1) also suggested that the acetylenic bound structure is the more favourable case in 3-methylphenylacetylene···CH_3OH complex therefore the binding preference in this complex is shifted towards the acetylenic coordination by deuteration and also shifted in the same direction in the PhAc···CH_3OH complex. In the FTIR jet spectra of the PhAc···CH_3OH complex, a vibrational frequency associated with hydrogen bonded O-H stretching was detected only at 3622 cm^{-1}. This value notably deviates from that previously reported by Singh *et al.* (3615 cm^{-1} for CH_3OH complex). This disparity in the experimentally obtained vibrational frequencies within the same complex are attributed to inaccuracies in calibration during the laser experiment. Additionally, there is a notable discrepancy between the result of 3622 cm^{-1} and the measured $\nu_{O\text{-}H}$ of 3613 cm^{-1} for the PhAc···H_2O complex, for which no explanation was provided. The DFT-predicted and experimentally observed vibrational frequencies (taken from reference 1) are given in *Table 3-24* of the Supplementary Information for the hydrogen bonded O-H in the acetylenic and phenyl bound conformations for PhAc···H_2O, PhAc···CH_3OH and 3-methylphenylacetylene···CH_3OH. As described above, the assignments for PhAc···CH_3OH complexes were based on consistent deviations between DFT predictions and experimental results across various systems, further supported by isotope effects in the methylated derivative of PhAc.

The second moment, P_{cc}, calculated from the optimized structures at the DFT and MP2 levels of theories are presented in *Table 3-1*. It is apparent that the P_{cc} values for the $(M\text{-}P)_{Ac}$ structure optimized at MP2 and DFT exhibit substantial discrepancies. This discrepancy can be attributed to the presence of a secondary interaction in the DFT-optimized $(M\text{-}P)_{Ac}$ structure, which significantly impacts the overall configuration, despite both structures involving CH_3OH donating a hydrogen bond to the acetylenic moiety. The experimentally-determined values of P_{cc} for the parent and other isotopologues are provided in *Table 3-3*, *Table 3-8* and *Table 3-9* obtained during *A*-state only fits and global fitting containing both *A*- and *E*-state transitions. The experimental second moments closely align with the DFT-calculated $(M\text{-}P)_{Ac}$ structure. The replacement of a bonded hydrogen atom of CH_3OH causes minimal changes to the P_{cc} value, whereas the substitution of all four hydrogen atoms of the CH_3OH moiety results in a notable increase.

By using the Kraitchman approach,[67] the singly substituted isotopologues enable a direct structural examination of the complex. These equations could be used to find the position of the substituted atom from the centre of mass. For a non-planar asymmetric top molecule, the coordinate (r_s) of the substituted atom is given as follows:

$$|a| = \left[\frac{\Delta P_a}{\mu}\left(1+\frac{\Delta P_b}{I_a - I_b}\right)\left(1+\frac{\Delta P_c}{I_a - I_c}\right)\right]^{\frac{1}{2}}$$

$$|b| = \left[\frac{\Delta P_b}{\mu}\left(1+\frac{\Delta P_c}{I_b - I_c}\right)\left(1+\frac{\Delta P_x}{I_b - I_a}\right)\right]^{\frac{1}{2}}$$

$$|c| = \left[\frac{\Delta P_c}{\mu}\left(1+\frac{\Delta P_a}{I_c - I_a}\right)\left(1+\frac{\Delta P_b}{I_c - I_b}\right)\right]^{\frac{1}{2}}$$

Where, P_a, P_b and P_c represent the planar moment of inertia. The Kraitchman analysis operates under the assumption that bond distances and angles remain constant upon isotopic substitution. While this assumption generally holds for heavier atoms, the substitution of hydrogen (H) with deuterium (D) can lead to significant alterations in zero-point average positions. Consequently, H/D substitution may not always yield accurate positions for the substituted atoms. The KRA program,[68] developed by Kisiel and available on the PROSPE[69] website, was employed for this analysis. In this context, the PhAc···CH_3OH complex served as the parent isotopologue.

In *Figure 3-5*, we present the labelling of atoms within the molecular complex, along with an approximate orientation of the inertial axis framework. The rotational constants obtained using XIAM fitting approach, which contains both *A*- and *E*-species transitions, were utilised for the derivation of r_s coordinates for the acetylenic H atom (H14) and the carbon atom of CH_3OH (C15).

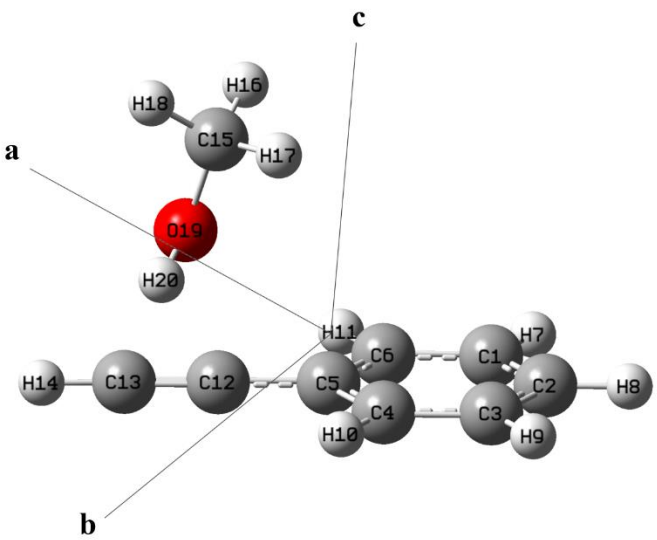

Figure 3-5: Labelling of the atoms used in the structural analysis for the PhAc···CH_3OH complex. The approximate location of the principal axes is shown.

These coordinates, along with associated Costain errors,[70] are provided in *Table 3-11*. It is noteworthy that the Kraitchman method does not yield the signs of atomic coordinates, which have been inferred from the outcomes of DFT calculations. The r_s coordinate of the bonding hydrogen atom (H20) of the CH_3OH sub-unit was found to deviate from the corresponding coordinate in the calculated structural model. This discrepancy can be attributed to the interplay between the methyl internal rotation and the large amplitude motion of the OH group in the CH_3OH.

Table 3-11: Kraitchman substitution coordinates (r_s) for the substituted atoms of the PhAc···CH_3OH complex. The coordinates are given in Å. Labelling of the atoms is shown in Figure 5.

Atom Number	**Method**	**Coordinates**		
		a	**b**	**c**
H14	Theory	2.4026	2.9476	-0.2607
	Experiment	2.3578(7)	2.9401(6)	-0.492(3)
C15	Theory	2.9851	-1.1981	0.9265
	Experiment	2.8282(5)	-1.296(1)	0.986(2)

Following a rigorous examination of the spectra of all five isotopologues, the structural configuration where CH_3OH forms a hydrogen bond with the phenyl π system could not be observed. Since the spectral assignment in case of results obtained by Singh *et al*. was exclusively based on the presence and absence of Fermi resonance, one possibility is that the PhAc···CH_3OH complex has a structure (CH_3OH is interacting with acetylenic-π system) that is observed by both FTIR spectroscopic study and the present study by microwave spectroscopy, while the Fermi resonance is unaffected. If this is the case, then all three experimental results give a consistent structure. The current study using microwave spectroscopy provides an unambiguous structure for PhAc···CH_3OH complex, wherein MeOH is forming hydrogen bond with the acetylenic π-system followed by a secondary weak C-H···O interaction. The present study further supports the conclusions drawn through FTIR spectroscopic results.[2]

3.4.3 Atoms in Molecules (AIM) Analysis:

The present study employs the Atoms in Molecules (AIM)[47] topological analysis to perform a comparative assessment of the bonding characteristics between PhAc···CH_3OH and PhAc···H_2O complexes. It is noteworthy that the AIM analysis for the PhAc··· H_2O complex has been previously reported.[9] The wavefunctions for PhAc···CH_3OH were obtained at the B3LYP-D3/aug-cc-pVDZ level of theory, whereas, for PhAc···H_2O, they were derived from previously reported coordinates optimized at the MP2/aug-cc-pVDZ level of theory.

The molecular graph for the PhAc···CH_3OH complex closely resembles that of the PhAc···H_2O complex except for the one additional bond critical point (BCP) and ring critical point (RCP) found in the PhAc···CH_3OH complex. The first BCP occurs between the hydroxyl hydrogen atom of CH_3OH/H_2O and the midpoint of the π-bond in PhAc, while the second BCP is situated between the oxygen atom of CH_3OH/H_2O and the ortho-hydrogen atom of PhAc. The third BCP in case of PhAc···CH_3OH complex is present between one of the hydrogen atoms of the methyl group to the ortho-carbon atom of the PhAc. The electron densities (ρ) and Laplacian ($\nabla^2\rho$) values for all BCPs are provided in *Table 3-12*. The molecular graphs showing BCP's and RCP's are given in

Figure 3-6. These ρ and $\nabla^2\rho$ values for both complexes fall within the range defined by Koch and Popelier for C-H···O hydrogen bonds.[71] A comparison of the electron densities at the BCP for O-H···π and C-H···O interactions in PhAc···CH_3OH and PhAc···H_2O complexes reveals that both interactions contribute equally to the stability of the observed geometry. Consistent with the findings in the PhAc···H_2O complex, the C-H···O interaction in the PhAc···CH_3OH complex is as strong as the O-H···π interaction.

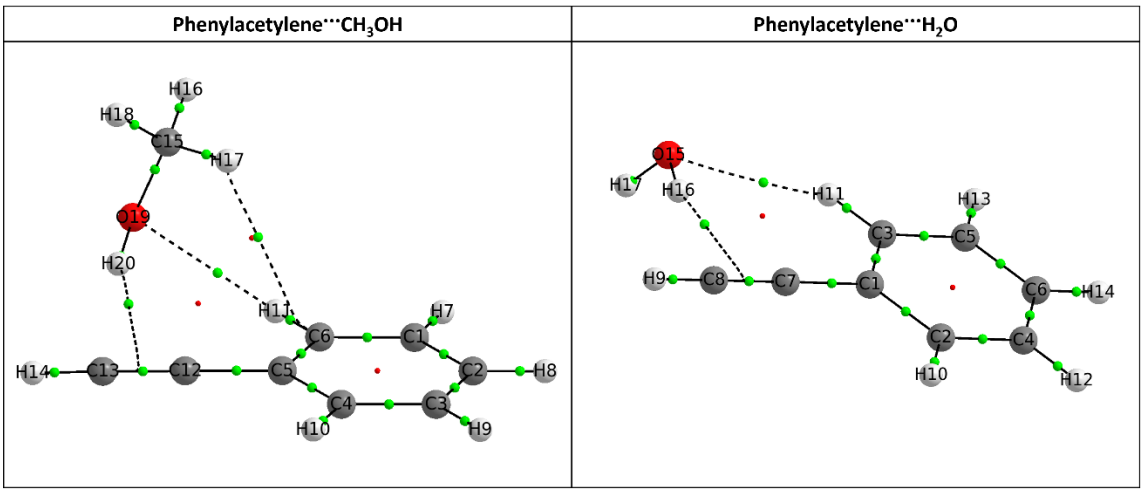

Figure 3-6: Atoms in Molecules (AIM) topology study for the PhAc···CH_3OH and PhAc···H_2O complexes. The green dots and red dots refer to the bond critical point and ring critical points respectively.

Table 3-12: Electron density (ρ) and the Laplacian of the electron density ($\nabla^2\rho$) of the PhAc···CH_3OH and PhAc···H_2O complexes.

Interactions	**PhAc···CH_3OH**		**Interactions**	**PhAc···H_2O**	
	ρ (a.u)	**$\nabla^2\rho$ (a.u)**		**ρ (a.u)**	**$\nabla^2\rho$ (a.u)**
O19-H20···π	0.013	+0.033	O15-H16···π	0.013	+0.036
C6-H11···O19	0.011	+0.031	C3-H11···O15	0.011	+0.032
C15-H17···C6	0.005	+0.020	--	--	--

3.4.4 Natural Bond Orbital Analysis:

In this study, we conducted a Natural Bond Orbital (NBO)[51,72] analysis to evaluate intermolecular orbital interactions at the B3LYP-D3/aug-cc-pVDZ and MP2/aug-cc-pVDZ level of optimizations for PhAc···CH_3OH and PhAc···H_2O systems respectively. The second-order perturbation energy ($E^{(2)}$) was utilized as a quantitative measure of the strength of delocalization interactions. The computed $E^{(2)}$ values for O-H···π and C-H···O interactions are provided in *Table 3-13* for both the complexes and shown in *Figure 3-7*. Similar to PhAc···H_2O system, for the PhAc···CH_3OH complex also, the NBO analysis reveals two significant stabilization interactions. The first interaction involves the delocalization between the π-cloud of PhAc and the σ* antibonding orbital of the CH_3OH/H_2O hydroxyl (OH), denoted as $\pi_{C=C} \rightarrow \sigma^*_{O-H}$. The second interaction is characterized by the interaction between the lone pair of electrons on the oxygen atom of CH_3OH/H_2O and the σ* antibonding orbital of the C-H group located at the ortho position in PhAc, represented as $n_O \rightarrow \sigma^*_{C-H}$. Our findings indicate that for the PhAc···CH_3OH complex, the $E^{(2)}$ value for the $\pi_{C=C} \rightarrow \sigma^*_{O-H}$ interaction is 10.8 kJ/mol and for $n_O \rightarrow \sigma^*_{C-H}$ interaction it is 7.1 kJ/mol. Whereas, for PhAc···H_2O complex, $E^{(2)}$ value for the $\pi_{C=C} \rightarrow \sigma^*_{O-H}$ interaction is 15.4 kJ/mol and for $n_O \rightarrow \sigma^*_{C-H}$ interaction it is 10.1 kJ/mol. These results highlight that the O-H···π interaction makes the most substantial contribution to the overall interaction strength.

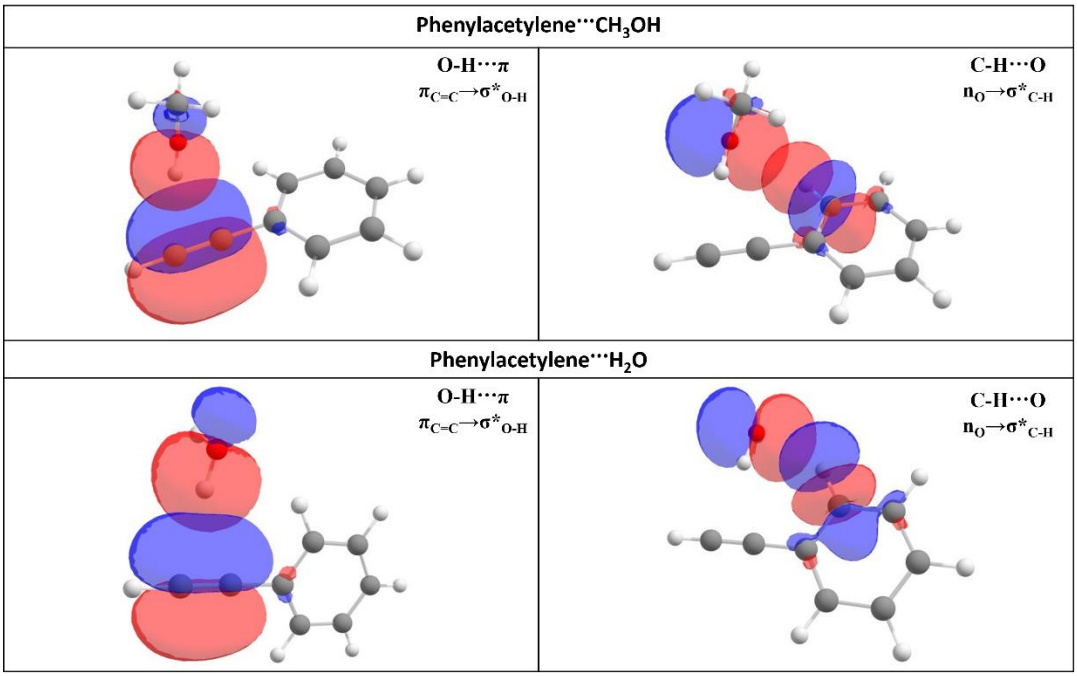

Figure 3-7: Interacting natural orbitals in PhAc···CH_3OH and PhAc···H_2O complexes.

Table 3-13: Second order perturbation energies ($E^{(2)}$) for interacting orbitals shown in Figure 7, calculated at B3LYP-D3/aug-cc-pVDZ level of theory.

Interaction	***E*$^{(2)}$ (kJ/mol)**	
	PhAc···CH_3OH	**PhAc···H_2O**
$\pi_{C=C}\rightarrow\sigma^{*}_{O-H}$	10.8	15.4
$n_O\rightarrow\sigma^{*}_{C-H}$	7.1	10.1

3.4.5 Non-covalent Interactions (NCI) Index Analysis:

The analysis of the non-covalent interactions (NCI) index[48,73–75] was also conducted to gain an understanding of the interactions found in the PhAc···CH_3OH complex. The NCI plots were acquired using the Multiwfn 3.6 software.[50] *Figure 3-8* shows the plots depicting the product of the sign of the second Eigenvalue (λ_2) of the electron density Hessian matrix and the electron density (ρ) in relation to the reduced density gradient (RDG). The sign of $\lambda_2*\rho$ holds significance, as negative values of this quantity indicate attractive interactions (such as

hydrogen bonds or van der Waals interactions), while positive values indicate non-bonded interactions (such as steric repulsion). The NCI plots exhibit spikes in both positive and negative directions, which can be regarded as an approximate indication of the critical points obtained from the AIM analysis. Similar to AIM analysis, presence of O-H···π, C-H···O and C-H···C interactions are indicated by the observed three green isosurfaces.

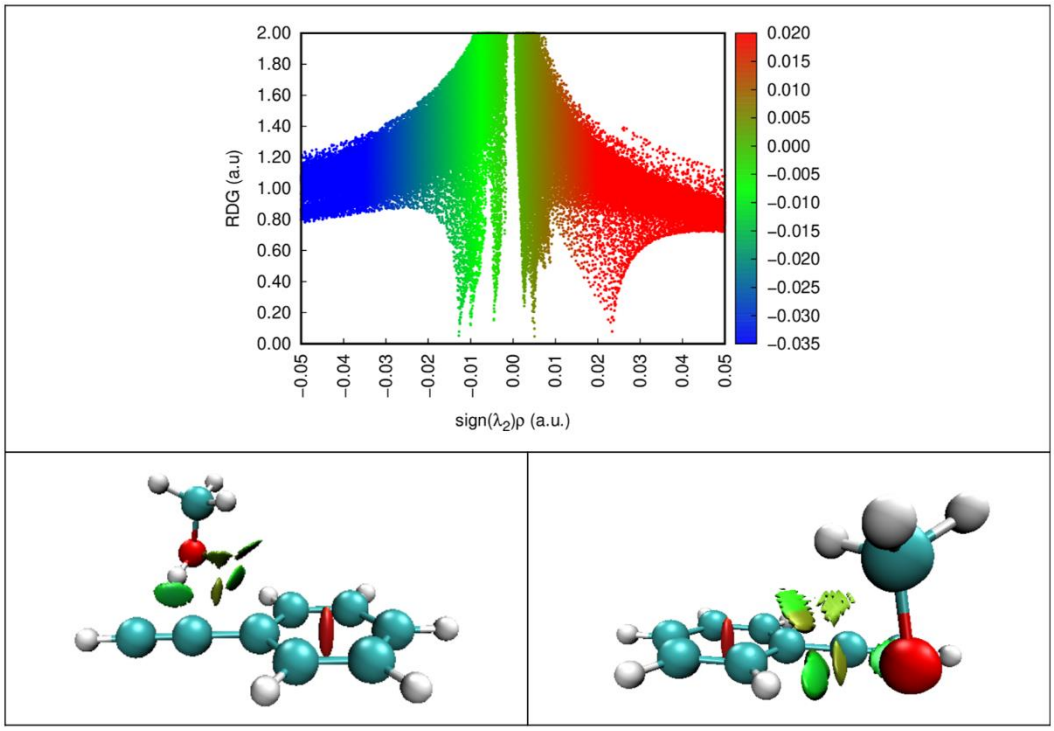

Figure 3-8: Non-covalent interactions (NCI) index plots for PhAc···CH_3OH complex.

3.4.6 Symmetry-Adapted Perturbation Theory (SAPT) Analysis:

In order to elucidate the primary forces responsible for stabilizing the acetylene-bound structure, we conducted Symmetry Adapted Perturbation Theory (SAPT)[52] calculations. All the SAPT Analysis were performed using PSI4 software.[53] As previously discussed in **Section 3.2.1**, there exists a notable disparity between the acetylene-bound structures optimized using the B3LYP-D3/aug-cc-pVDZ and MP2/aug-cc-pVDZ levels of theory. To shed light on the experimental observations, we employed SAPT-DFT and SAPT-'2+3' approaches, utilizing the aug-cc-pVDZ basis set. Specifically, SAPT-DFT was applied to the structures optimized at the

B3LYP-D3/aug-cc-pVDZ level of theory, while SAPT-'2+3' was performed on the structures optimized at the MP2/aug-cc-pVDZ level. The outcomes of the SAPT calculations are summarized in *Table 3-14*, and visual representations of the energy components are presented in *Figure 3-9*. A consistent trend emerges from both SAPT-DFT and SAPT-'2+3' analyses, revealing that the phenyl-bound structure exhibits similar energy component patterns, with the highest contribution stemming from dispersion forces. However, for acetylene-bound structures, SAPT-DFT and SAPT-'2+3' gave different results. SAPT-DFT results highlight the predominance of electrostatic forces, while SAPT-'2+3' identifies dispersion interactions as the dominant component. This discrepancy can be attributed to the distinct structural characteristics of acetylene-bound complexes at different levels of theory. As, in the structure optimized at the MP2/aug-cc-pVDZ level of theory, the methyl group is positioned atop the phenyl ring. In contrast, the structure optimized at the B3LYP-D3/aug-cc-pVDZ level of theory situates the methyl group away from the phenyl ring, accompanied by the presence of a secondary interaction between the lone pair of oxygen and the ortho C-H group of PhAc. This additional interaction contributes to the electrostatic energy component, accounting for the variation in SAPT results between the two acetylene-bound structures. Therefore, the observed structure demonstrates that electrostatics plays a significant role, contributing 48.4% to the total attractive component. Previous investigations on the PhAc···H_2O complex have revealed that electrostatics is the dominant force responsible for stabilizing the complex.[1] Conversely, in the case of the PhAc···H_2S complex, dispersion emerges as the prevailing force. The *Table 3-25* supplementary information provides the SAPT'2+3' calculations for both the PhAc···H_2O and PhAc···H_2S systems.

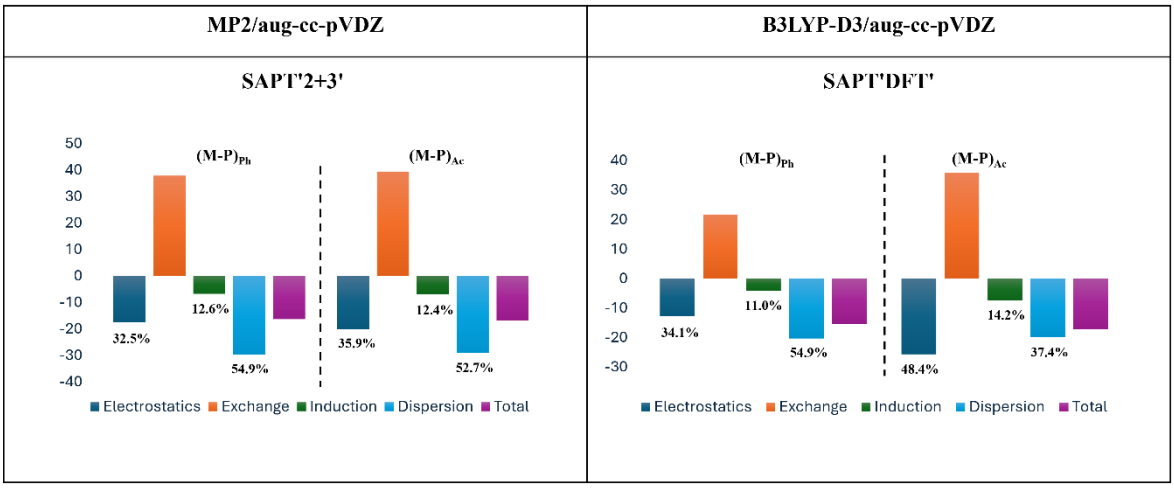

Figure 3-9: Bar charts depicting the energy decomposition using the SAPT-'2+3' and SAPT-DFT calculations for the PhAc···CH_3OH complex calculated at MP2/aug-cc-pVDZ and B3LYP-D3/au-cc-pVDZ level of theories respectively.

Table 3-14: SAPT'2+3' and SAPT-DFT interaction energy decomposition (kJ/mol) for PhAc···CH_3OH complex calculated at MP2/aug-cc-pVDZ and B3LYP-D3/aug-cc-pVDZ level of theories respectively.

Method	Structures	$E^{Electrostatics}$	$E^{Induction}$	$E^{Dispersion}$	$E^{Exchange}$	$E^{Interaction}$
SAPT'2+3' MP2/aug-cc-pVDZ	OH···π_{Ph}	-17.6	-6.8	-29.7	37.8	-16.3
	OH···π_{Ac}	-20.2	-7.0	-29.1	39.4	-16.9
SAPT'DFT' B3LYP-D3/aug-cc-pVDZ	OH···π_{Ph}	-12.7	-4.1	-20.4	21.7	-15.5
	OH···π_{Ac}	-25.6	-7.5	-19.8	35.8	-17.1

3.5 Conclusions:

The rotational spectra of a complex formed between PhAc and CH_3OH, as well as its isotopologues PhAc···CH_3OD, PhAc···CD_3OD, PhAc-D···CH_3OH, and PhAc···$^{13}CH_3OH$, were recorded and analysed. These findings indicate that the structure of the complex observed during the present work is consistent with that previously reported by Karir *et al*. In the proposed structure, CH_3OH donates a hydrogen bond to the acetylenic π-cloud, while the ortho C-H group of the PhAc complex forms a C-H···O hydrogen bond with the oxygen atom of the

CH_3OH moiety. Notably, the observed structure is consistent with the acetylenic bound structure calculated using the B3LYP-D3/aug-cc-pVDZ level of theory. The (V_3) barrier to internal rotation of the CH_3 group within the complex was determined to be 234 cm^{-1} in fits, where F_0 was also floated and determined to be 6.15(6) cm^{-1}. The result thus obtained for V_3 is in reasonable agreement with the barrier height calculated at the B3LYP-D3/aug-cc-pVDZ level of theory. However, as discussed in Section 4, tabulations of the reduced barrier height, $s = 4V_3 / 9F$ suggest that the value of this parameter may provide a more direct perspective on patterns of intramolecular bonding within CH_3OH-containing complexes. The result of s =16.97 for PhAc···CH_3OH is similar to the values reported for several other complexes in which CH_3OH acts as a hydrogen bond donor. The SAPT-DFT analysis suggests that the electrostatic energy component plays a significant role in stabilizing the experimentally observed structure. These findings provide valuable insights into the structural and energetic aspects of the observed PhAc···CH_3OH complex.

It should be noted that Singh *et al.*'s conclusion that PhAc···CH_3OH contains a hydrogen bond donated by the O-H group of CH_3OH to the phenyl π-cloud has been very well supported by IR/UV double resonance spectroscopic experiments and *ab-initio* computations. However, the evidence of the CH_3OH donating hydrogen bond to the phenyl π-system was concluded based on the presence or absence of the Fermi resonance in the FDIR spectra of the C-H stretch region. The Fermi resonance bands which involve the acetylenic π-cloud, was not affected in the PhAc···CH_3OH complex, whereas in the PhAc···H_2O complex, the Fermi resonance disappeared and gave only one peak corresponding to the C-H oscillator. In case, the interaction in PhAc···CH_3OH complex having similar structure as PhAc···H_2O complex does not affect the Fermi resonance, it is likely that there is no discrepancy in the experimental results about the global minimum structure.

There is clearly a need for further investigation which might rationalize all the observations made during this and previous works. One possible explanation can be immediately stated: it is possible that the isomer of PhAc···CH_3OH complex observed by Singh *et al.* authentically has a different structure from that observed during the present work. However, given the extensive similarities between the experimental conditions of this work and those used by Singh *et al.*, which each involved co-expansion of the PhAc and CH_3OH precursors within a buffer gas of helium, this seems very unlikely.

3.6 References:

(1) Maity, S.; Guin, M.; Singh, P. C.; Patwari, G. N. Phenylacetylene: A Hydrogen Bonding Chameleon. *ChemPhysChem* **2011**, *12* (1), 26–46. https://doi.org/10.1002/cphc.201000630.

(2) Karir, G.; Lüttschwager, N. O. B.; Suhm, M. A. Phenylacetylene as a Gas Phase Sliding Balance for Solvating Alcohols. *Physical Chemistry Chemical Physics* **2019**, *21* (15), 7831–7840. https://doi.org/10.1039/c9cp00435a.

(3) Sedlak, R.; Hobza, P.; Patwari, G. N. Hydrogen-Bonded Complexes of Phenylacetylene with Water, Methanol, Ammonia, and Methylamine. the Origin of Methyl Group-Induced Hydrogen Bond Switching. *Journal of Physical Chemistry A* **2009**, *113* (24), 6620–6625. https://doi.org/10.1021/jp900813n.

(4) Singh, P. C.; Patwari, G. N. IR-UV Double Resonance Spectroscopic Investigation of Phenylacetylene- Alcohol Complexes. Alkyl Group Induced Hydrogen Bond Switching. *Journal of Physical Chemistry A* **2008**, *112* (23), 5121–5125. https://doi.org/10.1021/jp800968g.

(5) Maity, S.; Patwari, G. N.; Sedlak, R.; Hobza, P. A π-Stacked Phenylacetylene Dimer. *Physical Chemistry Chemical Physics* **2011**, *13* (37), 16706–16712. https://doi.org/10.1039/c1cp20677j.

(6) Maity, S.; Maity, D. K.; Patwari, G. N. Interaction of Alcohols with 2-Fluoro- and 4-Fluorophenylacetylenes: Infrared-Optical Double Resonance Spectroscopic and Computational Investigation. *J. Phys. Chem. A* **2011**, *115* (41), 11229–11237. https://doi.org/10.1021/jp204286b.

(7) Singh, P. C.; Bandyopadhyay, B.; Patwari, G. N. Structure of the Phenylacetylene - Water Complex as Revealed by Infrared-Ultraviolet Double Resonance Spectroscopy. *Journal of Physical Chemistry A* **2008**, *112* (15), 3360–3363. https://doi.org/10.1021/jp710311p.

(8) Islam Mondal, S.; Dey, A.; Sen, S.; Naresh Patwari, G.; Ghosh, D. Spectroscopic and Ab Initio Investigation of 2,6-Difluorophenylacetylene–Amine Complexes: Coexistence of C–H···N and Lone-Pair···π Complexes and Intermolecular Coulombic Decay. *Physical Chemistry Chemical Physics* **2015**, *17* (1), 434–443. https://doi.org/10.1039/C4CP03445G.

(9) Goswami, M.; Arunan, E. Microwave Spectrum and Structure of C6H5CCH··· H2S Complex. *Journal of Molecular Spectroscopy* **2011**, *268* (1–2), 147–156. https://doi.org/10.1016/j.jms.2011.04.011.

(10) Goswami, M.; Arunan, E. *Microwave Spectroscopic and Theoretical Studies on Phenylacetylene•••H 2 O Complex: C-H•••O and O-H•••π Hydrogen Bonds as Equal Partners*; 2011.

(11) Siglow, K.; Neusser, H. J. Rotationally Resolved UV Spectroscopy of Weakly Bound Complexes: Structure and van Der Waals Vibronic Bands of phenylacetylene·Ar. *Chemical Physics Letters* **2001**, *343* (5), 475–481. https://doi.org/10.1016/S0009-2614(01)00737-0.

(12) Dreizler, H.; Hartke, B.; Dieter Rudolph, H. A Contribution to the Structure of the Van-Der-Waals Complex Phenylacetylene-Argon by Microwave Spectroscopy and Quantum Chemistry. *Journal of Molecular Structure* **2006**, *825* (1–3), 1–19. https://doi.org/10.1016/j.molstruc.2006.07.027.

(13) Karir, G.; Viswanathan, K. S. Phenylacetylene–Water Complex: Is It N···σ or H···π in the Matrix? *Journal of Molecular Structure* **2016**, *1107*, 145–156. https://doi.org/10.1016/j.molstruc.2015.11.030.

(14) De Lucia, F. C.; Herbst, E.; Anderson, T.; Helminger, P. *The Analysis of the Rotational Spectrum of Methanol to Microwave Accuracy*; 1989; pp 13–395.

(15) Lees, R. M. Torsion-Vibration-Rotation Interactions in Methanol. II Microwave Spectrum of CD3OD. *The Journal of Chemical Physics* **1972**, *56* (12), 5887–5890. https://doi.org/10.1063/1.1677131.

(16) Lees, R. M.; Baker, J. G. Torsion-Vibration-Rotation Interactions in Methanol. I. Millimeter Wave Spectrum. *The Journal of Chemical Physics* **1968**, *48* (12), 5299–5318. https://doi.org/10.1063/1.1668221.

(17) Ndao, M.; Kwabia Tchana, F.; Coudert, L. H.; Motiyenko, R. A.; Margulès, L.; Barros, J.; Manceron, L.; Roy, P. The Torsional and Rotation–Torsion Spectra of CD2HOH. *Journal of Molecular Spectroscopy* **2016**, *326*, 136–143. https://doi.org/10.1016/j.jms.2016.03.014.

(18) Duan, Y. B.; McCoy, A. B. Global Fit of Torsion-Rotational Transitions in the First Three Torsional States of CH3OD. *Journal of Molecular Spectroscopy* **2000**, *199* (2), 302–306. https://doi.org/10.1006/jmsp.1999.8025.

(19) El Hilali, A.; Coudert, L. H.; Konov, I.; Klee, S. Analysis of the Torsional Spectrum of Monodeuterated Methanol CH 2DOH. *Journal of Chemical Physics* **2011**, *135* (19). https://doi.org/10.1063/1.3662468.

(20) Lovas, F. J.; Hartwig, H. *The Microwave Spectrum of the Methanol Dimer for K Å 0 and 1 States*; 1997; Vol. 185, pp 98–109.

(21) Lugez, C. L.; Lovas, F. J.; Hougen, J. T.; Ohashi, N. *Global Analysis of A-, b-, and c-Type Transitions Involving Tunneling Components of K = 0 and 1 States of the Methanol Dimer*; 1999. http://www.idealibrary.com.

(22) Ohashi, N.; Hougen, J. T. Analysis and Global Fit of Tunneling Splittings in the K = 0 A-Type Microwave Spectrum of the Methanol Dimer. *Journal of Molecular Spectroscopy* **1995**, *170* (2), 493–505. https://doi.org/10.1006/jmsp.1995.1087.

(23) Medcraft, C.; Zinn, S.; Schnell, M.; Poblotzki, A.; Altnöder, J.; Heger, M.; Suhm, M. A.; Bernhard, D.; Stamm, A.; Dietrich, F.; Gerhards, M. Aromatic Embedding Wins over Classical Hydrogen Bonding-a Multi-Spectroscopic Approach for the Diphenyl Ether-Methanol Complex. *Physical Chemistry Chemical Physics* **2016**, *18* (37), 26975–26983. https://doi.org/10.1039/c6cp03557d.

(24) Lovas, F. J.; Suenram, R. D.; Fraser, G. T.; Gillies, C. W.; Zozom, J. The Microwave Spectrum of Formamide-Water and Formamide-Methanol Complexes. *The Journal of Chemical Physics* **1988**, *88* (2), 722–729. https://doi.org/10.1063/1.454151.

(25) Suenram, R. D.; Lovas, F. J.; Fraser, G. T.; Gillies, J. Z.; Gillies, C. W.; Onda, M. *Microwave Spectrum, Structure, and Electric Dipole Moment of Ar-CH30H*; 1989; Vol. 137, pp 127–164.

(26) Tan, X.-Q.; Ioannou, I. I.; Kuczkowski, R. L. The methanol·HCl Complex: Structure and Methyl Group Internal Rotation Barrier. *Journal of Molecular Structure* **1995**, *356* (2), 105–115. https://doi.org/10.1016/0022-2860(95)08936-P.

(27) Sun, L.; Tan, X. Q.; Oh, J. J.; Kuczkowski, R. L. The Microwave Spectrum and Structure of the methanol·SO2 Complex. *The Journal of Chemical Physics* **1995**, *103* (15), 6440–6449. https://doi.org/10.1063/1.470730.

(28) Tan, X.-Q.; Ioannou, I. I.; Foltz, K. B.; Kuczkowski, R. L. The Methanol·Trimethylamine Complex: Structure and Large Amplitude Motions. *Journal of Molecular Spectroscopy* **1996**, *177* (2), 181–193. https://doi.org/10.1006/jmsp.1996.0132.

(29) Haeckel, M.; Stahl, W. *The Microwave Spectrum and Molecular Structure of the Hydrogen-Bonded Aniline-Methanol Complex*; 1999. http://www.idealibrary.com.

(30) Lovas, F. J.; Belov, S. P.; Tretyakov, M. Y.; Ortigoso, J.; Suenram, R. D. The Microwave Spectrum and Structure of the CH3OH□CO Dimer. *Journal of Molecular Spectroscopy* **1994**, *167* (1), 191–204. https://doi.org/10.1006/jmsp.1994.1225.

(31) Ilyushin, V. V.; Lovas, F. J.; Plusquellic, D. F. Microwave Spectrum of the Heterodimers: CH3OH-CO2 and CH3OH-H2CO. *Journal of Molecular Spectroscopy* **2006**, *239* (1), 94–100. https://doi.org/10.1016/j.jms.2006.06.003.

(32) Westphal, A.; Jacoby, C.; Ratzer, C.; Reichelt, A.; Schmitt, M. Determination of the Intermolecular Geometry of the Phenol-Methanol Cluster. *Physical Chemistry Chemical Physics* **2003**, *5* (19), 4114–4122. https://doi.org/10.1039/b307223a.

(33) Gottschalk, H. C.; Poblotzki, A.; Fatima, M.; Obenchain, D. A.; Pérez, C.; Antony, J.; Auer, A. A.; Baptista, L.; Benoit, D. M.; Bistoni, G.; Bohle, F.; Dahmani, R.; Firaha, D.; Grimme, S.; Hansen, A.; Harding, M. E.; Hochlaf, M.; Holzer, C.; Jansen, G.; Klopper, W.; Kopp, W. A.; Krasowska, M.; Kröger, L. C.; Leonhard, K.; Mogren Al-Mogren, M.; Mouhib, H.; Neese, F.; Pereira, M. N.; Prakash, M.; Ulusoy, I. S.; Mata, R. A.; Suhm, M. A.; Schnell, M. The First Microsolvation Step for Furans: New Experiments and Benchmarking Strategies. *The Journal of Chemical Physics* **2020**, *152* (16), 164303. https://doi.org/10.1063/5.0004465.

(34) Bernhard, D.; Dietrich, F.; Fatima, M.; Pérez, C.; Gottschalk, H. C.; Wuttke, A.; Mata, R. A.; Suhm, M. A.; Schnell, M.; Gerhards, M. The Phenyl Vinyl Ether–Methanol Complex: A Model System for Quantum Chemistry Benchmarking. *Beilstein Journal of Organic Chemistry* **2018**, *14*, 1642–1654. https://doi.org/10.3762/bjoc.14.140.

(35) Gaussian 09, Revision A.02, M. J. Frisch, G. W. Trucks, H. B. Schlegel, G. E. Scuseria, M. A. Robb, J. R. Cheeseman, G. Scalmani, V. Barone, G. A. Petersson, H. Nakatsuji, X. Li, M. Caricato, A. Marenich, J. Bloino, B. G. Janesko, R. Gomperts, B. Mennucci, H. P. Hratchian, J. V. Ortiz, A. F. Izmaylov, J. L. Sonnenberg, D. Williams-Young, F. Ding, F. Lipparini, F. Egidi, J. Goings, B. Peng, A. Petrone, T. Henderson, D. Ranasinghe, V. G. Zakrzewski, J. Gao, N. Rega, G. Zheng, W. Liang, M. Hada, M. Ehara, K. Toyota, R. Fukuda, J. Hasegawa, M. Ishida, T. Nakajima, Y. Honda, O. Kitao, H. Nakai, T. Vreven, K. Throssell, J. A. Montgomery, Jr., J. E. Peralta, F. Ogliaro, M. Bearpark, J. J. Heyd, E. Brothers, K. N. Kudin, V. N. Staroverov, T. Keith, R. Kobayashi, J. Normand, K. Raghavachari, A. Rendell, J. C. Burant, S. S. Iyengar, J. Tomasi, M. Cossi, J. M. Millam, M. Klene, C. Adamo, R. Cammi, J. W. Ochterski, R. L. Martin, K. Morokuma, O. Farkas, J. B. Foresman, and D. J. Fox, Gaussian, Inc., Wallingford CT, 2016.

(36) Miehlich, B.; Savin, A.; Stoll, H.; Preuss, H. Results Obtained with the Correlation Energy Density Functionals of Becke and Lee, Yang and Parr. *Chemical Physics Letters* **1989**, *157* (3), 200–206. https://doi.org/10.1016/0009-2614(89)87234-3.

(37) Vosko, S. H.; Wilk, L.; Nusair, M. Accurate Spin-Dependent Electron Liquid Correlation Energies for Local Spin Density Calculations: A Critical Analysis. *Can. J. Phys.* **1980**, *58* (8), 1200–1211. https://doi.org/10.1139/p80-159.

(38) Becke, A. D. Density-Functional Thermochemistry. I. The Effect of the Exchange-Only Gradient Correction. *The Journal of Chemical Physics* **1992**, *96* (3), 2155–2160. https://doi.org/10.1063/1.462066.

(39) Grimme, S.; Steinmetz, M. Effects of London Dispersion Correction in Density Functional Theory on the Structures of Organic Molecules in the Gas Phase. *Phys. Chem. Chem. Phys.* **2013**, *15* (38), 16031. https://doi.org/10.1039/c3cp52293h.

(40) Møller, Chr.; Plesset, M. S. Note on an Approximation Treatment for Many-Electron Systems. *Phys. Rev.* **1934**, *46* (7), 618–622. https://doi.org/10.1103/PhysRev.46.618.

(41) Binkley, J. S.; Pople, J. A. Møller-Plesset Theory for Atomic Ground State Energies: MØLLER-PLESSET THEORY FOR ATOMIC GROUND STATE ENERGIES. *Int. J. Quantum Chem.* **1975**, *9* (2), 229–236. https://doi.org/10.1002/qua.560090204.

(42) Weigend, F.; Ahlrichs, R. Balanced Basis Sets of Split Valence, Triple Zeta Valence and Quadruple Zeta Valence Quality for H to Rn: Design and Assessment of Accuracy. *Phys. Chem. Chem. Phys.* **2005**, *7* (18), 3297. https://doi.org/10.1039/b508541a.

(43) Schäfer, A.; Huber, C.; Ahlrichs, R. Fully Optimized Contracted Gaussian Basis Sets of Triple Zeta Valence Quality for Atoms Li to Kr. *The Journal of Chemical Physics* **1994**, *100* (8), 5829–5835. https://doi.org/10.1063/1.467146.

(44) Dunning, T. H. Gaussian Basis Sets for Use in Correlated Molecular Calculations. I. The Atoms Boron through Neon and Hydrogen. *The Journal of Chemical Physics* **1989**, *90* (2), 1007–1023. https://doi.org/10.1063/1.456153.

(45) Kendall, R. A.; Dunning, T. H.; Harrison, R. J. Electron Affinities of the First-Row Atoms Revisited. Systematic Basis Sets and Wave Functions. *The Journal of Chemical Physics* **1992**, *96* (9), 6796–6806. https://doi.org/10.1063/1.462569.

(46) Boys, S. F.; Bernardi, F. The Calculation of Small Molecular Interactions by the Differences of Separate Total Energies. Some Procedures with Reduced Errors. *Molecular Physics* **1970**, *19* (4), 553–566. https://doi.org/10.1080/00268977000101561.

(47) Bader, R. F. W. *Atoms in Molecules: A Quantum Theory*; The International series of monographs on chemistry; Clarendon Press ; Oxford University Press: Oxford [England] : New York, 1994.

(48) Contreras-García, J.; Johnson, E. R.; Keinan, S.; Chaudret, R.; Piquemal, J.-P.; Beratan, D. N.; Yang, W. NCIPLOT: A Program for Plotting Noncovalent Interaction Regions. *J. Chem. Theory Comput.* **2011**, *7* (3), 625–632. https://doi.org/10.1021/ct100641a.

(49) Weinhold, F.; Landis, C. R.; Glendening, E. D. What Is NBO Analysis and How Is It Useful? *International Reviews in Physical Chemistry* **2016**, *35* (3), 399–440. https://doi.org/10.1080/0144235X.2016.1192262.

(50) Lu, T.; Chen, F. Multiwfn: A Multifunctional Wavefunction Analyzer. *J. Comput. Chem.* **2012**, *33* (5), 580–592. https://doi.org/10.1002/jcc.22885.

(51) Glendening, E. D.; Landis, C. R.; Weinhold, F. *NBO 6.0* : Natural Bond Orbital Analysis Program. *J. Comput. Chem.* **2013**, *34* (16), 1429–1437. https://doi.org/10.1002/jcc.23266.

(52) Parker, T. M.; Burns, L. A.; Parrish, R. M.; Ryno, A. G.; Sherrill, C. D. Levels of Symmetry Adapted Perturbation Theory (SAPT). I. Efficiency and Performance for Interaction Energies. *The Journal of Chemical Physics* **2014**, *140* (9), 094106. https://doi.org/10.1063/1.4867135.

(53) Parrish, R. M.; Burns, L. A.; Smith, D. G. A.; Simmonett, A. C.; DePrince, A. E.; Hohenstein, E. G.; Bozkaya, U.; Sokolov, A. Yu.; Di Remigio, R.; Richard, R. M.; Gonthier, J. F.; James, A. M.; McAlexander, H. R.; Kumar, A.; Saitow, M.; Wang, X.; Pritchard, B. P.; Verma, P.; Schaefer, H. F.; Patkowski, K.; King, R. A.; Valeev, E. F.; Evangelista, F. A.; Turney, J. M.; Crawford, T. D.; Sherrill, C. D. Psi4 1.1: An Open-Source Electronic Structure Program Emphasizing Automation, Advanced Libraries, and Interoperability. *J. Chem. Theory Comput.* **2017**, *13* (7), 3185–3197. https://doi.org/10.1021/acs.jctc.7b00174.

(54) Loru, D.; Bermúdez, M. A.; Sanz, M. E. Structure of Fenchone by Broadband Rotational Spectroscopy. *The Journal of Chemical Physics* **2016**, *145* (7), 074311. https://doi.org/10.1063/1.4961018.

(55) Zaleski, D. P.; Stephens, S. L.; Walker, N. R. A Perspective on Chemistry in Transient Plasma from Broadband Rotational Spectroscopy. *Phys. Chem. Chem. Phys.* **2014**, *16* (46), 25221–25228. https://doi.org/10.1039/C4CP04108A.

(56) Cooper, Graham. A.; Medcraft, C.; Littlefair, J. D.; Penfold, T. J.; Walker, N. R. Halogen Bonding Properties of 4-Iodopyrazole and 4-Bromopyrazole Explored by Rotational Spectroscopy and *Ab Initio* Calculations. *The Journal of Chemical Physics* **2017**, *147* (21), 214303. https://doi.org/10.1063/1.5002662.

(57) Arunan, E.; Tiwari, A. P.; Mandal, P. K.; Mathias, P. C. Pulsed Nozzle Fourier Transform Microwave Spectrometer: Ideal to Define Hydrogen Bond Radius. *Current Science* **2002**, *82* (5), 533–540.

(58) Cox, A. P.; Ewart, I. C.; Stigliani-, W. M. *Microwave Spectrum, Structure and Dipole Moment of Pheny Iacet Yl Ene*.

(59) Dreizler, H.; Rudolph, H. D.; Hartke, B. A Contribution to the Microwave Spectrum and Structure of Phenylacetylene. *Journal of Molecular Structure* **2004**, *698* (1–3), 1–24. https://doi.org/10.1016/j.molstruc.2004.03.046.

(60) Watson, J. K. G. Determination of Centrifugal Distortion Coefficients of Asymmetric-Top Molecules. III. Sextic Coefficients. *The Journal of Chemical Physics* **1968**, *48* (10), 4517–4524. https://doi.org/10.1063/1.1668020.

(61) Western, C. M. PGOPHER: A Program for Simulating Rotational, Vibrational and Electronic Spectra. *Journal of Quantitative Spectroscopy and Radiative Transfer* **2017**, *186*, 221–242. https://doi.org/10.1016/j.jqsrt.2016.04.010.

(62) Gougoula, E.; Cummings, C. N.; Medcraft, C.; Heitkämper, J.; Walker, N. R. Microwave Spectra, Molecular Geometries, and Internal Rotation of CH_3 in *N* -methylimidazole···H_2O and 2-methylimidazole···H_2O Complexes. *Phys. Chem. Chem. Phys.* **2022**, *24* (20), 12354–12362. https://doi.org/10.1039/D1CP05526G.

(63) Cummings, C. N.; Kleiner, I.; Walker, N. R. Noncovalent Interactions in the Molecular Geometries of 4-Methylthiazole···H2O and 5-Methylthiazole···H2O Revealed by Microwave Spectroscopy. *J. Phys. Chem. A* **2023**, *127* (39), 8133–8145. https://doi.org/10.1021/acs.jpca.3c05360.

(64) Schmitt, M.; K, J.; Spangenberg, D.; Westphal, A. *Determination of the Structures and Barriers to Hindered Internal Rotation of the Phenol±methanol Cluster in the S 0 and S 1 States*. www.elsevier.nl/locate/chemphys.

(65) Tan, X. Q.; Sun, L. H.; Kuczkowski, R. L. The Methanol · Ar Complex: Apparent Reduction of the Methyl Group Internal Rotation Barrier. *Journal of Molecular Spectroscopy* **1995**, *171* (1), 248–264. https://doi.org/10.1006/jmsp.1995.1115.

(66) Pribble, R. N.; Garrett, A. W.; Haber, K.; Zwier, T. S. Resonant Ion-Dip Infrared Spectroscopy of Benzene–H2O and Benzene–HOD. *The Journal of Chemical Physics* **1995**, *103* (2), 531–544. https://doi.org/10.1063/1.470139.

(67) Kraitchman, J. Determination of Molecular Structure from Microwave Spectroscopic Data. *American Journal of Physics* **1953**, *21* (1), 17–24. https://doi.org/10.1119/1.1933338.

(68) *Structural Calculations*. http://info.ifpan.edu.pl/~kisiel/struct/struct.htm#kra (accessed 2023-08-30).

(69) *PROSPE - Programs for ROtational SPEctroscopy*. http://info.ifpan.edu.pl/~kisiel/prospe.htm#table_of_programs (accessed 2023-08-30).

(70) Costain, C. C. Determination of Molecular Structures from Ground State Rotational Constants. *The Journal of Chemical Physics* **1958**, *29* (4), 864–874. https://doi.org/10.1063/1.1744602.

(71) Koch, U.; Popelier, P. L. A. Characterization of C-H-O Hydrogen Bonds on the Basis of the Charge Density. *J. Phys. Chem.* **1995**, *99* (24), 9747–9754. https://doi.org/10.1021/j100024a016.

(72) Reed, A. E.; Curtiss, L. A.; Weinhold, F. Intermolecular Interactions from a Natural Bond Orbital, Donor-Acceptor Viewpoint. *Chem. Rev.* **1988**, *88* (6), 899–926. https://doi.org/10.1021/cr00088a005.

(73) Johnson, E. R.; Keinan, S.; Mori-Sánchez, P.; Contreras-García, J.; Cohen, A. J.; Yang, W. Revealing Noncovalent Interactions. *J. Am. Chem. Soc.* **2010**, *132* (18), 6498–6506. https://doi.org/10.1021/ja100936w.

(74) Lane, J. R.; Contreras-García, J.; Piquemal, J.-P.; Miller, B. J.; Kjaergaard, H. G. Are Bond Critical Points Really Critical for Hydrogen Bonding? *J. Chem. Theory Comput.* **2013**, *9* (8), 3263–3266. https://doi.org/10.1021/ct400420r.

(75) Contreras-García, J.; Yang, W.; Johnson, E. R. Analysis of Hydrogen-Bond Interaction Potentials from the Electron Density: Integration of Noncovalent Interaction Regions. *J. Phys. Chem. A* **2011**, *115* (45), 12983–12990. https://doi.org/10.1021/jp204278k.

3.7 Supplementary Information:

Table 3-15: Equilibrium geometry coordinates (Å) of PhAc···CH_3OH complex for $(M\text{-}P)_{Ph}$ structure in the abc principal axes system optimised at MP2/aug-cc-pVDZ level of theory.

Atoms	a	b	c
C1	1.387	-0.953	-1.219
C2	2.090	-1.034	-0.001
C3	1.389	-0.946	1.219
C4	-0.006	-0.780	1.225
C5	-0.715	-0.695	0.001
C6	-0.009	-0.787	-1.223
H7	1.927	-1.011	-2.168
H8	3.177	-1.153	-0.002
H9	1.932	-0.998	2.167
H10	-0.555	-0.703	2.167
H11	-0.560	-0.716	-2.165
C12	-2.140	-0.504	0.002
C13	-3.362	-0.312	0.003
H14	-4.426	-0.165	0.003
C15	-0.251	2.563	-0.009
H16	-0.366	3.655	-0.019
H17	-0.754	2.158	0.886
H18	-0.740	2.144	-0.906
O19	1.157	2.300	0.003
H20	1.272	1.339	0.018

Table 3-16: Equilibrium geometry coordinates (Å) of PhAc···CH_3OH complex for $(M\text{-}P)_{Ac}$ structure in the abc principal axes system optimised at MP2/aug-cc-pVDZ level of theory.

Atoms	a	b	c
C1	-1.747	-0.282	-1.266

C2	-2.521	-0.322	-0.090
C3	-2.024	0.250	1.097
C4	-0.756	0.855	1.115
C5	0.025	0.889	-0.064
C6	-0.479	0.322	-1.260
H7	-2.129	-0.728	-2.189
H8	-3.506	-0.798	-0.098
H9	-2.623	0.221	2.012
H10	-0.358	1.293	2.035
H11	0.136	0.341	-2.164
C12	1.347	1.459	-0.042
C13	2.511	1.879	-0.014
H14	3.509	2.277	0.002
C15	0.992	-2.230	0.651
H16	1.000	-3.327	0.606
H17	0.001	-1.865	0.334
H18	1.173	-1.920	1.695
O19	2.034	-1.781	-0.226
H20	2.083	-0.816	-0.153

Table 3-17: Equilibrium geometry coordinates (Å) of PhAc···CH_3OH complex for $(P\text{-}M)_{OH}$ structure in the abc principal axes system optimised at MP2/aug-cc-pVDZ level of theory.

Atoms	**a**	**b**	**c**
C1	3.099	-1.189	0.218
C2	1.709	-1.225	0.017
C3	0.983	-0.021	-0.153
C4	1.672	1.215	-0.118
C5	3.062	1.242	0.083
C6	3.780	0.043	0.251
H7	3.652	-2.124	0.348
H8	1.174	-2.179	-0.010
H9	1.110	2.143	-0.251
H10	3.587	2.202	0.107
H11	4.863	0.068	0.408

C12	-0.441	-0.054	-0.358
C13	-1.667	-0.084	-0.533
H14	-2.737	-0.109	-0.682
C15	-4.998	0.195	0.942
H16	-5.940	-0.204	1.352
H17	-4.964	1.287	1.090
H18	-4.155	-0.262	1.476
O19	-4.836	-0.159	-0.444
H20	-5.553	0.250	-0.946

Table 3-18: Equilibrium geometry coordinates (Å) of PhAc···CH_3OH complex for $(M\text{-}P)_{Ph}$ structure in the abc principal axes system optimised at B3LYP-D3/aug-cc-pVDZ level of theory.

Atoms	**a**	**b**	**c**
C1	1.365	-1.006	-1.214
C2	2.062	-1.108	-0.003
C3	1.367	-1.012	1.209
C4	-0.016	-0.819	1.214
C5	-0.723	-0.717	0.000
C6	-0.017	-0.813	-1.216
H7	1.902	-1.072	-2.160
H8	3.142	-1.253	-0.004
H9	1.905	-1.082	2.154
H10	-0.557	-0.737	2.156
H11	-0.560	-0.727	-2.156
C12	-2.138	-0.499	0.002
C13	-3.335	-0.299	0.003
H14	-4.392	-0.131	0.004
C15	-0.221	2.665	-0.008
H16	-0.344	3.755	-0.014
H17	-0.729	2.255	0.880
H18	-0.705	2.250	-0.908
O19	1.181	2.410	0.012
H20	1.320	1.455	0.021

Table 3-19: Equilibrium geometry coordinates (Å) of PhAc···CH_3OH complex for $(M\text{-}P)_{Ac}$ structure in the abc principal axes system optimised at B3LYP-D3/aug-cc-pVDZ level of theory.

Atoms	a	b	c
C1	-1.488	-1.513	-0.476
C2	-2.699	-1.026	0.026
C3	-2.789	0.3	0.461
C4	-1.676	1.138	0.393
C5	-0.454	0.652	-0.113
C6	-0.368	-0.684	-0.55
H7	-1.414	-2.547	-0.815
H8	-3.571	-1.679	0.081
H9	-3.731	0.685	0.854
H10	-1.743	2.172	0.729
H11	0.577	-1.064	-0.934
C12	0.684	1.519	-0.182
C13	1.644	2.264	-0.236
H14	2.477	2.932	-0.289
C15	2.861	-1.225	0.962
H16	3.18	-2.272	1.034
H17	1.821	-1.15	1.322
H18	3.507	-0.615	1.614
O19	2.978	-0.849	-0.408
H20	2.674	0.064	-0.494

Table 3-20: Equilibrium geometry coordinates (Å) of PhAc···CH_3OH complex for $(P\text{-}M)_{OH}$ structure in the abc principal axes system optimised at B3LYP-D3/aug-cc-pVDZ level of theory.

Atoms	a	b	c
C1	3.184	-1.059	0.287
C2	1.806	-1.220	0.145
C3	0.981	-0.105	-0.111
C4	1.573	1.170	-0.221

C5	2.952	1.322	-0.077
C6	3.763	0.210	0.177
H7	3.811	-1.930	0.485
H8	1.354	-2.207	0.231
H9	0.940	2.034	-0.419
H10	3.397	2.314	-0.165
H11	4.841	0.333	0.289
C12	-0.434	-0.267	-0.257
C13	-1.636	-0.405	-0.375
H14	-2.700	-0.525	-0.484
C15	-5.004	0.670	0.660
H16	-5.979	0.608	1.168
H17	-4.902	1.658	0.183
H18	-4.209	0.561	1.407
O19	-4.827	-0.396	-0.280
H20	-5.495	-0.324	-0.971

Table 3-21: Normal modes of vibrations for the structures $(M\text{-}P)_{Ph}$, $(M\text{-}P)_{Ac}$ and $(P\text{-}M)_{OH}$ of the PhAc···CH_3OH complex calculated at MP2/aug-cc-pVDZ level of theory. Frequency in cm^{-1}.

Modes (cm^{-1})	**$(M\text{-}P)_{Ph}$**	**$(M\text{-}P)_{Ac}$**	**$(P\text{-}M)_{OH}$**
1	38.1	32.1	8.4
2	44.4	48.1	17.8
3	53.0	66.9	29.1
4	105.8	102.5	47.9
5	124.1	112.1	73.3
6	137.6	139.8	124.5
7	144.9	145.2	147.9
8	145.9	180.4	164.2
9	321.3	331.5	314.4
10	329.4	392.5	319.8
11	397.6	410.4	397.6
12	459.5	460.1	463.2
13	495.0	494.7	496.8
14	499.5	506.4	506.1

15	562.3	570.9	615.5
16	612.1	612.0	637.5
17	614.7	614.7	689.5
18	660.0	658.0	741.4
19	750.8	745.4	750.9
20	762.2	762.9	762.8
21	844.7	840.3	837.7
22	901.4	899.4	888.6
23	958.1	954.6	932.1
24	958.9	956.9	941.0
25	997.7	997.6	996.5
26	1037.1	1038.3	1035.6
27	1048.4	1046.7	1038.6
28	1080.1	1084.1	1072.8
29	1085.7	1087.8	1085.5
30	1164.9	1166.1	1164.3
31	1165.4	1167.7	1168.7
32	1183.5	1184.3	1183.0
33	1216.1	1214.9	1215.2
34	1306.6	1308.3	1304.9
35	1371.6	1377.0	1361.9
36	1429.4	1432.6	1427.0
37	1459.3	1459.1	1466.4
38	1479.3	1482.5	1477.8
39	1489.5	1490.3	1490.6
40	1490.6	1492.0	1493.3
41	1497.0	1500.3	1505.6
42	1598.5	1602.5	1601.4
43	1627.2	1629.8	1630.5
44	2104.6	2098.8	2093.2
45	3037.6	3041.8	3059.3
46	3114.0	3120.8	3142.5
47	3174.3	3174.3	3190.2
48	3206.8	3203.6	3200.7
49	3212.6	3211.4	3208.3

50	3221.0	3219.9	3217.8
51	3227.8	3227.0	3224.3
52	3235.7	3233.7	3231.5
53	3479.1	3476.2	3390.1
54	3799.0	3792.1	3837.8

Table 3-22: Normal modes of vibrations for the structures $(M\text{-}P)_{Ph}$, $(M\text{-}P)_{Ac}$ and $(P\text{-}M)_{OH}$ of the PhAc···CH_3OH complex calculated at B3LYP-D3/aug-cc-pVDZ level of theory. Frequency in cm^{-1}.

Modes (cm^{-1})	**$(M\text{-}P)_{Ph}$**	**$(M\text{-}P)_{Ac}$**	**$(P\text{-}M)_{OH}$**
1	17.1	22.4	7.1
2	34.9	48.9	21.8
3	43.9	75.3	38.4
4	91.0	99.8	51.9
5	116.3	110.1	72.7
6	127.4	118.7	113.5
7	139.0	138.0	154.9
8	152.9	162.2	175.4
9	337.3	345.1	314.8
10	338.8	413.2	347.1
11	408.8	469.7	412.2
12	469.5	496.5	472.2
13	527.1	526.0	526.9
14	534.4	533.0	543.9
15	580.0	570.8	630.1
16	629.3	630.0	704.9
17	656.6	655.8	717.7
18	704.5	709.6	769.0
19	773.1	771.2	772.5
20	778.5	776.4	778.4
21	846.9	856.5	846.3
22	926.3	942.3	927.7
23	980.6	992.0	985.0
24	999.2	1004.3	1004.3

25	1006.1	1009.2	1004.7
26	1043.8	1043.4	1032.4
27	1046.9	1048.0	1045.5
28	1081.1	1084.0	1073.1
29	1098.8	1104.7	1097.7
30	1154.5	1161.9	1157.9
31	1182.5	1182.4	1179.9
32	1198.4	1207.7	1196.7
33	1220.3	1216.0	1218.4
34	1314.4	1319.1	1312.8
35	1347.7	1354.4	1347.0
36	1369.1	1381.6	1355.3
37	1450.1	1449.2	1454.1
38	1459.6	1459.4	1457.9
39	1468.1	1467.0	1468.0
40	1477.1	1481.0	1479.3
41	1508.6	1511.7	1507.6
42	1606.4	1608.0	1606.3
43	1639.9	1641.5	1640.9
44	2208.2	2195.8	2194.7
45	2992.3	2991.6	3004.1
46	3048.1	3046.5	3065.7
47	3114.4	3113.2	3126.1
48	3178.7	3173.6	3170.8
49	3186.7	3183.4	3179.6
50	3196.3	3193.4	3190.8
51	3203.3	3201.0	3198.4
52	3208.1	3204.4	3202.9
53	3478.1	3473.3	3386.8
54	3816.1	3755.2	3829.7

Table 3-23: Experimental rotational constants (MHz), centrifugal distortion constants (kHz) and second moment obtained from the global fit containing A- and E- state transitions (fit includes transitions obtained from the CP-FTMW spectrometer). F_0 is being fixed in this fit.

Constants	PhAc···CH_3OH	PhAc···CH_3OD	PhAc-D···CH_3OH	PhAc···$^{13}CH_3OH$
A_0	1955.314(3)	1962.815(7)	1891.333(6)	1935.974(5)
B_0	796.5548(2)	785.982(2)	789.216(2)	785.487(2)
C_0	625.9941(1)	619.316(2)	615.2276(1)	618.631(1)
D_J	1.12(1)	1.05(2)	1.03(1)	1.13(3)
D_{JK}	-6.15(7)	-5.43(9)	-4.8(1)	-6.3(2)
D_K	17.2(3)	53.2(8)	16(1)	19.2(6)
d_1	-0.137(4)	-0.17(2)	-0.10(2)	-0.13(2)
d_2	0.002(3)	-0.03(2)	-0.02(1)	-0.01(1)
$D_{\pi 2J}$	-266(4)	-218(5)	-265(3)	-267(4)
$D_{\pi 2K}$	843(1)	656(6)	766(2)	780(1)
V_3 (cm^{-1})	200.1(1)	217.7(3)	200.5(1)	200.7(1)
F_0 (cm^{-1})	[5.24]	[5.24]	[5.24]	[5.24]
∠(i, a) (degree)	67.2(3)	67.4(6)	68.2(4)	67.8(4)
∠(i, b) (degree)	23.7(3)	23.4(6)	22.9(4)	23.0(3)
∠(i, c) (degree)	96.12(2)	95.59(3)	96.76(2)	95.74(1)
P_{cc} (u $Å^2$)	42.80	42.22	43.06	43.77
N_A/N_E	59/39	31/26	29/24	44/38
σ (kHz)	21.5	14.9	15.9	25.1

P_{cc} is the second moment given by: $P_{cc} = \frac{I_b - I_a - I_c}{2}$

Table 3-24: Calculated harmonic and experimentally obtained vibrational frequencies (cm^{-1}) in the O-H stretch region of H_2O and CH_3OH and their complexes with PhAc reported in reference 1 and 2.

Method	PhAc···CH_3OH	PhAc···H_2O	3-methylphenylacetylene···CH_3OH
IR/UV double resonance spectroscopic results[1]			
Experiment	3615	3629[a], 3724[b]	----
Monomer	3681	3657[a], 3756[b]	----
Theory (Ac bound)	3633	3587[a], 3735[b]	----
Theory (Ph bound)	3637	3621[a], 3744[b]	----
FTIR spectroscopic results[2]			

Experiment	3622	3613[a]	3639, 3620 (2685, 2671)[c]
Monomer	3686	3657[a]	3686 (2718)[c]
Theory (Ac bound)	3613	3603[a]	3610 (2661)
Theory (Ph bound)	3637	3621[a]	3659 (2697)

[a]The vibrational frequencies for hydrogen-bonded O-H. [b]The vibrational frequencies for free O-H. [c]The values in the parentheses correspond to the 3-methylphenylacetylene···CH_3OD complex.

[1]Singh, P. C.; Patwari, G. N. IR-UV Double Resonance Spectroscopic Investigation of Phenylacetylene- Alcohol Complexes. Alkyl Group Induced Hydrogen Bond Switching. Journal of Physical Chemistry A 2008, 112 (23), 5121–5125.

[2]Karir, G.; Lüttschwager, N. O. B.; Suhm, M. A. Phenylacetylene as a Gas Phase Sliding Balance for Solvating Alcohols. Physical Chemistry Chemical Physics 2019, 21 (15), 7831–7840.

Table 3-25: SAPT'2+3' interaction energy decomposition (kJ/mol) for PhAc···H_2O and PhAc···H_2S complexes calculated at MP2/aug-cc-pVDZ level of theory.

Method	**Complex**	$\mathbf{E}^{\mathbf{Electrostatics}}$	$\mathbf{E}^{\mathbf{Induction}}$	$\mathbf{E}^{\mathbf{Dispersion}}$	$\mathbf{E}^{\mathbf{Exchange}}$	$\mathbf{E}^{\mathbf{Interaction}}$
SAPT'2+3' MP2/aug-cc-pVDZ	PhAc···H_2O	-24.9	-8.8	-15.2	33.5	-15.5
	PhAc···H_2S	-16.3	-5.0	-25.4	33.6	-13.2

CHAPTER 4

Revisiting the Microwave Spectrum and Molecular Structure of 1-Fluoronaphthalene

CHAPTER 4 | Revisiting the Microwave Spectrum and Molecular Structure of 1-Fluoronaphthalene |

4.1 Introduction:

1-Fluoronaphthalene (1FN) belongs to the class of aromatic compounds, which are known for their stable and resonance-rich structures. It has a boiling point of approximately 224-225 °C at standard atmospheric pressure and a relatively low vapour pressure at room temperature. Microwave spectrum of 1FN was first reported in 1973.[1] Karlsson provided initial values for rotational constants of 1FN by measuring high J transitions in the 18-40 GHz range with a standard deviation of approximately 69 kHz.[1] He used a Hewlett Packard Model 8460 A MRR spectrometer .[1] Later, the rotationally resolved fluorescence excitation spectrum of 0_0^0 band in the $A^1A' \leftarrow X^1A'$ ($S_1 \leftarrow S_0$) transition of 1FN was observed.[2] In this study, the rotational constants of both vibronic states had an accuracy of ±100 kHz.[2] Kukolich and coworkers reported the low J transitions within the frequency range of 1.8-10 GHz and refined the rotational constants of 1FN to a standard deviation of 2.36 kHz.[3] They used the Balle-Flygare Fourier transform microwave spectrometer. All these above-mentioned measurements did not include the ^{13}C isotopologues, which would provide accurate structural information. The current study uses the advantage of a chirped-pulse Fourier transform microwave spectrometer to record the microwave spectrum of 1FN, including all 10 mono-substituted ^{13}C isotopologues, and builds upon the prior research conducted.[1–3] In the present investigation, we have employed the chirped-pulse Fourier-transform microwave (CP-FTMW) spectrometer, as it offers the benefits of conventional narrowband rotational spectroscopy while encompassing multiple GHz regions in a single chirp. In the present study, our objective is to provide the accurate structure of 1FN monomer derived from the microwave spectra of all ten monosubstituted ^{13}C 1FN-isotopologues. This has helped in evaluating the accuracy of quantum chemical predictions.

4.2 Methods:

4.2.1 Experimental Details:

The 1-fluoronaphthalene (99%) was purchased from Sigma-Aldrich and used without further purification. All the ^{13}C isotopologues were recorded in natural abundance. The 1FN was introduced into a neon flow under a backing pressure of 5 bar. Due to the notably lower vapour pressure of 1FN, in order to produce the mixtures with the carrier gas, a modified general valve was utilized to heat the 1FN to 50°C.[4] The experiments to record the spectra were conducted by means of the chirped pulse Fourier transform microwave (CP-FTMW) spectrometer available at Newcastle University, which operated within the frequency range of 2.0 to 8.0 GHz.[5] Detailed information pertaining to the spectrometer can be found elsewhere.[5] A chirped pulse with a frequency range spanning from 2.0 to 8.0 GHz and a duration of 1 μs was generated by ab Arbitrary Waveform Generator (Tektronix AWG7102) and was directly transmitted to a 450 W travelling-wave tube amplifier (TWTA) (Applied Systems Engineering). The molecules within the sample are polarised after introducing the chirp from the horn antenna to the vacuum chamber. The microwave radiation and the flow of the expanding gas jet are mutually perpendicular. A second horn antenna is used to record the free induction decay (FID) of the molecular emission over the course of 20 microseconds after the microwave pulse. FIDs are then digitised using a 100 GS/s oscilloscope (Tektronix DPO72304XS). The interaction of the gas pulse (~200 μs) over a temporal domain enables eight consecutive measurements of the Free Induction Decay (FID) following each gas pulse (25 μs) using the 'fast frame' operational mode of the oscilloscope. Then, prior to the Fourier transformation, the FIDs are co-added in the time domain using a high-resolution window function. The linewidth in the frequency domain spectra is observed as a single peak with a full width at a half-maximum of ca. 100 kHz with an estimated accuracy of 10 kHz. To ensure phase coherence within the temporal domain, as well as precision in the transition frequencies, the arbitrary waveform generator (AWG), the phase-locked dielectric resonator oscillator (PDRO), and the oscilloscope, were all referenced to a 10 MHz local oscillator obtained from an analog signal generator.

4.2.2 Computational Details:

The optimisation of the 1FN structure was performed utilizing Gaussian 09 [6] at different levels of theory. In this report, we present the findings obtained by employing the theoretical methods of MP2/cc-pVTZ, MP2/aug-cc-pVDZ, MP2/aug-cc-pVTZ, B3LYP-D3/cc-pVTZ, B3LYP-D3/aug-cc-pVDZ, and B3LYP-D3/aug-cc-pVTZ and compare them with the experimental results. Harmonic frequency calculations were performed to ascertain that the structure obtained is a minimum in the potential energy hypersurface. The anharmonic correction to the frequency has been calculated using the *freq=anharmonic* keyword. The Raman activity was estimated using the *freq=raman* keyword. The determination of the centrifugal distortion constants was achieved through the implementation of the *freq=vibrot* keyword. The KRA [7] and EVAL [8] programs, which can be found on the PROSPE website [9], were utilized to assess the structural parameters.

4.3 Results:

4.3.1 Rotational Spectra and Fitted Spectroscopic Constants:

The spectra of 1FN were recorded in the 2.0-8.0 GHz range, and the data were averaged for 1980k FIDs. The broadband rotational spectrum, covering the frequency bands of 2000 to 8000 MHz, is shown in the top panel of *Figure 4-1* and two small segments ranging from 3996 to 4038 and 6129 to 6177 MHz are displayed in the bottom panel. Since the *c*-dipole moment is zero for this planar molecule, the spectra exhibit a combination of *a*- and *b*-type transitions. The spectra demonstrate prominent *b*-type transitions, with a lower intensity observed in *a*-type transitions. A signal-to-noise ratio of approximately 200:1 was successfully achieved for the parent isotopologues of 1FN, thereby enabling the detection of spectra associated with ^{13}C-containing isotopologues in their natural abundance. Transition frequency for the parent and all the isotopologues are given in *Table 4-1* to *Table 4-11*. Spectroscopic parameters were determined by fitting them to the measured transition frequencies, utilizing Western's PGOPHER [10] program and Watson's S-reduced Hamiltonian [11] in the I^r representation.

$$H_R = A\hat{J}_a^2 + B\hat{J}_b^2 + C\hat{J}_c^2$$

Where H_R is the energy operator for a semirigid, near prolate asymmetric rotor.

Fitted rotational constants (A_0, B_0, C_0) are given in *Table 4-12*. The centrifugal distortion constants (D_J, D_{JK}, D_K, d_1, d_2) were not needed in the experimental fit and were fixed to zero. The incorporation of these distortion constants did not result in any discernible modifications in the standard deviation or uncertainties of the evaluated parameters during the process of fitting the 1FN parent and all ^{13}C isotopologues. The values of the calculated centrifugal distortion constants were small, with an order of approximately 10^{-2} kHz (*Table 4-13)*. Consequently, it was reasonable to disregard the effects of centrifugal distortion for J values that were below 10, which was anticipated for this notably rigid molecule.

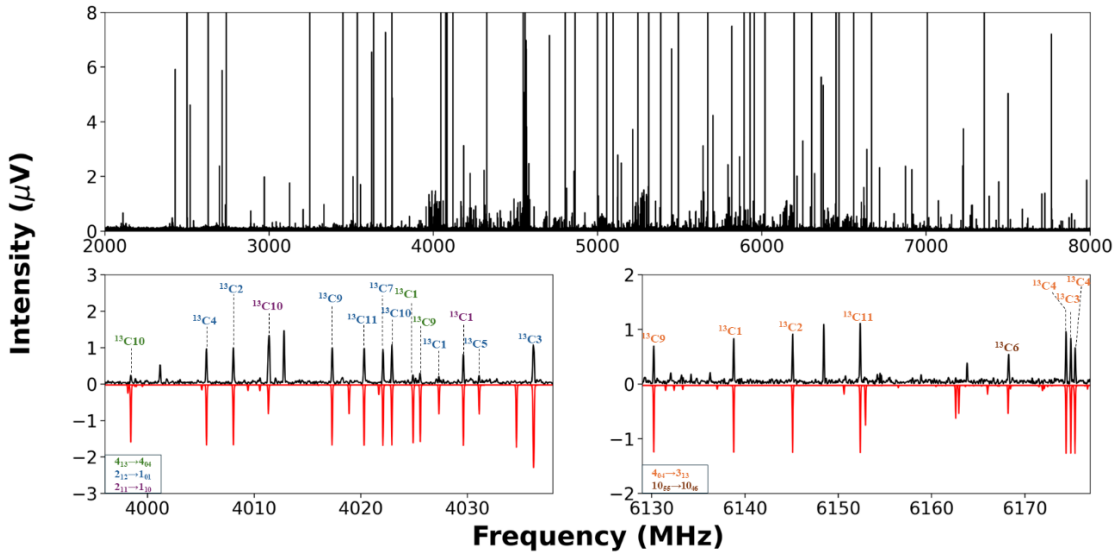

Figure 4-1: (Top panel) The broadband rotational spectrum of 1FN recorded at CP-FTMW spectrometer. (Bottom panel) Zoom to the broadband rotational spectrum (black) along with the simulated spectrum (red) illustrating a few selected transitions of ^{13}C isotopologues. The colour scheme for the transitions with their respective isotopologues is given at the bottom left corner.

Table 4-1: Experimentally observed rotational transition and their assignments for 1-fluoronaphthalene.

Transitions	Observed (MHz)	Calculated (MHz)	Obs-Cal (MHz)

$1_{11} \rightarrow 0_{00}$	2629.0650	2629.0641	0.0009
$1_{10} \rightarrow 0_{00}$	3042.8320	3042.8193	0.0127
$2_{02} \rightarrow 1_{01}$	3537.5330	3537.5317	0.0013
$2_{02} \rightarrow 1_{11}$	2739.1890	2739.1883	0.0007
$2_{12} \rightarrow 1_{01}$	4046.0320	4046.0296	0.0024
$2_{12} \rightarrow 1_{11}$	3247.6890	3247.6862	0.0028
$2_{11} \rightarrow 1_{10}$	4075.2010	4075.1966	0.0044
$2_{21} \rightarrow 2_{12}$	3636.3010	3636.2958	0.0052
$2_{21} \rightarrow 2_{02}$	4144.7890	4144.7937	-0.0047
$2_{21} \rightarrow 1_{10}$	6470.2350	6470.2268	0.0082
$2_{20} \rightarrow 1_{11}$	7007.8980	7007.8917	0.0063
$2_{20} \rightarrow 2_{11}$	2518.9440	2518.9399	0.0041
$3_{03} \rightarrow 2_{12}$	4547.0720	4547.0671	0.0049
$3_{03} \rightarrow 2_{02}$	5055.5680	5055.5650	0.0030
$3_{13} \rightarrow 2_{02}$	5311.3810	5311.3791	0.0019
$3_{13} \rightarrow 2_{12}$	4802.8840	4802.8812	0.0028
$3_{12} \rightarrow 3_{03}$	2713.8730	2713.8675	0.0055
$3_{12} \rightarrow 2_{21}$	3624.6430	3624.6388	0.0042
$3_{12} \rightarrow 2_{11}$	6019.6750	6019.6690	0.0060
$3_{12} \rightarrow 3_{13}$	2458.0560	2458.0534	0.0026
$3_{22} \rightarrow 3_{13}$	4325.5810	4325.5767	0.0043
$3_{22} \rightarrow 3_{03}$	4581.4000	4581.3908	0.0092
$3_{22} \rightarrow 2_{21}$	5492.1650	5492.1621	0.0029
$3_{22} \rightarrow 2_{11}$	7887.2010	7887.1923	0.0087
$3_{21} \rightarrow 2_{20}$	5928.7640	5928.7591	0.0049
$3_{21} \rightarrow 3_{12}$	2428.0360	2428.0300	0.0060
$3_{31} \rightarrow 3_{22}$	5094.7570	5094.7531	0.0039
$3_{30} \rightarrow 3_{21}$	4558.7270	4558.7242	0.0028
$4_{04} \rightarrow 3_{03}$	6452.3980	6452.3947	0.0033
$4_{04} \rightarrow 3_{13}$	6196.5820	6196.5806	0.0014
$4_{14} \rightarrow 3_{03}$	6559.8420	6559.8389	0.0031
$4_{14} \rightarrow 3_{13}$	6304.0250	6304.0248	0.0002
$4_{13} \rightarrow 4_{04}$	4083.3490	4083.3426	0.0064
$4_{13} \rightarrow 3_{12}$	7821.8770	7821.8698	0.0072
$4_{13} \rightarrow 3_{22}$	5954.3490	5954.3465	0.0025

$4_{13} \rightarrow 4_{14}$	35.9030	3975.8984	0.0046
$4_{23} \rightarrow 3_{22}$	7224.3450	7224.3436	0.0014
$4_{23} \rightarrow 4_{04}$	5353.3480	5353.3397	0.0083
$4_{23} \rightarrow 4_{14}$	5245.9000	5245.8955	0.0045
$4_{22} \rightarrow 4_{13}$	2697.0170	2697.0133	0.0037
$4_{22} \rightarrow 3_{31}$	3556.6080	3556.6067	0.0013
$4_{32} \rightarrow 4_{23}$	5384.6470	5384.6399	0.0071
$4_{32} \rightarrow 3_{31}$	7514.2250	7514.2304	-0.0054
$4_{31} \rightarrow 3_{30}$	7651.4120	7651.4061	0.0059
$4_{31} \rightarrow 4_{22}$	4119.2800	4119.2772	0.0028
$4_{41} \rightarrow 4_{32}$	6875.0910	6875.0905	0.0005
$4_{40} \rightarrow 4_{31}$	6717.4150	6717.4157	-0.0007
$5_{05} \rightarrow 4_{14}$	7723.9000	7723.9022	-0.0022
$5_{05} \rightarrow 4_{04}$	7831.3450	7831.3464	-0.0014
$5_{15} \rightarrow 4_{14}$	7764.1870	7764.1866	0.0004
$5_{15} \rightarrow 4_{04}$	7871.6290	7871.6308	-0.0018
$5_{14} \rightarrow 5_{05}$	5671.6040	5671.6006	0.0034
$5_{14} \rightarrow 5_{15}$	5631.3240	5631.3162	0.0078
$5_{24} \rightarrow 5_{15}$	6362.1260	6362.1225	0.0035
$5_{24} \rightarrow 4_{31}$	3334.1210	3334.1202	0.0008
$5_{23} \rightarrow 5_{14}$	3449.5740	3449.5731	0.0009
$5_{23} \rightarrow 4_{32}$	6214.5380	6214.5405	-0.0025
$5_{33} \rightarrow 5_{24}$	5892.0460	5892.0462	-0.0002
$5_{32} \rightarrow 5_{23}$	3747.7080	3747.7079	0.0001
$5_{42} \rightarrow 5_{33}$	6914.0590	6914.0640	-0.0050
$5_{41} \rightarrow 5_{32}$	6374.1200	6374.1206	-0.0006
$6_{15} \rightarrow 6_{06}$	7277.7810	7277.7786	0.0024
$6_{25} \rightarrow 5_{32}$	3992.0440	3992.0430	0.0010
$6_{25} \rightarrow 6_{16}$	7620.5060	7620.5038	0.0022
$6_{24} \rightarrow 6_{25}$	4350.2480	4350.2519	-0.0039
$6_{24} \rightarrow 6_{15}$	4707.0510	4707.0558	-0.0048
$6_{34} \rightarrow 5_{41}$	4257.9300	4257.9362	-0.0062
$6_{34} \rightarrow 6_{25}$	6640.0100	6640.0138	-0.0038
$6_{33} \rightarrow 6_{24}$	3708.6860	3708.6904	-0.0044
$6_{33} \rightarrow 5_{42}$	5711.3440	5711.3499	-0.0059

$6_{43} \rightarrow 6_{34}$	7075.6790	7075.6849	-0.0059
$6_{42} \rightarrow 6_{33}$	5817.6540	5817.6583	-0.0043
$7_{26} \rightarrow 6_{33}$	3911.2480	3911.2535	-0.0055
$7_{25} \rightarrow 7_{16}$	6321.5930	6321.6026	-0.0096
$7_{35} \rightarrow 7_{26}$	7616.4080	7616.4177	-0.0097
$7_{35} \rightarrow 6_{42}$	5710.0070	5710.0129	-0.0059
$7_{34} \rightarrow 7_{25}$	4184.7510	4184.7588	-0.0078
$7_{44} \rightarrow 6_{52}$	4565.2810	4565.2936	-0.0126
$7_{44} \rightarrow 7_{35}$	7427.4190	7427.4302	-0.0112
$7_{43} \rightarrow 7_{34}$	5214.1340	5214.1391	-0.0051
$8_{44} \rightarrow 8_{35}$	4856.6060	4856.6150	-0.0090
$9_{45} \rightarrow 9_{36}$	5002.2840	5002.3052	-0.0212
$9_{54} \rightarrow 9_{45}$	6829.6970	6829.6837	0.0133
$10_{55} \rightarrow 10_{46}$	6179.2550	6179.2748	-0.0198
$11_{56} \rightarrow 11_{47}$	5964.8960	5964.9154	-0.0194

Table 4-2: Experimentally observed rotational transition and their assignments for 1-fluoronaphthalene-^{13}C1.

Transitions	**Observed (MHz)**	**Calculated (MHz)**	**Obs-Cal (MHz)**
$1_{11} \rightarrow 0_{00}$	2623.1760	2623.1711	0.0049
$2_{02} \rightarrow 1_{01}$	3506.4890	3506.4853	0.0037
$2_{12} \rightarrow 1_{11}$	3218.9420	3218.9460	-0.0040
$2_{12} \rightarrow 1_{01}$	4029.6110	4029.6059	0.0051
$2_{11} \rightarrow 1_{10}$	4031.1020	4031.0988	0.0032
$2_{21} \rightarrow 2_{12}$	3650.2090	3650.2088	0.0002
$2_{21} \rightarrow 1_{10}$	6463.0790	6463.0784	0.0006
$2_{20} \rightarrow 1_{11}$	6987.6960	6987.6918	0.0042
$3_{03} \rightarrow 2_{12}$	4494.4340	4494.4535	-0.0195
$3_{03} \rightarrow 2_{02}$	5017.5800	5017.5740	0.0060
$3_{13} \rightarrow 2_{12}$	4762.5930	4762.5907	0.0023
$3_{13} \rightarrow 2_{02}$	5285.7170	5285.7112	0.0058
$3_{12} \rightarrow 2_{21}$	3526.0780	3526.0765	0.0015
$3_{12} \rightarrow 2_{11}$	5958.0570	5958.0561	0.0009
$3_{22} \rightarrow 2_{21}$	5437.5230	5437.5336	-0.0106

$3_{22} \rightarrow 3_{13}$	4325.1530	4325.1517	0.0013
$3_{21} \rightarrow 2_{20}$	5857.5000	5857.4931	0.0069
$3_{31} \rightarrow 3_{22}$	5134.3240	5134.3187	0.0053
$3_{30} \rightarrow 3_{21}$	4618.5730	4618.5858	-0.0128
$4_{04} \rightarrow 3_{03}$	6406.9300	6406.9267	0.0033
$4_{04} \rightarrow 3_{13}$	6138.7910	6138.7895	0.0015
$4_{14} \rightarrow 3_{03}$	6521.8910	6521.8902	0.0008
$4_{14} \rightarrow 3_{13}$	6253.7430	6253.7530	-0.0100
$4_{13} \rightarrow 3_{22}$	5838.5400	5838.5384	0.0016
$4_{13} \rightarrow 4_{04}$	4024.8980	4024.9006	-0.0026
$4_{23} \rightarrow 4_{14}$	5227.2850	5227.2816	0.0034
$4_{32} \rightarrow 4_{23}$	5412.6090	5412.6195	-0.0105
$4_{31} \rightarrow 4_{22}$	4185.4340	4185.4295	0.0045
$5_{14} \rightarrow 5_{05}$	5595.2580	5595.2507	0.0073
$5_{23} \rightarrow 5_{14}$	3410.1460	3410.1602	-0.0142
$5_{32} \rightarrow 5_{23}$	3803.5180	3803.5120	0.0060

Table 4-3: Experimentally observed rotational transition and their assignments for 1-fluoronaphthalene-^{13}C2.

Transitions	**Observed (MHz)**	**Calculated (MHz)**	**Obs-Cal (MHz)**
$1_{11} \rightarrow 0_{00}$	2603.3920	2603.3954	-0.0034
$2_{02} \rightarrow 1_{01}$	3507.7760	3507.7749	0.0011
$2_{02} \rightarrow 1_{11}$	2720.1560	2720.1586	-0.0026
$2_{12} \rightarrow 1_{11}$	3220.4300	3220.4301	-0.0001
$2_{12} \rightarrow 1_{01}$	4008.0440	4008.0464	-0.0024
$2_{11} \rightarrow 1_{10}$	4042.6880	4042.6863	0.0017
$2_{21} \rightarrow 1_{10}$	6405.5370	6405.5353	0.0017
$2_{21} \rightarrow 2_{12}$	3596.2360	3596.2333	0.0027
$2_{20} \rightarrow 1_{11}$	6940.4540	6940.4467	0.0073
$3_{03} \rightarrow 2_{02}$	5011.6970	5011.6958	0.0012
$3_{03} \rightarrow 2_{12}$	4511.4240	4511.4243	-0.0003
$3_{13} \rightarrow 2_{02}$	5262.3690	5262.3729	-0.0039
$3_{13} \rightarrow 2_{12}$	4762.0980	4762.1014	-0.0034
$3_{12} \rightarrow 2_{11}$	5970.8890	5970.8877	0.0013

$3_{22} \rightarrow 3_{13}$	4281.4750	4281.4692	0.0058
$3_{21} \rightarrow 2_{20}$	5882.9800	5882.9788	0.0012
$3_{31} \rightarrow 3_{22}$	5034.4420	5034.4455	-0.0035
$3_{30} \rightarrow 3_{21}$	4499.6170	4499.6189	-0.0019
$4_{04} \rightarrow 3_{03}$	6395.7990	6395.7959	0.0031
$4_{04} \rightarrow 3_{13}$	6145.1200	6145.1188	0.0012
$4_{14} \rightarrow 3_{03}$	6500.6270	6500.6243	0.0027
$4_{13} \rightarrow 4_{04}$	4053.7800	4053.7767	0.0033
$4_{13} \rightarrow 3_{22}$	5917.4290	5917.4262	0.0028
$4_{23} \rightarrow 4_{14}$	5196.1790	5196.1761	0.0029
$4_{31} \rightarrow 4_{22}$	4063.4220	4063.4303	-0.0083
$5_{14} \rightarrow 5_{05}$	5629.4100	5629.4103	-0.0003
$5_{23} \rightarrow 4_{32}$	6190.1580	6190.1654	-0.0074
$5_{23} \rightarrow 5_{14}$	3422.7530	3422.7604	-0.0074
$5_{33} \rightarrow 5_{24}$	5829.9150	5829.9184	-0.0034

Table 4-4: Experimentally observed rotational transition and their assignments for 1-fluoronaphthalene-$^{13}C3$.

Transitions	**Observed (MHz)**	**Calculated (MHz)**	**Obs-Cal (MHz)**
$1_{11} \rightarrow 0_{00}$	2623.6710	2623.6744	-0.0034
$2_{02} \rightarrow 1_{01}$	3525.5620	3525.5546	0.0074
$2_{12} \rightarrow 1_{11}$	3236.6370	3236.6321	0.0049
$2_{12} \rightarrow 1_{01}$	4036.2190	4036.2310	-0.0120
$2_{21} \rightarrow 2_{12}$	3633.3420	3633.3534	-0.0114
$2_{21} \rightarrow 1_{10}$	6458.4660	6458.4666	-0.0006
$2_{20} \rightarrow 1_{11}$	6992.5820	6992.5820	0.0000
$3_{03} \rightarrow 2_{12}$	4529.0880	4529.0888	-0.0008
$3_{03} \rightarrow 2_{02}$	5039.7640	5039.7652	-0.0012
$3_{13} \rightarrow 2_{02}$	5297.6730	5297.6708	0.0022
$3_{13} \rightarrow 2_{12}$	4786.9970	4786.9944	0.0026
$3_{12} \rightarrow 2_{11}$	5997.4770	5997.4726	0.0044
$3_{22} \rightarrow 3_{13}$	4318.5850	4318.5855	-0.0005
$3_{22} \rightarrow 2_{21}$	5472.2260	5472.2265	-0.0005
$3_{21} \rightarrow 2_{20}$	5904.6930	5904.6878	0.0052

$3_{30} \rightarrow 3_{21}$	4563.7700	4563.7662	0.0038
$4_{04} \rightarrow 3_{03}$	6432.8380	6432.8348	0.0032
$4_{04} \rightarrow 3_{13}$	6174.9260	6174.9292	-0.0032
$4_{14} \rightarrow 3_{03}$	6541.6150	6541.6187	-0.0037
$4_{14} \rightarrow 3_{13}$	6283.7120	6283.7131	-0.0011
$4_{13} \rightarrow 4_{04}$	4064.8420	4064.8473	-0.0053
$4_{13} \rightarrow 3_{22}$	5921.1880	5921.1910	-0.0030
$4_{23} \rightarrow 4_{14}$	5233.6920	5233.7023	-0.0103
$4_{32} \rightarrow 4_{23}$	5381.7740	5381.7689	0.0051
$5_{14} \rightarrow 5_{05}$	5646.9850	5646.9785	0.0065
$5_{23} \rightarrow 5_{14}$	3435.8390	3435.8371	0.0019
$5_{33} \rightarrow 5_{24}$	5884.5670	5884.5625	0.0045
$5_{32} \rightarrow 5_{23}$	3753.0470	3753.0458	0.0012

Table 4-5: Experimentally observed rotational transition and their assignments for 1-fluoronaphthalene-^{13}C4.

Transitions	**Observed (MHz)**	**Calculated (MHz)**	**Obs-Cal (MHz)**
$2_{02} \rightarrow 1_{01}$	3522.7230	3522.7257	-0.0027
$2_{12} \rightarrow 1_{11}$	3234.5570	3234.5510	0.0060
$2_{12} \rightarrow 1_{01}$	4005.5250	4005.5250	0.0000
$2_{11} \rightarrow 1_{10}$	4068.9090	4068.9100	-0.0010
$2_{21} \rightarrow 1_{10}$	6381.8300	6381.8318	-0.0018
$2_{21} \rightarrow 2_{12}$	3564.4640	3564.4603	0.0037
$2_{20} \rightarrow 1_{11}$	6928.0150	6928.0162	-0.0012
$3_{03} \rightarrow 2_{02}$	5026.2880	5026.2869	0.0011
$3_{03} \rightarrow 2_{12}$	4543.4870	4543.4876	-0.0006
$3_{13} \rightarrow 2_{02}$	5263.3690	5263.3709	-0.0019
$3_{13} \rightarrow 2_{12}$	4780.5710	4780.5716	-0.0006
$3_{12} \rightarrow 2_{11}$	6005.7120	6005.7021	0.0099
$3_{22} \rightarrow 3_{13}$	4261.4830	4261.4844	-0.0014
$3_{22} \rightarrow 2_{21}$	5477.5990	5477.5958	0.0032
$3_{31} \rightarrow 3_{22}$	4969.0790	4969.0733	0.0057
$3_{30} \rightarrow 3_{21}$	4415.1620	4415.1676	-0.0056
$4_{04} \rightarrow 3_{13}$	6174.4080	6174.4136	-0.0056

$4_{04} \rightarrow 3_{03}$	6411.4930	6411.4977	-0.0047
$4_{14} \rightarrow 3_{03}$	6508.4750	6508.4771	-0.0021
$4_{14} \rightarrow 3_{13}$	6271.3980	6271.3931	0.0049
$4_{13} \rightarrow 3_{22}$	6008.0680	6008.0683	-0.0003
$4_{13} \rightarrow 4_{04}$	4095.1550	4095.1391	0.0159
$4_{23} \rightarrow 4_{14}$	5190.8070	5190.8097	-0.0027
$4_{32} \rightarrow 4_{23}$	5269.5200	5269.5249	-0.0049
$4_{31} \rightarrow 4_{22}$	3975.3230	3975.3293	-0.0063
$5_{14} \rightarrow 5_{05}$	5680.6130	5680.6195	-0.0065
$5_{33} \rightarrow 5_{24}$	5792.8200	5792.8209	-0.0009
$5_{41} \rightarrow 5_{32}$	6162.5940	6162.5849	0.0091
$6_{24} \rightarrow 6_{15}$	4742.3220	4742.3276	-0.0056

Table 4-6: Experimentally observed rotational transition and their assignments for 1-fluoronaphthalene-^{13}C5.

Transitions	Observed (MHz)	Calculated (MHz)	Obs-Cal (MHz)
$2_{02} \rightarrow 1_{01}$	3533.3730	3533.3779	-0.0049
$2_{12} \rightarrow 1_{11}$	3243.9630	3243.9561	0.0069
$2_{12} \rightarrow 1_{01}$	4036.1650	4036.1657	-0.0007
$2_{11} \rightarrow 1_{10}$	4072.7040	4072.7012	0.0028
$2_{21} \rightarrow 2_{12}$	3619.7530	3619.7465	0.0065
$2_{21} \rightarrow 1_{10}$	6449.3310	6449.3300	0.0010
$2_{20} \rightarrow 1_{11}$	6988.6540	6988.6533	0.0007
$3_{03} \rightarrow 2_{02}$	5047.8890	5047.8905	-0.0015
$3_{03} \rightarrow 2_{12}$	4545.1050	4545.1027	0.0023
$3_{13} \rightarrow 2_{12}$	4796.7550	4796.7540	0.0010
$3_{13} \rightarrow 2_{02}$	5299.5400	5299.5418	-0.0018
$3_{12} \rightarrow 2_{11}$	6015.0010	6014.9994	0.0016
$3_{22} \rightarrow 3_{13}$	4310.4870	4310.4855	0.0015
$3_{22} \rightarrow 2_{21}$	5487.4860	5487.4930	-0.0070
$3_{21} \rightarrow 2_{20}$	5927.0930	5927.0955	-0.0025
$4_{04} \rightarrow 3_{13}$	6190.1630	6190.1634	-0.0004
$4_{04} \rightarrow 3_{03}$	6441.8150	6441.8146	0.0004
$4_{14} \rightarrow 3_{03}$	6546.9200	6546.9192	0.0008

$4_{1\,4} \rightarrow 3_{1\,3}$	6295.2660	6295.2679	-0.0019
$4_{1\,3} \rightarrow 4_{0\,4}$	4084.7280	4084.7218	0.0062
$4_{1\,3} \rightarrow 3_{2\,2}$	5964.4040	5964.3997	0.0043
$4_{2\,3} \rightarrow 4_{1\,4}$	5232.4730	5232.4771	-0.0041
$5_{1\,4} \rightarrow 5_{0\,5}$	5672.0510	5672.0531	-0.0021
$5_{2\,3} \rightarrow 5_{1\,4}$	3448.3720	3448.3775	-0.0055

Table 4-7: Experimentally observed rotational transition and their assignments for 1-fluoronaphthalene-^{13}C6.

Transitions	Observed (MHz)	Calculated (MHz)	Obs-Cal (MHz)
$1_{1\,1} \rightarrow 0_{0\,0}$	2627.7690	2627.7766	-0.0076
$2_{0\,2} \rightarrow 1_{0\,1}$	3537.1100	3537.1116	-0.0016
$2_{0\,2} \rightarrow 1_{1\,1}$	2739.9710	2739.9632	0.0078
$2_{1\,2} \rightarrow 1_{0\,1}$	4044.4650	4044.4661	-0.0011
$2_{1\,2} \rightarrow 1_{1\,1}$	3247.3150	3247.3177	-0.0027
$2_{2\,1} \rightarrow 1_{1\,0}$	6466.6410	6466.6401	0.0009
$2_{2\,0} \rightarrow 1_{1\,1}$	7004.7250	7004.7234	0.0016
$3_{0\,3} \rightarrow 2_{0\,2}$	5054.6020	5054.5979	0.0041
$3_{1\,3} \rightarrow 2_{1\,2}$	4802.2110	4802.2077	0.0033
$3_{1\,3} \rightarrow 2_{0\,2}$	5309.5650	5309.5622	0.0028
$3_{2\,2} \rightarrow 3_{1\,3}$	4322.9380	4322.9378	0.0002
$3_{2\,1} \rightarrow 2_{2\,0}$	5929.1690	5929.1710	-0.0020
$3_{3\,1} \rightarrow 3_{2\,2}$	5089.3570	5089.3575	-0.0005
$3_{3\,0} \rightarrow 3_{2\,1}$	4552.4900	4552.4899	0.0001
$4_{0\,4} \rightarrow 3_{1\,3}$	6196.0290	6196.0292	-0.0002
$4_{0\,4} \rightarrow 3_{0\,3}$	6450.9880	6450.9935	-0.0055
$4_{1\,4} \rightarrow 3_{1\,3}$	6302.9870	6302.9901	-0.0031
$4_{1\,4} \rightarrow 3_{0\,3}$	6557.9550	6557.9544	0.0006
$4_{1\,3} \rightarrow 4_{0\,4}$	4084.1600	4084.1571	0.0029
$4_{1\,3} \rightarrow 3_{2\,2}$	5957.2500	5957.2485	0.0015
$4_{2\,3} \rightarrow 4_{1\,4}$	5243.7270	5243.7279	-0.0009
$4_{3\,2} \rightarrow 4_{2\,3}$	5379.7320	5379.7353	-0.0033
$4_{4\,1} \rightarrow 4_{3\,2}$	6867.1370	6867.1421	-0.0051
$5_{1\,4} \rightarrow 5_{0\,5}$	5672.4280	5672.4282	-0.0002

$5_{14} \rightarrow 5_{05}$	3742.2800	3742.2660	0.0140

Table 4-8: Experimentally observed rotational transition and their assignments for 1-fluoronaphthalene-^{13}C7.

Transitions	Observed (MHz)	Calculated (MHz)	Obs-Cal (MHz)
$2_{02} \rightarrow 1_{01}$	3524.5610	3524.5658	-0.0048
$2_{12} \rightarrow 1_{11}$	3235.9410	3235.9368	0.0042
$2_{12} \rightarrow 1_{01}$	4022.0750	4022.0749	0.0001
$2_{11} \rightarrow 1_{10}$	4064.3610	4064.3662	-0.0052
$2_{21} \rightarrow 1_{10}$	6422.7770	6422.7805	-0.0035
$2_{21} \rightarrow 2_{12}$	3601.0520	3601.0584	-0.0064
$2_{20} \rightarrow 1_{11}$	6962.5920	6962.5809	0.0111
$3_{03} \rightarrow 2_{02}$	5033.9270	5033.9230	0.0040
$3_{03} \rightarrow 2_{12}$	4536.4190	4536.4139	0.0051
$3_{13} \rightarrow 2_{02}$	5281.9140	5281.9182	-0.0042
$3_{13} \rightarrow 2_{12}$	4784.4000	4784.4091	-0.0091
$3_{12} \rightarrow 2_{11}$	6001.9060	6001.9030	0.0030
$3_{22} \rightarrow 3_{13}$	4291.8730	4291.8766	-0.0036
$3_{22} \rightarrow 2_{21}$	5475.2150	5475.2272	-0.0122
$3_{21} \rightarrow 2_{20}$	5916.5280	5916.5314	-0.0034
$4_{04} \rightarrow 3_{03}$	6423.3860	6423.3783	0.0077
$4_{04} \rightarrow 3_{13}$	6175.3860	6175.3832	0.0028
$4_{14} \rightarrow 3_{03}$	6526.4950	6526.4940	0.0010
$4_{13} \rightarrow 4_{04}$	4079.4450	4079.4426	0.0024
$4_{23} \rightarrow 4_{14}$	5213.7560	5213.7531	0.0029

Table 4-9: Experimentally observed rotational transition and their assignments for 1-fluoronaphthalene-^{13}C9.

Transitions	Observed (MHz)	Calculated (MHz)	Obs-Cal (MHz)
$2_{02} \rightarrow 1_{01}$	3500.9700	3500.9661	0.0039
$2_{12} \rightarrow 1_{01}$	4017.3150	4017.3097	0.0053
$2_{12} \rightarrow 1_{11}$	3213.9400	3213.9396	0.0004
$2_{11} \rightarrow 1_{10}$	4027.3230	4027.3220	0.0010

$2_{21} \rightarrow 1_{10}$	6437.4330	6437.4322	0.0008
$2_{21} \rightarrow 2_{12}$	3630.1760	3630.1837	-0.0077
$2_{20} \rightarrow 1_{11}$	6963.7940	6963.7881	0.0059
$3_{03} \rightarrow 2_{02}$	5007.7040	5007.7029	0.0011
$3_{03} \rightarrow 2_{12}$	4491.3650	4491.3592	0.0058
$3_{13} \rightarrow 2_{02}$	5270.8560	5270.8476	0.0084
$3_{13} \rightarrow 2_{12}$	4754.4930	4754.5039	-0.0109
$3_{12} \rightarrow 2_{11}$	5951.3960	5951.3946	0.0014
$3_{22} \rightarrow 3_{13}$	4306.6270	4306.6259	0.0011
$3_{22} \rightarrow 2_{21}$	5430.9450	5430.9462	-0.0012
$3_{21} \rightarrow 2_{20}$	5854.1910	5854.1895	0.0015
$3_{31} \rightarrow 3_{22}$	5099.9770	5099.9838	-0.0068
$3_{30} \rightarrow 3_{21}$	4580.2670	4580.2585	0.0085
$4_{04} \rightarrow 3_{13}$	6130.2260	6130.2199	0.0061
$4_{04} \rightarrow 3_{03}$	6393.3690	6393.3646	0.0044
$4_{14} \rightarrow 3_{03}$	6505.4640	6505.4730	-0.0090
$4_{14} \rightarrow 3_{13}$	6242.3220	6242.3283	-0.0063
$4_{13} \rightarrow 3_{22}$	5849.1550	5849.1635	-0.0085
$4_{13} \rightarrow 4_{04}$	4025.5730	4025.5696	0.0034
$4_{23} \rightarrow 4_{14}$	5210.4740	5210.4694	0.0046
$4_{32} \rightarrow 4_{23}$	5380.6140	5380.6247	-0.0107
$4_{31} \rightarrow 4_{22}$	4146.9690	4146.9661	0.0029
$5_{14} \rightarrow 5_{05}$	5594.7740	5594.7734	0.0006
$5_{24} \rightarrow 5_{15}$	6308.4360	6308.4351	0.0009
$6_{42} \rightarrow 6_{34}$	7227.8000	7227.8031	-0.0031

Table 4-10: Experimentally observed rotational transition and their assignments for 1-fluoronaphthalene-^{13}C10.

Transitions	**Observed (MHz)**	**Calculated (MHz)**	**Obs-Cal (MHz)**
$1_{11} \rightarrow 0_{00}$	2621.0960	2621.1035	-0.0075
$2_{02} \rightarrow 1_{01}$	3492.6840	3492.6820	0.0020
$2_{12} \rightarrow 1_{11}$	3206.2090	3206.2002	0.0088
$2_{12} \rightarrow 1_{01}$	4022.9180	4022.9189	-0.0009
$2_{11} \rightarrow 1_{10}$	4011.3410	4011.3388	0.0022

$2_{21} \rightarrow 2_{12}$	3657.8710	3657.8641	0.0069
$2_{21} \rightarrow 1_{10}$	6461.5000	6461.4950	0.0050
$2_{20} \rightarrow 1_{11}$	6980.1560	6980.1518	0.0042
$3_{03} \rightarrow 2_{02}$	5000.8240	5000.8277	-0.0037
$3_{03} \rightarrow 2_{12}$	4470.5900	4470.5907	-0.0007
$3_{13} \rightarrow 2_{02}$	5274.9980	5274.9965	0.0015
$3_{13} \rightarrow 2_{12}$	4744.7640	4744.7596	0.0044
$3_{12} \rightarrow 2_{11}$	5930.4680	5930.4718	-0.0038
$3_{22} \rightarrow 2_{21}$	5413.1600	5413.1542	0.0058
$3_{22} \rightarrow 3_{13}$	4326.2600	4326.2587	0.0013
$3_{21} \rightarrow 3_{12}$	2461.2460	2461.2527	-0.0067
$3_{31} \rightarrow 3_{22}$	5154.5490	5154.5576	-0.0086
$4_{04} \rightarrow 3_{03}$	6387.0400	6387.0411	-0.0011
$4_{04} \rightarrow 3_{13}$	6112.8700	6112.8722	-0.0022
$4_{14} \rightarrow 3_{13}$	6231.5670	6231.5636	0.0034
$4_{14} \rightarrow 3_{03}$	6505.7300	6505.7325	-0.0025
$4_{13} \rightarrow 3_{22}$	5785.0330	5785.0419	-0.0089
$4_{13} \rightarrow 4_{04}$	3998.4270	3998.4285	-0.0015
$4_{32} \rightarrow 4_{23}$	5427.5690	5427.5633	0.0057
$4_{31} \rightarrow 4_{22}$	4218.0320	4218.0380	-0.0060

Table 4-11: Experimentally observed rotational transition and their assignments for 1-fluoronaphthalene-^{13}C11.

Transitions	Observed (MHz)	Calculated (MHz)	Obs-Cal (MHz)
$1_{11} \rightarrow 0_{00}$	2613.0650	2613.0682	-0.0032
$2_{02} \rightarrow 1_{01}$	3512.5750	3512.5616	0.0134
$2_{12} \rightarrow 1_{01}$	4020.3130	4020.3147	-0.0017
$2_{12} \rightarrow 1_{11}$	3224.7200	3224.7186	0.0014
$2_{11} \rightarrow 1_{10}$	4045.1780	4045.1698	0.0082
$2_{21} \rightarrow 1_{10}$	6431.9530	6431.9580	-0.0050
$2_{21} \rightarrow 2_{12}$	3617.4590	3617.4650	-0.0060
$2_{20} \rightarrow 1_{11}$	6964.5760	6964.5663	0.0097
$3_{03} \rightarrow 2_{02}$	5020.8470	5020.8403	0.0067
$3_{03} \rightarrow 2_{12}$	4513.0910	4513.0872	0.0038

$3_{13} \rightarrow 2_{02}$	5277.0050	5277.0046	0.0004
$3_{13} \rightarrow 2_{12}$	4769.2540	4769.2515	0.0025
$3_{12} \rightarrow 2_{11}$	5975.8450	5975.8545	-0.0095
$3_{22} \rightarrow 3_{13}$	4300.6200	4300.6298	-0.0098
$3_{22} \rightarrow 2_{21}$	5452.4080	5452.4163	-0.0083
$3_{21} \rightarrow 2_{20}$	5883.9970	5883.9923	0.0047
$4_{04} \rightarrow 3_{13}$	6152.3540	6152.3517	0.0023
$4_{04} \rightarrow 3_{03}$	6408.5190	6408.5161	0.0029
$4_{14} \rightarrow 3_{03}$	6516.4450	6516.4428	0.0022
$4_{14} \rightarrow 3_{13}$	6260.2720	6260.2785	-0.0065
$4_{13} \rightarrow 3_{22}$	5902.8260	5902.8392	-0.0132
$4_{13} \rightarrow 4_{04}$	4051.1210	4051.1173	0.0037
$4_{23} \rightarrow 4_{14}$	5212.9300	5212.9315	-0.0015
$5_{14} \rightarrow 5_{05}$	5627.6290	5627.6231	0.0059

Table 4-12: Fitted rotational constants of parent and isotopologues of 1FN. Labelling of the atoms is given in Figure 2.

Isotopologues	A_0	B_0	C_0	N_{lines}	**σ/kHz**
Parent [1]	1920.562	1122.232	708.4778	78	69.0
Parent [2]	1920.6(1)	1122.2(1)	708.5(1)	~4000	~100.0
Parent [3]	1920.581	1122.2370	708.4819	30	2.36
Parent [Present work]	1920.5814(3)	1122.2379(2)	708.4827(1)	85	6.6
^{13}C1	1919.9537(6)	1109.2938(4)	703.2174(3)	31	7.2
^{13}C2	1901.0699(3)	1113.4536(2)	702.3255(2)	29	4.0
^{13}C3	1917.3961(5)	1117.7972(3)	706.2783(2)	28	5.3
^{13}C4	1892.4963(4)	1121.5224(3)	704.3429(2)	29	5.6
^{13}C5	1913.9780(5)	1121.7684(2)	707.3959(2)	24	3.8
^{13}C6	1919.4318(4)	1122.2834(3)	708.3448(2)	25	4.6
^{13}C7	1905.7833(9)	1119.6452(5)	705.4305(3)	20	6.2
^{13}C9	1911.8733(5)	1108.5033(3)	701.8121(3)	29	5.9
^{13}C10	1920.1958(5)	1103.4770(4)	700.9077(3)	25	5.3
^{13}C11	1909.4449(9)	1113.8488(4)	703.6233(3)	24	7.1

4.3.2 Comparison with Theory and Experiment:

The optimization of the 1FN structure was carried out using DFT and *ab initio* quantum chemical calculations. In the present study, three different basis sets, cc-pVTZ, aug-cc-pVDZ and aug-cc-pVTZ, have been employed in the calculations with B3LYP-D3 and MP2 methods. The rotational constants, centrifugal distortion constants, the electric dipole moment components, and the inertial defects derived from these computations are presented in *Table 4-13*. The calculated atomic coordinates for the optimised structures are provided in the supplementary information in *Table 4-16* to *Table 4-21*. The geometry of the 1FN is displayed in *Figure 4-2*. The *a*- and *b*- principal axes lie in the plane of the aromatic ring and are mutually perpendicular to the *c*-axis. The determination of the dipole moment relies heavily on the relative position of the fluorine atom with respect to the three inertial axes. The 1FN is the near-prolate asymmetric rotor. The calculated rotational constants at the MP2 as well as B3LYP-D3 level employing the cc-pVTZ and aug-cc-pVTZ basis sets, are in close agreement with the experimental values. However, the aug-cc-pVDZ basis set with both the MP2 and B3LYP-D3 methods did not agree well with the experimental results. As previously noted, since 1FN falls under a class of rigid molecules, the estimated centrifugal distortion coefficients are small and, hence, were not needed in the experimental fit employing the low *J* transitions reported here.

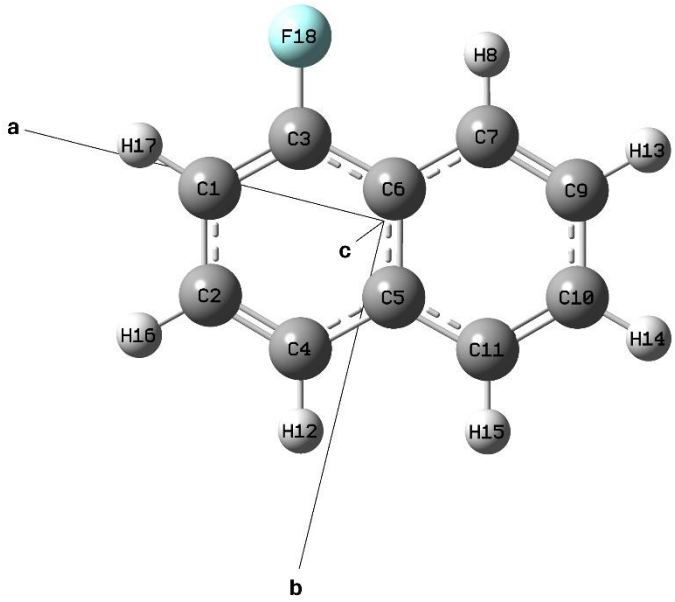

Figure 4-2: Optimised structure at MP2/aug-cc-pVTZ level of theory. Labelling of the atoms and the approximate locations of the principal axes are also shown.

Table 4-13: The rotational constants (MHz), centrifugal distortion constants (kHz), electric dipole moment components (Debye) and the inertial defects (u Å^2) calculated at the MP2/cc-pVTZ, MP2/aug-cc-pVDZ, MP2/aug-cc-pVTZ, B3LYP-D3/cc-pVTZ, B3LYP-D3/aug-cc-pVDZ and B3LYP-D3/aug-cc-pVTZ level of theories and the experimentally obtained rotational constants.

Parameters	MP2/cc-pVTZ	MP2/aug-cc-pVDZ	MP2/aug-cc-pVTZ	B3LYP-D3/cc-pVTZ	B3LYP-D3/aug-cc-pVDZ	B3LYP-D3/aug-cc-pVTZ	Experiment
A_e	1924.7957	1885.2208	1923.0747	1928.2756	1906.4843	1927.7268	1920.5817(2)
B_e	1127.6182	1105.8674	1126.3998	1127.4970	1115.0998	1126.7189	1122.2380(2)
C_e	711.0552	697.0052	710.3358	711.4813	703.5780	711.0967	708.4828(1)
D_J	0.0143	0.0138	0.0520	0.0139	0.0137	0.0140	-
D_K	0.0190	0.0180	0.0267	0.0199	0.0193	0.0200	-
D_{JK}	0.0439	0.0430	-0.0736	0.0435	0.0432	0.0436	-
d_1	-0.0065	-0.0063	-0.0116	-0.0063	-0.0062	-0.0064	-
d_2	-0.0019	-0.019	-0.0012	-0.0019	-0.0019	-0.0019	-
$\lvert\mu_a\rvert$	0.7	0.7	0.7	0.7	0.7	0.7	-
$\lvert\mu_b\rvert$	1.2	1.3	1.3	1.2	1.3	1.3	-
$\lvert\mu_c\rvert$	0.0	0.0	0.0	0.0	0.0	0.0	-
Δ_0	0.0	0.0	0.0	0.0	0.0	0.0	-0.144

Inertia defect calculated as $\Delta_0 = I_c - I_a - I_b$.

4.4 Structural Analysis:

The rotational constants of ten isotopologues containing the ^{13}C isotope have been identified and subsequently utilized to determine the positions of heavy atoms in the geometry. The determination of substitution coordinates (r_s) related to carbon atoms can be achieved by examining the rotational constants of both the parent and singly substituted isotopologues. This, in turn, enables a direct and comprehensive structural analysis of the molecule. This method was described by Kraitchman and implemented within the KRA program [7]. The shifts in the rotational constants on isotopic substitutions

allow for the determination of the atomic coordinates. The labelling of the atoms in the 1FN complex and the approximate location of the principal axes are shown in *Figure 4-2*.

Kraitchman's analysis does not provide the sign of the coordinates; hence, the signs are chosen in accordance with the signs produced by computational results. Few atoms were found to have imaginary coordinates, which suggests that these coordinates are minimal and can be considered as zero. The r_s coordinates determined for 1FN from these results are given in *Table 4-14* with Costain errors. The DFT/ab initio (r_e) calculated coordinates are in excellent agreement with the experimentally determined (r_s) coordinates, confirming the molecular geometry of 1FN is rigid. The EVAL program [8] was utilized to determine the bond distance separating the two carbon atoms that are adjacent to one another, as well as the angles that exist between three consecutive carbon atoms, with the assistance of substitution coordinates. The imaginary coordinates were assumed to be zero in computing the distances and angles. The experimentally determined bond distances and angles are given in *Table 4-15*. It is apparent, as demonstrated in *Table 4-14*, that a collection of rather surprising C-C distances and C-C-C angles results, implying that neither of the benzene nuclei (with unperturbed C-C distances of 1.395Å) conform to a uniform hexagonal shape. This perturbation to the benzene nuclei in the 1FN can be due to the presence of the fluorine atom, which can, in turn, exert the inductive effect due to its high electronegativity.

Table 4-14: The experimentally derived Kraitchman substitution coordinates for all ^{13}C atoms. The values in parentheses denote the uncertainties associated with the coordinates. The calculated coordinates are at the MP2/aug-cc-pVTZ level of theory.

Carbon Atom Number	**Methods**	**Coordinates**		
C1	Theory	2.2901	0.3180	0.0000
	Experiment	2.2959(7)	0.298(5)	[0]
C2	Theory	1.8689	1.6648	0.0000
	Experiment	1.8745(8)	1.6618(9)	[0]
C3	Theory	1.3413	-0.6704	0.0000
	Experiment	1.338(1)	-0.666(2)	[0]

C4	Theory	0.5286	1.9819	0.0000
	Experiment	0.531(3)	1.9811(8)	[0]
C5	Theory	-0.4521	0.9616	0.0000
	Experiment	-0.434(3)	0.955(2)	0.0(1)
C6	Theory	-0.0445	-0.4091	0.0000
	Experiment	[0]	-0.397(4)	0.0(1)
C7	Theory	-1.0151	-1.4364	0.0000
	Experiment	-1.017(1)	-1.436(1)	[0]
C9	Theory	-2.3551	-1.1148	0.0000
	Experiment	-2.3589(6)	-1.113(1)	[0]
C10	Theory	-2.7692	0.2341	0.0000
	Experiment	-2.7715(5)	0.235(6)	[0]
C11	Theory	-1.8373	1.2490	0.0000
	Experiment	-1.8373(8)	1.252(1)	[0]

Table 4-15: The bond distances and the angles determined from the r_s coordinates. Values are given in Å and degrees, respectively.

Bond distances (Å)		**Bond angles (degrees)**	
C1-C2	1.427(5)	**C1-C2-C4**	120.5(1)
C2-C4	1.380(3)	**C2-C4-C5**	119.9(1)
C4-C5	1.409(3)	**C4-C5-C6**	119.0(3)
C5-C6	1.420(7)	**C5-C6-C3**	119.1(3)
C6-C3	1.365(2)	**C6-C3-C1**	123.5(3)
C3-C1	1.358(4)	**C5-C11-C10**	120.6(2)
C5-C11	1.435(4)	**C11-C10-C9**	120.4(1)
C11-C10	1.381(5)	**C10-C9-C7**	120.5(1)
C10-C9	1.410(6)	**C9-C7-C6**	120.9(1)
C9-C7	1.3797(2)	**C7-C6-C5**	117.8(2)

C7-C6	1.4540(3)		

4.5 Discussion:

The rotational constants of 1FN were measured with great accuracy. The better signal-to-noise ratio facilitated the identification of the complete set of ten mono-substituted ^{13}C isotopologues, present in natural abundance. The measured rotational constants from this work agree with the previously reported rotational constants. Karlsson measured only higher J transitions, but the distortion constants were not determined; therefore, the RMS deviation of the fit was around 69 kHz [1]. The microwave spectrum of 1FN, as investigated by Carey et al., displays low J transitions [3] that are similar to those observed in the current study. The distortion constants were not determined because the centrifugal distortion effects were neglected for low J transitions for a rigid molecule like 1FN. We confirm that centrifugal distortion constants are not needed for fitting the low J spectra for all ^{13}C isotopologues of 1FN in this work.

The *ab initio* and DFT quantum chemical calculations were utilised to optimise the structure with cc-pVTZ, aug-cc-pVDZ and aug-cc-pVTZ basis sets. The rotational constants, as computed with cc-pVTZ and aug-cc-pVTZ basis sets using B3LYP-D3 and MP2 levels of theory, exhibit remarkable congruity with their experimentally derived values.

Inertial defect is an important parameter to understand the structure of a planar molecule. The Inertial defect (Δ_0) of a molecule is defined as

$$\Delta_0 = I_c - I_a - I_b$$

Where I_α (α= a, b, c) are the principal moments of inertia of the molecule, the molecule-fixed axes are chosen such that $I_a \leq I_b \leq I_c$. The value of Δ_0 should be nearly zero for a planar molecule. Nevertheless, this quantity could also manifest as either positive or negative owing to low-frequency out-of-plane vibrations that emerge as a consequence of either torsional motion or bending of the ring [12]. Numerous publications have discussed the origins of both negative and positive inertial defects [12–14]. It is anticipated that the magnitude of Δ_0 would be positive if the molecule in question does not have any out-of-plane modes with very low frequency. It is a firmly established fact that small

planar molecules exhibit a positive inertial defect, which is widely considered to be a key indication of the planarity of a given molecule. There have been instances of planar molecules that have displayed abnormally small or negative inertial defects [13]. The vinyl formate [15] was the first reported molecule to exhibit a large negative inertial defect, in contrast to malonaldehyde [16] with a positive inertial defect, despite having a similar structural framework. The presence of a significantly low out-of-plane vibration is believed to be the cause of the observed negative inertial defect in vinyl formate. Conversely, in the malonaldehyde, the strong hydrogen bonding between CHO and OH suppresses the large amplitudes of out-of-plane vibrations. Through MW spectroscopy, the inertial defect of various compounds such as fluorobenzene, 1,2,3,4-tetrafluorobenzene, 1-Chloro-3-fluorobenzene and meta-di-fluorobenzene have been experimentally determined [17–21]. All of these have small positive inertial defects except meta-di-fluorobenzene. Unless there exists one or more modes that are out-of-plane and exhibit very low frequencies, it is anticipated that the value of Δ_0 will be positive for the ground vibrational state [12]. The inertial defect for 1FN is found to be -0.144 amu Å^2 and agrees well with the values reported earlier [1,3]. The observed negative inertial defect is attributed to the low out-of-plane bending mode of the 1FN ring. The inertial defects for all the isotopologues do not change much with the substitutions, which indicates that the structure is effectively planar, with all the carbon atoms lying on the same plane. The inertial defects for 1FN and its isotopologues are given in *Table 4-12*. An empirical formula was derived by Takeshi Oka to correlate the inertial defect and the lowest out-of-plane bending mode [13]. The equation is given below:

$$\Delta_0 = -\frac{33.715}{\nu_1} + 0.00803\sqrt{I_{cc}}$$

In this equation, Δ_0 represents the inertial defect, I_{cc} denotes the principal moment of inertia along the c-axis, and ν_1 signifies the lowest out-of-plane bending mode in cm^{-1}.

For the 1FN monomer, the experimental values of Δ_0 and I_{cc} are known, enabling the calculation of ν_1 using the aforementioned empirical formula, yielding a value of 94 cm^{-1}. However, the experimental value of ν_1 for the 1FN monomer is unknown.

To address this, we employed all the methods reported in *Table 4-13* to perform harmonic frequency calculations. The calculated harmonic frequencies, along with its infrared intensity, are given in *Table 4-22* and *Table 4-23* of the Supplementary Information. The anharmonic frequency corrections are extremely computationally expensive for *ab initio* methods and also for Dunning's augmented triple-ζ aug-cc-pVTZ basis sets. Therefore, to address this constraint, the B3LYP-D3/cc-pVTZ level of theory was employed to perform anharmonic frequency calculations, which is given in *Table 4-24*, which also provides the infrared intensity and Raman activity in all the normal modes. Consequently, the normal modes of the 1FN molecule were obtained, revealing a calculated lowest out-of-plane bending mode of 142.84 cm^{-1} after the anharmonic correction. However, it should be noted that the difference between the harmonic and anharmonic frequencies is not very much for lower frequencies, as shown in *Table 4-24* of the Supplementary Information. The displacement vectors for this mode are shown in *Figure 4-3*. The determination of the experimental value of ν_1 for the 1FN molecule is necessary to validate the reliability of this empirical formula, which can be verified by the far-IR or THz experiments in the future.

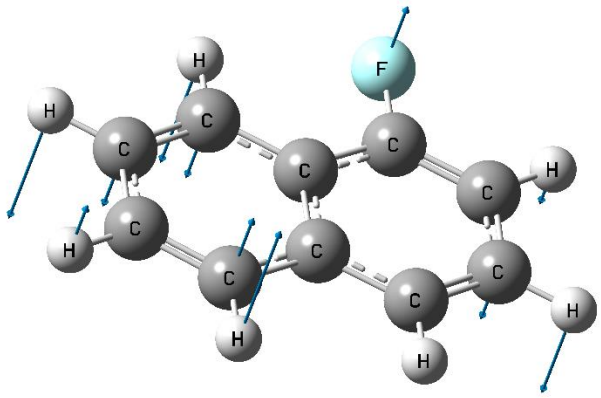

Figure 4-3: Displacements vectors for lowest out-of-plane bending mode of 1FN calculated at MP2/aug-cc-pVTZ level of theory.

4.6 Conclusions:

The rotational spectra of 1-fluoronaphthalene and its ^{13}C isotopologues were analysed within the frequency range of 2.0-8.0 GHz using a CP-FTMW spectrometer with neon as the carrier gas in this study. All the singly substituted ^{13}C isotopologues were assigned in natural abundance. The rotational constants A_0, B_0, and C_0 and inertial defects are determined from experimentally measured transition frequencies. Experimental rotational constants were in good agreement with the ones calculated at MP2/aug-cc-pVTZ level of theory. The atomic coordinates of all the carbon atoms of 1FN were determined using the substitution method. The small and negative inertial defect for parent and all ^{13}C isotopologues were observed which is attributed to the low out-of-plane bending mode of the 1FN ring. A formula based on empirical data was utilised for the computation of the lowest out-of-plane bending mode, which came out to be 94 cm^{-1}. The frequency before and after the anharmonic correction was calculated using the B3LYP-D3/cc-pVTZ level of theory and was estimated to be 146.47 cm^{-1} and 142.84 cm^{-1}, respectively.

4.7 References:

(1) Karlsson, H. Microwave Spectrum of 1-Fluoronaphthalene. *Acta Chem. Scand.* **1973**, *27*, 1435–1436. https://doi.org/10.3891/acta.chem.scand.27-1435.

(2) Majewski, W. A.; Plusquellic, D. F.; Pratt, D. W. The Rotationally Resolved Fluorescence Excitation Spectrum of 1-Fluoronaphthalene. *The Journal of Chemical Physics* **1989**, *90* (3), 1362–1367. https://doi.org/10.1063/1.456078.

(3) Carey, S. J.; Sun, M.; Kukolich, S. G. Microwave Spectra of 1-Fluoronaphthalene and 2-Fluoronaphthalene. *Journal of Molecular Spectroscopy* **2014**, *304*, 25–27. https://doi.org/10.1016/J.JMS.2014.08.004.

(4) Loru, D.; Bermúdez, M. A.; Sanz, M. E. Structure of Fenchone by Broadband Rotational Spectroscopy. *The Journal of Chemical Physics* **2016**, *145* (7), 074311. https://doi.org/10.1063/1.4961018.

(5) Zaleski, D. P.; Stephens, S. L.; Walker, N. R. A Perspective on Chemistry in Transient Plasma from Broadband Rotational Spectroscopy. *Phys. Chem. Chem. Phys.* **2014**, *16* (46), 25221–25228. https://doi.org/10.1039/C4CP04108A.

[5] Frisch, M. J.; Trucks, G. W.; Schlegel, H. B.; Scuseria, G. E.; Robb, M. A.; Cheeseman, J. R.; Scalmani, G.; Barone, V.; Mennucci, B.; Petersson, G. A.; et al. Gaussian 09, Revision D. 01, Gaussian, Inc., Wallingford, CT, 2009.

[6] Structural Calculation Program: http://info.ifpan.edu.pl/~kisiel/struct/struct.htm#kra.

[7] Structural Calculation Program: http://info.ifpan.edu.pl/~kisiel/struct/struct.htm#eval.

[8]PROSPE Website http://info.ifpan.edu.pl/~kisiel/prospe.htm#table_of_programs.

(10) Western, C. M. PGOPHER: A Program for Simulating Rotational, Vibrational and Electronic Spectra. *Journal of Quantitative Spectroscopy and Radiative Transfer* **2017**, *186*, 221–242. https://doi.org/10.1016/j.jqsrt.2016.04.010.

(11) Watson, J. K. G. Determination of Centrifugal Distortion Coefficients of Asymmetric-Top Molecules. III. Sextic Coefficients. *The Journal of Chemical Physics* **1968**, *48* (10), 4517–4524. https://doi.org/10.1063/1.1668020.

(12) Herschbach, D. R.; Laurie, V. W. Influence of Vibrations on Molecular Structure Determinations. III. Inertial Defects. *The Journal of Chemical Physics* **1964**, *40* (11), 3142–3153. https://doi.org/10.1063/1.1724977.

(13) Oka, T. *MOLECULAR STRUCTURE On Negative Inertial Defect*; 1995; Vol. 352, pp 225–233.

(14) Takeshi, C.; Mori, Y.; ~o, ; *Calculation of Inertia Defect Part 1. General Formulation*; 1961; Vol. 6, pp 472–482.

(15) Rao, V. M.; Curl, R. F. Microwave Spectrum of Vinyl Formate. *The Journal of Chemical Physics* **1964**, *40* (12), 3688–3690. https://doi.org/10.1063/1.1725074.

(16) Turner, P.; Baughcum, S. L.; Coy, S. L.; Smith, Z. Microwave Spectroscopic Study of Malonaldehyde. 4. Vibration-Rotation Interaction in Parent Species. *J. Am. Chem. Soc.* **1984**, *106* (8), 2265–2267. https://doi.org/10.1021/ja00320a008.

(17) McCulloh, K. E.; Pollnow, G. F. The Microwave Spectrum of Fluorobenzene. *The Journal of Chemical Physics* **1954**, *22* (6), 1144–1144. https://doi.org/10.1063/1.1740297.

(18) Bak, B.; Christensen, D.; Hansen-Nygaard, L.; Tannenbaum, E. Microwave Determination of the Structure of Fluorobenzene. *The Journal of Chemical Physics* **1957**, *26* (1), 134–137. https://doi.org/10.1063/1.1743237.

(19) Hartmann, T.; Botskor, I. Microwave Spectrum and Dipole Moment of 1,2,3,4-Tetra-Fluorobenzene. *Journal of Molecular Structure* **1974**, *22* (3), 337–342. https://doi.org/10.1016/0022-2860(74)85003-9.

(20) Onda, M.; Odaka, T.; Miyazaki, H.; Mori, M.; Yamaguchi, I.; Niide, Y. Microwave Spectrum, Quadrupole Coupling Constant Tensors, and Dipole Moments of 1-Chloro-3-Fluorobenzene. *Journal of Molecular Spectroscopy* **1994**, *165* (2), 426–432. https://doi.org/10.1006/jmsp.1994.1145.

(21) Rachmant, A. Investigations on the Microwave Spectrum of Meta-Di-Fluoro-Benzene. *Spectrochimica Acta* **1966**, *22* (9), 1551–1554. https://doi.org/10.1016/0371-1951(66)80154-6.

4.8 Supplementary Information:

Table 4-16: Equilibrium geometry coordinates (Å) of 1FN structure in the abc principal axes system optimised at MP2/cc-pVTZ level of theory.

Atoms	a	b	c
C1	2.2882	0.3181	0.0000
C2	1.8675	1.6644	0.0000
C3	1.3418	-0.6725	0.0000
C4	0.5282	1.9817	0.0000
C5	-0.4522	0.9616	0.0000
C6	-0.0437	-0.4082	0.0000
C7	-1.0140	-1.4352	0.0000
H8	-0.6905	-2.4660	0.0000
C9	-2.3534	-1.1150	0.0000
C10	-2.7682	0.2331	0.0000
C11	-1.8373	1.2480	0.0000
H12	0.2092	3.0158	0.0000
H13	-3.0935	-1.9034	0.0000
H14	-3.8234	0.4697	0.0000
H15	-2.1549	2.2831	0.0000
H16	2.6112	2.4490	0.0000
H17	3.3350	0.0514	0.0000
F18	1.7343	-1.9603	0.0000

Table 4-17: Equilibrium geometry coordinates (Å) of 1FN structure in the abc principal axes system optimised at MP2/aug-cc-pVDZ level of theory.

Atoms	a	b	c
C1	2.3114	0.3233	0.0000
C2	1.8846	1.6819	0.0000
C3	1.3526	-0.6740	0.0000
C4	0.5308	2.0017	0.0000
C5	-0.4573	0.9708	0.0000

C6	-0.0448	-0.4118	0.0000
C7	-1.0220	-1.4508	0.0000
H8	-0.6948	-2.4935	0.0000
C9	-2.3756	-1.1271	0.0000
C10	-2.7952	0.2337	0.0000
C11	-1.8552	1.2600	0.0000
H12	0.2080	3.0476	0.0000
H13	-3.1242	-1.9249	0.0000
H14	-3.8630	0.4718	0.0000
H15	-2.1775	2.3066	0.0000
H16	2.6367	2.4759	0.0000
H17	3.3706	0.0552	0.0000
F18	1.7539	-1.9824	0.0000

Table 4-18: Equilibrium geometry coordinates (Å) of 1FN structure in the abc principal axes system optimised at MP2/aug-cc-pVTZ level of theory.

Atoms	**a**	**b**	**c**
C1	2.2901	0.3180	0.0000
C2	1.8689	1.6648	0.0000
C3	1.3414	-0.6704	0.0000
C4	0.5286	1.9819	0.0000
C5	-0.4521	0.9616	0.0000
C6	-0.0445	-0.4091	0.0000
C7	-1.0151	-1.4364	0.0000
H8	-0.6914	-2.4683	0.0000
C9	-2.3551	-1.1148	0.0000
C10	-2.7692	0.2341	0.0000
C11	-1.8373	1.2490	0.0000
H12	0.2090	3.0169	0.0000
H13	-3.0970	-1.9028	0.0000
H14	-3.8254	0.4708	0.0000
H15	-2.1545	2.2854	0.0000
H16	2.6134	2.4498	0.0000
H17	3.3379	0.0512	0.0000

F18	1.7353	-1.9621	0.0000

Table 4-19: Equilibrium geometry coordinates (Å) of 1FN structure in the abc principal axes system optimised at B3LYP-D3/cc-pVTZ level of theory.

Atoms	**a**	**b**	**c**
C1	2.2861	0.3174	0.0000
C2	1.8644	1.6642	0.0000
C3	1.3428	-0.6678	0.0000
C4	0.5311	1.9796	0.0000
C5	-0.4532	0.9611	0.0000
C6	-0.0448	-0.4070	0.0000
C7	-1.0180	-1.4327	0.0000
H8	-0.6921	-2.4626	0.0000
C9	-2.3516	-1.1162	0.0000
C10	-2.7656	0.2331	0.0000
C11	-1.8403	1.2442	0.0000
H12	0.2129	3.0138	0.0000
H13	-3.0938	-1.9030	0.0000
H14	-3.8219	0.4670	0.0000
H15	-2.1594	2.2786	0.0000
H16	2.6097	2.4476	0.0000
H17	3.3333	0.0520	0.0000
F18	1.7384	-1.9599	0.0000

Table 4-20: Equilibrium geometry coordinates (Å) of 1FN structure in the abc principal axes system optimised at B3LYP-D3/aug-cc-pVDZ level of theory.

Atoms	**a**	**b**	**c**
C1	2.2999	0.3189	0.0000
C2	1.8752	1.6729	0.0000
C3	1.3485	-0.6693	0.0000
C4	0.5334	1.9901	0.0000
C5	-0.4550	0.9658	0.0000

C6	-0.0457	-0.4094	0.0000
C7	-1.0232	-1.4413	0.0000
H8	-0.6958	-2.4794	0.0000
C9	-2.3650	-1.1219	0.0000
C10	-2.7810	0.2350	0.0000
C11	-1.8491	1.2519	0.0000
H12	0.2130	3.0322	0.0000
H13	-3.1133	-1.9148	0.0000
H14	-3.8455	0.4713	0.0000
H15	-2.1703	2.2943	0.0000
H16	2.6264	2.4627	0.0000
H17	3.3555	0.0523	0.0000
F18	1.7476	-1.9718	0.0000

Table 4-21: Equilibrium geometry coordinates (Å) of 1FN structure in the abc principal axes system optimised at B3LYP-D3/aug-cc-pVTZ level of theory.

Atoms	**a**	**b**	**c**
C1	2.2863	0.3185	0.0000
C2	1.8638	1.6653	0.0000
C3	1.3429	-0.6663	0.0000
C4	0.5301	1.9797	0.0000
C5	-0.4535	0.9606	0.0000
C6	-0.0450	-0.4080	0.0000
C7	-1.0185	-1.4337	0.0000
H8	-0.6941	-2.4640	0.0000
C9	-2.3522	-1.1168	0.0000
C10	-2.7664	0.2328	0.0000
C11	-1.8408	1.2438	0.0000
H12	0.2117	3.0137	0.0000
H13	-3.0944	-1.9033	0.0000
H14	-3.8225	0.4667	0.0000
H15	-2.1601	2.2781	0.0000
H16	2.6085	2.4491	0.0000
H17	3.3337	0.0542	0.0000

F18	1.7414	-1.9598	0.0000

Table 4-22: Harmonic vibrational frequencies (cm^{-1}) and their respective infrared intensity (arbitrary unit) calculated at MP2 method with cc-pVTZ, aug-cc-pVDZ and aug-cc-pVTZ level of theory.

Modes	MP2/cc-pVTZ		MP2/aug-cc-pVDZ		MP2/aug-cc-pVTZ	
	Harmonic Frequency	Infrared Intensity	Harmonic Frequency	Infrared Intensity	Harmonic Frequency	Infrared Intensity
1	143.3	0.73	142.4	0.69	136.8	0.62
2	170.8	2.02	174.9	2.38	166.5	2.21
3	265.5	0.54	263.4	0.59	258.4	0.47
4	266.0	2.01	263.8	2.37	265.5	2.21
5	417.8	4.54	417.5	5.40	410.5	4.99
6	461.3	1.59	457.7	0.11	457.8	0.00
7	465.3	0.05	458.4	2.01	460.3	1.81
8	473.6	0.83	465.3	0.86	472.1	0.89
9	532.3	0.38	525.6	0.48	530.7	0.43
10	570.0	6.38	564.1	3.25	565.5	7.52
11	571.0	2.96	566.3	8.64	569.2	3.12
12	616.2	1.54	606.3	1.24	618.1	1.12
13	718.0	6.53	683.0	0.95	715.6	7.25
14	722.4	0.39	707.9	8.18	729.3	0.71
15	757.4	4.63	748.8	5.39	769.0	18.56
16	794.7	108.30	789.2	108.12	798.7	92.78
17	801.6	0.64	789.2	0.38	800.3	0.60
18	858.7	0.68	842.9	0.92	861.3	1.43
19	882.5	6.06	866.6	6.32	880.3	6.76
20	888.0	0.90	878.3	1.02	891.4	0.32
21	943.4	0.00	927.5	0.15	947.7	0.01
22	952.1	1.03	936.1	0.06	964.7	1.56
23	963.9	0.01	940.7	1.25	978.9	0.00
24	1043.2	10.66	1030.4	23.42	1039.6	13.66
25	1060.0	10.43	1044.3	9.88	1055.6	11.15
26	1096.3	14.72	1084.1	15.69	1091.8	16.65

27	1166.1	0.45	1151.5	0.48	1161.4	0.62
28	1176.4	0.24	1163.0	0.11	1171.0	0.15
29	1185.2	0.67	1169.1	1.21	1179.7	1.36
30	1252.6	7.78	1234.0	13.92	1247.8	11.78
31	1274.5	1.05	1257.6	0.65	1270.9	3.07
32	1291.7	47.78	1265.2	38.32	1282.2	47.60
33	1418.0	55.35	1397.7	54.76	1413.0	55.22
34	1446.8	0.96	1430.9	1.43	1441.8	0.73
35	1477.2	2.79	1471.0	21.07	1473.3	4.90
36	1487.0	2.64	1474.7	0.82	1483.7	1.25
37	1498.5	23.99	1497.1	4.25	1493.1	21.79
38	1559.1	19.61	1543.7	21.21	1551.6	20.15
39	1620.5	9.59	1607.9	7.18	1611.5	10.86
40	1638.1	30.18	1622.5	23.31	1630.0	24.00
41	1687.8	3.13	1677.7	2.45	1680.1	2.77
42	3202.5	0.74	3195.4	1.22	3191.5	1.06
43	3209.3	1.19	3201.1	2.12	3198.3	1.54
44	3216.1	7.18	3208.5	7.41	3205.5	6.19
45	3228.7	11.18	3221.2	11.73	3217.9	10.14
46	3230.0	10.01	3222.3	11.52	3219.2	8.71
47	3243.0	7.22	3234.3	8.95	3230.7	7.92
48	3245.4	0.78	3237.8	1.53	3234.7	0.71

Table 4-23: Harmonic vibrational frequencies (cm^{-1}) and their respective infrared intensity (arbitrary unit) calculated at B3LYP-D3 method with cc-pVTZ, aug-cc-pVDZ and aug-cc-pVTZ level of theory.

Modes	B3LYP-D3/cc-pVTZ		B3LYP-D3/aug-cc-pVDZ		B3LYP-D3/aug-cc-pVTZ	
	Harmonic Frequency	Infrared Intensity	Harmonic Frequency	Infrared Intensity	Harmonic Frequency	Infrared Intensity
1	146.5	0.74	146.6	0.77	144.8	0.76
2	175.3	1.83	179.5	2.09	174.8	2.01
3	268.9	0.42	268.2	0.50	266.9	0.43
4	275.6	2.20	273.7	2.48	274.5	2.39

5	426.9	4.35	429.0	5.19	426.0	4.88
6	469.8	2.23	469.1	3.11	469.1	2.41
7	480.6	0.06	475.3	0.77	479.3	0.05
8	481.3	1.12	486.9	0.06	479.8	1.23
9	540.8	0.50	535.6	0.57	539.6	0.55
10	579.6	3.33	574.8	3.61	578.3	3.56
11	583.9	7.64	583.8	10.04	582.3	8.30
12	644.2	0.51	647.9	0.16	643.8	0.37
13	723.9	7.91	718.6	9.26	722.4	8.59
14	751.6	0.04	746.5	0.05	751.8	0.27
15	791.5	70.28	786.6	102.40	792.1	70.53
16	805.6	1.87	796.3	1.46	804.8	1.82
17	816.3	38.30	826.6	9.76	819.9	41.79
18	888.4	2.28	879.7	8.56	889.3	2.21
19	890.9	8.82	892.2	2.56	889.3	9.46
20	910.2	0.23	911.6	0.29	913.3	0.08
21	977.4	0.14	970.9	0.36	983.8	0.12
22	986.6	2.13	984.4	2.45	995.2	2.24
23	1007.1	0.00	1005.6	0.05	1013.0	0.00
24	1040.8	11.68	1035.6	19.45	1038.9	13.72
25	1063.0	13.05	1053.2	15.52	1060.7	14.58
26	1099.7	23.65	1091.3	24.00	1097.3	25.82
27	1178.5	0.06	1166.9	0.13	1176.3	0.05
28	1192.4	2.98	1180.0	2.70	1189.8	3.95
29	1198.5	0.49	1184.8	0.37	1195.8	0.67
30	1244.8	1.30	1236.9	3.24	1243.1	1.68
31	1260.1	36.80	1246.0	34.32	1256.1	42.20
32	1296.1	25.62	1279.8	20.74	1293.0	23.76
33	1381.9	0.91	1385.6	7.24	1380.3	0.57
34	1403.8	0.29	1413.5	22.58	1400.9	0.15
35	1431.0	54.98	1418.5	25.40	1428.2	55.80
36	1481.9	9.64	1467.0	9.60	1479.5	9.96
37	1501.0	12.58	1484.8	17.04	1498.5	12.62
38	1549.5	16.84	1542.9	19.40	1546.5	17.08
39	1615.9	18.65	1620.1	17.00	1612.2	19.46

40	1645.8	21.69	1642.4	18.21	1642.4	17.94
41	1677.4	7.72	1677.3	6.88	1674.4	7.12
42	3161.0	0.58	3168.9	0.58	3161.0	0.57
43	3168.4	0.91	3175.7	1.15	3168.4	0.88
44	3173.6	11.74	3180.8	10.63	3173.5	10.37
45	3185.8	17.27	3193.2	14.53	3185.6	14.66
46	3186.8	18.73	3193.9	16.43	3186.5	16.17
47	3202.1	10.69	3209.1	8.63	3201.2	9.33
48	3203.1	1.71	3209.8	1.54	3202.0	1.14

Table 4-24: Anharmonic, harmonic vibrational frequencies (cm^{-1}) and their respective infrared intensity (arbitrary unit) and Raman activity calculated at B3LYP-D3/cc-pVTZ level of theory.

Modes	**Frequency (Harmonic)**	**Frequency (Anharmonic)**	**Δv**	**Infrared Intensity (Harmonic)**	**Infrared Intensity (Anharmonic)**	**ΔI**	**Raman Activity**
1	146.47	142.84	-3.63	0.7383	0.8139	0.0756	2.54
2	175.25	172.35	-2.90	1.8298	1.5914	-0.2384	0.11
3	268.92	264.01	-4.91	0.4216	0.3264	-0.0952	1.70
4	275.61	274.22	-1.38	2.1956	2.1662	-0.0294	0.93
5	426.87	420.63	-6.24	4.3470	4.1157	-0.2313	1.07
6	469.77	463.73	-6.03	2.2342	1.9292	-0.3050	5.40
7	480.62	473.71	-6.91	0.0639	0.1059	0.0421	0.04
8	481.26	476.04	-5.22	1.1163	1.4901	0.3738	5.50
9	540.85	535.60	-5.25	0.5033	0.3701	-0.1332	4.75
10	579.63	573.78	-5.85	3.3250	3.3890	0.0640	10.63
11	583.92	577.11	-6.81	7.6314	8.1911	0.5597	0.27
12	644.19	637.55	-6.65	0.5070	0.0636	-0.4434	0.09
13	723.88	713.97	-9.91	7.9104	7.6832	-0.2272	30.32
14	751.63	739.32	-12.31	0.0439	0.1654	0.1215	0.52
15	791.46	777.92	-13.53	70.2791	74.3245	4.0454	0.51
16	805.62	794.83	-10.78	1.8681	1.9382	0.0701	0.72
17	816.30	810.23	-6.08	38.2979	28.9328	-9.3650	0.79
18	888.35	872.54	-15.80	2.2735	1.9966	-0.2769	0.03
19	890.86	880.32	-10.54	8.8234	8.3744	-0.4490	6.11
20	910.20	896.48	-13.72	0.2300	0.1360	-0.0940	0.95
21	977.43	969.60	-7.83	0.1440	0.6410	0.4970	0.26
22	986.61	985.83	-0.78	2.1315	2.2767	0.1452	0.11
23	1007.07	999.69	-7.39	0.0024	0.0365	0.0341	0.33

24	1040.78	1022.30	-18.48	11.6740	9.8203	-1.8537	7.43
25	1062.98	1042.06	-20.92	13.0489	2.6636	-10.3853	10.35
26	1099.74	1082.70	-17.04	23.6367	22.2014	-1.4354	11.01
27	1178.52	1154.80	-23.72	0.0559	0.0855	0.0296	4.99
28	1192.36	1173.16	-19.20	2.9797	3.4140	0.4343	1.21
29	1198.50	1176.05	-22.45	0.4867	0.4362	-0.0504	0.74
30	1244.83	1219.71	-25.12	1.2946	0.5055	-0.7891	0.52
31	1260.09	1233.81	-26.28	36.7938	26.8488	-9.9450	5.02
32	1296.05	1271.86	-24.19	25.6241	14.8077	-10.8164	4.13
33	1381.90	1354.27	-27.63	0.9119	0.8734	-0.0385	12.97
34	1403.77	1371.48	-32.29	0.2945	0.6171	0.3226	153.76
35	1431.04	1400.49	-30.55	54.9915	7.8965	-47.0950	0.42
36	1481.90	1450.25	-31.64	9.6401	9.1302	-0.5098	59.52
37	1501.02	1468.88	-32.15	12.5772	6.1033	-6.4739	9.29
38	1549.50	1515.22	-34.28	16.8349	12.0394	-4.7956	1.13
39	1615.94	1576.27	-39.67	18.6409	13.0440	-5.5969	34.18
40	1645.83	1608.44	-37.39	21.6942	7.0497	-14.6444	0.38
41	1677.42	1637.46	-39.96	7.7235	2.8135	-4.9100	6.99
42	3161.03	3018.65	-142.38	0.5768	1.0432	0.4664	38.95
43	3168.39	3033.93	-134.45	0.9151	8.6760	7.7609	43.80
44	3173.62	3044.91	-128.71	11.7308	16.0475	4.3167	126.32
45	3185.82	3054.32	-131.50	17.2370	25.4701	8.2331	96.19
46	3186.80	3065.81	-120.99	18.7490	6.2283	-12.5207	222.61
47	3202.05	3079.32	-122.73	10.6408	8.8324	-1.8083	93.36
48	3203.04	3075.95	-127.09	1.7532	13.0812	11.3280	304.09

CHAPTER 5

Microwave Spectrum and Structure of the 1-Fluoronaphthalene···$(H_2O)_{1\text{-}2}$ Complexes

CHAPTER 5 | Microwave Spectrum and Structure of the 1-Fluoronaphthalene···$(H_2O)_{1-2}$ Complexes |

5.1 Introduction:

The 1-fluoronaphthalene is a chemical compound composed of a naphthalene ring and a fluorine atom bonded to one of the carbon positions within the ring. This molecular entity belongs to the class of aromatic compounds, which are widely recognised for their stable structures that exhibit resonance. It is important to note that this compound possesses two distinct sites where it can accept protons. One of these sites is associated with the π-electron cloud of the aromatic ring, while the other is linked to the presence of lone pairs on the fluorine atom. These notable characteristics present in the 1-fluoronaphthalene molecule make it an area of great interest for scientific investigation, particularly in the fields of intermolecular interactions, hydrogen bonding, and molecular spectroscopy. Understanding molecular interactions involves a complex interplay of various non-covalent forces, including hydrogen bonding, dispersion, dipole-dipole, and repulsive interactions. To obtain a deeper understanding of the effects of modifications in these non-covalent interactions on structural arrangements, it is imperative to examine systems consisting of a small number of molecular components. In a study conducted using microwave spectroscopy, the investigation of the benzene···H_2O complex revealed the presence of weak hydrogen bonds between benzene and the H_2O molecule.[1] In this complex, the H_2O molecule is positioned above the benzene ring, with its hydrogen atoms directed towards the π-cloud of the benzene ring. Importantly, the introduction of a highly electronegative fluorine atom within the benzene ring induces specific preferences in hydrogen bonding, as observed in the fluorobenzene···H_2O and p-difluorobenzene···H_2O complexes.[2] In these instances, the H_2O molecule engages in an O-H···F interaction and a weak C-H···O hydrogen bond while the structure remains planar. Moreover, a transition from dispersion to electrostatic forces as the dominant attractive energy components is observed when moving from benzene···H_2O to singly and doubly substituted fluorinated benzene···H_2O complexes. The use of rotational spectroscopy in studying hexafluorobenzene···water reveals the existence of a lone pair···π-hole interaction, with water positioned above the π-cloud, providing interesting

insights into the complexities of intermolecular interactions.[3] The water complexes of pyridine and its fluorinated derivatives also exhibit the same behaviour.[4–7] In the case of pyridine and its monosubstituted fluorine derivatives, the interaction with water occurs within the same plane, with the formation of O-H···N and weak C-H···O hydrogen bonds.[4–6] On the other hand, the pentafluoropyridine···H_2O complex experiences stabilization due to the interactions between the lone pair and the π-hole.[7] The intricate interplay between the water molecules and the various pyridine derivatives provides insight into the complex nature of their bonding interactions. The benzene···HCCH[8] and fluorobenzene···HCCH[9] complexes have been previously identified using rotational spectroscopy, both of which exhibit C-H···π interactions. In both complexes, the C-H···π interactions are observed to be positioned almost perpendicular to the aromatic ring, with a H···π distance of 2.492 Å in both instances.

The dihydrate complexes of the aforementioned molecules have not yet been investigated using rotational spectroscopy. Nevertheless, there are reports available on the monohydrate and dihydrate complexes of fused ring systems. The rotational spectra of acenaphthene and phenanthrene with H_2O and $(H_2O)_2$ describe the configurations in which H_2O/$(H_2O)_2$ interact with the aromatic ring through the formation of O-H···π hydrogen bonds.[10,11] In contrast, the monohydrate and dihydrate complexes of 1,4-naphthoquinone and phenanthridine exhibit a structure in which the H_2O/$(H_2O)_2$ donate hydrogen bonds to oxygen and nitrogen atoms, respectively, in an in-plane configuration.[11,12]

The structure of 1-fluoronaphthalene has been extensively studied using rotational spectroscopy, resulting in a well-established understanding of its structure.[13,14] The structure of 1-fluoronaphthalene is revisited and presented in *CHAPTER 4* of this thesis. In the current investigation, our aim is to provide a structural analysis of the microwave spectrum exhibited by the 1-fluoronaphthelene···$(H_2O)_{1-2}$ complexes. In this study, we employed pulsed supersonic-jet Fourier transform microwave (FTMW) spectroscopy, which allowed us to gather valuable insights into the conformational preferences of this system in its ground vibronic state. To analyse the relative orientation of the two components, additional comprehensive structural data was also obtained by recording the spectra of the isotope enriched water species.

5.2 Methods:

5.2.1 Computational Details:

The Gaussian09 software[15] package was utilized in order to carry out the structure optimization for both 1FN···H_2O and 1FN···$(H_2O)_2$ complexes. These calculations were performed by employing density functional theory (DFT) and *ab-initio* quantum chemical calculations. In order to optimize the structures, two different methods were used in this particular study. The first method involved using the harmonic hybrid functional[16–18] developed by Becke, Lee, Yang, and Parr, commonly referred to as B3LYP. This method was combined with Grimme's dispersion[19] correction effects to improve accuracy. The second method employed in the study was the MP2 functional.[20,21] Both of these methods were implemented using Dunning's augmented double-ζ (aug-cc-pVDZ) basis set.[22–25] After obtaining the optimized structures, harmonic frequency calculations were performed to confirm that the obtained structures corresponded to minima on the potential energy surface. The freq=vibrot keyword was utilized to calculate the centrifugal distortion constants for all isotopologues. Additionally, the binding energies of the complexes were determined using the supermolecule approach. The correction for the basis set superposition error (BSSE) in the binding energies was carried out by employing Boys and Bernardi's counterpoise method.[26]

In order to gain insight into the nature of the interactions present, the electron density topologies for the optimized structures were calculated. This calculation was performed using the AIMAll software.[27] Furthermore, the intermolecular interactions were characterized and visualized through the utilization of both the Noncovalent Interactions (NCI) index[28] and the Natural Bond Orbital (NBO) analysis.[29] The NCI plots were generated using the Multiwfn software,[30] while the NBO calculations were executed using the NBO 6.0 software.[31] The wavefunctions utilized for these calculations were obtained from Gaussian 09 calculations at the B3LYP-D3/aug-cc-pVDZ level of theory. The utilization of Symmetry Adapted Perturbation Theory (SAPT) allowed for the decomposition of the total interaction energy into distinct terms such as electrostatics, induction, dispersion, and exchange energy.[32] The PSI4[33] program was utilised for this study.

5.2.2 Experimental Details:

The spectra of the 1FN···$(H_2O)_{1-2}$ complexes were successfully obtained through the utilization of a chirped pulse Fourier transform microwave (CP-FTMW) spectrometer at Newcastle University, covering a wide frequency range of 2-8 GHz. These complexes were formed by means of a pulsed supersonic expansion technique, whereby a gaseous mixture containing neon as the carrier gas was employed. The 1-fluoronaphthalene (98%) was acquired from Sigma Aldrich and used without any additional purification steps. In the experiments conducted at Newcastle University, the introduction of 1FN into the neon flow was carried out under a backing pressure of 4 bars. Owing to the remarkably low vapour pressure shown by the 1FN compound, it was heated to a temperature of 65°C. This heating process was facilitated by means of a modified general valve,[34] and its purpose was to generate the desired mixture with the carrier gas. A very small quantity of $H_2{}^{16}O$ (0.1-0.3 ml) was kept in an external reservoir which is present before the pulsed nozzle. D_2O (Sigma-Aldrich, 99.9% D atoms) and $H_2{}^{18}O$ (Sigma-Aldrich, 97% ^{18}O atoms) were replaced with the $H_2{}^{16}O$ during the isotopic studies. A more detailed description about the spectrometer is available in an earlier publication.[35] A chirped pulse was transmitted directly to a travelling-wave tube amplifier (TWTA) with a duration of 1 μs and a frequency spectrum spanning from 2.0 GHz to 8.0 GHz. The polarization of the molecules within the sample was accomplished through the introduction of the chirp from the horn antenna into the vacuum chamber. It is worth noting that the microwave radiation and the expanding gas jet exhibit a spatial orientation that is mutually perpendicular to one another. The chirped pulse causes the excitation of all rotational transitions possible within the frequency range. Following this, the free induction decay (FID) of the molecules' emission is recorded by using a second horn antenna during a time span of 20 μs after the interaction with the microwave pulse. A 100 GS/s oscilloscope (Tektronix DPO72304XS) is then used to digitize the FID. The process involves employing a gas pulse that lasts for approximately 200 microseconds, which facilitates the capture of eight consecutive measurements of the Free Induction Decay (FID) that immediately follow each gas pulse. This capturing process is made possible through the implementation of the 'fast frame' operational mode of the oscilloscope. Once captured, the FIDs are merged together in the time domain, carefully utilising a high-resolution window function before undergoing Fourier transformation. In the frequency

domain, the width of the resulting spectra can be observed as a single peak, with a full width at half-maximum measuring approximately 100 kHz. The precision of this measurement is estimated to be around 10 kHz. To ensure phase coherence within the temporal domain and accuracy in the transition frequencies, the arbitrary waveform generator (AWG), the phase-locked dielectric resonator oscillator (PDRO), and the oscilloscope are referenced to a 10 MHz local oscillator.

5.3 Results:

5.3.1 Optimized Structures:

The molecular structure of the 1FN monomer has been extensively investigated using microwave spectroscopy (Reinvestigated in *CHAPTER 4*).[13,14] 1FN exhibits two distinct proton acceptor sites: the π-cloud and the lone pairs on the fluorine atom. Considering these, three optimized structures for the 1FN···H_2O and eight structures for the 1FN···$(H_2O)_2$ systems were obtained. These optimized structures are depicted in *Figure 5-1* and *Figure 5-2*. The optimization process utilised both the DFT and *ab-initio* quantum chemical methods, employing the aug-cc-pVDZ basis set. In the structures A and B of monohydrate complex, H_2O exhibits in-plane interaction with the 1FN by forming an O-H···F hydrogen bond. The difference between structures A and B lies in the fact that in structure A, H_2O forms a hydrogen bond by having C-H···O interaction in which the oxygen atom interacts with the nearest hydrogen atom present in the same ring containing the fluorine atom. Whereas, in structure B, this secondary interaction occurs from the C-H group of the fused benzene ring. Conversely, in the structure C of monohydrate complex, the H_2O molecule is positioned above the 1FN and contributes the hydrogen bond to the π-cloud of the 1FN ring. The relative energies for all the three structures are given in the *Figure 5-1*. The Supplementary Information provide the equilibrium cartesian coordinates for each of the three structures at the B3LYP-D3/aug-cc-pVDZ and MP2/aug-cc-pVDZ levels of theory. The binding energies reveal that structure A (repetition) represents the global minimum structure at both the B3LYP-D3/aug-cc-pVDZ and MP2/aug-cc-pVDZ levels of theories.

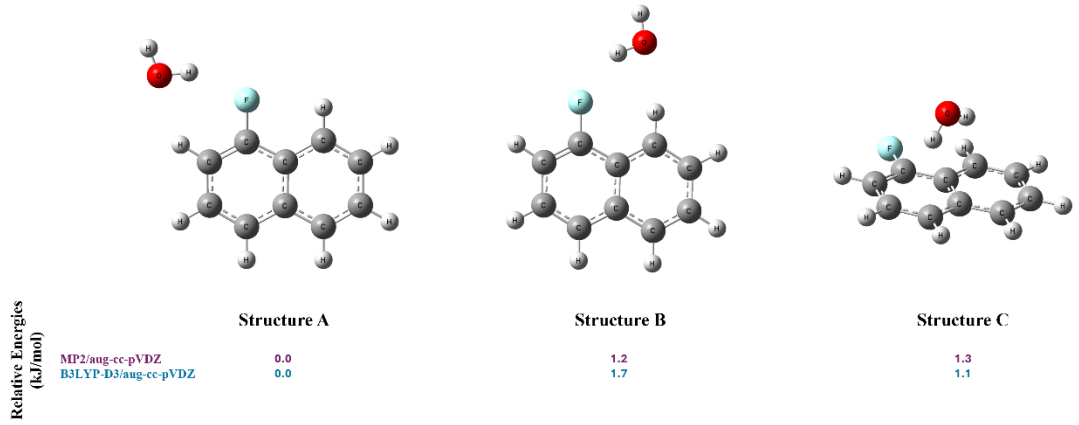

Figure 5-1: Structures of the 1FN···H_2O complex optimised at B3LYP-D3/aug-cc-pVDZ and MP2/aug-cc-pVDZ level of theory.

However, there is a discrepancy in the second minimum structure. At the MP2/aug-cc-pVDZ level, structure B is the second most stable structure, and at the B3LYP-D3/aug-cc-pVDZ level, structure C is the second minimum structure based on the energy ordering.

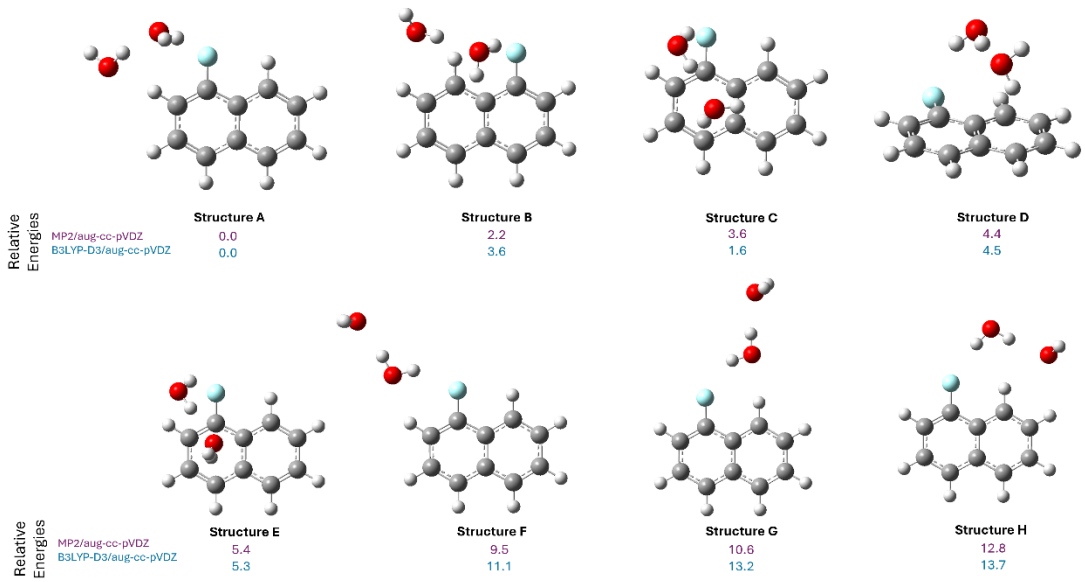

Figure 5-2: Structures of the 1FN···$(H_2O)_2$ complex optimised at B3LYP-D3/aug-cc-pVDZ and MP2/aug-cc-pVDZ level of theory.

In the case of dihydrate complexes, we obtained eight structures by optimizing them at the B3LYP-D3 and MP2 levels of theory with the aug-cc-pVDZ basis set. In all eight structures, two water molecules interact with each other through the formation of strong O-H···O hydrogen bonds. The relative energy ordering is presented in *Figure 5-2*. The energy differences among the structures shown in *Figure 5-2* are very small, indicating the possibility of observing more than one structure in the supersonic expansion. At the MP2/aug-cc-pVDZ level of theory, the second lowest energy structure is structure B, whereas at the B3LYP-D3/aug-cc-pVDZ level of theory, it is structure C. The Supplementary Information contains the equilibrium cartesian coordinates for each of the eight structures for the B3LYP-D3/aug-cc-pVDZ and MP2/aug-cc-pVDZ levels.

The comprehensive molecular parameters, such as rotational constants, centrifugal distortion constants, dipole moment components, and binding energies, corrected for basis set superposition error (BSSE) and zero-point energy, are given in *Table 5-1* and *Table 5-2* for monohydrate and dihydrate complexes respectively. All the possible structures of 1FN···$(H_2O)_2$ complexes possesses distinct rotational constants and dipole moment components, thus making the rotational spectrum, a reliable tool for determining the precise structure.

Table 5-1: Rotational Constants (MHz), Centrifugal Distortion Constants, Electric Dipole Moment (Debye), and the Binding Energy (ΔE) with BSSE Corrections (kJ/mol) for 1FN···H_2O complex calculated at MP2/aug-cc-pVDZ and B3LYP-D3/aug-cc-pVDZ level of theories.

Constants	Structure A		Structure B		Structure C	
	MP2/aug-cc-pVDZ	**B3LYP-D3/aug-cc-pVDZ**	**B3LYP-D3/aug-cc-pVDZ**	**MP2/aug-cc-pVDZ**	**B3LYP-D3/aug-cc-pVDZ**	**MP2/aug-cc-pVDZ**
A_e	1206.778	1192.382	1109.027	1120.066	1746.729	1760.741
B_e	815.650	805.908	822.151	817.137	591.748	593.272
C_e	683.706	686.526	472.141	472.458	442.007	443.752
D_J	0.427	0.323	0.124	0.137	0.025	0.027
D_{JK}	2.315	1.318	-0.204	-0.227	0.098	0.080

D_K	-2.435	-1.328	0.096	0.107	0.105	0.123
d_1	-0.030	-0.019	0.030	0.032	-0.008	-0.008
d_2	0.127	0.093	0.014	0.018	-0.002	-0.001
μ_a	-0.3	0.2	-0.8	-0.8	-1.0	-1.1
μ_b	1.3	-1.3	1.0	1.0	-0.5	-0.5
μ_c	-2.4	-2.5	0.0	0.0	0.0	0.0
ΔE_{BSSE}	11.8	14.5	11.9	13.9	13.1	15.6

Table 5-2: Rotational Constants (MHz), Centrifugal Distortion Constants, Electric Dipole Moment (Debye), and the Binding Energy (ΔE) with BSSE Corrections (kJ/mol) for 1FN···$(H_2O)_2$ complex calculated at MP2/aug-cc-pVDZ and B3LYP-D3/aug-cc-pVDZ level of theories.

Constants	Structure A		Structure B		Structure C		Structure D	
	MP2/aug-cc-pVDZ	B3LYP-D3/aug-cc-pVDZ	MP2/aug-cc-pVDZ	B3LYP-D3/aug-cc-pVDZ	MP2/aug-cc-pVDZ	B3LYP-D3/aug-cc-pVDZ	MP2/aug-cc-pVDZ	B3LYP-D3/aug-cc-pVDZ
A_e	1364.855	1400.8384	931.632	949.515	1007.296	1010.3079	827.756	794.193
B_e	422.6534	412.5591	635.624	615.692	593.906	590.047	742.6643	764.301
C_e	339.6541	327.8668	428.532	413.36	533.832	534.439	562.435	539.365
D_J	0.123	0.152	0.105	0.119	0.188	0.212	0.243	0.356
D_K	0.943	1.451	-0.445	-0.233	1.568	2.218	0.169	0.343
D_{JK}	-0.085	-0.274	0.586	0.337	-0.543	-0.752	-0.3	-0.401
d_1	0.002	0.006	-0.027	-0.031	0.002	0.005	0.002	-0.005
d_2	-0.003	-0.004	-0.02	-0.014	0.01	0.013	0.009	-0.018
μ_a	-1.7	-1.7	-2.1	2.2	-5	-4.9	-2.2	-1.2
μ_b	-0.3	-0.4	0.5	0.4	1.2	1.5	3.5	4
μ_c	1.1	0.8	0.8	-0.9	-1.3	-1.4	-0.1	0.4
ΔE_{BSSE}	40.3	47.9	38.1	44.3	36.7	46.3	35.9	43.4

Table 2 continued:

Constants	Structure E		Structure F		Structure G		Structure H	
	MP2/aug-cc-pVDZ	B3LYP-D3/aug-cc-pVDZ	MP2/aug-cc-pVDZ	B3LYP-D3/aug-cc-pVDZ	MP2/aug-cc-pVDZ	B3LYP-D3/aug-cc-pVDZ	MP2/aug-cc-pVDZ	B3LYP-D3/aug-cc-pVDZ
A_e	1046.148	1074.585	1653.554	1645.185	1102.124	1111.484	952.64	960.189
B_e	584.692	562.416	292.576	293.984	359.0277	356.534	527.477	529.788
C_e	522.453	499.022	248.878	249.707	271.15	270.285	340.033	341.96
D_J	0.34	0.449	0.015	0.018	0.011	0.009	0.022	0.022
D_K	3.142	5.179	1.479	2.01	-0.669	-0.868	-0.324	-0.301
D_{JK}	-1.365	-2.299	0.119	0.071	0.69	0.892	0.387	0.359
d_1	0.032	0.03	-0.004	-0.004	-0.005	-0.006	-0.014	-0.013
d_2	0.007	0.007	-0.001	-0.001	-0.005	-0.006	-0.009	-0.008
μ_a	-3.5	-3.6	1.7	1.6	1.5	1.4	0.6	0.6
μ_b	2.4	2.7	0.4	0.4	0.5	0.6	3.4	3.5
μ_c	0	0.2	0	0	0	0	0	0
ΔE_{BSSE}	34.9	42.6	30.8	36.8	29.7	34.7	27.5	34.2

5.3.2 Observations and Spectral Analysis:

The spectra of the 1FN···$(H_2O)_{1-2}$ complexes were recorded within the frequency range of 2.0 to 8.0 GHz, and the collected data was then averaged over 1.62 million Free Induction Decays (FIDs). The broadband rotational spectrum was acquired by utilising a mixture consisting of 1FN and H_2O, with neon as the carrier gas. The transitions of isotopologues of the 1FN monomer, which incorporate ^{13}C, are observable in their natural abundances. To obtain the initial approximation of the rotational constants and five centrifugal distortion constants for all potential structures listed in *Table 5-1* and *Table 5-2*, the DFT and *ab-initio* calculations were employed. For 1FN···H_2O complex, the assigned spectra agreed with structure A, wherein the H_2O molecule is engaged in forming hydrogen bonds to the 1FN through an in-plane O-H···F interaction and a secondary C-H···O interaction between the nearest hydrogen to the fluorine atom in the fluorine-containing ring. *Figure 5-3* offers an enlarged view of the spectrum recorded with 1FN and H_2O, that specifically highlights selected transitions of 1FN, $^{13}C2$ isotopologue of 1FN and 1FN···H_2O complex.

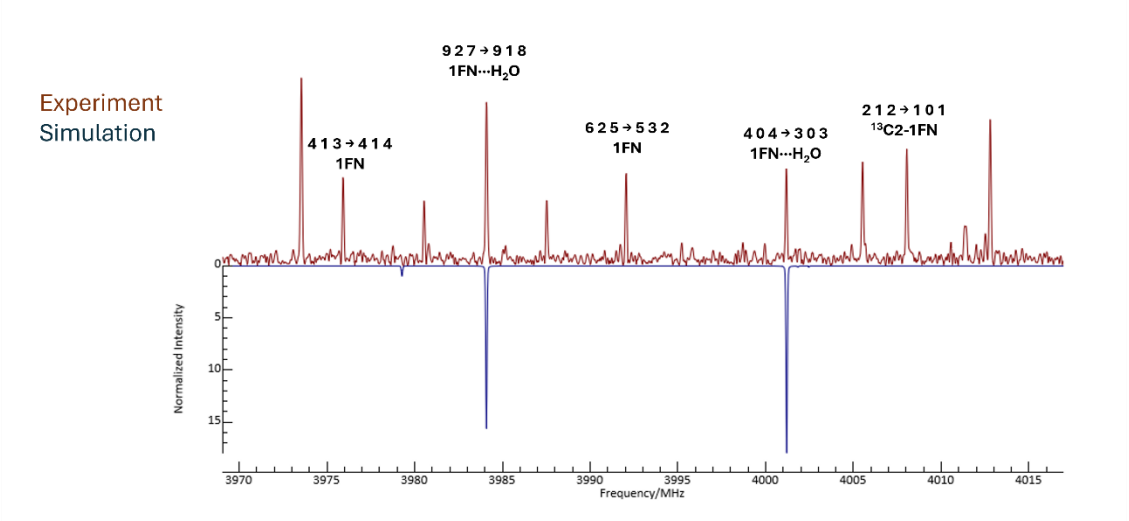

Figure 5-3: A portion of the spectrum of 1FN···H_2O recorded at CP-FTMW spectrometer.

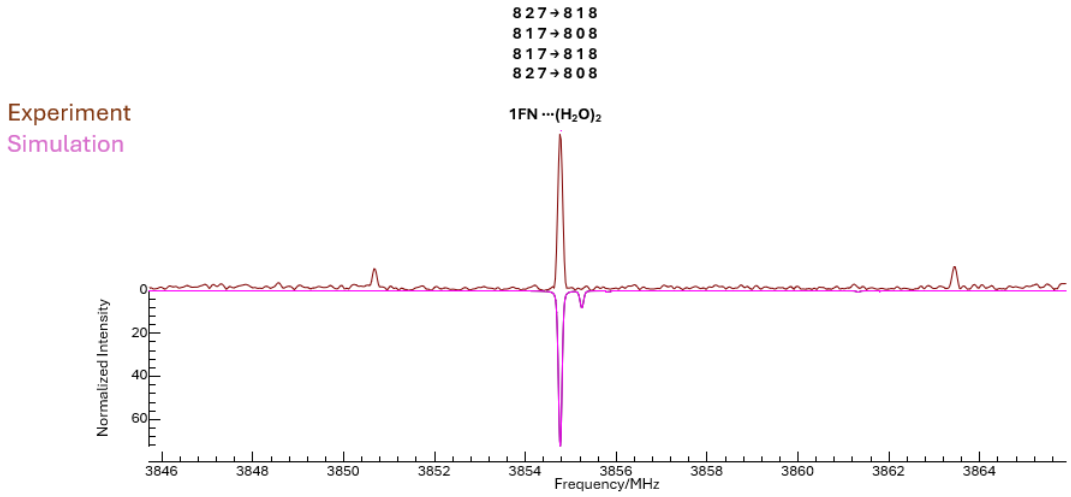

Figure 5-4: A portion of the spectrum of 1FN···$(H_2O)_2$ recorded at CP-FTMW spectrometer.

It should be noted that the spectrum fitted for 1FN···H_2O complex exclusively covers *a*- and *b*-type transitions, as *c*-type transitions were not observed due to the absence of the *c*-dipole moment. A total of 30 transitions were successfully fit to Watson's S-reduced asymmetric rotor Hamiltonian[36] within the I^r representation using the PGOPHER software[37] developed by Western. The rotational constants that were determined through fitting, as well as all five of the centrifugal distortion constants for all four isotopologues,

can be found in *Table 5-3*. The calculated rotational constants at B3LYP-D3/aug-cc-pVDZ level of theory (*Table 5-1*) are in good agreement with experimentally observed rotational constants. The experimentally observed rotational constants play a vital role in aiding us in the process of identifying and fitting transitions for three additional isotopologues, namely 1FN···D_2O, 1FN···DOH, and 1FN···$^{18}H_2O$. The assignment of these isotopologues is essential to determine the intricate structure of the complex under investigation.

For the 1FN···$(H_2O)_2$ complex, the preliminary fitting suggests that the water dimer is interacting with the top of the 1FN plane through the formation of an O-H···F and O-H···C hydrogen bonds, which resembles Structure D shown in *Figure 5-2*. As mentioned previously for the 1FN···H_2O complex, the spectroscopic parameters for the parent complex were derived by fitting the observed transitions using Western's PGOPHER program. However, the calculated rotational constants for Structure D at the B3LYP-D3/aug-cc-pVDZ and MP2/aug-cc-pVDZ level of theory are significantly different from each other. It is worth noting that the observed Structure D is not the global minimum structure at either level of theory. Additionally, two additional isotopologues, 1FN···$(D_2O)_2$ and 1FN···$(H_2{}^{18}O)_2$, have been observed. The recorded spectrum still contains many transitions that have not been assigned. Due to the relatively small energy difference among all the possible structures shown in *Figure 5-2*, it is possible that multiple conformers may be observed for the 1FN···$(H_2O)_2$ complex. *Figure 5-4* shows some of the fitted transitions for the 1FN···$(H_2O)_2$ complex.

It is important to note that all isotopologues were recorded under the exact same experimental conditions as the parent complex. The assigned transition frequencies for all the isotopologues of the 1FN···$(H2O)_{1-2}$ complexes have been given in *Table 5-5* to *Table 5-11*.

Table 5-3: Experimental rotational constants (MHz) and centrifugal distortion constants (kHz) of the 1FN···H_2O complex.

Constants	**1FN···H_2O**	**1FN···D_2O**	**1FN···DOH**	**1FN···$H_2{}^{18}O$**
A_0	1761.311(9)	1747.968(5)	1752.83(4)	1758.83(1)
B_0	589.339(1)	563.078(1)	580.414(1)	562.366(2)

C_0	442.086(1)	426.4216(7)	436.545(1)	426.571(2)
D_J	0.168(9)	0.077(7)	0.13(1)	0.138(9)
D_{JK}	-0.719(6)	-0.83(9)	-0.26(6)	-0.8(1)
D_K	-99.5(6)	-62.3(8)	-93(3)	-13(2)
d_1	-0.026(6)	0.010(5)	-0.012(9)	0.02(2)
d_2	-0.024(2)	0.038(2)	0.034(2)	0.118(4)
Δ (amu Å^2)	-1.2997	-1.4902	-1.3643	-1.2561
N_{lines}	30	21	19	20
σ (kHz)	18.3	5.0	4.6	10.0

Table 5-4: Experimental rotational constants (MHz) and centrifugal distortion constants (kHz) of the 1FN···$(H_2O)_2$ complex.

Constants	1FN···$(H_2O)_2$	1FN···$(D_2O)_2$	1FN···$(H_2{}^{18}O)_2$
A_0	794.670(1)	778.526(9)	777.98(2)
B_0	789.593(1)	758.58(1)	760.09(2)
C_0	539.0952(3)	525.399(4)	523.276(3)
D_J	16.511(3)	11.7(3)	5.4(7)
D_{JK}	-470.20(1)	-20(1)	-19(4)
D_K	91.351(2)	40(1)	21(3)
d_1	40.450(1)	3.3(2)	-0.2(2)
d_2	44.4588(5)	1.816(6)	1.0(1)
Δ (amu Å^2)	-338.551	-353.468	-348.698
N_{lines}	53	18	21
σ (kHz)	9.0	13.8	12.3

Table 5-5: Experimentally observed rotational transition and their assignments for 1FN···H_2O complex.

Transitions	Observed (MHz)	Calculated (MHz)	Obs-Cal (MHz)
$3_{03} \rightarrow 2_{02}$	3042.832	3042.8466	-0.0146
$2_{12} \rightarrow 1_{01}$	3087.687	3087.6667	0.0203
$5_{23} \rightarrow 5_{14}$	3119.556	3119.5558	0.0002
$3_{21} \rightarrow 2_{20}$	3145.66	3145.6763	-0.0163
$3_{12} \rightarrow 2_{11}$	3306.592	3306.6118	-0.0198
$12_{3\,10} \rightarrow 11_{4\,7}$	3311.648	3311.6504	-0.0024

$4_{14} \rightarrow 3_{13}$	3807.186	3807.1654	0.0206
$9_{27} \rightarrow 9_{18}$	3984.083	3984.0823	0.0007
$4_{04} \rightarrow 3_{03}$	4001.178	4001.1811	-0.0031
$4_{23} \rightarrow 3_{22}$	4115.514	4115.5504	-0.0364
$4_{22} \rightarrow 3_{21}$	4239.987	4239.9782	0.0088
$4_{13} \rightarrow 3_{12}$	4391.834	4391.8569	-0.0229
$5_{15} \rightarrow 4_{14}$	4739.057	4739.0499	0.0071
$10_{37} \rightarrow 10_{28}$	4748.597	4748.6072	-0.0102
$5_{05} \rightarrow 4_{04}$	4922.651	4922.6508	0.0002
$8_{17} \rightarrow 8_{08}$	5130.275	5130.2723	0.0027
$5_{42} \rightarrow 4_{41}$	5186.038	5186.0208	0.0172
$5_{33} \rightarrow 4_{32}$	5194.734	5194.7573	-0.0233
$5_{32} \rightarrow 4_{31}$	5209.651	5209.6707	-0.0197
$5_{23} \rightarrow 4_{22}$	5362.334	5362.3046	0.0294
$11_{29} \rightarrow 11_{110}$	5430.952	5430.9523	-0.0003
$5_{14} \rightarrow 4_{13}$	5460.338	5460.3752	-0.0372
$6_{16} \rightarrow 5_{15}$	5660.965	5660.9471	0.0179
$6_{06} \rightarrow 5_{05}$	5814.368	5814.3759	-0.0079
$4_{31} \rightarrow 4_{22}$	6092.613	6092.6342	-0.0212
$3_{31} \rightarrow 3_{22}$	6242.322	6242.3039	0.0181
$6_{33} \rightarrow 5_{32}$	6280.61	6280.5895	0.0205
$6_{24} \rightarrow 5_{23}$	6503.095	6503.0747	0.0203
$6_{15} \rightarrow 5_{14}$	6505.468	6505.4416	0.0264
$10_{28} \rightarrow 9_{37}$	6631.476	6631.4819	-0.0059

Table 5-6: Experimentally observed rotational transition and their assignments for 1FN···D_2O complex.

Transitions	**Observed (MHz)**	**Calculated (MHz)**	**Obs-Cal (MHz)**
$3_{03} \rightarrow 2_{02}$	2924.389	2924.3778	0.0112
$7_{25} \rightarrow 7_{16}$	3213.939	3213.9357	0.0033
$4_{14} \rightarrow 3_{13}$	3663.993	3663.9906	0.0024
$4_{04} \rightarrow 3_{03}$	3850.689	3850.6896	-0.0006
$4_{23} \rightarrow 3_{22}$	3949.313	3949.3154	-0.0024
$7_{16} \rightarrow 7_{07}$	3957.754	3957.7488	0.0052

$4_{22} \rightarrow 3_{21}$	4056.597	4056.5964	0.0006
$3_{22} \rightarrow 3_{13}$	4177.283	4177.288	-0.005
$4_{13} \rightarrow 3_{12}$	4207.207	4207.2093	-0.0023
$5_{15} \rightarrow 4_{14}$	4562.679	4562.669	0.01
$5_{05} \rightarrow 4_{04}$	4743.855	4743.858	-0.003
$5_{24} \rightarrow 4_{23}$	4922.724	4922.7303	-0.0063
$5_{23} \rightarrow 4_{22}$	5126.164	5126.1723	-0.0083
$5_{14} \rightarrow 4_{13}$	5234.132	5234.1327	-0.0007
$14_{3\,11} \rightarrow 14_{2\,12}$	5475.215	5475.2152	-0.0002
$7_{34} \rightarrow 7_{25}$	5559.801	5559.8005	0.0005
$6_{06} \rightarrow 5_{05}$	5608.68	5608.6739	0.0061
$6_{25} \rightarrow 5_{24}$	5887.039	5887.0387	0.0003
$6_{15} \rightarrow 5_{14}$	6241.388	6241.3953	-0.0073
$7_{17} \rightarrow 6_{16}$	6333.714	6333.7143	-0.0003
$7_{07} \rightarrow 6_{06}$	6455.574	6455.5707	0.0033

Table 5-7: Experimentally observed rotational transition and their assignments for 1FN···DOH complex.

Transitions	Observed (MHz)	Calculated (MHz)	Obs-Cal (MHz)
$3_{13} \rightarrow 2_{12}$	2827.594	2827.5993	-0.0053
$3_{03} \rightarrow 2_{02}$	3001.71	3001.7077	0.0023
$3_{12} \rightarrow 2_{11}$	3258.528	3258.5301	-0.0021
$4_{14} \rightarrow 3_{13}$	3757.098	3757.0999	-0.0019
$4_{04} \rightarrow 3_{03}$	3948.625	3948.629	-0.004
$4_{23} \rightarrow 3_{22}$	4058.114	4058.121	-0.007
$4_{22} \rightarrow 3_{21}$	4177.287	4177.2811	0.0059
$4_{13} \rightarrow 3_{12}$	4328.543	4328.5411	0.0019
$5_{15} \rightarrow 4_{14}$	4677.271	4677.27	0.001
$11_{38} \rightarrow 11_{29}$	4717.118	4717.1183	-0.0003
$5_{05} \rightarrow 4_{04}$	4859.825	4859.822	0.003
$5_{24} \rightarrow 4_{23}$	5057.129	5057.131	-0.002
$5_{14} \rightarrow 4_{13}$	5382.644	5382.6432	0.0008
$6_{16} \rightarrow 5_{15}$	5587.804	5587.7912	0.0128
$6_{25} \rightarrow 5_{24}$	6046.004	6046.0065	-0.0025

$4_{31} \rightarrow 4_{22}$	6091.941	6091.9408	0.0002
$6_{34} \rightarrow 5_{33}$	6152.8	6152.796	0.004
$6_{24} \rightarrow 5_{23}$	6404.925	6404.927	-0.002
$7_{17} \rightarrow 6_{16}$	6489.216	6489.2233	-0.0073

Table 5-8: Experimentally observed rotational transition and their assignments for 1FN···$H_2{}^{18}O$ complex.

Transitions	Observed (MHz)	Calculated (MHz)	Obs-Cal (MHz)
$2_{12} \rightarrow 1_{01}$	3038.57	3038.558	0.012
$3_{12} \rightarrow 2_{11}$	3163.374	3163.3752	-0.0012
$3_{21} \rightarrow 3_{12}$	3447.177	3447.1765	0.0005
$4_{04} \rightarrow 3_{03}$	3850.561	3850.5668	-0.0058
$4_{22} \rightarrow 3_{21}$	4052.375	4052.3825	-0.0075
$4_{13} \rightarrow 3_{12}$	4203.741	4203.7479	-0.0069
$9_{27} \rightarrow 8_{36}$	4347.475	4347.4779	-0.0029
$5_{15} \rightarrow 4_{14}$	4562.791	4562.8035	-0.0125
$5_{05} \rightarrow 4_{04}$	4744.833	4744.8148	0.0182
$12_{39} \rightarrow 12_{210}$	4842.815	4842.8132	0.0018
$6_{06} \rightarrow 5_{15}$	5074.975	5074.968	0.007
$9_{36} \rightarrow 9_{27}$	5081.831	5081.8357	-0.0047
$5_{23} \rightarrow 4_{22}$	5120.075	5120.0774	-0.0024
$5_{14} \rightarrow 4_{13}$	5230.363	5230.3648	-0.0018
$6_{16} \rightarrow 5_{15}$	5452.994	5452.9736	0.0204
$6_{06} \rightarrow 5_{05}$	5610.766	5610.7888	-0.0228
$6_{25} \rightarrow 5_{24}$	5884.563	5884.5527	0.0103
$6_{16} \rightarrow 5_{05}$	5988.785	5988.7944	-0.0094
$6_{33} \rightarrow 5_{32}$	6009.34	6009.3365	0.0035
$7_{07} \rightarrow 6_{06}$	6458.59	6458.5865	0.0035

Table 5-9: Experimentally observed rotational transition and their assignments for 1FN···$(H_2O)_2$ complex.

Transitions	Observed (MHz)	Calculated (MHz)	Obs-Cal (MHz)

$14_{10\ 4} \rightarrow 14_{9\ 5}$	3047.048	3047.0479	0.0001
$14_{1\ 13} \rightarrow 13_{3\ 10}$	3224.723	3224.7225	0.0005
$14_{2\ 13} \rightarrow 13_{4\ 10}$	3224.723	3224.7225	0.0005
$14_{1\ 13} \rightarrow 13_{4\ 10}$	3224.723	3224.7225	0.0005
$14_{2\ 13} \rightarrow 13_{3\ 10}$	3224.723	3224.7225	0.0005
$18_{1\ 18} \rightarrow 17_{2\ 15}$	3243.964	3243.9657	-0.0017
$18_{0\ 18} \rightarrow 17_{3\ 15}$	3243.964	3243.9657	-0.0017
$18_{0\ 18} \rightarrow 17_{2\ 15}$	3243.967	3243.9657	0.0013
$18_{1\ 18} \rightarrow 17_{3\ 15}$	3243.967	3243.9657	0.0013
$9_{3\ 6} \rightarrow 9_{3\ 7}$	3633.284	3633.2936	-0.0096
$9_{4\ 6} \rightarrow 9_{2\ 7}$	3633.286	3633.294	-0.008
$9_{3\ 6} \rightarrow 9_{2\ 7}$	3633.286	3633.2936	-0.0076
$9_{4\ 6} \rightarrow 9_{3\ 7}$	3633.286	3633.294	-0.008
$8_{1\ 7} \rightarrow 8_{1\ 8}$	3854.758	3854.7617	-0.0037
$8_{2\ 7} \rightarrow 8_{1\ 8}$	3854.758	3854.7617	-0.0037
$8_{2\ 7} \rightarrow 8_{0\ 8}$	3854.758	3854.7617	-0.0037
$8_{1\ 7} \rightarrow 8_{0\ 8}$	3854.758	3854.7617	-0.0037
$9_{2\ 7} \rightarrow 9_{2\ 8}$	4036.171	4036.1663	0.0047
$9_{2\ 7} \rightarrow 9_{1\ 8}$	4036.171	4036.1663	0.0047
$9_{3\ 7} \rightarrow 9_{2\ 8}$	4036.171	4036.1663	0.0047
$9_{3\ 7} \rightarrow 9_{1\ 8}$	4036.171	4036.1663	0.0047
$4_{1\ 4} \rightarrow 3_{1\ 3}$	4563.344	4563.3476	-0.0036
$4_{0\ 4} \rightarrow 3_{0\ 3}$	4563.344	4563.3476	-0.0036
$4_{1\ 4} \rightarrow 3_{0\ 3}$	4563.344	4563.3476	-0.0036
$4_{0\ 4} \rightarrow 3_{1\ 3}$	4563.344	4563.3476	-0.0036
$11_{3\ 8} \rightarrow 11_{2\ 9}$	4846.081	4846.0673	0.0137
$11_{4\ 8} \rightarrow 11_{2\ 9}$	4846.081	4846.0673	0.0137
$11_{4\ 8} \rightarrow 11_{3\ 9}$	4846.081	4846.0673	0.0137
$11_{3\ 8} \rightarrow 11_{3\ 9}$	4846.081	4846.0673	0.0137
$10_{2\ 9} \rightarrow 10_{0\ 10}$	4851.852	4851.8523	-0.0003
$10_{1\ 9} \rightarrow 10_{1\ 10}$	4851.852	4851.8523	-0.0003
$10_{2\ 9} \rightarrow 10_{1\ 10}$	4851.853	4851.8523	0.0007
$10_{1\ 9} \rightarrow 10_{0\ 10}$	4851.853	4851.8523	0.0007
$15_{8\ 7} \rightarrow 15_{7\ 8}$	5453.187	5453.2169	-0.0299
$15_{8\ 7} \rightarrow 15_{8\ 8}$	5453.187	5453.1613	0.0257

$3_{2\,1} \rightarrow 2_{0\,2}$	5547.895	5547.9091	-0.0141
$3_{2\,1} \rightarrow 2_{1\,2}$	5547.895	5547.8781	0.0169
$5_{0\,5} \rightarrow 4_{0\,4}$	5637.945	5637.9384	0.0066
$5_{1\,5} \rightarrow 4_{1\,4}$	5637.946	5637.9384	0.0076
$5_{1\,5} \rightarrow 4_{0\,4}$	5637.946	5637.9384	0.0076
$5_{0\,5} \rightarrow 4_{1\,4}$	5637.946	5637.9384	0.0076
$12_{2\,10} \rightarrow 12_{2\,11}$	5702.84	5702.8446	-0.0046
$12_{3\,10} \rightarrow 12_{2\,11}$	5702.84	5702.8446	-0.0046
$12_{3\,10} \rightarrow 12_{1\,11}$	5702.84	5702.8446	-0.0046
$12_{2\,10} \rightarrow 12_{1\,11}$	5702.84	5702.8446	-0.0046
$15_{5\,10} \rightarrow 15_{4\,11}$	6921.781	6921.7818	-0.0008
$15_{6\,10} \rightarrow 15_{5\,11}$	6921.781	6921.7819	-0.0009
$15_{5\,10} \rightarrow 15_{5\,11}$	6921.781	6921.7818	-0.0008
$15_{6\,10} \rightarrow 15_{4\,11}$	6921.781	6921.7819	-0.0009
$6_{2\,5} \rightarrow 5_{1\,4}$	7227.689	7227.6937	-0.0047
$6_{1\,5} \rightarrow 5_{2\,4}$	7227.689	7227.6936	-0.0046
$6_{1\,5} \rightarrow 5_{1\,4}$	7227.689	7227.6937	-0.0047
$6_{2\,5} \rightarrow 5_{2\,4}$	7227.689	7227.6936	-0.0046

Table 5-10: Experimentally observed rotational transition and their assignments for 1FN···$(D_2O)_2$ complex.

Transitions	Observed (MHz)	Calculated (MHz)	Obs-Cal (MHz)
$3_{1\,3} \rightarrow 2_{1\,2}$	3393.166	3393.1348	0.0312
$3_{0\,3} \rightarrow 2_{1\,2}$	3393.169	3393.1994	-0.0304
$9_{2\,7} \rightarrow 9_{2\,8}$	3645.946	3645.9488	-0.0028
$9_{3\,7} \rightarrow 9_{2\,8}$	3645.95	3645.9488	0.0012
$9_{3\,7} \rightarrow 9_{1\,8}$	3645.95	3645.9488	0.0012
$9_{2\,7} \rightarrow 9_{1\,8}$	3645.95	3645.9488	0.0012
$13_{5\,9} \rightarrow 13_{3\,10}$	4618.573	4618.573	0
$13_{5\,9} \rightarrow 13_{4\,10}$	4618.573	4618.573	0
$13_{4\,9} \rightarrow 13_{4\,10}$	4618.573	4618.573	0
$13_{4\,9} \rightarrow 13_{3\,10}$	4618.573	4618.573	0
$11_{3\,9} \rightarrow 11_{2\,10}$	4620.679	4620.6798	-0.0008
$11_{2\,9} \rightarrow 11_{1\,10}$	4620.679	4620.6798	-0.0008

$11_{3\,9} \rightarrow 11_{1\,10}$	4620.68	4620.6798	0.0002
$11_{2\,9} \rightarrow 11_{2\,10}$	4620.681	4620.6798	0.0012
$4_{2\,2} \rightarrow 3_{2\,1}$	5335.491	5335.4915	-0.0005
$3_{2\,1} \rightarrow 2_{1\,2}$	5401.083	5401.0831	-0.0001
$4_{4\,0} \rightarrow 3_{3\,1}$	6467.58	6467.5804	-0.0004
$5_{3\,3} \rightarrow 4_{2\,2}$	6473.044	6473.0437	0.0003

Table 5-11: Experimentally observed rotational transition and their assignments for 1FN···$(H_2{}^{18}O)_2$ complex.

Transitions	Observed (MHz)	Calculated (MHz)	Obs-Cal (MHz)
$15_{7\,8} \rightarrow 15_{7\,9}$	4167.8040	4167.8045	-0.0005
$15_{8\,8} \rightarrow 15_{6\,9}$	4167.8040	4167.8055	-0.0015
$15_{8\,8} \rightarrow 15_{7\,9}$	4167.8060	4167.8056	0.0004
$15_{7\,8} \rightarrow 15_{6\,9}$	4167.8060	4167.8045	0.0015
$4_{1\,4} \rightarrow 3_{1\,3}$	4431.0140	4431.0375	-0.0235
$4_{0\,4} \rightarrow 3_{0\,3}$	4431.0180	4430.9955	0.0225
$4_{1\,4} \rightarrow 3_{0\,3}$	4431.0180	4430.9969	0.0211
$4_{0\,4} \rightarrow 3_{1\,3}$	4431.0180	4431.036	-0.0180
$4_{1\,3} \rightarrow 3_{2\,2}$	4920.1260	4920.1301	-0.0041
$17_{7\,10} \rightarrow 17_{7\,11}$	5151.7640	5151.7640	0.0000
$17_{8\,10} \rightarrow 17_{7\,11}$	5151.7640	5151.7640	0.0000
$17_{7\,10} \rightarrow 17_{6\,11}$	5151.7640	5151.7640	0.0000
$17_{8\,10} \rightarrow 17_{6\,11}$	5151.7640	5151.764	0.0000
$4_{3\,2} \rightarrow 3_{2\,1}$	5361.0940	5361.0931	0.0009
$4_{2\,2} \rightarrow 3_{3\,1}$	5453.1920	5453.1908	0.0012
$5_{2\,4} \rightarrow 4_{1\,3}$	5967.9740	5967.9807	-0.0067
$5_{1\,4} \rightarrow 4_{1\,3}$	5967.9740	5967.9673	0.0067
$15_{4\,12} \rightarrow 15_{2\,13}$	6138.1750	6138.1782	-0.0032
$15_{3\,12} \rightarrow 15_{3\,13}$	6138.1780	6138.1782	-0.0002
$15_{3\,12} \rightarrow 15_{2\,13}$	6138.1800	6138.1782	0.0018
$15_{4\,12} \rightarrow 15_{3\,13}$	6138.1800	6138.1782	0.0018

5.4 Discussions:

5.1.1. Structural Analysis:

The first insights into the molecular/complex structure can be obtained through the experimentally obtained inertial defect. The inertial defect can be calculated by the following formula:

$$\Delta = I_c - I_a - I_b$$

Where I_α (α= a, b, c) are the principal moments of inertia of the molecule, the molecule-fixed axes are chosen such that $I_a \leq I_b \leq I_c$. The inertial defect is assumed to be ideally zero for a planar molecule. However, the reported value of the 1FN monomer is -0.144 amu Å^2.[13,14] The small negative value observed in the 1FN monomer is due to the out of plane bending motion of the ring.

For the 1FN···H_2O complex, fitted rotational constants confirm the in-plane interaction of the H_2O molecule, and this interaction is accompanied by a secondary interaction in which the oxygen atom of the H_2O molecule accepts a weak hydrogen bond through the α-hydrogen of the ring containing fluorine atom. The inertial defect for the complex is -1.2997 μÅ^2, calculated from the experimentally obtained rotational constants. The inertial defects calculated for the 1FN···$D_2{}^{16}O$, 1FN···$D^{16}OH$, and 1FN···$H_2{}^{18}O$ are also small, and the values are -1.4902 amu Å^2, -1.3643 amu Å^2 and -1.2561 amu Å^2 respectively. The larger value for the complex in comparison to 1FN monomer results from the contribution of the non-bonded hydrogen atom to the out-of-plane mass. It is evident that the experimental inertial defects for all four isotopologues are small, indicating that all the heavy atoms are lying in the same plane and the complex has an effectively planar vibrationally averaged geometry. Also, interestingly, from the experimentally derived values of inertial defects, it is clear that the substitution of the hydrogen of the H_2O moiety produces little change in the inertial defect, which confirms that all four isotopologues lead to the same average structure. Expectedly, the 1FN···D_2O has a slightly larger inertial defect as D is out of plane, compared to the other isotopologues having H out of plane. For 1FN···$(H_2O)_2$ complex, the experimentally observed inertial defect is given in *Table 5-4* and it is expectedly very high (-338.551 amu Å^2) because in this case the water dimer is interacting from the top of the 1FN ring

system. And the same trend has been observed for other two isotopologues 1FN···$(D_2O)_2$, 1FN···$(H_2{}^{18}O)_2$ complexes also.

By employing the Kraitchman method,[38] it is possible to determine the coordinates of the atom, substituted by an isotope. In the case of a non-planar asymmetric top molecule, the substituted atom's coordinate (r_s) is described in the following manner:

$$|a| = \left[\frac{\Delta P_a}{\mu}(1+\frac{\Delta P_b}{I_a - I_b})(1+\frac{\Delta P_c}{I_a - I_c})\right]^{\frac{1}{2}}$$

$$|b| = \left[\frac{\Delta P_b}{\mu}\left(1+\frac{\Delta P_c}{I_b - I_c}\right)\left(1+\frac{\Delta P_x}{I_b - I_a}\right)\right]^{\frac{1}{2}}$$

$$|c| = \left[\frac{\Delta P_c}{\mu}\left(1+\frac{\Delta P_a}{I_c - I_a}\right)\left(1+\frac{\Delta P_b}{I_c - I_b}\right)\right]^{\frac{1}{2}}$$

Wherein, P_a, P_b, and P_c are the planar moments of inertia. It is important to note that the Kraitchman analysis is contingent upon the assumption that bond distances and angles remain constant following isotopic substitution. While this assumption generally holds true for heavier atoms, substituting hydrogen (H) with deuterium (D) can introduce significant deviations in the zero-point average positions. Consequently, the structural information obtained by substitution of H/D would have larger uncertainty. In the course of our analysis, we utilized the KRA program,[39] developed by Kisiel and available through the PROSPE website.[40]

We could only do the substitution analysis for monohydrate complex and not for dihydrate complex. As in case of dihydrate complex, the monosubstituted isotopologues were not observed. For the monohydrate complex, the 1FN···H_2O complex was taken as a parent isotopologue. *Figure 5-5* illustrates the atomic labelling within the 1FN···H_2O complex and provides an estimated representation of the principal axes. By considering 1FN···H_2O complex as the parent and 1FN···$H_2{}^{18}O$, 1FN···DOH as singly substituted isotopologues, the coordinates of atoms O_{20} and H_{19} were obtained. Detailed spatial coordinates, along with associated Costain errors,[41] and the coordinates calculated at B3LYP-D3/aug-cc-pVDZ level of theory are presented in *Table 5-12*. The c coordinate of O_{20} was observed to have imaginary value, indicating that this coordinate is of very small magnitude and can be regarded as approaching zero. It is noteworthy to mention that the Kraitchman approach does not offer the explicit signs of atomic coordinates,

which have been inferred from the outcomes of quantum chemical computations. The coordinates obtained from Kraitchman method are in very good agreement with the same calculated at B3LYP-D3/aug-cc-pVDZ level of theory, which supports the observed structure.

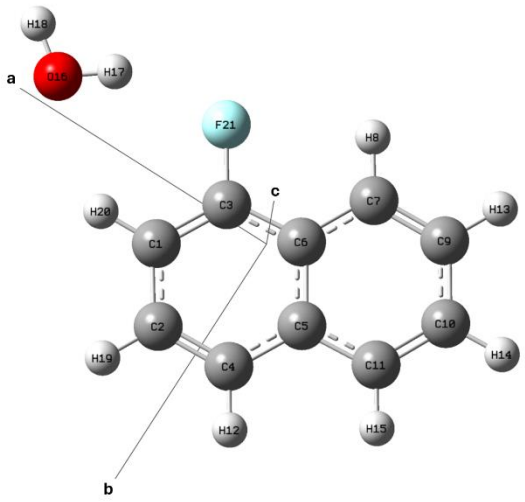

Figure 5-5: Labelling of the atoms used in the structural analysis for the 1FN···H_2O complex. The approximate location of the principal axes is shown.

Table 5-12: Kraitchman substitution co-ordinates (rs) for the substituted atoms of the 1FN···H_2O complex. The co-ordinates are given in Å. Labelling of the atoms is shown in Figure 5-5.

Atom Number	**Coordinates**			
	Method	**x**	**y**	**z**
H19	Theory (r_e)	3.7484	-1.0800	-0.0001
	Experiment (r_s)	3.6218(7)	-1.179(2)	-0.19(1)
O20	Theory (r_e)	4.5132	-0.4890	0.0000
	Experiment (r_s)	4.5573(4)	-0.484(5)	[0]

The four independent sets of rotational constants acquired from experiments were utilized to estimate the approximate position of H_2O with respect to the 1FN monomer. The internal coordinates were directly fitted to the moments of inertia in order to determine an r_0 structure for the 1FN···H_2O complex. This r_0 methodology is

incorporated within Kisiel's STRFIT program,[42] utilizing a non-linear least square fitting routine.

The complex's connectivity was assessed based on the labelling presented in *Figure 5-5*. The geometrical parameters of the monomer subunits, 1FN and water, were assumed to be equivalent to their values in the B3LYP-D3/aug-cc-pVDZ (r_e) geometry of the 1FN···H_2O complex. The experimentally determined rotational constants were utilized to fit the length of the intermolecular hydrogen bond, r(H_{19}···F_{16}), and angle defining the position and orientation of the water molecule, ∠(O_{20}-H_{19}···F_{16}) in the 1FN···H_2O complex. The fitted structural parameters are in excellent agreement with the outcomes of the DFT (B3LYP-D3/aug-cc-pVDZ) calculations. A comparative analysis of the fitted structural parameters with those calculated by DFT is presented in *Table 5-13*. The r_0 Cartesian coordinates (vibrationally averaged coordinates) and r_e cartesian coordinates (equilibrium coordinates) for the 1FN···H_2O complex can be found in the Supplementary Information in *Table 5-18* and *Table 5-19*, respectively.

Table 5-14 details the derived internal parameters of the 1FN···H_2O complex from fitting the r_0 structure. These parameters are not directly fitted but rather dependent on the fitted parameters in the r_0 Cartesian coordinates. The distances were calculated using the EVAL program,[43] available on the PROSPE website.[40] Notably, the distance between the interacting hydrogen of the 1FN ring and the oxygen atom of the H_2O moiety is measured at 2.419 Å, which is less than the sum of the van der Waals radii of H (1.2 Å) and O (1.4 Å).[44–46] This observed distance aligns closely with the predicted value based on hydrogen bond radii for a CH donor and O acceptor,[45] suggesting a strong indication of a secondary hydrogen bonding interaction within the complex.

Table 5-13: Fitted structural parameters for the 1FN···H_2O complex. Labelling of the atoms is shown in Figure 5.

Parameter	Method	Value
r(H_{19}···F_{16})	Theory (r_e)	2.09
	Experiment (r_o)	2.18(2)
∠(O_{20}-H_{19}···F_{16})	Theory (r_e)	149.5
	Experiment (r_o)	145(1)

Table 5-14: Derived parameters for the 1FN···H_2O complex. Labelling of the atoms is shown in Figure 5. These parameters should have uncertainties comparable to those reported in Table 13.

Parameter	Method	Value
r(O_{20}···H_{17})	Theory (r_e)	2.423
	Derived	2.419(8)
∠(C_8-H_{17}···O_{20})	Theory (r_e)	137.8
	Derived	139.5(8)

5.4.1 Atoms in Molecules (AIM) Analysis:

The purpose of the Atoms in Molecules (AIM)[27] analysis conducted in this study was to gain insight into the intermolecular interactions that exist within the 1FN···H_2O complex. In order to carry out the AIM calculations for this complex, the wavefunction was obtained using two different levels of theory, B3LYP-D3/aug-cc-pVDZ and MP2/aug-cc-pVDZ. The electron densities (ρ) and Laplacian ($\nabla^2\rho$) values obtained from both levels of theory were found to be consistent with each other, indicating the reliability of the results. The electron density and Laplacian values at the Bond Critical Points (BCPs) can be found in *Table 5-15*. *Figure 5-6* showcases the molecular graphs for the experimentally obtained structure A, allowing for a visual representation of the findings. In the structure A, two intermolecular bond critical points (BCPs) and three ring critical points (RCPs) were observed. The presence of these two bond critical points indicates the existence of two hydrogen bonds between the 1FN and H_2O moieties. The first bond critical point can be found between the fluorine atom and the hydroxyl hydrogen atom of the H_2O molecule i.e. O-H···F hydrogen bond. The second bond critical point is situated between the oxygen atom of the H_2O molecule and nearest hydrogen of the 1FN ring, that is, C-H···O hydrogen bond. Moreover, aside from the two-phenyl ring bound ring critical points, another ring critical point is observed, signifying the occurrence of a closed interaction resulting from the O-H···F and C-H···O hydrogen bonds. The electron density for the O···H-C hydrogen bond in the 1FN···H_2O complex falls within the range described by Koch and Popelier for the C-H···O hydrogen bonds.[47]. Similarly, the O-

H···F interactions also fall within the range of hydrogen bonded systems, providing further support for their existence. A thorough examination of the electron density at the bond critical point for the C-H···O interaction in the complexes PhAc···MeOH (***CHAPTER 3***) and PhAc···H_2O,[48] in comparison with the 1FN···H_2O complex, demonstrates that the strength of the hydrogen bond remains similar in all these complexes. Notably, the presence of a positive $\nabla^2\rho$ value indicates that the nature of the interaction can be characterized as a closed shell type.

The analysis using the Atoms in Molecules (AIM) method was conducted on the 1FN···$(H_2O)_2$ complex in order to gain a deeper understanding of the disparities observed in the optimized structures at both the B3LYP-D3/aug-cc-pVDZ and MP2/aug-cc-pVDZ levels of theory. As previously discussed, the rotational constants obtained for structure D at both levels of theory are significantly different from each other. Therefore, AIM can provide detailed structural insights based on the electron density topology.

Figure 5-7 illustrates the molecular graph at both levels of theory, highlighting the Bond Critical Points (BCPs) and Ring Critical Points (RCPs) for the 1FN···$(H_2O)_2$ complex. The observed BCPs indicate that the water dimer is slightly displaced in one of the calculated structures compared to the other. In both molecular graphs shown in *Figure 5-7*, four intermolecular BCPs have been identified. The electron density and Laplacian values at the BCPs are presented in *Table 5-16*. The difference lies in the bond path lengths between the two atoms involved. At the B3LYP-D3/aug-cc-pVDZ level of theory, two BCPs are present between O_{16} and H_8, and H_{24} and C_{10}. However, at the MP2/aug-cc-pVDZ level of theory, these BCPs are present between O_{16} and C_7, and H_{24} and C_{11}. These observations regarding bond path lengths confirm that the water dimer is slightly displaced over the 1FN ring system. This analysis represents only the preliminary stage of the investigation into the 1FN···$(H_2O)_2$ complex, and further analysis is needed.

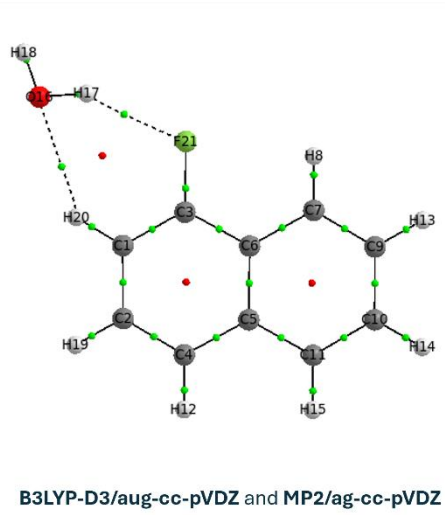

Figure 5-6: Atoms in Molecules (AIM) topology study for 1FN···H_2O complex. Bond critical points and ring critical points are shown in green and red dots respectively.

Table 5-15: Electron density (ρ) and the Laplacian of the electron density ($\nabla^2\rho$) of the 1FN···H_2O complex, calculated at B3LYP-D3/aug-cc-pVDZ and MP2/aug-cc-pVDZ level of theories.

Interactions	ρ (a.u)		$\nabla^2\rho$ (a.u)	
	B3LYP-D3/aug-cc-pVDZ	MP2/aug-cc-pVDZ	B3LYP-D3/aug-cc-pVDZ	MP2/aug-cc-pVDZ
O-H···F	0.015	0.014	+0.054	+0.055
C-H···O	0.009	0.010	+0.033	+0.036

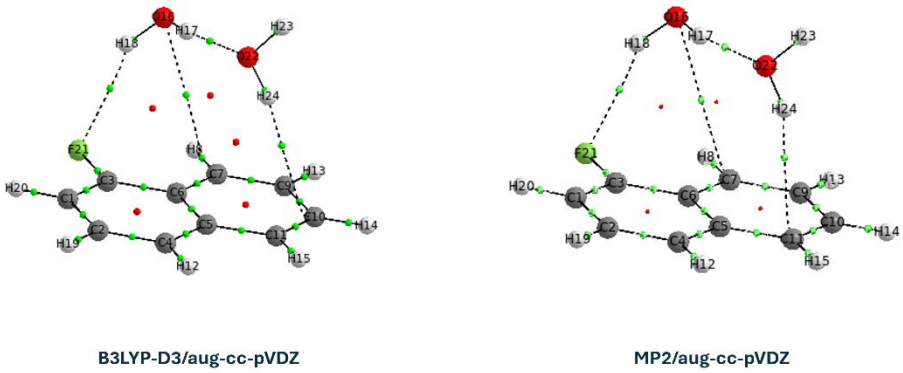

Figure 5-7: Bond critical points (green) and ring critical points (red) of the 1FN···$(H_2O)_2$ complexes.

Table 5-16: Electron density (ρ) and the Laplacian of the electron density ($\nabla^2\rho$) of the 1FN···$(H_2O)_2$ complex, calculated at B3LYP-D3/aug-cc-pVDZ and MP2/aug-cc-pVDZ level of theories.

Interactions	B3LYP-D3/aug-cc-pVDZ	
	ρ (a.u)	$\nabla^2\rho$ (a.u)
O_{16}-H_{18}···F_{21}	0.010	+0.036
C_7-H_8···O_{16}	0.006	+0.021
O_{22}-H_{24}···C_{10}	0.007	+0.019
O_{16}-H_{17}···O_{22}	0.024	+0.080

Interactions	MP2/aug-cc-pVDZ	
	ρ (a.u)	$\nabla^2\rho$ (a.u)
O_{16}-H_{18}···F_{21}	0.010	+0.037
H_8-C_7···O_{16}	0.006	+0.019
O_{22}-H_{24}···C_{11}	0.010	+0.031
O_{16}-H_{17}···O_{22}	0.023	+0.083

5.4.2 Natural Bond Orbital (NBO) Analysis:

The 1FN···H_2O complex was subjected to a natural bond orbital (NBO)[49] study using the NBO 6.0 program[31] at the B3LYP-D3/aug-cc-pVDZ optimization level. In order to assess intermolecular orbital interactions, we employed the second-order perturbation energy ($E^{(2)}$) as a quantitative measure of the strength of delocalization interactions. In the 1FN···H_2O system, the NBO analysis reveals three significant stabilization interactions. The first two interactions involve the delocalization between the lone pairs of the fluorine atom in 1FN and the σ* antibonding orbital of the OH group in H_2O, which is directed towards the 1FN ring. These interactions are denoted as $n_{1F}\rightarrow\sigma^*_{O\text{-}H}$ and $n_{2F}\rightarrow\sigma^*_{O\text{-}H}$ for the first and second lone pairs of the fluorine atom, respectively. One point to note here is that one of the lone pairs (n_1) of the fluorine atom which point in the direction of the H_2O moiety, exhibit more favourable $n_{1F}\rightarrow\sigma^*_{O\text{-}H}$ interaction and has the second order perturbation energy more (2.15 kJ/mol) than the other interaction, $n_{2F}\rightarrow\sigma^*_{O\text{-}H}$, which has less second order perturbation energy (0.43 kJ/mol). The other major interaction in the 1FN···H_2O complex is characterized by the interaction between the nearest hydrogen of the 1FN unit and the oxygen atom of the H_2O moiety, $n_O\rightarrow\sigma^*_{C\text{-}H}$, and for which the observed second order perturbation energy is 1.4 kJ/mol. The computed $E^{(2)}$ values for three mentioned interactions are provided in *Table 5-17*, and these results are visually represented in *Figure 5-8*.

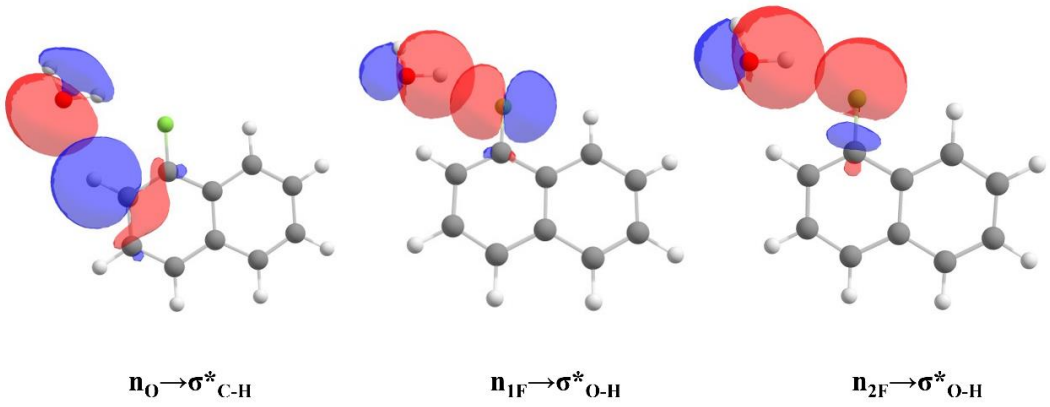

Figure 5-8: Interacting natural orbitals in 1FN···H_2O complex.

Table 5-17: Second order perturbation energies ($E^{(2)}$) for interacting orbitals shown in Figure 5, calculated at B3LYP-D3/aug-cc-pVDZ level of theory.

Interaction	$E^{(2)}$ (kJ/mol)
$\mathbf{n_{1F} \rightarrow \sigma^*_{O\text{-}H}}$	2.15
$\mathbf{n_{2F} \rightarrow \sigma^*_{O\text{-}H}}$	0.43
$\mathbf{n_{O} \rightarrow \sigma^*_{C\text{-}H}}$	1.40

5.4.3 Non-covalent Interactions (NCI) Index Analysis:

The validation of the interactions present in the 1FN···H_2O complex was also carried out using the non-covalent interactions (NCI) index analysis.[28,50–52] This was carried out using the Multiwfn 3.6 software[30] . The NCI plot, shown in *Figure 5-9*, has sign of $\lambda_2*\rho$ on the x-axis and the reduced density gradient (RDG) on the y-axis. Here, λ_2 and ρ represent the second Eigenvalue of the electron density Hessian matrix and the electron density, respectively. Reduced density gradient (s) is defined as:

$$s = \frac{1}{2(3\pi^2)^{1/3}} \frac{[\nabla\rho]}{\rho^{4/3}}$$

Sign of λ_2 can be negative or positive and these correspond to the BCP and RCP, respectively. These are usually interpreted as bonded and non-bonded interactions. For the 1FN···H_2O complex, it becomes evident that the O-H···F and C-H···O interactions play a significant role in stabilizing the complex, as can be seen from the NCI isosurfaces (left) and plots of RDG *vs* sign($\lambda_2*\rho$) (right) shown in *Figure 5-9*. The isosurfaces shown in the negative region of the plot corresponds to the O-H···F and C-H···O interactions. The results show that the sign($\lambda_2*\rho$) value for the O-H···F hydrogen bond is slightly more negative than that for the C-H···O hydrogen bond, thereby indicating that the O-H···F hydrogen bond is stronger than the C-H···O hydrogen bond.

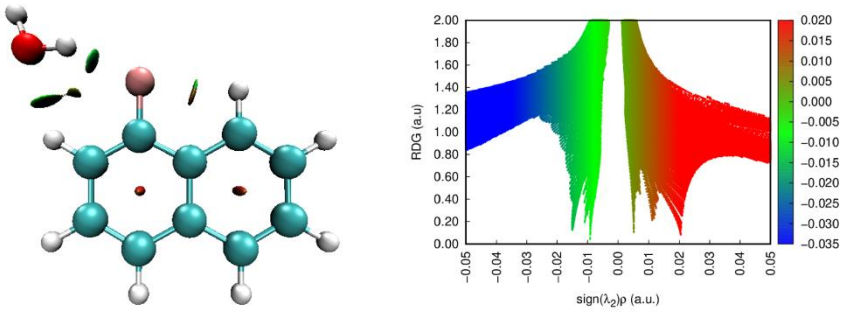

Figure 5-9: Non-covalent interactions (NCI) index plots for 1FN···H_2O complex.

5.4.4 Symmetry-Adapted Perturbation Theory (SAPT) Analysis:

Symmetry Adapted Perturbation Theory (SAPT)[32] has been specifically developed to study and quantify the intermolecular interactions occurring within molecular complexes. This approach effectively dissects the interaction energy into various components that possess significant physical meanings, such as electrostatic interactions, exchange-repulsion, polarization, and dispersion. Through this process of energy decomposition, one can estimate the relative contributions that different forces have in governing the attractions and repulsions between molecules.

We carried out SAPT analysis for the 1FN···H_2O complex, based on the optimized geometry at the MP2/aug-cc-pVDZ level of theory, employing the PSI4 software.[33] The SAPT 2+3 level was utilized to break down the overall interaction energy of the complex into its electrostatic, induction, dispersion, and exchange constituents. The results demonstrate that the electrostatics component plays a significant role in stabilizing the 1FN···H_2O complex, contributing approximately 38.8% of the total attractive interaction energies. Although the dispersion and induction components are smaller in magnitude compared to the electrostatics, their combined effect is comparable to that of the electrostatics, constituting 46.2% of the total attractive interaction energies. The bar chart of energy decomposition is shown in the *Figure 5-10*.

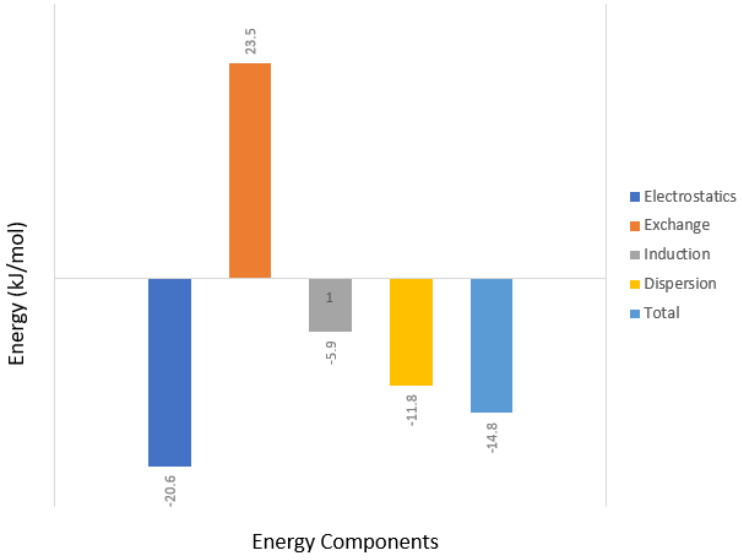

Figure 5-10: Bar charts depicting the energy decomposition using the SAPT-'2+3' calculations for the 1FN···H_2O complex calculated at MP2/aug-cc-pVDZ level of theory.

5.5 Conclusions:

The rotational spectra of four different isotopologues of the 1FN···H_2O complex have been reported. These isotopologues exhibit distinct rotational constants that are in accordance with the lowest energy structure A. In this particular structure, it is observed that H_2O serves as a proton donor, forming an O-H···F hydrogen bond. Additionally, H_2O also acts as a weak proton acceptor through a C-H···O hydrogen bond, which significantly contributes to the overall stability of the 1FN···H_2O structure. Quantum chemical calculations using *ab-initio* and Density Functional Theory (DFT) methods, specifically at MP2/aug-cc-pVDZ and B3LYP-D3/aug-cc-pVDZ levels, have confirmed that the experimentally observed geometry is indeed the most stable one. Furthermore, thorough analysis of the inertial defects for all four isotopologues has revealed that the heavy atoms of the complex are all situated in the same plane, indicating an effectively planar geometry. Remarkably, the AIM (Atoms in Molecules), NBO (Natural Bond Orbital), and NCI (Non-covalent Interaction) analyses have provided compelling evidence supporting the existence of O-H···F and C-H···O hydrogen bonds within the

1FN···H_2O complex. The SAPT analysis indicates that the electrostatic interaction plays a dominant role in stabilizing the complex.

The initial investigation of the 1FN···$(H_2O)_2$ complex indicates that the water dimer interacts with the 1FN plane from the top, by forming O-H···F and O-H···C hydrogen bonds, as well as a strong hydrogen bond between the two water molecules. The optimized structure at the B3LYP-D3/aug-cc-pVDZ and MP2/aug-cc-pVDZ levels of theory yielded distinct rotational constants. Consequently, AIM analysis was conducted, revealing a slight displacement of the water dimer in one of the calculated structures in comparison to the other. Further investigation of this dihydrate complex is needed to identify more isotopologues of the structure found and identify other conformers.

5.6 References:

(1) Gutowsky, H. S.; Emilsson, T.; Arunan, E. Low- *J* Rotational Spectra, Internal Rotation, and Structures of Several Benzene–Water Dimers. *The Journal of Chemical Physics* **1993**, *99* (7), 4883–4893. https://doi.org/10.1063/1.466038.

(2) Brendel, K.; Mäder, H.; Xu, Y.; Jäger, W. The Rotational Spectra of the Fluorobenzene···water and P-Difluorobenzene···water Dimers: Structure and Internal Dynamics. *Journal of Molecular Spectroscopy* **2011**, *268* (1–2), 47–52. https://doi.org/10.1016/j.jms.2011.03.032.

(3) Evangelisti, L.; Brendel, K.; Mäder, H.; Caminati, W.; Melandri, S. Rotational Spectroscopy Probes Water Flipping by Full Fluorination of Benzene. *Angewandte Chemie* **2017**, *129* (44), 13887–13891. https://doi.org/10.1002/ange.201707155.

(4) Mackenzie, R. B.; Dewberry, C. T.; Cornelius, R. D.; Smith, C. J.; Leopold, K. R. Multidimensional Large Amplitude Dynamics in the Pyridine–Water Complex. *J. Phys. Chem. A* **2017**, *121* (4), 855–860. https://doi.org/10.1021/acs.jpca.6b11255.

(5) Gou, Q.; Spada, L.; Vallejo-Lopez, M.; Melandri, S.; Lesarri, A.; Cocinero, E. J.; Caminati, W. Intermolecular Hydrogen Bonding in 2-Fluoropyridine-Water. *ChemistrySelect* **2016**, *1* (6), 1273–1277. https://doi.org/10.1002/slct.201600370.

(6) Calabrese, C.; Gou, Q.; Spada, L.; Maris, A.; Caminati, W.; Melandri, S. Effects of Fluorine Substitution on the Microsolvation of Aromatic Azines: The Microwave Spectrum of 3-Fluoropyridine-Water. *Journal of Physical Chemistry A* **2016**, *120* (27), 5163–5168. https://doi.org/10.1021/acs.jpca.6b00785.

(7) Calabrese, C.; Gou, Q.; Maris, A.; Caminati, W.; Melandri, S. Probing the Lone Pair···π-Hole Interaction in Perfluorinated Heteroaromatic Rings: The Rotational Spectrum of Pentafluoropyridine·Water. *J. Phys. Chem. Lett.* **2016**, *7* (8), 1513–1517. https://doi.org/10.1021/acs.jpclett.6b00473.

(8) Ulrich, N. W.; Seifert, N. A.; Dorris, R. E.; Peebles, R. A.; Pate, B. H.; Peebles, S. A. Benzene···acetylene: A Structural Investigation of the Prototypical CH···π Interaction. *Phys. Chem. Chem. Phys.* **2014**, *16* (19), 8886–8894. https://doi.org/10.1039/C4CP00845F.

(9) Ulrich, N. W.; Songer, T. S.; Peebles, R. A.; Peebles, S. A.; Seifert, N. A.; Pérez, C.; Pate, B. H. Effect of Aromatic Ring Fluorination on CH···π Interactions: Rotational

Spectrum and Structure of the Fluorobenzene···acetylene Weakly Bound Dimer. *Phys. Chem. Chem. Phys.* **2013**, *15* (41), 18148. https://doi.org/10.1039/c3cp53399a.

(10) Steber, A. L.; Pérez, C.; Temelso, B.; Shields, G. C.; Rijs, A. M.; Pate, B. H.; Kisiel, Z.; Schnell, M. Capturing the Elusive Water Trimer from the Stepwise Growth of Water on the Surface of the Polycyclic Aromatic Hydrocarbon Acenaphthene. *J. Phys. Chem. Lett.* **2017**, *8* (23), 5744–5750. https://doi.org/10.1021/acs.jpclett.7b02695.

(11) Loru, D.; Steber, A. L.; Pinacho, P.; Gruet, S.; Temelso, B.; Rijs, A. M.; Pérez, C.; Schnell, M. *How Does the Composition of a PAH Influence Its Microsolvation? A Rotational Spectroscopy Study of the Phenanthrene-Water and Phenanthridine-Water Clusters*; 2021.

(12) Baweja, S.; Panchagnula, S.; Sanz, M. E.; Evangelisti, L.; Pérez, C.; West, C.; Pate, B. H. Competition between In-Plane vs Above-Plane Configurations of Water with Aromatic Molecules: Non-Covalent Interactions in 1,4-Naphthoquinone-(H2O)1-3Complexes. *Journal of Physical Chemistry Letters* **2022**, *13* (40), 9510–9516. https://doi.org/10.1021/acs.jpclett.2c02618.

(13) Karlsson, H. Microwave Spectrum of 1-Fluoronaphthalene. *Acta Chem. Scand.* **1973**, *27*, 1435–1436. https://doi.org/10.3891/acta.chem.scand.27-1435.

(14) Carey, S. J.; Sun, M.; Kukolich, S. G. Microwave Spectra of 1-Fluoronaphthalene and 2-Fluoronaphthalene. *Journal of Molecular Spectroscopy* **2014**, *304*, 25–27. https://doi.org/10.1016/J.JMS.2014.08.004.

(15) Gaussian 09, Revision A.02, M. J. Frisch, G. W. Trucks, H. B. Schlegel, G. E. Scuseria, M. A. Robb, J. R. Cheeseman, G. Scalmani, V. Barone, G. A. Petersson, H. Nakatsuji, X. Li, M. Caricato, A. Marenich, J. Bloino, B. G. Janesko, R. Gomperts, B. Mennucci, H. P. Hratchian, J. V. Ortiz, A. F. Izmaylov, J. L. Sonnenberg, D. Williams-Young, F. Ding, F. Lipparini, F. Egidi, J. Goings, B. Peng, A. Petrone, T. Henderson, D. Ranasinghe, V. G. Zakrzewski, J. Gao, N. Rega, G. Zheng, W. Liang, M. Hada, M. Ehara, K. Toyota, R. Fukuda, J. Hasegawa, M. Ishida, T. Nakajima, Y. Honda, O. Kitao, H. Nakai, T. Vreven, K. Throssell, J. A. Montgomery, Jr., J. E. Peralta, F. Ogliaro, M. Bearpark, J. J. Heyd, E. Brothers, K. N. Kudin, V. N. Staroverov, T. Keith, R. Kobayashi, J. Normand, K. Raghavachari, A. Rendell, J. C. Burant, S. S. Iyengar, J. Tomasi, M. Cossi, J. M. Millam, M. Klene, C. Adamo, R. Cammi, J. W. Ochterski, R. L. Martin, K. Morokuma, O. Farkas, J. B. Foresman, and D. J. Fox, Gaussian, Inc., Wallingford CT, 2016.

(16) Miehlich, B.; Savin, A.; Stoll, H.; Preuss, H. Results Obtained with the Correlation Energy Density Functionals of Becke and Lee, Yang and Parr. *Chemical Physics Letters* **1989**, *157* (3), 200–206. https://doi.org/10.1016/0009-2614(89)87234-3.

(17) Vosko, S. H.; Wilk, L.; Nusair, M. Accurate Spin-Dependent Electron Liquid Correlation Energies for Local Spin Density Calculations: A Critical Analysis. *Can. J. Phys.* **1980**, *58* (8), 1200–1211. https://doi.org/10.1139/p80-159.

(18) Becke, A. D. Density-Functional Thermochemistry. I. The Effect of the Exchange-Only Gradient Correction. *The Journal of Chemical Physics* **1992**, *96* (3), 2155–2160. https://doi.org/10.1063/1.462066.

(19) Grimme, S.; Steinmetz, M. Effects of London Dispersion Correction in Density Functional Theory on the Structures of Organic Molecules in the Gas Phase. *Phys. Chem. Chem. Phys.* **2013**, *15* (38), 16031. https://doi.org/10.1039/c3cp52293h.

(20) Møller, Chr.; Plesset, M. S. Note on an Approximation Treatment for Many-Electron Systems. *Phys. Rev.* **1934**, *46* (7), 618–622. https://doi.org/10.1103/PhysRev.46.618.

(21) Binkley, J. S.; Pople, J. A. Møller-Plesset Theory for Atomic Ground State Energies: MØLLER-PLESSET THEORY FOR ATOMIC GROUND STATE ENERGIES. *Int. J. Quantum Chem.* **1975**, *9* (2), 229–236. https://doi.org/10.1002/qua.560090204.

(22) Weigend, F.; Ahlrichs, R. Balanced Basis Sets of Split Valence, Triple Zeta Valence and Quadruple Zeta Valence Quality for H to Rn: Design and Assessment of Accuracy. *Phys. Chem. Chem. Phys.* **2005**, *7* (18), 3297. https://doi.org/10.1039/b508541a.

(23) Schäfer, A.; Huber, C.; Ahlrichs, R. Fully Optimized Contracted Gaussian Basis Sets of Triple Zeta Valence Quality for Atoms Li to Kr. *The Journal of Chemical Physics* **1994**, *100* (8), 5829–5835. https://doi.org/10.1063/1.467146.

(24) Dunning, T. H. Gaussian Basis Sets for Use in Correlated Molecular Calculations. I. The Atoms Boron through Neon and Hydrogen. *The Journal of Chemical Physics* **1989**, *90* (2), 1007–1023. https://doi.org/10.1063/1.456153.

(25) Kendall, R. A.; Dunning, T. H.; Harrison, R. J. Electron Affinities of the First-Row Atoms Revisited. Systematic Basis Sets and Wave Functions. *The Journal of Chemical Physics* **1992**, *96* (9), 6796–6806. https://doi.org/10.1063/1.462569.

(26) Boys, S. F.; Bernardi, F. The Calculation of Small Molecular Interactions by the Differences of Separate Total Energies. Some Procedures with Reduced Errors. *Molecular Physics* **1970**, *19* (4), 553–566. https://doi.org/10.1080/00268977000101561.

(27) Bader, R. F. W. *Atoms in Molecules: A Quantum Theory*; The International series of monographs on chemistry; Clarendon Press ; Oxford University Press: Oxford [England] : New York, 1994.

(28) Contreras-García, J.; Johnson, E. R.; Keinan, S.; Chaudret, R.; Piquemal, J.-P.; Beratan, D. N.; Yang, W. NCIPLOT: A Program for Plotting Noncovalent Interaction Regions. *J. Chem. Theory Comput.* **2011**, *7* (3), 625–632. https://doi.org/10.1021/ct100641a.

(29) Weinhold, F.; Landis, C. R.; Glendening, E. D. What Is NBO Analysis and How Is It Useful? *International Reviews in Physical Chemistry* **2016**, *35* (3), 399–440. https://doi.org/10.1080/0144235X.2016.1192262.

(30) Lu, T.; Chen, F. Multiwfn: A Multifunctional Wavefunction Analyzer. *J. Comput. Chem.* **2012**, *33* (5), 580–592. https://doi.org/10.1002/jcc.22885.

(31) Glendening, E. D.; Landis, C. R.; Weinhold, F. *NBO 6.0* : Natural Bond Orbital Analysis Program. *J. Comput. Chem.* **2013**, *34* (16), 1429–1437. https://doi.org/10.1002/jcc.23266.

(32) Parker, T. M.; Burns, L. A.; Parrish, R. M.; Ryno, A. G.; Sherrill, C. D. Levels of Symmetry Adapted Perturbation Theory (SAPT). I. Efficiency and Performance for Interaction Energies. *The Journal of Chemical Physics* **2014**, *140* (9), 094106. https://doi.org/10.1063/1.4867135.

(33) Parrish, R. M.; Burns, L. A.; Smith, D. G. A.; Simmonett, A. C.; DePrince, A. E.; Hohenstein, E. G.; Bozkaya, U.; Sokolov, A. Yu.; Di Remigio, R.; Richard, R. M.; Gonthier, J. F.; James, A. M.; McAlexander, H. R.; Kumar, A.; Saitow, M.; Wang, X.; Pritchard, B. P.; Verma, P.; Schaefer, H. F.; Patkowski, K.; King, R. A.; Valeev, E. F.; Evangelista, F. A.; Turney, J. M.; Crawford, T. D.; Sherrill, C. D. Psi4 1.1: An Open-Source Electronic Structure Program Emphasizing Automation, Advanced Libraries, and Interoperability. *J. Chem. Theory Comput.* **2017**, *13* (7), 3185–3197. https://doi.org/10.1021/acs.jctc.7b00174.

(34) Loru, D.; Bermúdez, M. A.; Sanz, M. E. Structure of Fenchone by Broadband Rotational Spectroscopy. *The Journal of Chemical Physics* **2016**, *145* (7), 074311. https://doi.org/10.1063/1.4961018.

(35) Zaleski, D. P.; Stephens, S. L.; Walker, N. R. A Perspective on Chemistry in Transient Plasma from Broadband Rotational Spectroscopy. *Phys. Chem. Chem. Phys.* **2014**, *16* (46), 25221–25228. https://doi.org/10.1039/C4CP04108A.

(36) Watson, J. K. G. Determination of Centrifugal Distortion Coefficients of Asymmetric-Top Molecules. III. Sextic Coefficients. *The Journal of Chemical Physics* **1968**, *48* (10), 4517–4524. https://doi.org/10.1063/1.1668020.

(37) Western, C. M. PGOPHER: A Program for Simulating Rotational, Vibrational and Electronic Spectra. *Journal of Quantitative Spectroscopy and Radiative Transfer* **2017**, *186*, 221–242. https://doi.org/10.1016/j.jqsrt.2016.04.010.

(38) Kraitchman, J. Determination of Molecular Structure from Microwave Spectroscopic Data. *American Journal of Physics* **1953**, *21* (1), 17–24. https://doi.org/10.1119/1.1933338.

(39) *Structural Calculations*. http://info.ifpan.edu.pl/~kisiel/struct/struct.htm#kra (accessed 2023-08-30).

(40) *PROSPE - Programs for ROtational SPEctroscopy*. http://info.ifpan.edu.pl/~kisiel/prospe.htm#table_of_programs (accessed 2023-08-30).

(41) Costain, C. C. Determination of Molecular Structures from Ground State Rotational Constants. *The Journal of Chemical Physics* **1958**, *29* (4), 864–874. https://doi.org/10.1063/1.1744602.

(42) *STRucture FITting to rotational data (STRFIT)*. http://info.ifpan.edu.pl/~kisiel/struct/struct.htm#strfit (accessed 2023-08-30).

(43) *EVALuation of internals from Cartesians (EVAL)*. http://info.ifpan.edu.pl/~kisiel/struct/struct.htm#eval (accessed 2023-08-30).

(44) Raghavendra, B.; Mandal, P. K.; Arunan, E. Ab Initio and AIM Theoretical Analysis of Hydrogen-Bond Radius of HD (D = F, Cl, Br, CN, HO, HS and CCH) Donors and Some Acceptors. *Phys. Chem. Chem. Phys.* **2006**, *8* (45), 5276. https://doi.org/10.1039/b611033a.

(45) Mandal, P. K.; Arunan, E. Hydrogen Bond Radii for the Hydrogen Halides and van Der Waals Radius of Hydrogen. *The Journal of Chemical Physics* **2001**, *114* (9), 3880–3882. https://doi.org/10.1063/1.1343905.

(46) Batsanov, S. S. Van Der Waals Radii of Elements. *Inorganic Materials* **2001**, *37* (9), 871–885. https://doi.org/10.1023/A:1011625728803.

(47) Koch, U.; Popelier, P. L. A. Characterization of C-H-O Hydrogen Bonds on the Basis of the Charge Density. *J. Phys. Chem.* **1995**, *99* (24), 9747–9754. https://doi.org/10.1021/j100024a016.

(48) Goswami, M.; Arunan, E. Microwave Spectroscopic and Theoretical Studies on the phenylacetylene···H2O Complex: C-H···O and O-H···π Hydrogen Bonds as Equal Partners. *Physical Chemistry Chemical Physics* **2011**, *13* (31), 14153–14162. https://doi.org/10.1039/c1cp20690g.

(49) Reed, A. E.; Curtiss, L. A.; Weinhold, F. Intermolecular Interactions from a Natural Bond Orbital, Donor-Acceptor Viewpoint. *Chem. Rev.* **1988**, *88* (6), 899–926. https://doi.org/10.1021/cr00088a005.

(50) Johnson, E. R.; Keinan, S.; Mori-Sánchez, P.; Contreras-García, J.; Cohen, A. J.; Yang, W. Revealing Noncovalent Interactions. *J. Am. Chem. Soc.* **2010**, *132* (18), 6498–6506. https://doi.org/10.1021/ja100936w.

(51) Lane, J. R.; Contreras-García, J.; Piquemal, J.-P.; Miller, B. J.; Kjaergaard, H. G. Are Bond Critical Points Really Critical for Hydrogen Bonding? *J. Chem. Theory Comput.* **2013**, *9* (8), 3263–3266. https://doi.org/10.1021/ct400420r.

(52) Contreras-García, J.; Yang, W.; Johnson, E. R. Analysis of Hydrogen-Bond Interaction Potentials from the Electron Density: Integration of Noncovalent Interaction Regions. *J. Phys. Chem. A* **2011**, *115* (45), 12983–12990. https://doi.org/10.1021/jp204278k.

5.7 Supplementary Information:

Table 5-18: The cartesian co-ordinates (Å) of the 1FN···H_2O complex in the abc principal axes system of the complex derived from the fitting of the r_0 structure to the experimentally derived moments of inertia of all the isotopologues. Labelling of the atoms are shown in the Figure 5-4.

Atom	a	b	c
C_1	1.263	-0.870	-0.000
C_2	2.682	-0.762	-0.000
C_3	3.299	0.471	-0.000
C_4	2.525	1.661	-0.000
C_5	1.147	1.600	0.000
C_6	0.491	0.339	0.000
C_7	-0.919	0.199	0.000
C_8	-1.569	-1.008	0.000
C_9	-0.784	-2.191	-0.000
C_{10}	0.593	-2.127	0.000
H_{11}	1.188	-3.040	-0.000
H_{12}	3.277	-1.677	0.000
H_{13}	4.387	0.537	-0.000
H_{14}	3.027	2.630	0.000
F_{15}	0.549	2.509	0.000
H_{16}	-1.66	1.356	0.000
H_{17}	-2.657	-1.045	0.000
H_{18}	-1.289	-3.157	-0.000
H_{19}	-3.821	1.096	0.000
O_{20}	-4.550	0.461	0.000
H_{21}	-5.068	1.274	-0.002

Table 5-19: Equilibrium geometry coordinates (Å) of 1FN···H_2O complex for structure A in the abc principal axes system optimised at B3LYP-D3/aug-cc-pVDZ level of theory.

Atoms	a	b	c
C_1	1.567	1.021	0.000
C_2	0.775	2.200	0.000
C_3	0.923	-0.189	0.000
C_4	-0.602	2.128	0.000
C_5	-1.264	0.868	0.000
C_6	-0.485	-0.337	0.000
C_7	-1.135	-1.602	0.000

H_8	-0.531	-2.507	0.000
C_9	-2.512	-1.671	0.000
C_{10}	-3.292	-0.485	0.000
C_{11}	-2.683	0.752	0.000
H_{12}	-1.202	3.038	0.000
H_{13}	-3.008	-2.642	0.000
H_{14}	-4.380	-0.557	0.000
H_{15}	-3.283	1.663	0.000
O_{16}	4.513	-0.489	0.000
H_{17}	3.748	-1.080	0.000
H_{18}	5.284	-1.067	0.000
H_{19}	1.274	3.168	0.000
H_{20}	2.654	1.065	0.000
F_{21}	1.671	-1.342	0.000

Table 5-20: Equilibrium geometry coordinates (Å) of 1FN···H_2O complex for structure B in the abc principal axes system optimised at B3LYP-D3/aug-cc-pVDZ level of theory.

Atoms	a	b	c
C_1	-0.337	2.373	0.000
C_2	-1.750	2.243	0.001
C_3	0.425	1.234	-0.001
C_4	-2.339	0.997	0.001
C_5	-1.546	-0.185	0.000
C_6	-0.113	-0.077	0.000
C_7	0.688	-1.252	-0.001
H_8	1.773	-1.170	-0.001
C_9	0.086	-2.493	-0.001
C_{10}	-1.328	-2.612	0.000
C_{11}	-2.123	-1.485	0.000
H_{12}	-3.425	0.901	0.001
H_{13}	0.703	-3.392	-0.001
H_{14}	-1.785	-3.602	0.000
H_{15}	-3.210	-1.576	0.001
O_{16}	4.098	-0.533	0.002
H_{17}	5.024	-0.265	0.002
H_{18}	3.594	0.292	0.001
H_{19}	-2.364	3.143	0.001
H_{20}	0.147	3.348	0.000
F_{21}	1.791	1.367	-0.001

Table 5-21: Equilibrium geometry coordinates (Å) of 1FN···H_2O complex for structure C in the abc principal axes system optimised at B3LYP-D3/aug-cc-pVDZ level of theory.

Atoms	a	b	c
C_1	-2.409	-0.329	-0.040
C_2	-1.971	-1.671	-0.183
C_3	-1.480	0.678	-0.115
C_4	-0.639	-1.960	-0.396
C_5	0.326	-0.917	-0.472
C_6	-0.097	0.447	-0.324
C_7	0.861	1.496	-0.370
H_8	0.525	2.524	-0.250
C_9	2.197	1.203	-0.557
C_{10}	2.625	-0.142	-0.712
C_{11}	1.712	-1.174	-0.672
H_{12}	-0.310	-2.993	-0.507
H_{13}	2.931	2.009	-0.587
H_{14}	3.684	-0.356	-0.858
H_{15}	2.042	-2.207	-0.783
O_{16}	1.105	-0.297	2.767
H_{17}	1.499	0.255	2.079
H_{18}	0.473	-0.846	2.285
H_{19}	-2.704	-2.475	-0.123
H_{20}	-3.456	-0.086	0.129
F_{21}	-1.889	1.968	0.024

Table 5-22: Equilibrium geometry coordinates (Å) of 1FN···H_2O complex for structure A in the abc principal axes system optimised at MP2/aug-cc-pVDZ level of theory.

Atoms	a	b	c
C_1	1.585	1.014	0.000
C_2	0.797	2.201	0.000
C_3	0.928	-0.202	0.000
C_4	-0.593	2.138	0.000
C_5	-1.262	0.877	0.000
C_6	-0.485	-0.340	0.000
C_7	-1.140	-1.608	0.000
H_8	-0.540	-2.521	0.000
C_9	-2.530	-1.668	0.000
C_{10}	-3.307	-0.474	0.000
C_{11}	-2.685	0.771	0.000
H_{12}	-1.190	3.056	0.000
H_{13}	-3.031	-2.640	0.000

H_{14}	-4.399	-0.539	0.000
H_{15}	-3.283	1.689	0.000
O_{16}	4.500	-0.483	0.000
H_{17}	3.753	-1.099	0.000
H_{18}	5.282	-1.048	-0.001
H_{19}	1.302	3.171	0.000
H_{20}	2.677	1.047	0.000
F_{21}	1.672	-1.364	0.000

Table 5-23: Equilibrium geometry coordinates (Å) of 1FN···H_2O complex for structure B in the abc principal axes system optimised at MP2/aug-cc-pVDZ level of theory.

Atoms	a	b	c
C_1	-0.374	2.384	0.000
C_2	-1.789	2.230	0.000
C_3	0.415	1.248	0.000
C_4	-2.362	0.962	0.000
C_5	-1.542	-0.207	0.000
C_6	-0.104	-0.075	0.000
C_7	0.725	-1.237	0.000
H_8	1.813	-1.140	0.001
C_9	0.136	-2.498	0.000
C_{10}	-1.280	-2.643	0.000
C_{11}	-2.102	-1.520	0.000
H_{12}	-3.451	0.846	-0.001
H_{13}	0.772	-3.388	0.001
H_{14}	-1.724	-3.643	0.000
H_{15}	-3.191	-1.629	-0.001
O_{16}	4.063	-0.501	-0.001
H_{17}	4.996	-0.252	-0.002
H_{18}	3.587	0.341	-0.001
H_{19}	-2.423	3.121	-0.001
H_{20}	0.097	3.370	0.000
F_{21}	1.783	1.405	0.001

Table 5-24: Equilibrium geometry coordinates (Å) of 1FN···H_2O complex for structure C in the abc principal axes system optimised at MP2/aug-cc-pVDZ level of theory.

Atoms	a	b	c
C_1	2.257	-0.063	0.494
C_2	1.875	-1.403	0.792
C_3	1.267	0.866	0.226
C_4	0.532	-1.772	0.818
C_5	-0.488	-0.813	0.535

C_6	-0.119	0.548	0.225
C_7	-1.126	1.509	-0.086
H_8	-0.833	2.535	-0.321
C_9	-2.466	1.130	-0.089
C_{10}	-2.841	-0.209	0.219
C_{11}	-1.872	-1.160	0.526
H_{12}	0.245	-2.803	1.046
H_{13}	-3.237	1.867	-0.331
H_{14}	-3.898	-0.491	0.211
H_{15}	-2.160	-2.190	0.757
O_{16}	0.513	-1.213	-2.587
H_{17}	-0.199	-0.595	-2.369
H_{18}	0.866	-1.448	-1.716
H_{19}	2.651	-2.144	1.001
H_{20}	3.306	0.241	0.465
F_{21}	1.623	2.151	-0.067

Table 5-25: Normal modes of vibrations for Structure A, Structure B and Structure C of the 1FN···H_2O complex calculated at B3LYP-D3/aug-cc-pVDZ level of theory.

Modes (cm^{-1})	Structure A	Structure B	Structure C
1	28.0	22.4	23.5
2	72.6	67.9	32.9
3	107.2	101.0	108.4
4	120.4	110.7	119.0
5	145.5	145.0	145.6
6	181.5	178.2	182.7
7	267.3	214.3	206.3
8	267.6	266.8	220.7
9	286.5	274.6	267.7
10	328.5	284.1	273.7
11	429.6	433.7	426.6
12	471.5	469.2	468.8
13	475.4	473.8	475.1
14	489.3	488.3	481.7
15	535.7	535.5	535.6
16	574.0	575.1	574.4
17	583.6	584.6	583.0
18	651.0	652.7	641.1
19	716.1	715.9	718.5
20	750.7	750.3	746.6
21	792.6	787.6	787.4
22	28.0	22.4	23.5
23	72.6	67.9	32.9

24	107.2	101.0	108.4
25	120.4	110.7	119.0
26	145.5	145.0	145.6
27	181.5	178.2	182.7
28	267.3	214.3	206.3
29	267.6	266.8	220.7
30	286.5	274.6	267.7
31	328.5	284.1	273.7
32	429.6	433.7	426.6
33	471.5	469.2	468.8
34	475.4	473.8	475.1
35	489.3	488.3	481.7
36	535.7	535.5	535.6
37	574.0	575.1	574.4
38	583.6	584.6	583.0
39	651.0	652.7	641.1
40	716.1	715.9	718.5
41	750.7	750.3	746.6
42	792.6	787.6	787.4
43	28.0	22.4	23.5
44	72.6	67.9	32.9
45	107.2	101.0	108.4
46	120.4	110.7	119.0
47	145.5	145.0	145.6
48	181.5	178.2	182.7
49	267.3	214.3	206.3
50	267.6	266.8	220.7
51	286.5	274.6	267.7
52	328.5	284.1	273.7
53	429.6	433.7	426.6
54	471.5	469.2	468.8
55	475.4	473.8	475.1
56	489.3	488.3	481.7
57	535.7	535.5	535.6

Table 5-26: Normal modes of vibrations for Structure A, Structure B and Structure C of the 1FN···H_2O complex calculated at MP2/aug-cc-pVDZ level of theory.

Modes (cm^{-1})	Structure A	Structure B	Structure C
1	25.7	23.8	27.1
2	71.5	60.3	38.3
3	104.3	71.7	102.3
4	109.0	108.3	112.4
5	143.7	141.9	142.6

6	177.9	175.7	156.7
7	258.4	217.8	182.1
8	263.0	261.9	243.2
9	276.0	265.3	264.2
10	319.0	274.5	268.2
11	418.5	421.3	418.3
12	459.8	458.6	457.0
13	460.3	459.1	458.9
14	466.0	465.1	465.6
15	526.1	525.3	525.4
16	563.1	564.6	563.8
17	568.5	565.5	569.3
18	607.8	605.9	609.0
19	686.5	677.8	685.6
20	705.4	705.5	707.6
21	749.7	750.5	754.9
22	25.7	23.8	27.1
23	71.5	60.3	38.3
24	104.3	71.7	102.3
25	109.0	108.3	112.4
26	143.7	141.9	142.6
27	177.9	175.7	156.7
28	258.4	217.8	182.1
29	263.0	261.9	243.2
30	276.0	265.3	264.2
31	319.0	274.5	268.2
32	418.5	421.3	418.3
33	459.8	458.6	457.0
34	460.3	459.1	458.9
35	466.0	465.1	465.6
36	526.1	525.3	525.4
37	563.1	564.6	563.8
38	568.5	565.5	569.3
39	607.8	605.9	609.0
40	686.5	677.8	685.6
41	705.4	705.5	707.6
42	749.7	750.5	754.9
43	25.7	23.8	27.1
44	71.5	60.3	38.3
45	104.3	71.7	102.3
46	109.0	108.3	112.4
47	143.7	141.9	142.6
48	177.9	175.7	156.7
49	258.4	217.8	182.1
50	263.0	261.9	243.2
51	3208.4	3210.4	3210.3

52	3222.2	3221.8	3223.0
53	3223.2	3224.3	3224.0
54	3234.1	3238.2	3235.0
55	3240.7	3246.5	3240.3
56	3781.3	3789.0	3771.3
57	3921.3	3924.6	3891.6

Table 5-27: Equilibrium geometry coordinates (Å) of 1FN···$(H_2O)_2$ complex for structure A in the abc principal axes system optimised at MP2/aug-cc-pVDZ level of theory.

Atoms	**a**	**b**	**c**
C_1	1.190	0.949	-0.355
C_2	0.491	2.153	-0.049
C_3	0.461	-0.223	-0.406
C_4	-0.881	2.147	0.186
C_5	-1.622	0.928	0.128
C_6	-0.938	-0.306	-0.178
C_7	-1.665	-1.532	-0.241
H_8	-1.136	-2.459	-0.477
C_9	-3.037	-1.535	-0.006
C_{10}	-3.723	-0.325	0.297
C_{11}	-3.029	0.881	0.363
H_{12}	-1.408	3.077	0.419
H_{13}	-3.594	-2.476	-0.056
H_{14}	-4.802	-0.343	0.479
H_{15}	-3.557	1.812	0.595
O_{16}	3.497	-1.587	1.001
H_{17}	3.210	-1.533	1.922
H_{18}	2.674	-1.674	0.496
H_{19}	1.053	3.089	-0.001
H_{20}	2.269	0.948	-0.535
F_{21}	1.119	-1.406	-0.697
O_{22}	4.468	0.833	-0.142
H_{23}	5.347	0.739	-0.529
H_{24}	4.294	-0.027	0.286

Table 5-28: Equilibrium geometry coordinates (Å) of 1FN···$(H_2O)_2$ complex for structure B in the abc principal axes system optimised at MP2/aug-cc-pVDZ level of theory.

Atoms	**a**	**b**	**c**

C_1	-2.003	-1.755	-0.132
C_2	-2.978	-0.831	0.341
C_3	-0.746	-1.278	-0.455
C_4	-2.668	0.518	0.483
C_5	-1.367	1.005	0.152
C_6	-0.367	0.088	-0.345
C_7	0.936	0.560	-0.686
H_8	1.690	-0.130	-1.069
C_9	1.248	1.906	-0.514
C_{10}	0.272	2.819	-0.022
C_{11}	-1.009	2.379	0.299
H_{12}	-3.420	1.222	0.854
H_{13}	2.257	2.252	-0.754
H_{14}	0.532	3.874	0.105
H_{15}	-1.760	3.082	0.674
O_{16}	2.012	-1.514	1.547
H_{17}	1.392	-0.776	1.642
H_{18}	1.581	-2.075	0.884
H_{19}	-3.977	-1.196	0.597
H_{20}	-2.224	-2.819	-0.242
F_{21}	0.210	-2.168	-0.892
O_{22}	3.976	-0.122	-0.044
H_{23}	4.885	-0.365	0.169
H_{24}	3.433	-0.641	0.580

Table 5-29: Equilibrium geometry coordinates (Å) of 1FN···$(H_2O)_2$ complex for structure C in the abc principal axes system optimised at MP2/aug-cc-pVDZ level of theory.

Atoms	a	b	c
C_1	1.542	0.761	-1.204
C_2	0.906	2.012	-0.967
C_3	0.830	-0.398	-0.953
C_4	-0.403	2.069	-0.491
C_5	-1.131	0.868	-0.225
C_6	-0.502	-0.411	-0.459
C_7	-1.207	-1.618	-0.176
H_8	-0.718	-2.579	-0.356
C_9	-2.503	-1.559	0.327
C_{10}	-3.135	-0.304	0.559
C_{11}	-2.463	0.885	0.288
H_{12}	-0.885	3.035	-0.311
H_{13}	-3.043	-2.485	0.545
H_{14}	-4.155	-0.275	0.953

H_{15}	-2.949	1.850	0.466
O_{16}	3.335	-0.796	1.267
H_{17}	2.586	-0.293	1.634
H_{18}	2.923	-1.398	0.634
H_{19}	1.460	2.935	-1.156
H_{20}	2.576	0.698	-1.548
F_{21}	1.440	-1.608	-1.157
O_{22}	1.078	0.784	2.272
H_{23}	0.308	0.273	2.559
H_{24}	0.746	1.288	1.511

Table 5-30: Equilibrium geometry coordinates (Å) of 1FN···$(H_2O)_2$ complex for structure D in the abc principal axes system optimised at MP2/aug-cc-pVDZ level of theory.

Atoms	a	b	c
C_1	2.309	0.953	0.074
C_2	1.705	2.094	0.674
C_3	1.496	0.019	-0.541
C_4	0.325	2.264	0.646
C_5	-0.511	1.296	0.013
C_6	0.081	0.134	-0.606
C_7	-0.744	-0.847	-1.231
H_8	-0.284	-1.731	-1.678
C_9	-2.127	-0.686	-1.235
C_{10}	-2.726	0.452	-0.621
C_{11}	-1.933	1.425	-0.013
H_{12}	-0.135	3.140	1.114
H_{13}	-2.759	-1.444	-1.705
H_{14}	-3.814	0.564	-0.629
H_{15}	-2.394	2.299	0.459
O_{16}	0.584	-3.015	0.936
H_{17}	0.112	-2.264	1.339
H_{18}	1.327	-2.608	0.472
H_{19}	2.341	2.836	1.164
H_{20}	3.391	0.801	0.091
F_{21}	2.071	-1.086	-1.116
O_{22}	-1.100	-0.998	2.217
H_{23}	-1.801	-1.530	2.617
H_{24}	-1.559	-0.466	1.549

Table 5-31: Equilibrium geometry coordinates (Å) of 1FN···$(H_2O)_2$ complex for structure E in the abc principal axes system optimised at MP2/aug-cc-pVDZ level of theory.

Atoms	a	b	c
C_1	1.532	0.710	-1.183
C_2	0.911	1.975	-0.977
C_3	0.804	-0.433	-0.907
C_4	-0.399	2.060	-0.508
C_5	-1.145	0.875	-0.222
C_6	-0.532	-0.417	-0.424
C_7	-1.258	-1.607	-0.126
H_8	-0.780	-2.578	-0.278
C_9	-2.560	-1.520	0.356
C_{10}	-3.177	-0.252	0.556
C_{11}	-2.484	0.921	0.272
H_{12}	-0.870	3.036	-0.355
H_{13}	-3.115	-2.434	0.587
H_{14}	-4.201	-0.201	0.935
H_{15}	-2.957	1.896	0.426
O_{16}	3.463	-0.679	1.115
H_{17}	3.125	-1.448	0.638
H_{18}	2.662	-0.273	1.493
H_{19}	1.478	2.886	-1.188
H_{20}	2.568	0.625	-1.517
F_{21}	1.397	-1.655	-1.083
O_{22}	1.113	0.659	2.219
H_{23}	0.707	1.189	1.516
H_{24}	1.347	1.304	2.900

Table 5-32: Equilibrium geometry coordinates (Å) of 1FN···$(H_2O)_2$ complex for structure F in the abc principal axes system optimised at MP2/aug-cc-pVDZ level of theory.

Atoms	a	b	c
C_1	0.726	1.244	0.000
C_2	-0.197	2.329	0.000
C_3	0.218	-0.042	0.000
C_4	-1.570	2.103	0.000
C_5	-2.085	0.771	0.000
C_6	-1.170	-0.345	0.000
C_7	-1.670	-1.681	0.000
H_8	-0.966	-2.517	0.000

C_9	-3.044	-1.906	0.000
C_{10}	-3.957	-0.813	0.000
C_{11}	-3.486	0.497	0.000
H_{12}	-2.271	2.943	0.000
H_{13}	-3.426	-2.931	0.000
H_{14}	-5.034	-1.006	0.000
H_{15}	-4.188	1.338	0.000
O_{16}	3.795	0.235	-0.001
H_{17}	3.206	-0.531	-0.001
H_{18}	4.693	-0.138	0.000
H_{19}	0.189	3.352	0.000
H_{20}	1.808	1.401	0.000
F_{21}	1.092	-1.106	0.000
O_{22}	6.578	-0.627	0.000
H_{23}	7.044	-0.263	0.764
H_{24}	7.045	-0.259	-0.762

Table 5-33: Equilibrium geometry coordinates (Å) of 1FN···$(H_2O)_2$ complex for structure G in the abc principal axes system optimised at MP2/aug-cc-pVDZ level of theory.

Atoms	**a**	**b**	**c**
C_1	-1.236	-2.365	0.000
C_2	-2.637	-2.109	0.000
C_3	-0.366	-1.290	0.000
C_4	-3.117	-0.803	0.000
C_5	-2.214	0.304	0.000
C_6	-0.789	0.068	0.000
C_7	0.124	1.165	0.000
H_8	1.202	0.988	0.000
C_9	-0.373	2.466	0.000
C_{10}	-1.775	2.714	0.000
C_{11}	-2.676	1.654	0.000
H_{12}	-4.194	-0.609	0.000
H_{13}	0.326	3.307	0.000
H_{14}	-2.145	3.744	0.000
H_{15}	-3.755	1.842	0.000
O_{16}	3.370	0.295	0.000
H_{17}	4.321	0.094	0.000
H_{18}	2.932	-0.566	0.000
H_{19}	-3.333	-2.952	0.000
H_{20}	-0.838	-3.382	0.000
F_{21}	0.985	-1.543	0.000
O_{22}	6.266	-0.026	0.000

H_{23}	6.646	0.430	0.763
H_{24}	6.646	0.430	-0.763

Table 5-34: Equilibrium geometry coordinates (Å) of 1FN···$(H_2O)_2$ complex for structure H in the abc principal axes system optimised at MP2/aug-cc-pVDZ level of theory.

Atoms	a	b	c
C_1	1.826	-2.084	0.000
C_2	3.042	-1.343	-0.001
C_3	0.630	-1.391	0.001
C_4	3.026	0.048	-0.001
C_5	1.787	0.759	0.000
C_6	0.543	0.027	0.001
C_7	-0.699	0.727	0.001
H_8	-1.641	0.176	0.002
C_9	-0.711	2.118	0.001
C_{10}	0.510	2.852	0.000
C_{11}	1.732	2.186	-0.001
H_{12}	3.963	0.614	-0.002
H_{13}	-1.670	2.642	0.002
H_{14}	0.486	3.946	0.000
H_{15}	2.671	2.750	-0.001
O_{16}	-3.680	-1.833	-0.002
H_{17}	-3.721	-0.863	-0.001
H_{18}	-2.734	-2.034	-0.001
H_{19}	3.994	-1.881	-0.001
H_{20}	1.819	-3.177	0.000
F_{21}	-0.545	-2.104	0.002
O_{22}	-4.057	1.108	0.000
H_{23}	-4.627	1.280	0.762
H_{24}	-4.626	1.279	-0.763

Table 5-35: Equilibrium geometry coordinates (Å) of 1FN···$(H_2O)_2$ complex for structure A in the abc principal axes system optimised at B3LYP-D3/aug-cc-pVDZ level of theory.

Atoms	a	b	c
C_1	1.140	0.962	-0.245
C_2	0.412	2.159	-0.011
C_3	0.439	-0.213	-0.293
C_4	-0.956	2.136	0.159

C_5	-1.676	0.909	0.105
C_6	-0.964	-0.314	-0.129
C_7	-1.670	-1.547	-0.187
H_8	-1.117	-2.467	-0.368
C_9	-3.038	-1.567	-0.017
C_{10}	-3.753	-0.363	0.216
C_{11}	-3.087	0.844	0.275
H_{12}	-1.506	3.061	0.337
H_{13}	-3.578	-2.513	-0.062
H_{14}	-4.835	-0.397	0.348
H_{15}	-3.637	1.769	0.453
O_{16}	3.746	-1.634	0.724
H_{17}	3.614	-1.740	1.673
H_{18}	2.858	-1.676	0.337
H_{19}	0.957	3.102	0.032
H_{20}	2.222	0.979	-0.378
F_{21}	1.125	-1.390	-0.516
O_{22}	4.491	0.959	-0.134
H_{23}	5.290	0.957	-0.672
H_{24}	4.389	0.040	0.181

Table 5-36: Equilibrium geometry coordinates (Å) of 1FN···$(H_2O)_2$ complex for structure B in the abc principal axes system optimised at B3LYP-D3/aug-cc-pVDZ level of theory.

Atoms	**a**	**b**	**c**
C_1	1.992	-1.793	0.128
C_2	3.002	-0.892	-0.301
C_3	0.748	-1.292	0.409
C_4	2.731	0.453	-0.440
C_5	1.437	0.970	-0.150
C_6	0.405	0.079	0.300
C_7	-0.890	0.583	0.600
H_8	-1.668	-0.088	0.954
C_9	-1.164	1.924	0.434
C_{10}	-0.153	2.813	-0.013
C_{11}	1.116	2.349	-0.293
H_{12}	3.509	1.139	-0.776
H_{13}	-2.168	2.290	0.644
H_{14}	-0.384	3.872	-0.135
H_{15}	1.893	3.035	-0.633
O_{16}	-2.295	-1.584	-1.407
H_{17}	-1.683	-0.902	-1.714
H_{18}	-1.791	-2.063	-0.732

H_{19}	3.996	-1.279	-0.525
H_{20}	2.185	-2.859	0.233
F_{21}	-0.239	-2.161	0.804
O_{22}	-4.046	0.096	0.141
H_{23}	-4.983	-0.106	0.042
H_{24}	-3.585	-0.528	-0.451

Table 5-37: Equilibrium geometry coordinates (Å) of 1FN···$(H_2O)_2$ complex for structure C in the abc principal axes system optimised at B3LYP-D3/aug-cc-pVDZ level of theory.

Atoms	a	b	c
C_1	1.492	0.935	-1.136
C_2	0.828	2.136	-0.776
C_3	0.820	-0.251	-0.993
C_4	-0.464	2.111	-0.289
C_5	-1.159	0.877	-0.135
C_6	-0.503	-0.348	-0.494
C_7	-1.174	-1.589	-0.323
H_8	-0.662	-2.510	-0.597
C_9	-2.457	-1.616	0.186
C_{10}	-3.116	-0.410	0.539
C_{11}	-2.483	0.806	0.382
H_{12}	-0.968	3.038	-0.015
H_{13}	-2.970	-2.569	0.317
H_{14}	-4.130	-0.448	0.938
H_{15}	-2.990	1.732	0.655
O_{16}	3.406	-0.888	1.143
H_{17}	2.652	-0.487	1.610
H_{18}	3.007	-1.396	0.427
H_{19}	1.355	3.084	-0.884
H_{20}	2.520	0.935	-1.491
F_{21}	1.458	-1.414	-1.310
O_{22}	1.089	0.427	2.375
H_{23}	0.295	-0.122	2.354
H_{24}	0.898	1.142	1.752

Table 5-38: Equilibrium geometry coordinates (Å) of 1FN···$(H_2O)_2$ complex for structure D in the abc principal axes system optimised at B3LYP-D3/aug-cc-pVDZ level of theory.

Atoms	a	b	c

C_1	2.487	0.359	0.124
C_2	2.209	1.614	0.725
C_3	1.464	-0.314	-0.492
C_4	0.937	2.142	0.696
C_5	-0.126	1.442	0.059
C_6	0.136	0.176	-0.564
C_7	-0.917	-0.537	-1.199
H_8	-0.709	-1.507	-1.643
C_9	-2.194	-0.015	-1.212
C_{10}	-2.467	1.233	-0.592
C_{11}	-1.457	1.944	0.027
H_{12}	0.727	3.103	1.167
H_{13}	-3.001	-0.568	-1.691
H_{14}	-3.482	1.632	-0.609
H_{15}	-1.668	2.903	0.502
O_{16}	-0.329	-3.249	0.632
H_{17}	-0.607	-2.475	1.151
H_{18}	0.513	-2.995	0.238
H_{19}	3.018	2.155	1.217
H_{20}	3.485	-0.075	0.146
F_{21}	1.722	-1.528	-1.062
O_{22}	-1.412	-1.001	2.161
H_{23}	-2.203	-1.335	2.602
H_{24}	-1.737	-0.351	1.522

Table 5-39: Equilibrium geometry coordinates (Å) of 1FN···$(H_2O)_2$ complex for structure E in the abc principal axes system optimised at B3LYP-D3/aug-cc-pVDZ level of theory.

Atoms	a	b	c
C_1	1.447	0.633	-1.204
C_2	0.840	1.907	-1.050
C_3	0.721	-0.479	-0.864
C_4	-0.449	2.023	-0.567
C_5	-1.201	0.865	-0.217
C_6	-0.605	-0.431	-0.366
C_7	-1.339	-1.595	-0.010
H_8	-0.870	-2.571	-0.124
C_9	-2.625	-1.478	0.472
C_{10}	-3.226	-0.201	0.619
C_{11}	-2.531	0.942	0.284
H_{12}	-0.909	3.005	-0.454
H_{13}	-3.187	-2.372	0.745
H_{14}	-4.245	-0.127	1.001

H_{15}	-2.993	1.923	0.398
O_{16}	3.641	-0.691	0.872
H_{17}	3.183	-1.418	0.433
H_{18}	2.936	-0.217	1.347
H_{19}	1.409	2.798	-1.316
H_{20}	2.474	0.526	-1.543
F_{21}	1.304	-1.708	-0.982
O_{22}	1.498	0.809	2.169
H_{23}	1.067	1.332	1.479
H_{24}	1.764	1.446	2.843

Table 5-40: Equilibrium geometry coordinates (Å) of 1FN···$(H_2O)_2$ complex for structure F in the abc principal axes system optimised at B3LYP-D3/aug-cc-pVDZ level of theory.

Atoms	a	b	c
C_1	2.487	0.359	0.124
C_2	2.209	1.614	0.725
C_3	1.464	-0.314	-0.492
C_4	0.937	2.142	0.696
C_5	-0.126	1.442	0.059
C_6	0.136	0.176	-0.564
C_7	-0.917	-0.537	-1.199
H_8	-0.709	-1.507	-1.643
C_9	-2.194	-0.015	-1.212
C_{10}	-2.467	1.233	-0.592
C_{11}	-1.457	1.944	0.027
H_{12}	0.727	3.103	1.167
H_{13}	-3.001	-0.568	-1.691
H_{14}	-3.482	1.632	-0.609
H_{15}	-1.668	2.903	0.502
O_{16}	-0.329	-3.249	0.632
H_{17}	-0.607	-2.475	1.151
H_{18}	0.513	-2.995	0.238
H_{19}	3.018	2.155	1.217
H_{20}	3.485	-0.075	0.146
F_{21}	1.722	-1.528	-1.062
O_{22}	-1.412	-1.001	2.161
H_{23}	-2.203	-1.335	2.602
H_{24}	-1.737	-0.351	1.522

Table 5-41: Equilibrium geometry coordinates (Å) of 1FN···$(H_2O)_2$ complex for structure G in the abc principal axes system optimised at B3LYP-D3/aug-cc-pVDZ level of theory.

Atoms	a	b	c
C_1	1.239	-2.352	0.000
C_2	2.635	-2.098	0.001
C_3	0.377	-1.285	-0.001
C_4	3.112	-0.804	0.001
C_5	2.217	0.302	0.001
C_6	0.800	0.068	-0.001
C_7	-0.105	1.166	-0.001
H_8	-1.178	0.987	-0.002
C_9	0.386	2.456	-0.001
C_{10}	1.783	2.700	0.000
C_{11}	2.676	1.649	0.001
H_{12}	4.186	-0.613	0.002
H_{13}	-0.309	3.296	-0.002
H_{14}	2.151	3.727	0.000
H_{15}	3.751	1.836	0.002
O_{16}	-3.406	0.285	0.001
H_{17}	-4.356	0.083	0.001
H_{18}	-2.957	-0.569	0.002
H_{19}	3.327	-2.940	0.002
H_{20}	0.844	-3.366	0.000
F_{21}	-0.968	-1.537	-0.002
O_{22}	-6.295	-0.022	0.001
H_{23}	-6.645	0.448	-0.766
H_{24}	-6.646	0.449	0.767

Table 5-42: Equilibrium geometry coordinates (Å) of 1FN···$(H_2O)_2$ complex for structure H in the abc principal axes system optimised at B3LYP-D3/aug-cc-pVDZ level of theory.

Atoms	a	b	c
C_1	2.487	0.359	0.124
C_2	2.209	1.614	0.725
C_3	1.464	-0.314	-0.492
C_4	0.937	2.142	0.696
C_5	-0.126	1.442	0.059
C_6	0.136	0.176	-0.564
C_7	-0.917	-0.537	-1.199
H_8	-0.709	-1.507	-1.643

C_9	-2.194	-0.015	-1.212
C_{10}	-2.467	1.233	-0.592
C_{11}	-1.457	1.944	0.027
H_{12}	0.727	3.103	1.167
H_{13}	-3.001	-0.568	-1.691
H_{14}	-3.482	1.632	-0.609
H_{15}	-1.668	2.903	0.502
O_{16}	-0.329	-3.249	0.632
H_{17}	-0.607	-2.475	1.151
H_{18}	0.513	-2.995	0.238
H_{19}	3.018	2.155	1.217
H_{20}	3.485	-0.075	0.146
F_{21}	1.722	-1.528	-1.062
O_{22}	-1.412	-1.001	2.161
H_{23}	-2.203	-1.335	2.602
H_{24}	-1.737	-0.351	1.522

Table 5-43: Normal modes of vibrations for the structures A, B, C, D, E, F, G and H of the $(1FN\cdots H_2O)_2$ complex optimised at MP2/aug-cc-pVDZ level of theory.

Modes (cm^{-1})	Structure A	Structure B	Structure C	Structure D	Structure E	Structure F	Structure G	Structure H
1	29.9	32.2	35.1	40.6	32.9	22.9	21.0	24.4
2	41.2	43.2	54.0	50.3	52.0	37.9	32.7	42.4
3	97.6	83.1	87.2	89.9	84.4	66.6	63.8	75.5
4	116.0	118.3	103.9	94.5	97.7	76.1	71.3	86.1
5	148.1	145.7	135.3	145.0	142.7	83.0	86.7	106.8
6	154.4	155.4	146.9	146.2	147.7	143.7	143.3	140.0
7	181.7	177.7	168.3	159.7	168.3	150.5	144.3	155.2
8	191.6	184.3	180.7	177.6	176.6	175.6	171.3	175.2
9	205.2	189.7	208.5	189.1	195.4	179.4	176.0	187.0
10	254.1	241.4	250.0	217.4	219.0	208.1	202.6	227.6
11	266.8	264.5	265.3	264.1	265.2	263.7	262.5	261.8
12	274.6	266.9	273.2	265.7	270.5	272.5	263.3	263.6
13	363.2	321.6	336.9	304.7	283.8	318.4	280.2	265.5
14	417.8	419.5	403.3	417.1	395.7	419.1	403.9	418.2
15	455.4	451.3	421.1	433.7	417.9	424.0	423.4	421.7
16	461.4	456.3	457.3	455.8	456.3	460.9	458.5	458.5
17	464.2	457.8	457.9	457.9	458.1	460.9	459.3	460.9
18	480.2	464.6	465.4	464.9	465.2	466.2	464.9	465.9
19	526.0	525.2	524.9	525.1	524.9	526.2	525.4	525.0
20	563.1	562.5	563.4	562.5	563.4	563.4	564.5	563.9
21	565.9	566.7	568.0	565.4	567.7	569.3	566.4	564.0

22	605.2	598.5	605.3	590.9	604.5	609.3	607.5	590.4
23	677.5	687.9	641.9	603.1	617.6	652.6	646.4	608.4
24	704.5	691.3	686.2	689.7	685.0	687.2	677.0	684.0
25	714.0	705.1	706.7	706.2	706.9	706.0	705.7	707.3
26	748.7	752.3	754.9	754.6	752.0	749.7	751.2	754.8
27	788.8	789.4	789.7	789.8	789.7	790.6	789.0	788.5
28	799.1	792.5	797.8	791.2	794.5	797.0	791.6	795.1
29	843.6	857.6	848.9	850.3	845.3	844.7	858.1	855.4
30	865.0	864.2	866.0	866.3	865.9	866.1	865.1	864.7
31	915.7	878.9	884.9	883.2	883.0	914.8	879.9	882.9
32	933.5	930.7	943.1	937.0	940.6	932.5	924.0	925.1
33	939.0	946.0	952.0	947.5	948.5	940.1	936.4	938.3
34	949.9	962.9	954.0	958.0	951.4	945.4	967.3	956.3
35	1026.2	1025.9	1030.0	1028.4	1030.3	1027.9	1027.3	1026.1
36	1041.3	1044.0	1043.9	1043.3	1044.1	1042.2	1048.1	1042.9
37	1090.1	1081.9	1084.6	1084.1	1084.5	1091.3	1083.4	1082.6
38	1150.5	1152.0	1151.9	1151.2	1151.8	1150.4	1152.8	1149.3
39	1164.6	1163.2	1164.3	1164.1	1163.7	1163.8	1164.7	1159.6
40	1172.8	1168.4	1170.5	1170.3	1170.0	1175.3	1173.2	1166.8
41	1234.6	1230.9	1234.0	1233.6	1233.3	1236.6	1231.2	1231.6
42	1257.8	1256.7	1258.2	1261.1	1258.0	1258.3	1260.3	1253.7
43	1263.4	1260.3	1265.0	1263.2	1265.3	1266.3	1269.5	1261.3
44	1395.3	1394.6	1398.4	1397.8	1398.4	1397.5	1398.6	1392.9
45	1429.8	1429.4	1429.6	1430.7	1430.0	1429.6	1432.1	1429.1
46	1470.4	1467.4	1471.0	1470.2	1471.4	1471.7	1468.3	1468.2
47	1474.2	1473.2	1473.7	1473.9	1474.2	1474.3	1473.8	1473.2
48	1497.9	1499.7	1499.4	1499.7	1500.0	1497.5	1498.1	1497.6
49	1540.6	1540.8	1542.1	1541.7	1542.7	1542.5	1543.7	1541.5
50	1604.4	1604.4	1604.2	1604.6	1604.5	1605.6	1606.4	1605.4
51	1620.2	1619.7	1612.2	1618.8	1621.6	1620.3	1621.5	1621.0
52	1631.9	1631.6	1621.1	1621.6	1626.6	1622.8	1622.7	1627.9
53	1648.3	1650.9	1647.8	1646.6	1654.5	1647.0	1643.2	1650.1
54	1678.7	1676.7	1676.2	1677.4	1676.1	1677.7	1677.3	1678.1
55	3195.5	3195.7	3196.7	3195.4	3195.1	3194.2	3193.2	3194.3
56	3201.0	3201.6	3202.5	3203.0	3199.1	3199.5	3199.5	3200.8
57	3208.2	3215.5	3210.3	3211.2	3209.8	3207.4	3208.8	3213.5
58	3218.9	3222.4	3223.7	3223.3	3222.3	3221.2	3220.6	3221.7
59	3221.9	3230.1	3225.0	3223.9	3223.3	3221.6	3222.7	3228.3
60	3229.2	3238.0	3235.0	3238.9	3235.6	3233.5	3237.3	3238.4
61	3233.1	3246.9	3246.4	3243.4	3249.0	3237.7	3240.3	3261.0
62	3636.1	3641.3	3682.1	3676.8	3676.7	3701.4	3702.1	3729.9
63	3757.7	3763.8	3746.5	3748.1	3742.5	3796.0	3795.9	3785.2

64	3894.5	3874.5	3881.7	3885.5	3883.9	3875.8	3884.7	3885.9
65	3899.7	3891.6	3885.7	3888.3	3889.4	3925.9	3925.6	3915.0

Table 5-44: Normal modes of vibrations for the structures A, B, C, D, E, F, G and H of the $(1FN···H_2O)_2$ complex optimised at B3LYP-D3/aug-cc-pVDZ level of theory.

Modes (cm^{-1})	**Structure A**	**Structure B**	**Structure C**	**Structure D**	**Structure E**	**Structure F**	**Structure G**	**Structure H**
1	10.0	26.3	20.1	22.8	14.9	22.8	12.4	22.8
2	31.2	31.1	36.3	37.6	34.6	37.6	18.6	37.6
3	39.3	46.0	46.3	45.1	50.3	45.1	32.0	45.1
4	90.2	85.0	93.6	84.5	83.5	84.5	48.6	84.5
5	113.9	120.8	112.8	99.4	101.6	99.4	70.0	99.4
6	125.7	155.2	149.3	138.7	144.0	138.7	84.7	138.7
7	150.5	156.3	165.5	154.5	153.0	154.5	146.2	154.5
8	182.9	179.5	170.5	167.8	172.1	167.8	154.5	167.8
9	197.0	189.3	183.1	180.8	180.1	180.8	179.7	180.8
10	208.8	207.4	235.0	202.8	224.6	202.8	183.4	202.8
11	251.3	242.9	261.4	253.9	264.9	253.9	203.0	253.9
12	269.4	270.4	270.9	266.4	273.2	266.4	267.3	266.4
13	282.1	275.8	278.5	275.8	276.1	275.8	271.4	275.8
14	367.6	345.3	333.0	279.2	282.9	279.2	277.9	279.2
15	429.4	429.1	406.7	425.6	395.1	425.6	418.6	425.6
16	467.0	465.0	428.9	436.6	427.4	436.6	434.9	436.6
17	474.5	468.1	468.2	468.3	468.2	468.3	469.5	468.3
18	484.5	475.0	475.1	474.7	475.0	474.7	473.7	474.7
19	489.7	482.4	479.7	481.1	480.2	481.1	489.9	481.1
20	536.0	535.9	535.4	535.7	535.8	535.7	535.6	535.7
21	573.1	573.3	574.3	574.1	574.5	574.1	575.0	574.1
22	579.6	582.9	582.3	579.1	581.0	579.1	586.3	579.1
23	644.0	637.2	635.2	600.3	616.8	600.3	650.1	600.3
24	714.4	687.0	639.5	637.6	637.2	637.6	654.8	637.6
25	724.1	716.1	717.8	717.4	718.0	717.4	716.4	717.4
26	750.9	749.9	749.4	743.7	748.8	743.7	750.4	743.7
27	792.0	785.7	787.9	787.1	785.7	787.1	788.2	787.1
28	795.4	796.3	796.5	796.7	796.8	796.7	796.7	796.7
29	825.8	831.6	824.6	820.0	822.2	820.0	837.3	820.0
30	876.4	877.1	879.1	880.1	879.4	880.1	877.7	880.1
31	898.5	887.4	886.8	885.5	883.3	885.5	897.2	885.5

32	937.3	911.7	908.0	907.0	905.6	907.0	916.7	907.0
33	971.5	973.7	970.0	965.0	968.5	965.0	980.5	965.0
34	995.1	986.5	981.2	980.0	980.7	980.0	991.2	980.0
35	1003.3	1006.2	1000.8	995.2	1001.1	995.2	1025.6	995.2
36	1032.7	1031.7	1035.3	1034.4	1035.8	1034.4	1033.9	1034.4
37	1047.9	1051.8	1052.3	1052.7	1052.9	1052.7	1054.5	1052.7
38	1096.6	1086.9	1092.2	1090.6	1092.4	1090.6	1090.0	1090.6
39	1165.7	1166.9	1167.1	1166.5	1167.0	1166.5	1167.3	1166.5
40	1178.9	1180.9	1181.2	1183.5	1181.8	1183.5	1183.3	1183.5
41	1187.5	1184.2	1185.9	1185.3	1185.4	1185.3	1188.7	1185.3
42	1236.9	1234.7	1236.2	1236.9	1236.8	1236.9	1235.3	1236.9
43	1249.7	1239.7	1247.1	1244.4	1247.3	1244.4	1242.4	1244.4
44	1277.0	1279.4	1280.7	1283.5	1280.6	1283.5	1285.1	1283.5
45	1389.1	1385.2	1386.4	1385.2	1387.1	1385.2	1385.8	1385.2
46	1409.6	1410.3	1413.2	1411.5	1413.4	1411.5	1409.2	1411.5
47	1416.7	1416.6	1417.3	1419.5	1417.0	1419.5	1420.4	1419.5
48	1468.8	1466.8	1465.0	1468.0	1467.9	1468.0	1468.6	1468.0
49	1485.0	1482.1	1484.8	1483.8	1484.7	1483.8	1483.5	1483.8
50	1541.3	1541.0	1542.3	1541.6	1542.3	1541.6	1543.5	1541.6
51	1616.7	1616.8	1617.0	1617.7	1617.4	1617.7	1615.7	1617.7
52	1626.4	1632.6	1621.8	1624.4	1624.2	1624.4	1617.9	1624.4
53	1641.8	1641.9	1642.4	1641.2	1642.4	1641.2	1638.6	1641.2
54	1645.2	1647.3	1646.7	1647.4	1654.5	1647.4	1642.5	1647.4
55	1680.0	1677.4	1678.0	1678.3	1676.4	1678.3	1677.0	1678.3
56	3169.9	3170.4	3172.6	3171.2	3170.2	3171.2	3167.5	3171.2
57	3176.7	3176.9	3179.1	3177.6	3175.6	3177.6	3174.6	3177.6
58	3181.1	3188.5	3184.1	3185.1	3182.4	3185.1	3181.6	3185.1
59	3192.7	3195.0	3197.3	3195.5	3195.3	3195.5	3192.8	3195.5
60	3194.4	3205.7	3198.3	3196.9	3195.9	3196.9	3194.5	3196.9
61	3202.2	3211.0	3211.7	3211.7	3211.7	3211.7	3210.0	3211.7
62	3208.6	3232.7	3221.7	3225.6	3225.8	3225.6	3223.6	3225.6
63	3602.1	3621.0	3667.6	3665.2	3667.0	3665.2	3684.2	3665.2
64	3744.2	3769.2	3770.9	3774.2	3763.6	3774.2	3789.9	3774.2
65	3872.9	3861.2	3866.8	3865.4	3861.1	3865.4	3866.2	3865.4
66	3874.7	3874.5	3872.5	3882.9	3882.9	3882.9	3896.4	3882.9

CHAPTER 6

Ammonia@Crown Ether: Hydrogen Bonding, Inversion and Tunnelling

CHAPTER 6 | Ammonia@Crown Ether: Hydrogen Bonding, Inversion and Tunnelling |

6.1 Introduction:

Crown ethers are cyclic organic compounds comprising a ring with multiple ether groups. The most prevalent crown ethers are cyclic oligomers of ethylene oxide, wherein the repeating unit is the ethylene oxy (-CH_2-CH_2-O-) group. The initial discovery of crown ethers was made by Charles J. Pederson.[1–3] It was observed that these molecules possess the ability to encapsulate specific metallic atoms. A strong correlation exists between the stability of these complexes and the size of both the cation and the cavity of the crown ethers. Later, Donald J. Cram and Jean-Marie Lehn identified related molecules capable of encapsulating certain types of molecules that exert a significant influence on biological processes.[1,4,5] In recognition of their contributions to developing and utilising molecules exhibiting structure-specific interactions of high selectivity, the Nobel Prize in Chemistry was jointly awarded to Donald J. Cram, Jean Marie Lehn, and Charles J. Pederson in 1987.[1]

Crown ethers play a vital role in phase transfer catalysis and are considered fundamental building blocks in host-guest supramolecular systems. They possess the ability to accommodate a diverse range of guest species, characterised by variations in size, shape, and donor properties. Notably, a stable complex between a crown ether and a noble gas, specifically 15-crown-5 and XeO_3, has recently been reported.[6] Furthermore, an unexpectedly strong binding of Xe by the host-guest interaction between 18-crown-6 and XeO_3 has been found, with a binding energy of 36.4 kcal/mol, comparable to strong cation-π interactions.[7]

In 2019, a crystal structure resulting from the co-crystallization of 18-crown-6 and acetylene in liquid ammonia was reported.[8] *Figure 6-1* depicts this crystal structure. The 18-crown-6 molecule exhibits a threefold roto inversion symmetry, with the acetylene and ammonia molecules positioned along the threefold axis and an inversion centre generating the entire molecule. Within the crystal, the ammonia molecules are situated

above and below the crown ether plane, connected through intermolecular N-H···O hydrogen bonds.[8] The acetylene molecules, on the other hand, are linked by weak C-H···N interactions. This arrangement leads to the formation of one-dimensional strands aligned along the crystallography c-axis, packed in a hexagonal close packing arrangement.[8] Particularly intriguing about this crystal structure is the fact that ammonia molecules serve as hydrogen bond donors, which is a rare occurrence. Only two examples of ammonia acting as a hydrogen bond donor have been documented thus far, which include benzene···ammonia and ammonia dimer.[9,10] This crystal structure serves as an ideal demonstration of NH_3 forming hydrogen bonds, not only in the gas phase but also within the crystal lattice. In biological systems, N-H hydrogen bonds are commonly observed, albeit predominantly in the form of amides rather than amines. The structure of the acetylene···NH_3 complex closely resembles the crystal structure shown in *Figure 6-1*.[11,12] The inversion motion of ammonia has been extensively studied through microwave spectroscopy.[13–18] The effects of the confinement of the NH_3 inside the fullerenes (C50 and C60) on the NH_3 inversion have been studied, which suggests that the inversion barrier for the NH_3 inside C_{50} and C_{60} is found to be 1kJ/mol and 2.5 kJ/mol higher than that of the free ammonia.[19] The primary objective of this study is to investigate the impact of hydrogen bonding on the inversion motion of the NH_3 molecule in the NH3@CE complex.

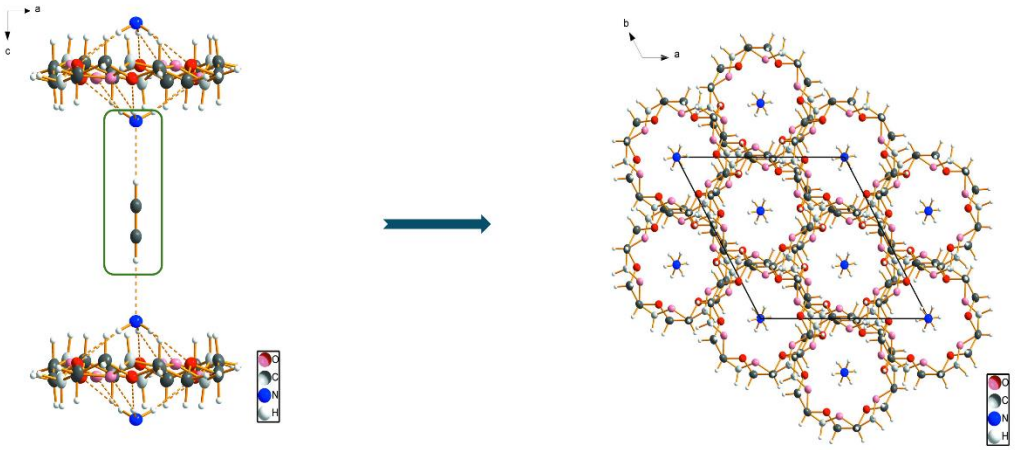

Figure 6-1: Crystal structure with a view along the crystallographic b-axis (left) and c-axis (right) showing the hydrogen bonding interactions.[8]

The solvation of the crown ether by ions is dependent on the size of the crown ether. It is well known that the size of the tunnelling phenomenon of alkali metal ions through crown ethers involves the ions passing through the crown ether ring, facilitated by the size compatibility between the ion and the crown ether, such as 18-crown-6, have a cavity that can encapsulate alkali metal ions like potassium (K^+) or sodium (Na^+). These complexes are stabilized by the electrostatic interactions with the oxygen atoms of the ether ring. Due to quantum tunnelling, even if there is a small energy barrier for the ion to pass through the crown ether structure, the ion can effectively tunnel through this barrier. The molecular mass of the NH_3 molecule is less than that of K^+ and Na^+ ions. Unlike alkali metal ions which interacts through electrostatics forces within the crown ether, NH_3 is a neutral molecule has a trigonal pyramidal shape and interacts primarily through three N-H···O hydrogen bonds with the crown ether. For NH_3 to tunnel through the 18-crown-6, the potential barrier created by the ring must be low enough, and the alignment must be perfect. Therefore, we aimed to explore whether neutral molecules like NH_3 can undergo tunnelling through the CE ring. Given the big size of the system under consideration, the resulting rotational constants are small (specifically, A=312.29 MHz, B=312.29 MHz, and C=164.51 MHz, at M06-2X/aug-cc-pVDZ level of theory). The CE is a solid at room temperature with very low vapour pressure. Therefore, the use of our spectrometer for experimental investigations is not viable at present. Hence, we employed a computational method for the investigation of the aforementioned system.

The primary objective of this study is to investigate the impact of hydrogen bonding on NH_3 inversion in the complex NH_3@18-crown-6 and to determine if inversion leads to a configurationally inverted crown in the complex. Additionally, we want to determine the barrier encountered by NH_3 during its tunnelling through the CE ring.

6.2 Computational Methods:

The optimisation of the geometry was performed using the Gaussian 09 software package.[20] We have utilised the Minnesota functional (M06-2X)[21,22] in this investigation with Dunning's augmented double-ζ aug-cc-pVDZ basis set.[23–26] Upon obtaining the optimised structures, harmonic frequency calculations were conducted to verify whether

the acquired structures corresponded to minima or saddle points on the potential energy hypersurface. Furthermore, the binding energies of the complexes were determined by employing the supermolecule approach. The basis set superposition error (BSSE) correction in the binding energies was conducted using Boys and Bernardi's counterpoise technique.[27] The Atoms in Molecules (AIM) analysis was performed to acquire insight into the nature of the interactions present.[28] A natural bond orbital (NBO) analysis was executed to evaluate intermolecular orbital interactions.[29,30] The wavefunctions employed in AIM and NBO calculations were obtained from the optimised structures computed at the M06-2X/aug-cc-pVDZ level of theory. 1D relaxed and 2D rigid potential energy scans were conducted using the Gaussian 09 software program.

6.3 Results and Discussion:

6.3.1 Optimised Structures:

The optimised configurations of the NH_3, CE, and NH_3@CE complexes are shown in *Figure 6-2*, while various hydrogen bond parameters, including bond lengths and angles, are provided in *Table 6-1*. It is important to emphasise that NH_3 exhibits a C_{3V} point group symmetry in the gas phase, whereas 18-crown-6 possesses D_{3d} symmetry. The optimised geometry of the NH_3@CE complex closely resembles the C_{3V} point group. This similarity arises from the fact that NH_3 has a C_{3V} point group and 18-crown-6 possesses a D_{3d} point group, and these two molecules are connected by three N-H···O hydrogen bonds. The binding energy for the NH_3@CE complex is 43.7 kJ/mol, and the BSSE corrected binding energy is 37.9 kJ/mol.

In the NH_3@CE complex, the hydrogen bonding parameters, such as all three H···O hydrogen bond distances, are measured at 2.176 Å, and the ∠N-H···O bond angles are found to be 178.1°. This N-H···O bond angle is close to linear, contributing to strong hydrogen bonding between NH_3 and CE. The H···O distance in the NH_3@CE complex is 0.544 Å shorter than the sum of the van der Waals radii of O and H atoms.[31]

Significantly, within the NH_3@CE complex, all three N-H bond distances are determined to be 1.020 Å, and the ∠H-N-H bond angles are measured at 104.2°. for comparison, in free NH_3 molecule, the N-H bond distances are 1.017 Å, and the ∠H-N-H bond angles are 106.7°. Examining the impact of hydrogen bonding on both molecules suggests that N-H covalent bonds in NH_3 of the CE@NH_3 complex experience a slight elongation (0.003 Å) relative to the unbound NH_3 molecule. In the case of CE in the complex, the C-O bonds exhibit a slight elongation (0.001 Å) compared to the isolated CE. Furthermore, the changes in covalent bond lengths and angles of both molecules and a notable decrease (2.5°) in ∠H-N-H bond angles of NH_3 mean the presence of a strong binding between the two.

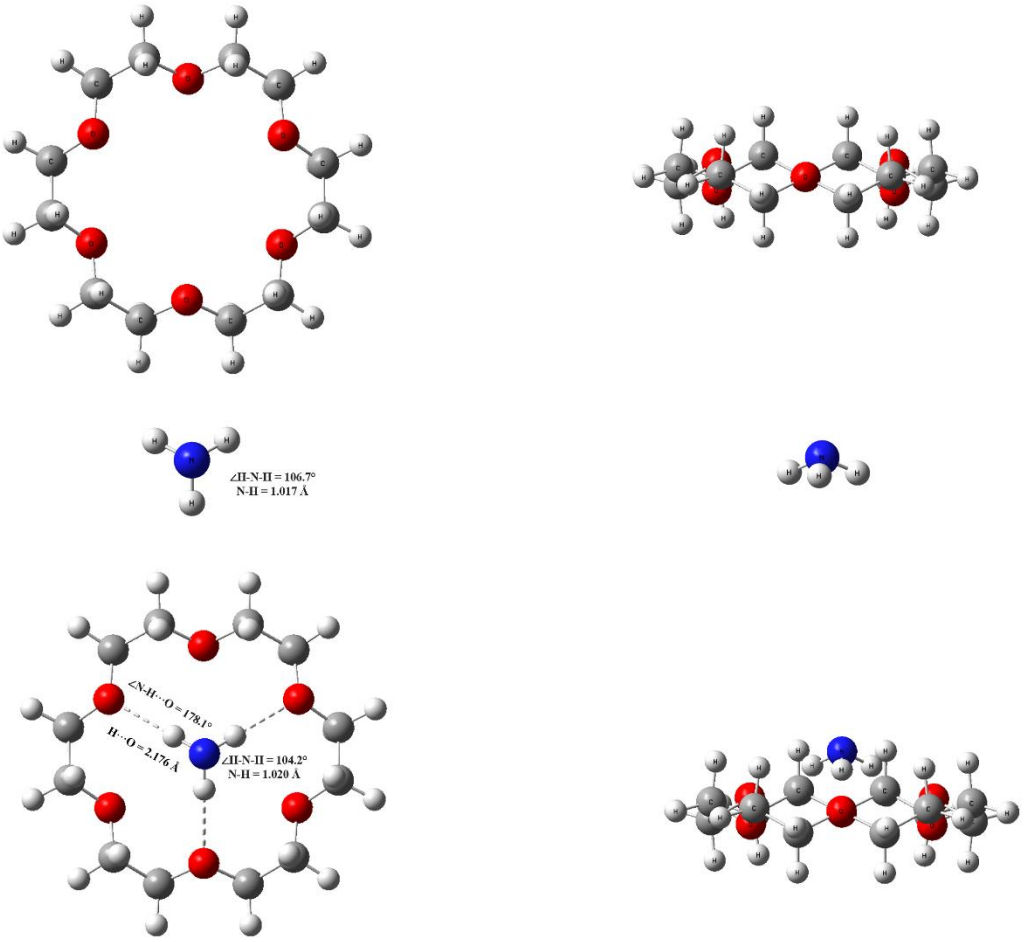

Figure 6-2: Optimised structures of NH_3, CE and NH_3@CE complex at the M06-2X/aug-cc-pVDZ level of theory. Left: Top view and Right: Side view.

Table 6-1: Hydrogen bond parameters: bond lengths (Å) and bond angles (°) calculated at M06-2X/aug-cc-pVDZ level of theory.

Complex	**Bond Length (Å)**			**Bond Angle (°)**	
	N-H	H···O	N···O	H-N-H	N-H···O
NH_3@CE	1.020	2.176	3.407	104.2	178.1
NH_3	1.017	---	---	106.7	---

6.3.2 Hydrogen Bonding in NH_3@18-crown-6 Complex:

The present study employed the Atoms in Molecules (AIM) analysis to gain a deeper understanding of the existence of hydrogen bonds within the NH_3@CE complex. The wave function utilised for the AIM calculation was obtained from the optimised structure at the M06-2X/aug-cc-pVDZ level of theory. In addition to the covalent bonds, the molecular graph depicted in *Figure 6-3* revealed the presence of six bond critical points (BCPs) and six ring critical points (RCPs) from intermolecular interactions. *Table 6-2* provides the electron densities (ρ) and Laplacian ($\nabla^2\rho$) values at the BCPs. The NH_3@CE complex exhibited two types of intermolecular BCPs. The first type of intermolecular bond was established between the hydrogen atoms of the NH_3 molecule and the oxygen atoms of the CE ring, which point towards the N-H bond of the NH_3 molecule. The second type of BCP was observed between the nitrogen atom and the oxygen atoms of the CE ring, pointing towards the nitrogen atom. While the occurrence of N-H···O hydrogen bonds was anticipated, the presence of N···O interactions was unexpected. These N···O interactions may be real interactions such as pnictogen bonds or chalcogen bonds,[32–34] or they could be artefacts. Furthermore, the presence of six RCPs indicated closed interactions resulting from the N-H···O and N···O interactions. The electron density topology associated with the N-H···O interactions in the NH_3@CE complex falls

within the range described by Koch and Popelier for C-H···O hydrogen bonds.[35] Notably, the values of ρ and $\nabla^2\rho$ are identical for all three N-H···O hydrogen bonds as well as for all three N···O interactions, providing evidence that the NH_3@CE complex possesses the C_{3V} point group.

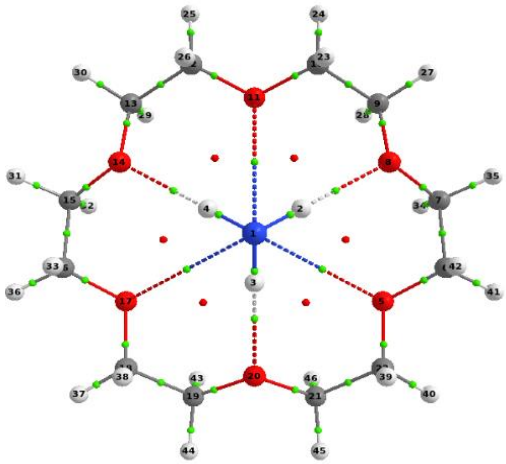

Figure 6-3: Atoms in Molecules (AIM) topology study in NH_3@CE complex. Bond and ring critical points are shown in green and red, respectively.

Table 6-2: Electron density (ρ) and the Laplacian of the electron density ($\nabla^2\rho$) of the NH_3@CE complex, calculated at M06-2X/aug-cc-pVDZ level of theory.

Properties	**N···O**	**H···O**
ρ (au)	0.0054	0.0157
$\nabla^2\rho$ (au)	+0.020	+0.0607

To assess intermolecular orbital interactions, the strength of the delocalisation interactions was quantitatively evaluated using the second-order perturbation energy ($E^{(2)}$). The natural bond orbital analysis was performed on the NH_3@CE complex to obtain the $E^{(2)}$ values. The NBO analysis revealed three strong N-H···O hydrogen bonding interactions, all of which involved delocalisation between the lone pairs of the three oxygen atoms and the σ* antibonding orbital of the N-H bonds.

Figure 6-4 illustrates the atom labelling scheme. *Table 6-3* provides the second-order perturbation energy values for the donor-acceptor interactions calculated at the M06-

2X/aug-cc-pVDZ level of theory, and these interactions are visually represented in *Figure 6-5*. It should be noted that the $E^{(2)}$ values are highest for the interactions in which the lone pairs of the oxygen atoms are directed towards the N-H bonds, with a delocalisation energy of 12.3 kJ/mol for all three N-H···O hydrogen bonds. On the other hand, the lone pairs that are perpendicular to the N-H···O bond directions exhibit a delocalisation energy of 2 kJ/mol. Therefore, the AIM and NBO analysis further confirms the presence of three hydrogen bonds within the NH_3@CE complex.

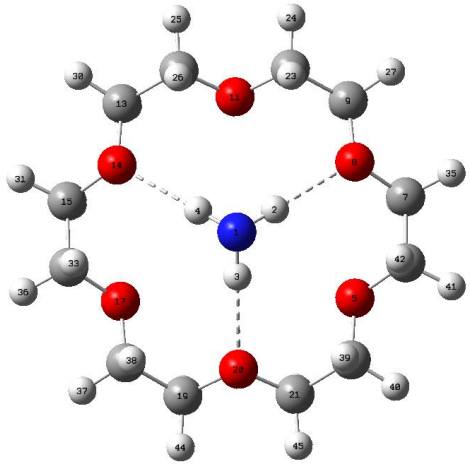

Figure 6-4: Labelling of the atoms is shown used in the structural analysis for the NH_3@CE complex.

Table 6-3: The second-order perturbation energies for the corresponding donor-acceptor interactions calculated at M06-2X/aug-cc-pVDZ level of theory.

Donor-acceptor delocalisation interaction	**E^2 (kJ/mol)**
	M06-2X/aug-cc-pvdz
$n1_{O8} \rightarrow \sigma^*_{N1\text{-}H2}$	12.3
$n1_{O14} \rightarrow \sigma^*_{N1\text{-}H4}$	12.3
$n1_{O20} \rightarrow \sigma^*_{N1\text{-}H3}$	12.3
$n2_{O8} \rightarrow \sigma^*_{N1\text{-}H2}$	2.00
$n2_{O14} \rightarrow \sigma^*_{N1\text{-}H4}$	2.00

$n2_{O20} \rightarrow \sigma^*_{N1\text{-}H3}$	2.00

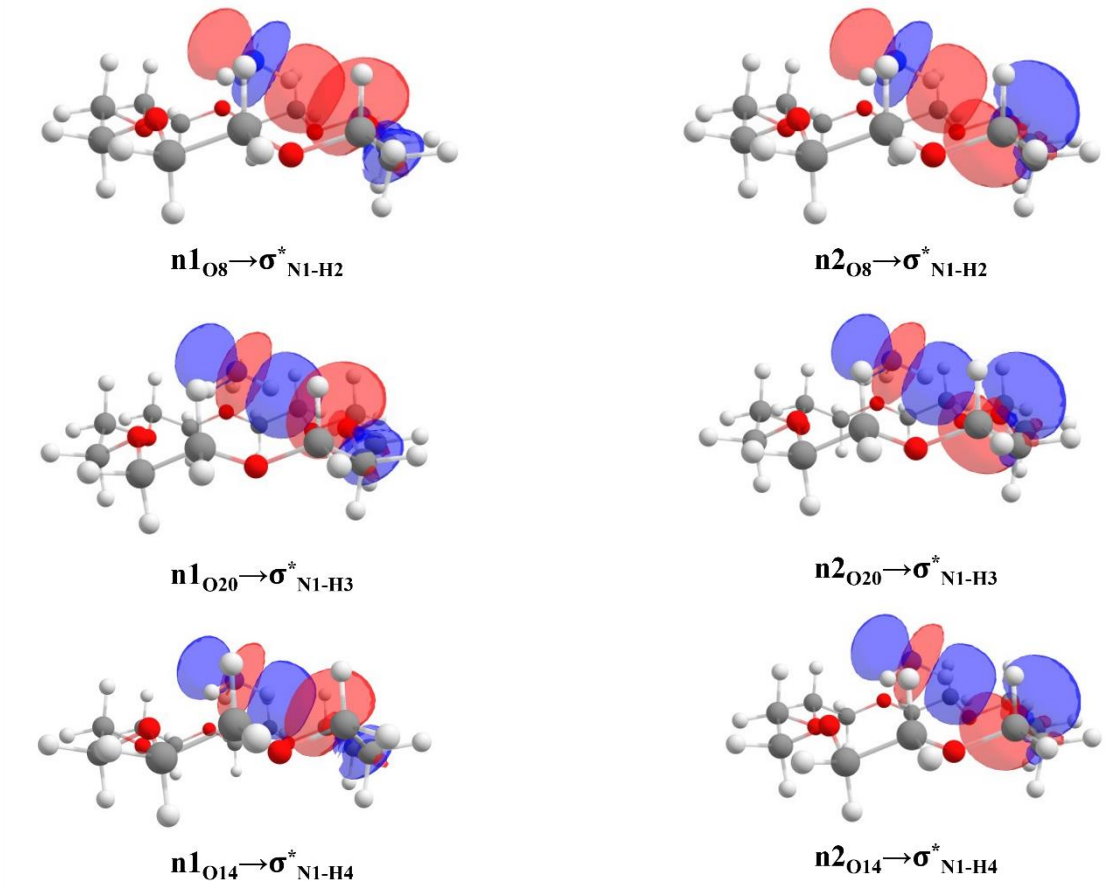

Figure 6-5: Interacting natural orbitals in NH_3@CE complex.

6.3.3 Normal modes of NH_3:

In the harmonic normal mode approach, the ammonia molecule displays two non-degenerate modes, specifically the symmetric stretch (ν_1) and the symmetric bending (ν_2), as well as two degenerate bending modes (ν_3 and ν_4). *Figure 6-6* illustrates the displacement vectors for all the aforementioned normal modes of the NH_3 molecule. The degenerate modes correspond to two components denoted as ν_{3a} and ν_{3b} or ν_{4a} and ν_{4b} in *Figure 6-6*, which vibrate at the same frequencies. The ν_2 normal mode, also known as

the inversion motion or umbrella motion of the NH_3 molecule, has been the focus of significant attention in numerous theoretical studies.[13,14,17,18] This v_2 normal mode involves the three hydrogen atoms tunnelling from one side of the N atom to the other side. The umbrella motion of the NH_3 molecule is shown in *Figure 6-7*. In this figure, the NH_3 molecule possesses two equivalent equilibrium configurations, with the plane σ_h perpendicular to the C_3 axis (the z-axis).

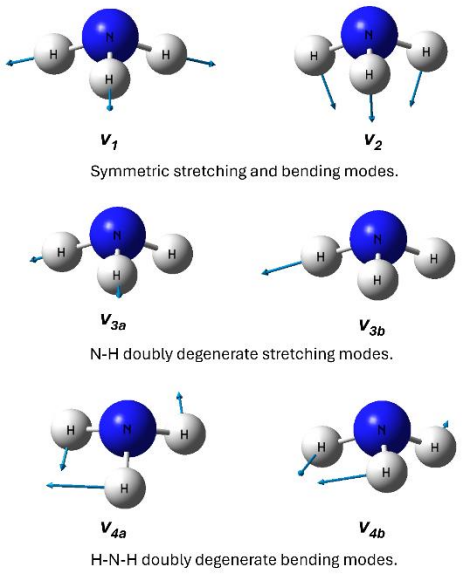

Figure 6-6: The vibrational modes of NH_3 molecule.

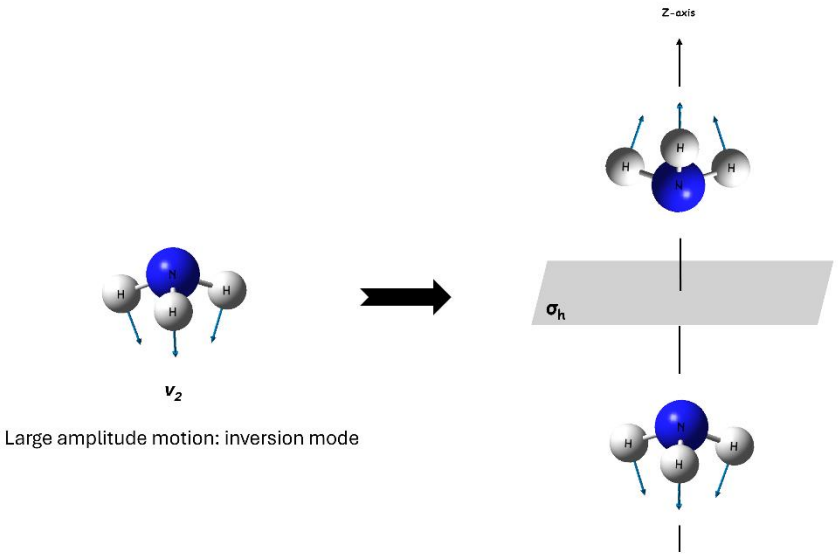

Figure 6-7: Umbrella motion of NH_3 molecule.

6.3.4 Inversion Motion of NH_3:

The inversion of ammonia, a phenomenon where hydrogen atoms move from one side of the nitrogen atom to the other, has been extensively researched by various scientists. In the microwave region, the ground state and first excited state splitting in ammonia, as well as its various deuterated species, have been accurately determined.[17,36–39] The experimental inversion barrier height was determined to be 2020±12 cm^{-1} (24.2±0.1 kJ/mol).[18] To evaluate the efficacy of the employed functional and basis set, we conducted a potential energy scan of the inversion motion of the ammonia molecule at the M06-2X/aug-cc-pVDZ level of theory. The potential energy scan for NH_3 inversion is depicted in *Figure 6-8*, and the barrier height was assessed to be 22.2 kJ/mol. In comparison with the experimentally obtained barrier height, it can be concluded that the selected method is performing satisfactorily.

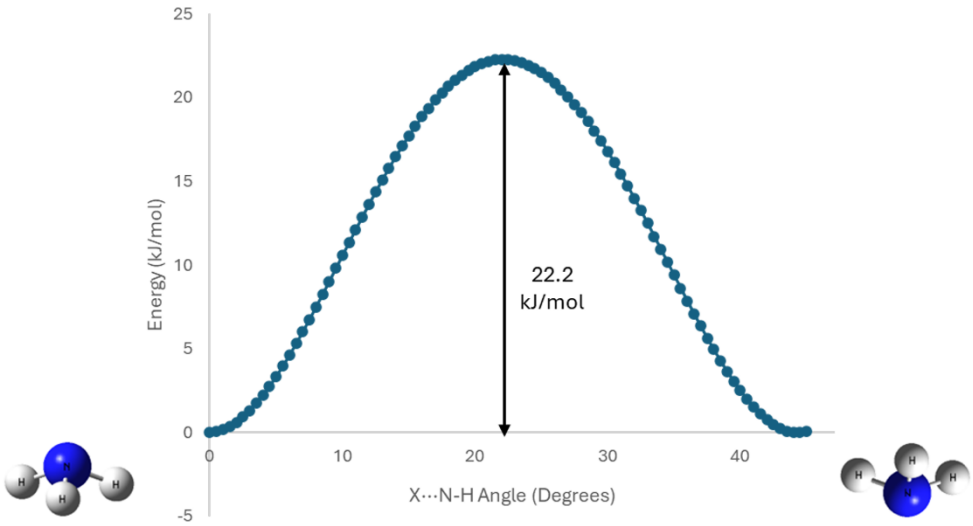

Figure 6-8: Potential energy scan for NH_3 inversion in free NH_3. In the angle, X denotes the position of the dummy atom.

Subsequently, we performed a potential energy scan for the ammonia molecule when it was associated with the CE ring via three hydrogen bonds. In this case, ammonia was not free, and the barrier height for the inversion motion was approximately 51.5 kJ/mol, which is approximately equivalent to three hydrogen bonding energies. This increase in the barrier height was thus expected. The potential energy scan for NH_3 inversion in the NH_3@CE complex is presented in *Figure 6-9*. *Figure 6-9* also displays the starting equilibrium geometry, transition state, and the minimum structure achieved after NH_3 inverts in the NH_3@CE complex. When NH_3 is inverted, the nitrogen atom faces towards the oxygen atoms, and therefore, this structure was not anticipated to be a minimum. However, during the 1D relaxed scan, we did observe a minimum, which was somewhat surprising.

The harmonic frequency calculation was carried out for the transition state and the observed minimum structure. It was determined that the transition state possesses a single imaginary frequency, wherein the motion corresponds to the inversion motion of the ammonia molecule. Additionally, the harmonic frequency calculation for the second minimum structure (with inverted NH_3) also yielded one imaginary frequency. Hence, it can be concluded that this structure is not a true minimum but rather a first-order saddle point. Notably, the motion associated with this imaginary frequency resembles a

dissociation coordinate. *Figure 6-10* illustrates the displacement vectors linked to the transition state and the first-order saddle point.

Subsequently, a potential energy scan was conducted to investigate the dissociation of NH_3 from the CE in the NH_3@CE complex. It is important to determine whether the dissociation energy exceeds or falls below the inversion barrier. If the dissociation energy exceeds the inversion barrier, the inversion could potentially facilitate the dissociation process. *Figure 6-11* depicts the potential energy scan conducted for the dissociation of NH_3 from the NH_3@CE complex. It was observed that the dissociation energy is lower than the height of the inversion barrier. Hence, it can be inferred that the inversion does not contribute to the dissociation process.

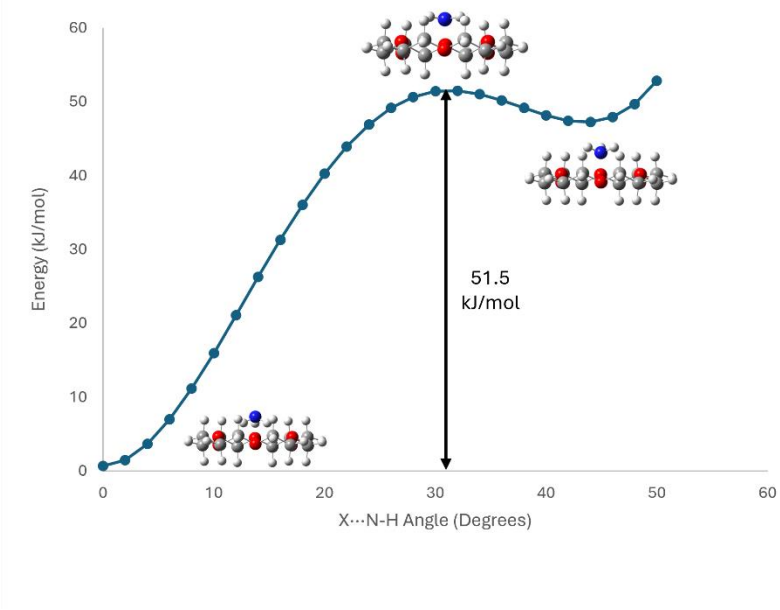

Figure 6-9: Potential energy scan for NH_3 inversion in NH_3@CE. In the angle, X denotes the centre of the CE.

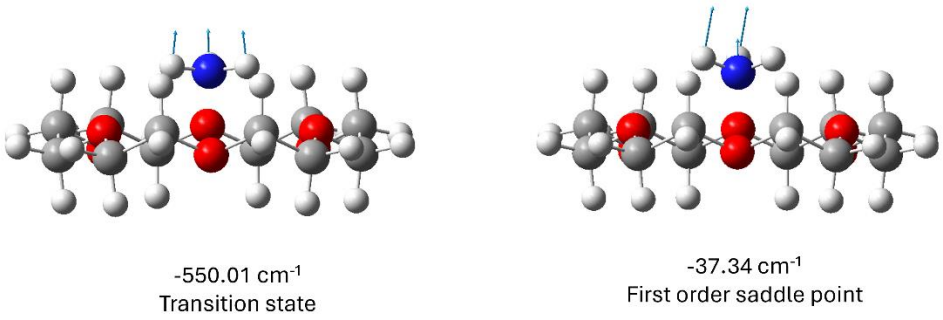

Figure 6-10: Displacements for the transition state (left) and first-order saddle point (right) obtained in the potential energy scan for NH_3 inversion in NH_3@CE.

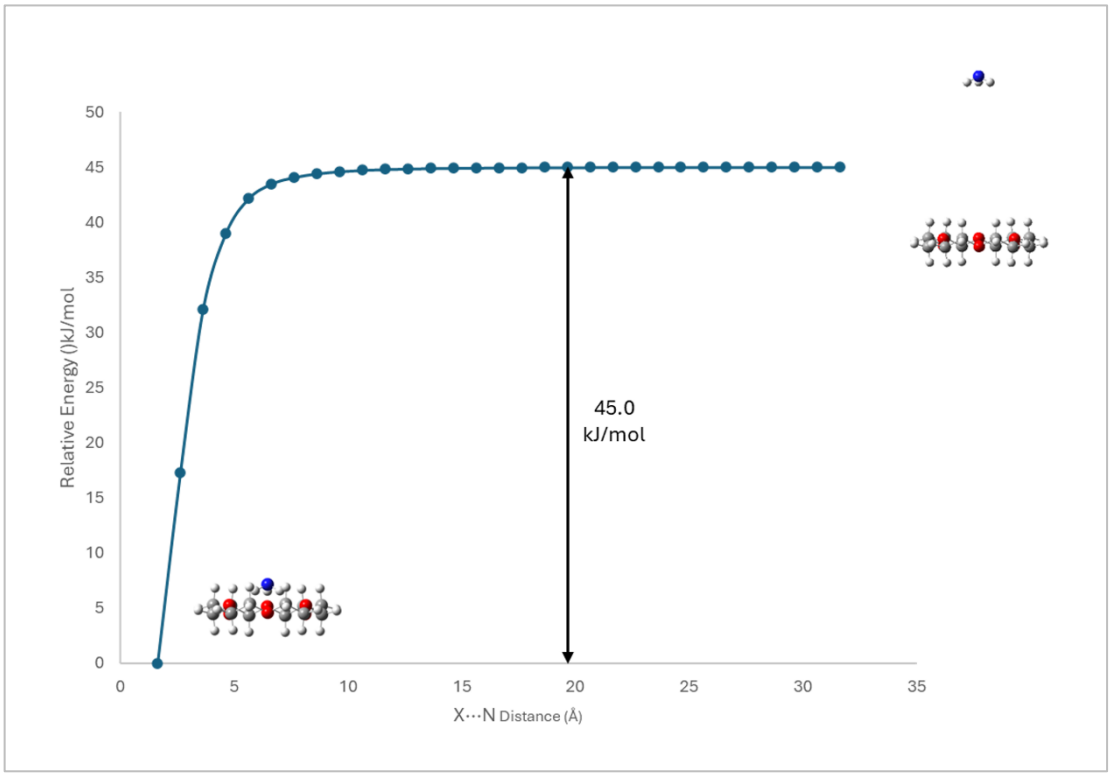

Figure 6-11: Potential energy scan for the dissociation of NH_3 in NH_3@CE. In the angle, X denotes the centre of the CE.

6.3.5 Tunnelling of NH_3 through CE ring:

The molecular rattles, a class of molecular machines, comprise complexes of molecules paired with ions that can undergo umbrella-like inversion similar to ammonia molecules. The potential of tunnelling of ions (H^+, Li^+, Na^+, and K^+) through the ring structure exhibits a double well minima, where the lowest energy geometry corresponds to either side of the ring. The transition state aligns with the geometry in which the ion is within the plane of the ring.

Numerous studies have explored the feasibility of small ions tunnelling through ring-like systems. Sathyamurthy et al. investigated proton tunnelling through a benzene ring, revealing a barrier of 249 kJ/mol for this oscillatory motion.[40] The possibility of a proton entering a fullerene cage without disrupting any C-C bonds has also been reported.[41] In another theoretical study, Sebastian et al. explored the potential for through-ring umbrella inversion of a molecular rattle involving the cyclononatetraenyllithium ion.[42] Here, the potential energy landscape displayed a double well with an activation barrier of 48.1 kJ/mol.[42] Furthermore, the rattling motion of alkali metal ions through the cavities of graphyne ($C_{12}H_6$ and $C_{24}H_{12}$) and graphdiyne ($C_{26}H_{12}$, $C_{28}H_{12}$, and $C_{30}H_{12}$) has been investigated.[43] The energy barriers for the rattling motion of Li^+ across the rings of graphyne and graphdiyne were found to range from 0 to 21 kJ/mol.[43]

The tunnelling of protons through different five-membered ring systems has been studied and reported.[44] The barriers for proton tunnelling by substituting the cyclopentadienyl anion with various heteroatoms were compared.[44] The barriers encountered for proton motion through these substituted rings fall within the range of 184-377 kJ/mol.[44]

In addition to small ions such as protons and alkali metal ions, reports have highlighted the permeation of larger molecules like fullerenes through graphynes.[45] This investigation aimed to provide theoretical insights into the design of nanomechanical oscillators. The fullerenes examined in this study encompassed C_{20}, C_{42}, C_{50}, C_{60}, C_{70}, and C_{84}. Moreover, the graphynes featured both triangular (γ-GY-4, γ-GY-5, γ-GY-6) and rhombus (r-GY-4, r-GY-5) nanopores.[45] The frequencies associated with the rattling motion of fullerenes through the nanoporous carbon membranes were observed to reside within the terahertz regime.[45]

The study of the tunnelling of the NH_3 molecule through the CE ring in the NH_3@CE complex and the determination of the barrier height for this process present intriguing prospects. The conceptual framework underlying the tunnelling phenomenon of the ammonia molecule through the CE ring is depicted in *Figure 6-12*. This concept encompasses the passage of the NH_3 molecule through the ring, with the NH_3 ring adopting a planar geometry at the centre and assuming the lowest energy structure on either side of the potential energy surface.

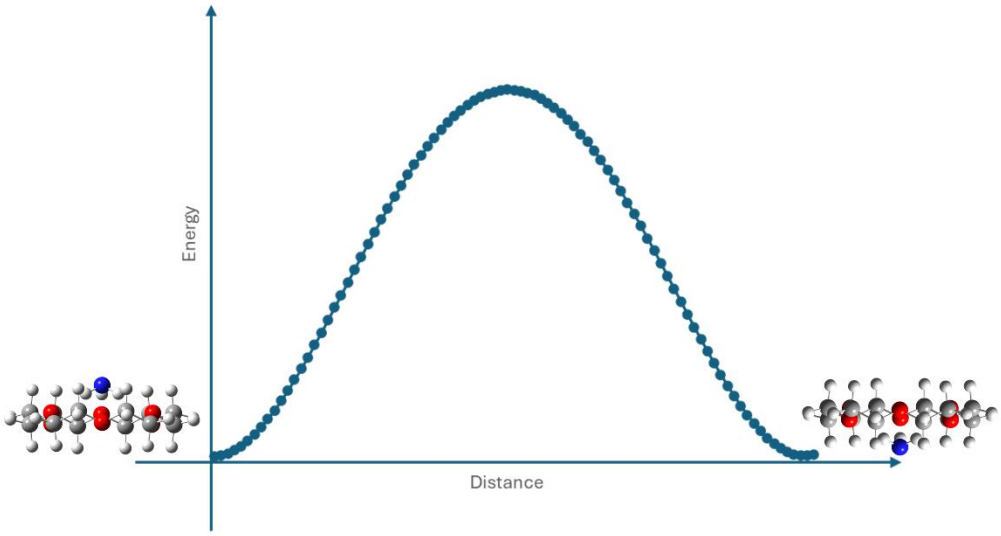

Figure 6-12: The idea behind the tunnelling of NH_3 through the CE ring.

To investigate the feasibility of NH_3 tunnelling through the centroid of the ring, a relaxed scan was conducted, utilizing the optimized structure as the initial geometry. This scan involved the calculation of interaction energies by varying the distance of the NH_3 molecule through the CE ring. A 1D relaxed scan was performed for this purpose. However, it is worth noting that the actual tunnelling of the ammonia molecule through the CE ring occurs in a three-dimensional (3D) manner. During this tunnelling process, the ammonia molecule traverses the ring, resulting in changes in the angles and rotations along its C_3 axis. It is likely that these changes occur as the ammonia molecule proceeds through the tunnelling motion. Specifically, the ammonia molecule initially passes through the CE ring, leading to an inversion-induced alteration in the angles, and subsequently undergoes rotation along its C_3 axis. The 1D potential energy scan for the

tunnelling motion of the NH_3 molecule through the CE ring is presented in *Figure 6-13*. The rotational coordinate is required in the tunnelling process since in the CE, there are three oxygen atoms above the centre of mass and three below. Moreover, in the minimum energy structure of the NH_3@CE complex, the N-H bond of the ammonia molecule forms hydrogen bonds with the oxygen atoms that are oriented towards the N-H bond and located above the centre of mass of the CE. Consequently, when the NH_3 molecule tunnels through the ring, the rotation about its C_3 axis ensures the formation of hydrogen bonds with the oxygen atom closest to the N-H bond of the NH_3 molecule.

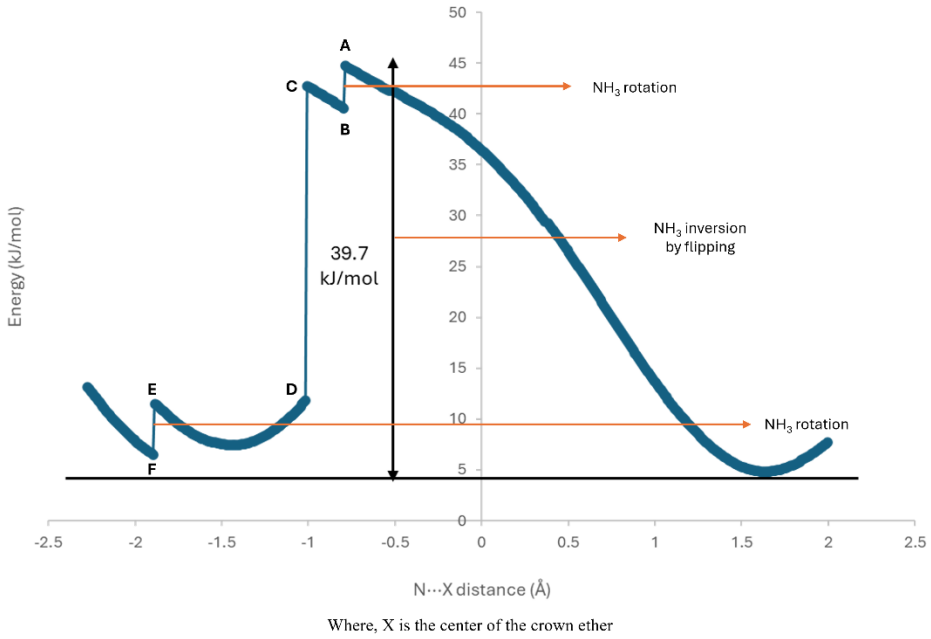

Figure 6-13: The 1D relaxed potential energy scan for the tunnelling of NH_3 through the centre of the CE ring.

In order to gain a deeper understanding of the dynamic behaviour depicted in the 1D potential energy curve shown in *Figure 6-13*, the natural bond orbitals analysis was conducted for steps A to E. *Figure 6-14* to *Figure 6-16* present snapshots of both the top view and side view for each step. The second-order perturbation energies for each step (A to E) are provided in *Table 6-4* to *Table 6-6*. The natural bond orbitals analysis reveals that in this tunnelling motion, rotation and inversion take place to stabilise the complex

by maximising the interactions between the lone pairs of oxygen atoms and the σ* antibonding orbital of N-H in NH_3. Upon examining the data in *Table 6-4*, it becomes apparent that from steps A to B, following the rotation of the ammonia molecule, both the lone pairs of oxygen atoms interact with the σ* antibonding orbital of the N-H bond, which was not the case prior to the rotation. Likewise, the inversion (from step C to step D, *Table 6-5*, *Figure 6-15*) and rotation (from step E to step F, *Table 6-6*, *Figure 6-16*) occur to maximise the delocalisation energy. Consequently, it can be inferred that the driving force behind all of these steps lies in the maximisation of interaction in N-H···O hydrogen bonds.

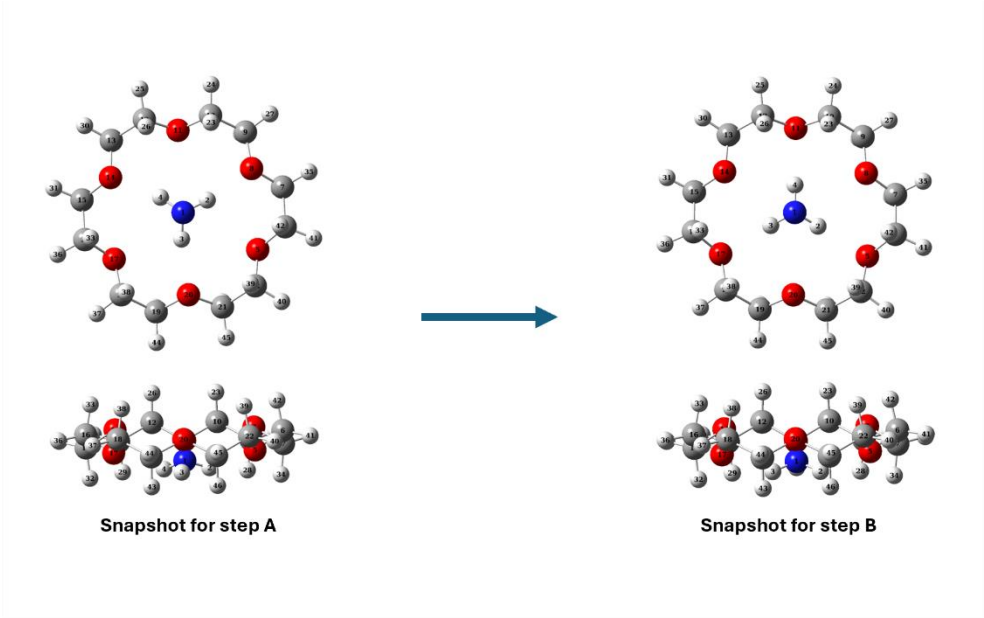

Figure 6-14: The snapshots of steps A and B in the 1D relaxed potential energy scan.

Table 6-4: The second-order perturbation energies for the corresponding donor-acceptor interactions for steps A and B calculated at M06-2X/aug-cc-pVDZ level of theory.

Donor-acceptor delocalisation interaction	**E^2 (kJ/mol)**	**Donor-acceptor delocalisation interaction**	**E^2 (kJ/mol)**
Step A		**Step B**	
$n1_{O8} \rightarrow \sigma^*_{N1-H2}$	---	$n1_{O5} \rightarrow \sigma^*_{N1-H2}$	9.29

$n1_{O14}\rightarrow\sigma^*_{N1\text{-}H4}$	---	$n1_{O11}\rightarrow\sigma^*_{N1\text{-}H4}$	9.62
$n1_{O20}\rightarrow\sigma^*_{N1\text{-}H3}$	---	$n1_{O17}\rightarrow\sigma^*_{N1\text{-}H3}$	9.87
$n2_{O8}\rightarrow\sigma^*_{N1\text{-}H2}$	4.43	$n2_{O5}\rightarrow\sigma^*_{N1\text{-}H2}$	3.30
$n2_{O14}\rightarrow\sigma^*_{N1\text{-}H4}$	3.97	$n2_{O11}\rightarrow\sigma^*_{N1\text{-}H4}$	3.56
$n2_{O20}\rightarrow\sigma^*_{N1\text{-}H3}$	4.14	$n2_{O17}\rightarrow\sigma^*_{N1\text{-}H3}$	3.51

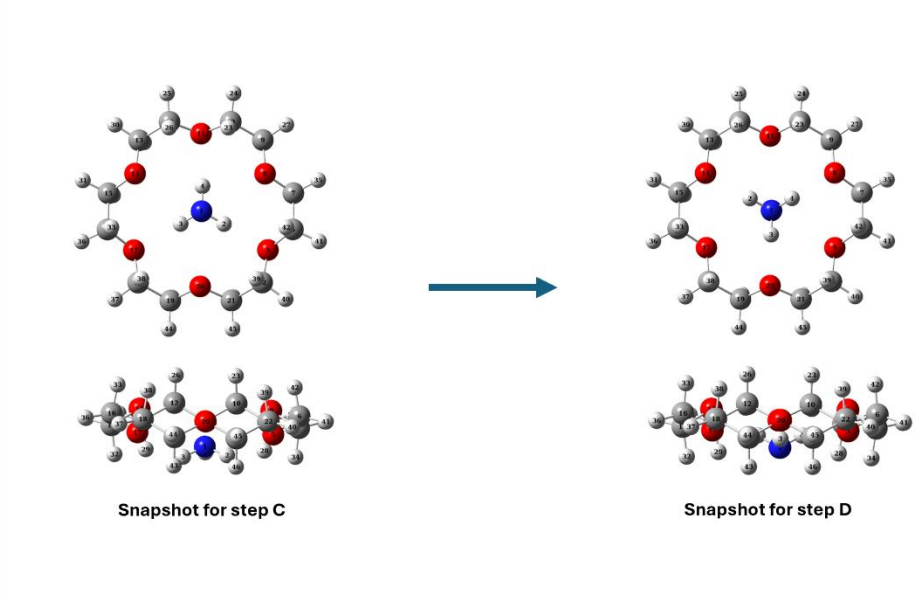

Figure 6-15: The snapshots of steps C and D in the 1D relaxed potential energy scan.

Table 6-5: The second-order perturbation energies for the corresponding donor-acceptor interactions for steps C and D calculated at M06-2X/aug-cc-pVDZ level of theory.

Donor-acceptor delocalisation interaction	**E^2 (kJ/mol)**	**Donor-acceptor delocalisation interaction**	**E^2 (kJ/mol)**
Step C		**Step D**	
$n1_{O5}\rightarrow\sigma^*_{N1\text{-}H2}$	9.00	$n1_{O8}\rightarrow\sigma^*_{N1\text{-}H4}$	2.97
$n1_{O11}\rightarrow\sigma^*_{N1\text{-}H4}$	7.78	$n1_{O14}\rightarrow\sigma^*_{N1\text{-}H2}$	3.26
$n1_{O17}\rightarrow\sigma^*_{N1\text{-}H3}$	6.90	$n1_{O20}\rightarrow\sigma^*_{N1\text{-}H3}$	3.10

$n2_{O5} \rightarrow \sigma^*_{N1-H2}$	1.76	$n2_{O8} \rightarrow \sigma^*_{N1-H4}$	14.90
$n2_{O11} \rightarrow \sigma^*_{N1-H4}$	1.38	$n2_{O14} \rightarrow \sigma^*_{N1-H2}$	14.52
$n2_{O17} \rightarrow \sigma^*_{N1-H3}$	1.00	$n2_{O20} \rightarrow \sigma^*_{N1-H3}$	13.97

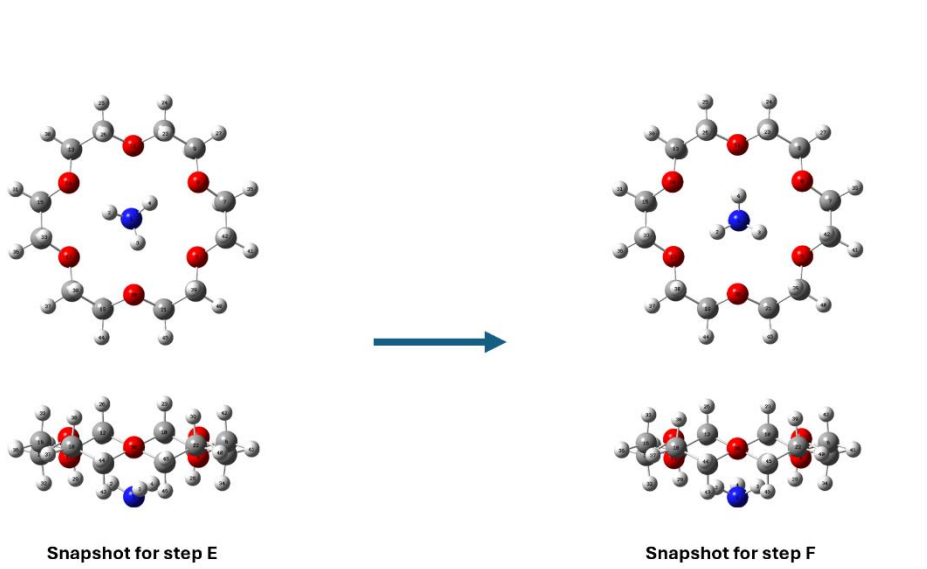

Figure 6-16: The snapshots of steps E and F in the 1D relaxed potential energy scan.

Table 6-6: The second-order perturbation energies for the corresponding donor-acceptor interactions for steps E and F calculated at M06-2X/aug-cc-pVDZ level of theory.

Donor-acceptor delocalisation interaction	**E^2 (kJ/mol)**	**Donor-acceptor delocalisation interaction**	**E^2 (kJ/mol)**
Step E		**Step F**	
$n1_{O8} \rightarrow \sigma^*_{N1-H4}$	---	$n1_{O5} \rightarrow \sigma^*_{N1-H3}$	9.62
$n1_{O14} \rightarrow \sigma^*_{N1-H2}$	---	$n1_{O11} \rightarrow \sigma^*_{N1-H4}$	9.04
$n1_{O20} \rightarrow \sigma^*_{N1-H3}$	---	$n1_{O17} \rightarrow \sigma^*_{N1-H2}$	9.71
$n2_{O8} \rightarrow \sigma^*_{N1-H4}$	3.01	$n2_{O5} \rightarrow \sigma^*_{N1-H3}$	0.54

$n2_{O14} \rightarrow \sigma^*_{N1\text{-}H2}$	3.26	$n2_{O11} \rightarrow \sigma^*_{N1\text{-}H4}$	0.33
$n2_{O20} \rightarrow \sigma^*_{N1\text{-}H3}$	2.22	$n2_{O17} \rightarrow \sigma^*_{N1\text{-}H2}$	0.42

After observing discontinuity in the 1D scan, the 2D scan was performed. The 2D rigid scan is shown in *Figure 6-17*. The reaction coordinate in the 2D scan is a combination of inversion and translation. The translation coordinate involves the NH_3 molecule moving through the CE ring towards the dummy atom (*Figure 6-17*), while the inversion coordinate includes the change in all three X···N-H angles altogether. The barrier height determined from this scan corresponds to a value of 47.2 kJ/mol, which is in good agreement with the value obtained from the 1D potential energy scan. It is worth noting that this scan does not yield the same minimum structure as, in this 2D scan, as the third coordinate, which is rotation, is not taken into account.

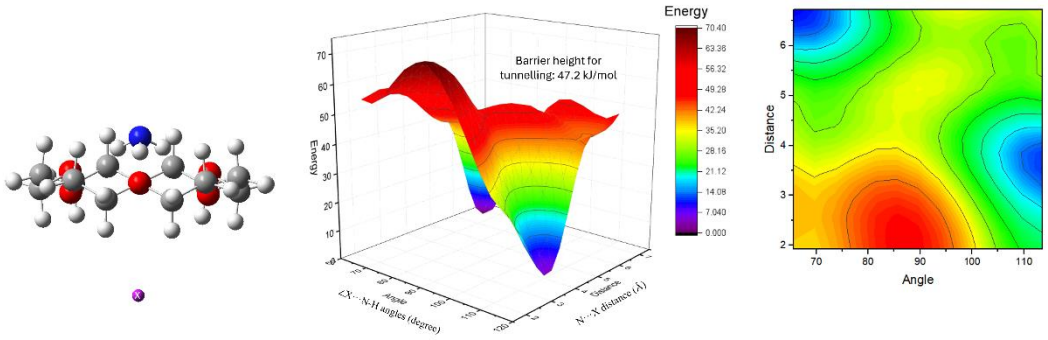

Figure 6-17: The 2D rigid potential energy scan for the tunnelling of NH_3 through the centre of the CE ring.

6.4 Conclusions:

The NH_3@CE complex is characterised by the presence of three hydrogen bonds, which have been confirmed through both the atoms in the molecule and natural bond orbital analyses. The examination of the NH_3 inversion potential energy scan has indicated that the inversion barriers are significantly influenced by the N-H···O hydrogen bonding interactions. This is evident as the inversion barrier height for the free ammonia molecule

is measured at 22.2 kJ/mol, whereas for NH_3 in the NH_3@CE complex, it is found to be 51.5 kJ/mol. It is important to note that the inversion motion of the ammonia molecule is not possible as on the potential energy scan of the NH_3@CE complex, the structure with the inverted ammonia molecule represents a first-ordered saddle point, thereby making it unstable. The study of the tunnelling motion of ammonia through the CE ring has revealed that the 1D relaxed potential energy scan results in a barrier height of 39.7 kJ/mol. However, it is worth mentioning that this scan exhibits many discontinuities in the curve. The occurrence of these discontinuities can be attributed to the fact that the tunnelling of ammonia through the CE ring poses a 3D problem rather than a 1D problem. In order to further explore the characteristics of the system, a 2D rigid scan has been conducted. This scan involves one coordinate representing the inversion motion while the other coordinate represents the translation of the ammonia molecule. The results of this 2D scan indicate a barrier height of 47.2 kJ/mol. It is important to acknowledge that the minima obtained at the end of the potential energy curve do not coincide with the starting geometry. This discrepancy arises from the fact that the potential energy scan does not take into account the third coordinate, which represents rotation.

To the best of our knowledge, this could be the first report of a neutral molecule tunnelling through a CE molecule. It is likely that a neutral molecule tunnelling through a pore could have application in different fields.

6.5 References:

(1) *The Nobel Prize in Chemistry 1987*. NobelPrize.org. https://www.nobelprize.org/prizes/chemistry/1987/summary/ (accessed 2024-02-01).

(2) Pedersen, C. J. The Discovery of Crown Ethers (Noble Lecture). *Angewandte Chemie International Edition in English* **1988**, *27* (8), 1021–1027. https://doi.org/10.1002/anie.198810211.

(3) Pedersen, C. J. The Discovery of Crown Ethers. *Science* **1988**, *241* (4865), 536–540. https://doi.org/10.1126/science.241.4865.536.

(4) Lehn, J. Supramolecular Chemistry—Scope and Perspectives Molecules, Supermolecules, and Molecular Devices (Nobel Lecture). *Angew. Chem. Int. Ed. Engl.* **1988**, *27* (1), 89–112. https://doi.org/10.1002/anie.198800891.

(5) Cram, D. J. The Design of Molecular Hosts, Guests, and Their Complexes (Nobel Lecture). *Angew. Chem. Int. Ed. Engl.* **1988**, *27* (8), 1009–1020. https://doi.org/10.1002/anie.198810093.

(6) Marczenko, K. M.; Mercier, H. P. A.; Schrobilgen, G. J. A Stable Crown Ether Complex with a Noble-Gas Compound. *Angewandte Chemie* **2018**, *130* (38), 12628–12632. https://doi.org/10.1002/ange.201806640.

(7) Miao, J.; Xiong, Z.; Gao, Y. Unexpectedly Strong Xe Binding by Host–Guest Interaction. *Phys. Chem. Chem. Phys.* **2019**, *21* (47), 26232–26236. https://doi.org/10.1039/C9CP05562B.

(8) Grassl, T.; Hamberger, M.; Korber, N. Acetyl-ene–Ammonia–18-Crown-6 (1/2/1). *Acta Cryst E* **2012**, *68* (10), o2933–o2933. https://doi.org/10.1107/S1600536812038792.

(9) Nelson, D. D.; Fraser, G. T.; Klemperer, W. Ammonia Dimer: A Surprising Structure. *The Journal of Chemical Physics* **1985**, *83* (12), 6201–6208. https://doi.org/10.1063/1.449566.

(10) Rodham, D. A.; Suzuki, S.; Suenram, R. D.; Lovas, F. J.; Dasgupta, S.; Goddard, W. A.; Blake, G. A. Hydrogen Bonding in the Benzene–Ammonia Dimer. *Nature* **1993**, *362* (6422), 735–737. https://doi.org/10.1038/362735a0.

(11) Fraser, G. T.; Leopold, K. R.; Klemperer, W. The Structure of NH3–Acetylene. *The Journal of Chemical Physics* **1984**, *80* (4), 1423–1426. https://doi.org/10.1063/1.446878.

(12) Liu, X.; Xu, Y. Infrared and Microwave Spectra of the Acetylene –Ammonia and Carbonyl Sulfide – Ammonia Complexes: A Comparative Study of a Weak C–H···N Hydrogen Bond and an S···N Bond. *Physical Chemistry Chemical Physics* **2011**, *13* (31), 14235–14242. https://doi.org/10.1039/C1CP21554J.

(13) Good, W. E. The Inversion Spectrum of Ammonia. *Phys. Rev.* **1946**, *70* (3–4), 213–218. https://doi.org/10.1103/PhysRev.70.213.

(14) Léonard, C.; Carter, S.; Handy, N. C. The Barrier to Inversion of Ammonia. *Chemical Physics Letters* **2003**, *370* (3), 360–365. https://doi.org/10.1016/S0009-2614(03)00107-6.

(15) Cress, D. H.; Quade, C. R. The Interaction of Inversion with Other Vibrations in Ammonia. *The Journal of Chemical Physics* **1977**, *67* (12), 5695–5701. https://doi.org/10.1063/1.434824.

(16) Papoušek, D. The Story of the Ammonia Molecule: Ten Years of Investigation of Molecular Inversion. *Journal of Molecular Structure* **1983**, *100*, 179–198. https://doi.org/10.1016/0022-2860(83)90091-1.

(17) Scappini, F.; Guarnieri, A.; Di Lonardo, G. The Pure Inversion Spectrum of 14ND3 in the v2 = 1 State. *Journal of Molecular Spectroscopy* **1982**, *95* (1), 20–29. https://doi.org/10.1016/0022-2852(82)90232-6.

(18) Swalen, J. D.; Ibers, J. A. Potential Function for the Inversion of Ammonia. *The Journal of Chemical Physics* **1962**, *36* (7), 1914–1918. https://doi.org/10.1063/1.1701290.

(19) Mallick, S.; Mishra, B. K.; Kumar, P.; Sathyamurthy, N. Effect of Confinement on Ammonia Inversion. *European Physical Journal D* **2021**, *75* (3). https://doi.org/10.1140/epjd/s10053-021-00118-3.

(20) Gaussian 09, Revision A.02, M. J. Frisch, G. W. Trucks, H. B. Schlegel, G. E. Scuseria, M. A. Robb, J. R. Cheeseman, G. Scalmani, V. Barone, G. A. Petersson, H. Nakatsuji, X. Li, M. Caricato, A. Marenich, J. Bloino, B. G. Janesko, R. Gomperts, B. Mennucci, H. P. Hratchian, J. V. Ortiz, A. F. Izmaylov, J. L. Sonnenberg, D. Williams-Young, F. Ding, F. Lipparini, F. Egidi, J. Goings, B. Peng, A. Petrone, T. Henderson, D. Ranasinghe, V. G. Zakrzewski, J. Gao, N. Rega, G. Zheng, W. Liang, M. Hada, M. Ehara, K. Toyota, R. Fukuda, J. Hasegawa, M. Ishida, T. Nakajima, Y.

Honda, O. Kitao, H. Nakai, T. Vreven, K. Throssell, J. A. Montgomery, Jr., J. E. Peralta, F. Ogliaro, M. Bearpark, J. J. Heyd, E. Brothers, K. N. Kudin, V. N. Staroverov, T. Keith, R. Kobayashi, J. Normand, K. Raghavachari, A. Rendell, J. C. Burant, S. S. Iyengar, J. Tomasi, M. Cossi, J. M. Millam, M. Klene, C. Adamo, R. Cammi, J. W. Ochterski, R. L. Martin, K. Morokuma, O. Farkas, J. B. Foresman, and D. J. Fox, Gaussian, Inc., Wallingford CT, 2016.

(21) Zhao, Y.; Truhlar, D. G. The M06 Suite of Density Functionals for Main Group Thermochemistry, Thermochemical Kinetics, Noncovalent Interactions, Excited States, and Transition Elements: Two New Functionals and Systematic Testing of Four M06-Class Functionals and 12 Other Functionals. *Theor Chem Account* **2008**, *120* (1–3), 215–241. https://doi.org/10.1007/s00214-007-0310-x.

(22) Wang, Y.; Verma, P.; Jin, X.; Truhlar, D. G.; He, X. Revised M06 Density Functional for Main-Group and Transition-Metal Chemistry. *Proc Natl Acad Sci U S A* **2018**, *115* (41), 10257–10262. https://doi.org/10.1073/pnas.1810421115.

(23) Weigend, F.; Ahlrichs, R. Balanced Basis Sets of Split Valence, Triple Zeta Valence and Quadruple Zeta Valence Quality for H to Rn: Design and Assessment of Accuracy. *Phys. Chem. Chem. Phys.* **2005**, *7* (18), 3297. https://doi.org/10.1039/b508541a.

(24) Schäfer, A.; Huber, C.; Ahlrichs, R. Fully Optimized Contracted Gaussian Basis Sets of Triple Zeta Valence Quality for Atoms Li to Kr. *The Journal of Chemical Physics* **1994**, *100* (8), 5829–5835. https://doi.org/10.1063/1.467146.

(25) Dunning, T. H. Gaussian Basis Sets for Use in Correlated Molecular Calculations. I. The Atoms Boron through Neon and Hydrogen. *The Journal of Chemical Physics* **1989**, *90* (2), 1007–1023. https://doi.org/10.1063/1.456153.

(26) Kendall, R. A.; Dunning, T. H.; Harrison, R. J. Electron Affinities of the First-Row Atoms Revisited. Systematic Basis Sets and Wave Functions. *The Journal of Chemical Physics* **1992**, *96* (9), 6796–6806. https://doi.org/10.1063/1.462569.

(27) Boys, S. F.; Bernardi, F. The Calculation of Small Molecular Interactions by the Differences of Separate Total Energies. Some Procedures with Reduced Errors. *Molecular Physics* **1970**, *19* (4), 553–566. https://doi.org/10.1080/00268977000101561.

(28) Bader, R. F. W. *Atoms in Molecules: A Quantum Theory*; The International series of monographs on chemistry; Clarendon Press ; Oxford University Press: Oxford [England] : New York, 1994.

(29) Weinhold, F.; Landis, C. R.; Glendening, E. D. What Is NBO Analysis and How Is It Useful? *International Reviews in Physical Chemistry* **2016**, *35* (3), 399–440. https://doi.org/10.1080/0144235X.2016.1192262.

(30) Reed, A. E.; Curtiss, L. A.; Weinhold, F. Intermolecular Interactions from a Natural Bond Orbital, Donor-Acceptor Viewpoint. *Chem. Rev.* **1988**, *88* (6), 899–926. https://doi.org/10.1021/cr00088a005.

(31) Alvarez, S. A Cartography of the van Der Waals Territories. *Dalton Transactions* **2013**, *42* (24), 8617–8636. https://doi.org/10.1039/C3DT50599E.

(32) Pascoe, D. J.; Ling, K. B.; Cockroft, S. L. The Origin of Chalcogen-Bonding Interactions. *J. Am. Chem. Soc.* **2017**, *139* (42), 15160–15167. https://doi.org/10.1021/jacs.7b08511.

(33) Vogel, L.; Wonner, P.; Huber, S. M. Chalcogen Bonding: An Overview. *Angew Chem Int Ed* **2019**, *58* (7), 1880–1891. https://doi.org/10.1002/anie.201809432.

(34) Brammer, L. Halogen Bonding, Chalcogen Bonding, Pnictogen Bonding, Tetrel Bonding: Origins, Current Status and Discussion. *Faraday Discuss.* **2017**, *203*, 485–507. https://doi.org/10.1039/C7FD00199A.

(35) Koch, U.; Popelier, P. L. A. Characterization of C-H-O Hydrogen Bonds on the Basis of the Charge Density. *J. Phys. Chem.* **1995**, *99* (24), 9747–9754. https://doi.org/10.1021/j100024a016.

(36) Cleeton, C. E.; Williams, N. H. Electromagnetic Waves of 1.1 Cm Wave-Length and the Absorption Spectrum of Ammonia. *Phys. Rev.* **1934**, *45* (4), 234–237. https://doi.org/10.1103/PhysRev.45.234.

(37) Weiss, M. T.; Strandberg, M. W. P. The Microwave Spectra of the Deutero-Ammonias. *Phys. Rev.* **1951**, *83* (3), 567–575. https://doi.org/10.1103/PhysRev.83.567.

(38) Townes, C. H. The Ammonia Spectrum and Line Shapes Near 1.25-Cm Wave-Length. *Phys. Rev.* **1946**, *70* (9–10), 665–671. https://doi.org/10.1103/PhysRev.70.665.

(39) Bleaney, B.; Penrose, R. P. Ammonia Spectrum in the 1 Cm. Wave-Length Region. *Nature* **1946**, *157* (3985), 339–340. https://doi.org/10.1038/157339c0.

(40) Shresth, R. S.; Manickavasagam, R.; Mahapatra, S.; Sathyamurthy, N. Possibility of Proton Oscillations through the Benzene Ring. *Current Science* **1996**, *71* (1), 49–50.

(41) Maheshwari, S.; Chakraborty, D.; Sathyamurthy, N. Possibility of Proton Motion through Buckminsterfullerene. *Chemical Physics Letters* **1999**, *315* (3), 181–186. https://doi.org/10.1016/S0009-2614(99)01229-4.

(42) Das, B.; Sebastian, K. L. Through Ring Umbrella Inversion of a Molecular Rattle. *Chemical Physics Letters* **2002**, *365* (3), 320–326. https://doi.org/10.1016/S0009-2614(02)01445-8.

(43) Chandra Shekar, S.; Swathi, R. S. Rattling Motion of Alkali Metal Ions through the Cavities of Model Compounds of Graphyne and Graphdiyne. *J. Phys. Chem. A* **2013**, *117* (36), 8632–8641. https://doi.org/10.1021/jp402896v.

(44) Chamoli, S.; Chakraborty, A. Rattling Motion of Proton through Five Membered Aromatic Ring Systems. *Computational and Theoretical Chemistry* **2020**, *1183*, 112825. https://doi.org/10.1016/j.comptc.2020.112825.

(45) James, A.; Swathi, R. S. Permeation of Fullerenes through Graphynes: Theoretical Design of Nanomechanical Oscillators. *J. Phys. Chem. C* **2019**, *123* (16), 10544–10556. https://doi.org/10.1021/acs.jpcc.9b00992.

6.6 Supplementary Information:

Table 6-7: Equilibrium geometry coordinates (Å) of NH_3 structure in the abc principal axes system optimised at M06-2X/aug-cc-pVDZ level of theory.

Atoms	a	b	c
N_1	0.0001	0.0000	0.0000
H_2	0.0000	0.0001	0.0000
H_3	0.0000	-0.0001	-0.0001
H_4	0.0000	-0.0001	0.0001

Table 6-8: Equilibrium geometry coordinates (Å) of 18-crown-6 structure in the abc principal axes system optimised at M06-2X/aug-cc-pVDZ level of theory.

Atoms	a	b	c
O_1	-0.000014	0.000005	0.000000
C_2	0.00002	-0.000005	-0.000001
C_3	0.000002	0.000001	-0.000002
O_4	-0.000011	-0.000006	0.000006
C_5	0.00001	0.000001	0.000000
C_6	0.000008	0.000021	0.000000
O_7	0.000000	-0.00001	-0.000015
C_8	-0.000008	0.000021	0.000000
C_9	-0.00001	0.000001	0.000000
O_{10}	0.000011	-0.000006	0.000006
C_{11}	-0.000002	0.000001	-0.000002
C_{12}	-0.00002	-0.000005	-0.000001
O_{13}	0.000014	0.000005	0.000000
C_{14}	-0.000014	-0.000011	0.000001
C_{15}	0.000000	-0.000003	0.000001
O_{16}	0.000000	0.000016	0.000003
C_{17}	0.000000	-0.000003	0.000001
C_{18}	0.000014	-0.000011	0.000001
H_{19}	0.000000	-0.000004	-0.000005
H_{20}	-0.000003	-0.000004	0.000000
H_{21}	0.000003	-0.000004	0.000000
H_{22}	0.000000	-0.000004	-0.000005
H_{23}	0.000004	0.000000	-0.000006
H_{24}	-0.000004	-0.000001	0.000001
H_{25}	0.000004	-0.000001	0.000001
H_{26}	-0.000004	0.000000	-0.000006

H_{27}	-0.000002	0.000003	-0.000002
H_{28}	0.000000	-0.000003	0.000002
H_{29}	0.000002	0.000004	-0.000001
H_{30}	0.000000	-0.000003	0.000002
H_{31}	0.000002	0.000003	-0.000002
H_{32}	0.000004	0.000000	0.000001
H_{33}	0.000000	0.000005	0.000003
H_{34}	0.000004	0.000001	0.000000
H_{35}	-0.000004	0.000001	0.000000
H_{36}	0.000000	0.000005	0.000003
H_{37}	-0.000004	0.000000	0.000001
H_{38}	-0.000002	0.000004	-0.000001
H_{39}	-0.000002	0.000000	0.000005
H_{40}	0.000002	-0.000004	0.000001
H_{41}	-0.000002	-0.000004	0.000001
H_{42}	0.000002	0.000000	0.000005

Table 6-9: Equilibrium geometry coordinates (Å) of NH_3@18-crown-6 structure in the abc principal axes system optimised at M06-2X/aug-cc-pVDZ level of theory.

Atoms	a	b	c
N_1	0.000000	0.000000	-0.000006
H_2	-0.00001	-0.000006	-0.000012
H_3	0.000000	0.000012	-0.000012
H_4	0.00001	-0.000006	-0.000012
O_5	0.000016	-0.000009	-0.000027
C_6	-0.000036	-0.00006	0.000028
C_7	-0.000034	0.000033	-0.000023
O_8	0.000038	0.000022	0.000027
C_9	0.000011	-0.000047	-0.000023
C_{10}	-0.00007	-0.000001	0.000028
O_{11}	0.000000	0.000018	-0.000027
C_{12}	0.00007	-0.000001	0.000028
C_{13}	-0.000011	-0.000047	-0.000023
O_{14}	-0.000038	0.000022	0.000027
C_{15}	0.000034	0.000033	-0.000023
C_{16}	0.000036	-0.00006	0.000028
O_{17}	-0.000016	-0.000009	-0.000027
C_{18}	-0.000034	0.000062	0.000028
C_{19}	0.000046	0.000013	-0.000023
O_{20}	0.000000	-0.000044	0.000027
C_{21}	-0.000046	0.000013	-0.000023
C_{22}	0.000034	0.000062	0.000028
H_{23}	0.000009	0.000014	-0.000016

H_{24}	0.000005	-0.00002	0.000022
H_{25}	-0.000005	-0.00002	0.000022
H_{26}	-0.000009	0.000014	-0.000016
H_{27}	-0.000025	-0.000005	-0.000028
H_{28}	0.000009	0.000007	0.000024
H_{29}	-0.000009	0.000007	0.000024
H_{30}	0.000025	-0.000005	-0.000028
H_{31}	0.000017	-0.000019	-0.000028
H_{32}	-0.000011	0.000004	0.000024
H_{33}	-0.000016	0.000001	-0.000016
H_{34}	0.000011	0.000004	0.000024
H_{35}	-0.000017	-0.000019	-0.000028
H_{36}	0.000015	0.000015	0.000022
H_{37}	0.00002	0.000005	0.000022
H_{38}	-0.000007	-0.000015	-0.000016
H_{39}	0.000007	-0.000015	-0.000016
H_{40}	-0.00002	0.000005	0.000022
H_{41}	-0.000015	0.000015	0.000022
H_{42}	0.000016	0.000001	-0.000016
H_{43}	-0.000002	-0.000011	0.000024
H_{44}	-0.000008	0.000024	-0.000028
H_{45}	0.000008	0.000024	-0.000028
H_{46}	0.000002	-0.000011	0.000024

Table 6-10: Normal modes of vibrations of NH_3@18-crown-6 calculated at M06-2X/aug-cc-pVDZ level of theory. Frequencies are given in cm^{-1}.

Mode	Frequency (cm^{-1})	Mode	Frequency (cm^{-1})
1	35.2	67	1228.6
2	35.5	68	1245.8
3	64.8	69	1255.3
4	65.2	70	1255.3
5	70.5	71	1267.7
6	96.3	72	1267.7
7	110.6	73	1273.2
8	117.2	74	1294.8
9	118.0	75	1299.6
10	127.8	76	1299.6
11	128.2	77	1308.6
12	130.5	78	1308.7
13	161.9	79	1313.2
14	162.2	80	1350.5
15	165.5	81	1362.0

16	209.8	82	1362.0
17	224.1	83	1380.1
18	232.3	84	1380.1
19	232.4	85	1402.6
20	238.2	86	1402.6
21	239.6	87	1432.0
22	246.3	88	1432.0
23	246.4	89	1459.2
24	275.2	90	1459.2
25	282.3	91	1465.6
26	325.2	92	1469.5
27	325.2	93	1469.6
28	373.2	94	1473.8
29	373.2	95	1474.3
30	373.8	96	1475.2
31	523.1	97	1475.2
32	525.6	98	1491.5
33	525.7	99	1491.5
34	565.9	100	1493.4
35	565.9	101	1494.0
36	609.1	102	1494.1
37	861.5	103	1495.9
38	861.5	104	1665.5
39	867.7	105	1666.8
40	867.8	106	3003.6
41	876.7	107	3004.5
42	896.6	108	3004.5
43	943.0	109	3006.9
44	953.7	110	3006.9
45	971.9	111	3008.6
46	971.9	112	3014.7
47	983.9	113	3016.9
48	983.9	114	3016.9
49	1103.4	115	3021.4
50	1113.0	116	3021.4
51	1113.1	117	3024.5
52	1114.9	118	3055.3
53	1114.9	119	3055.3
54	1120.2	120	3055.5
55	1149.8	121	3057.6
56	1149.9	122	3057.6
57	1158.4	123	3058.0
58	1163.0	124	3070.8

59	1163.0	125	3070.9
60	1167.3	126	3070.9
61	1180.2	127	3072.2
62	1190.3	128	3072.2
63	1208.8	129	3072.5
64	1208.9	130	3488.3
65	1226.5	131	3592.6
66	1226.5	132	3593.3

APPENDIX A

Preliminary Investigations on

1-Fluoronaphthalene···Neon Complex: A Microwave

Spectroscopic and Computational Study

APPENDIX A | Preliminary Investigation on 1-Fluoronaphthalene···Ne Complex: A Microwave Spectroscopic and Computational Study |

A.1 Introduction:

The weakly bonded complexes formed between an aromatic/aliphatic molecule and rare gas atoms have been the subject of extensive research.[1–28] The benzene···Ne, benzene···Ar, benzene···Kr, and benzene···Xe complexes have been previously studied using rotational spectroscopy.[16,23] In addition, the rotational spectra of fluorobenzene and iodobenzene complexes with Ne have been investigated.[9,27] Microwave spectroscopic studies have also been conducted on rare gas complexes with pyridine and its various substituted pyridine compounds.[3,11,14,28] In all of the aforementioned aromatic···rare gas complexes, the rare gas atom is positioned on one side of the aromatic ring. To the best of our knowledge, no rare gas complex of any fused ring system has been examined using rotational spectroscopy. We present preliminary results obtained from rotational spectroscopic and computational studies on the 1-fluoronaphthalene···Ne dimer.

A.2 Experimental and Computational Details:

The 1-fluoronaphthalene (99%) (1FN) was purchased from Sigma Aldrich and utilized without any additional purification. Neon was used as the carrier gas. The 1FN was introduced into the neon flow under a backing pressure of 5 bar. The 1FN was heated to 50°C due to its low vapor pressure. The broadband spectrum was recorded using the chirped pulse Fourier transform microwave (CP-FTMW) spectrometer at Newcastle University. The specific details of the spectrometer can be found elsewhere.[29]

The structure of the 1FN···Ne complex was optimized using the Gaussian 09 software suite.[30] Both *ab-initio* and DFT methods were employed to obtain the optimized structures. MP2 method and B3LYP-D3 functional were utilized in conjunction with an

aug-cc-pVDZ basis set.[31–35] Harmonic frequency calculations were also carried out for the optimized structure to ensure that the structure is minimum at the potential energy hypersurface. The freq=vibrot keyword was employed to calculate the centrifugal distortion constants. To gain further insights into the nature of the interactions present, Atoms in Molecules (AIM) analysis was performed.[36] The wavefunction for the AIM calculation was obtained from the optimized geometry. The PGOPHER program was utilized to fit the rotational transitions to the observed frequencies.[37]

A.3 Preliminary Results:

A.3.1 Optimised Structures:

The structures of the 1FN···Ne complex optimised using the MP2/aug-cc-pVDZ method (Structure A), and the B3LYP-D3/aug-cc-pVDZ method (Structure B) are depicted in *Figure A-1*. Notably, the Ne atom is positioned on top of the 1FN ring; however, there is a difference between the two structures in terms of the Ne position. In Structure A, the Ne atom is located near the centre of the 1FN ring, whereas in Structure B, the Ne is shifted towards the aromatic ring containing fluorine atom. The rotational constants, centrifugal distortion constants, dipole moment components, and binding energies are presented in *Table A-1*. It is important to note that both structures exhibit very similar rotational constants and dipole moment components, as the structures are nearly identical except for the position of the Ne atom.

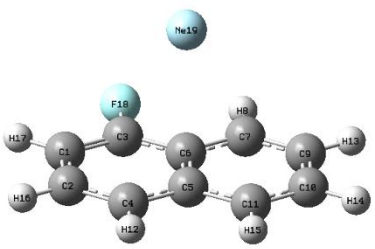

Structure A
MP2/aug-cc-pVDZ

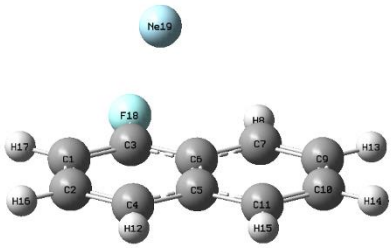

Structure B
B3LYP-D3/aug-cc-pVDZ

Figure A-1: Optimised structures of 1FN···Ne complex.

Table A-1: Rotational Constants (MHz), Centrifugal Distortion Constants, Electric Dipole Moment (Debye), and the Binding Energy (ΔE) with BSSE Corrections (kJ/mol) for 1FN···Ne complex calculated at MP2/aug-cc-pVDZ and B3LYP-D3/aug-cc-pVDZ level of theories.

Constants	**Structure A**	**Structure B**
	MP2/aug-cc-pVDZ	**B3LYP-D3/aug-cc-pVDZ**
A_e	1121.2700	1148.9222
B_e	793.4104	811.1717
C_e	693.5660	688.0434
D_J	1.6368	0.4552
D_K	-26.3340	-1.7403
D_{JK}	26.1253	2.4175
d_1	-0.1097	-0.0286
d_2	0.6778	0.1201
μ_a	0.7	-0.7
μ_b	-1.3	-1.3
μ_c	-0.2	0.3
ΔE	4.1	3.2
ΔE_{BSSE}	1.4	2.4

A.3.2 Rotational Spectrum and Preliminary Fit:

The 1FN···Ne broadband spectrum was acquired within the frequency range of 2.0 to 8.0 GHz. The predicted transition frequencies were obtained using the rotational constants derived from computational analysis. Subsequently, the observed spectral transitions were fitted based on these computational predictions. The *Table A-2* provides the experimentally determined rotational constants and centrifugal distortion constants. The fitted constants are in very good agreement with the structure B, wherein the neon atom slightly deviates towards the ring containing the F atom within the 1FN ring. A total of

38 transitions are included in the fitting. The corresponding transition frequencies and their assignments can be found in *Table A-3*.

Table A-2: Experimental rotational constants (MHz) and centrifugal distortion constants (kHz) of the 1FN···Ne complex.

Constants	1FN···Ne
A_0	1149.039(4)
B_0	815.697(4)
C_0	688.053(3)
D_J	0.34(7)
D_K	1.98(7)
D_{JK}	1.35(2)
d_1	-0.115(1)
d_2	0.0267(3)
N_{lines}	38
σ (kHz)	29.3

Table A-3: Experimentally observed rotational transition and their preliminary assignments for 1FN···Ne complex.

Transitions	Observed (MHz)	Calculated (MHz)	Obs-Cal (MHz)
$2_{0\,2} \rightarrow 1_{1\,1}$	2643.997	2643.9562	0.0408
$7_{3\,5} \rightarrow 7_{2\,6}$	2682.398	2682.4014	-0.0034
$4_{4\,1} \rightarrow 4_{3\,2}$	2737.342	2737.3221	0.0199
$3_{1\,3} \rightarrow 2_{1\,2}$	2757.988	2757.9976	-0.0096
$7_{1\,6} \rightarrow 7_{0\,7}$	2932.582	2932.5355	0.0465
$8_{3\,6} \rightarrow 8_{2\,7}$	3024.059	3024.0915	-0.0325
$9_{5\,4} \rightarrow 9_{4\,5}$	3041.017	3041.0164	0.0006
$9_{2\,7} \rightarrow 9_{2\,8}$	3087.679	3087.6844	-0.0054
$9_{4\,6} \rightarrow 9_{3\,7}$	3166.045	3166.0417	0.0033
$10_{4\,7} \rightarrow 10_{3\,8}$	3442.147	3442.1261	0.0209
$11_{5\,7} \rightarrow 11_{4\,8}$	3681.448	3681.4858	-0.0378

12 $_{6\ 7}$ → 12 $_{5\ 8}$	4168.498	4168.5439	-0.0459
13 $_{5\ 9}$ → 13 $_{4\ 10}$	4169.485	4169.4828	0.0022
12 $_{4\ 9}$ → 12 $_{3\ 10}$	4188.658	4188.6543	0.0037
8 $_{6\ 2}$ → 8 $_{5\ 3}$	4225.496	4225.4657	0.0303
13 $_{6\ 8}$ → 13 $_{5\ 9}$	4235.326	4235.2927	0.0333
8 $_{6\ 3}$ → 8 $_{5\ 4}$	4242.189	4242.2129	-0.0239
3 $_{1\ 2}$ → 2 $_{1\ 1}$	4680.937	4680.9601	-0.0231
8 $_{1\ 7}$ → 8 $_{0\ 8}$	4818.45	4818.4932	-0.0432
12 $_{3\ 9}$ → 12 $_{2\ 10}$	4835.591	4835.6433	-0.0523
13 $_{7\ 7}$ → 13 $_{6\ 8}$	4844.386	4844.383	0.003
17 $_{8\ 9}$ → 17 $_{7\ 10}$	4871.389	4871.3916	-0.0026
16 $_{7\ 10}$ → 16 $_{6\ 11}$	4897.313	4897.292	0.021
14 $_{4\ 11}$ → 14 $_{3\ 12}$	5100.788	5100.8051	-0.0171
19 $_{8\ 12}$ → 19 $_{7\ 13}$	5541.279	5541.2814	-0.0024
4 $_{0\ 4}$ → 3 $_{1\ 3}$	5641.429	5641.4208	0.0082
4 $_{1\ 4}$ → 3 $_{0\ 3}$	5849.048	5849.038	0.01
6 $_{3\ 4}$ → 5 $_{3\ 3}$	5982.65	5982.6987	-0.0487
4 $_{2\ 3}$ → 3 $_{2\ 2}$	5991.034	5991.0496	-0.0156
7 $_{0\ 7}$ → 6 $_{0\ 6}$	6461.688	6461.6587	0.0293
6 $_{3\ 3}$ → 5 $_{4\ 2}$	6661.76	6661.7494	0.0106
16 $_{2\ 14}$ → 16 $_{1\ 15}$	6754.227	6754.2455	-0.0185
16 $_{2\ 14}$ → 16 $_{2\ 15}$	6754.229	6754.2074	0.0216
7 $_{5\ 2}$ → 6 $_{5\ 1}$	6965.251	6965.2623	-0.0113
7 $_{5\ 3}$ → 6 $_{5\ 2}$	6965.251	6965.2144	0.0366
5 $_{1\ 4}$ → 4 $_{2\ 3}$	7031.784	7031.8213	-0.0373
5 $_{0\ 5}$ → 4 $_{0\ 4}$	7143.961	7143.9409	0.0201
8 $_{1\ 8}$ → 7 $_{1\ 7}$	7212.778	7212.7797	-0.0017

A.3.3 Atoms in Molecules (AIM) Analysis:

AIM analysis was conducted to gain insights into the interactions present in the 1FN···Ne complex. The resulting electron density topologies are shown in *Figure A-2*. The AIM analysis reveals the presence of one intermolecular bond critical point (BCP) between the Ne and the C_5-C_6 double bond, indicating Ne···π-cloud interactions. The values of electron density (ρ) and Laplacian ($\nabla^2\rho$) at the BCP are provided in *Table A-4*.

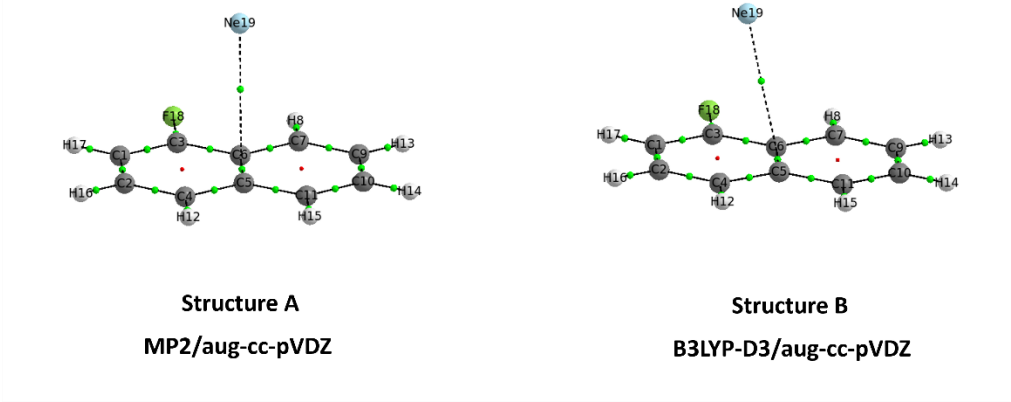

Figure A-2: Atoms in molecules topology for 1FN···Ne Complex.

Table A-4: Electron density (ρ) and the Laplacian of the electron density ($\nabla^2\rho$) of the 1FN···Ne complex, calculated at B3LYP-D3/aug-cc-pVDZ and MP2/aug-cc-pVDZ level of theories.

Interactions	**Structure A MP2/aug-cc-pVDZ**		**Structure B B3LYP-D3/aug-cc-pVDZ**	
	ρ (a.u)	**$\nabla^2\rho$ (a.u)**	**ρ (a.u)**	**$\nabla^2\rho$ (a.u)**
$C_6\cdots Ne_{19}$	0.004	+0.018	0.004	+0.017

A.4 Conclusions and Future Directions:

The fit of 1FN···Ne complex indicates a configuration in which the Ne atom resides atop the 1FN ring and displaced towards the ring containing the F atom. Additional experimental data for isotopologues is necessary to accurately assign the structure. The spectrum still includes unassigned transitions, and it is possible that these transitions may belong to the 1FN···^{22}Ne isotopologue, given that the isotopic abundance of ^{22}Ne is approximately 9.25%, it can be observed in the natural abundance.[38] This study is currently in progress.

A.4 References:

(1) Zheng, Y.; Li, X.; Feng, G.; Xia, Z.; Gou, Q. Rotational Spectrum of the Pentafluoroethane-Argon van Der Waals Complex. *Chemical Physics Letters* **2018**, *691*, 206–210. https://doi.org/10.1016/j.cplett.2017.11.012.

(2) Wang, J.; Chen, J.; Feng, G.; Xia, Z.; Gou, Q. Rotational Study on the van Der Waals Complex 1-Chloro-1,1-Difluoroethane-Argon. *Spectrochimica Acta Part A: Molecular and Biomolecular Spectroscopy* **2018**, *193*, 447–450. https://doi.org/10.1016/j.saa.2017.12.062.

(3) Velino, B.; Caminati, W. Fourier Transform Microwave Spectrum of Pyridine–Neon. *Journal of Molecular Spectroscopy* **2008**, *251* (1–2), 176–179. https://doi.org/10.1016/j.jms.2008.02.017.

(4) Tanjaroon, C.; Jäger, W. High-Resolution Microwave Spectrum of the Weakly Bound Helium-Pyridine Complex. *The Journal of Chemical Physics* **2007**, *127* (3), 034302. https://doi.org/10.1063/1.2751186.

(5) Sun, L.; Tan, X. Q.; Oh, J. J.; Kuczkowski, R. L. The Microwave Spectrum and Structure of the methanol·SO2 Complex. *The Journal of Chemical Physics* **1995**, *103* (15), 6440–6449. https://doi.org/10.1063/1.470730.

(6) Spycher, R.; Petitprez, D.; Bettens, F.; Bauder, A. Rotational Spectra of Pyridine-(Argon) n, N= 1, 2, Complexes and Their Vibrationally Averaged Structures. *The Journal of Physical Chemistry* **1994**, *98* (46), 11863–11869.

(7) Peña, I.; Cabezas, C. Rotational Spectra of van Der Waals Complexes: Pyrrole–Ne and Pyrrole–Ne 2. *Physical Chemistry Chemical Physics* **2020**, *22* (44), 25652–25660. https://doi.org/10.1039/D0CP04580B.

(8) Ottaviani, P.; Maris, A.; Caminati, W.; Tatamitani, Y.; Suzuki, Y.; Ogata, T.; Alonso, J. L. Free Jet Rotational Spectrum and Ar Inversion in the Dimethyl Ether–Argon Complex. *Chemical Physics Letters* **2002**, *361* (3), 341–348. https://doi.org/10.1016/S0009-2614(02)00958-2.

(9) Neill, J. L.; Shipman, S. T.; Alvarez-Valtierra, L.; Lesarri, A.; Kisiel, Z.; Pate, B. H. Rotational Spectroscopy of Iodobenzene and Iodobenzene–Neon with a Direct Digital

2–8GHz Chirped-Pulse Fourier Transform Microwave Spectrometer. *Journal of Molecular Spectroscopy* **2011**, *269* (1), 21–29. https://doi.org/10.1016/j.jms.2011.04.016.

(10) Melandri, S.; Maccaferri, G.; Maris, A.; Millemaggi, A.; Caminati, W.; Favero, P. G. Observation of the Rotational Spectra of van Der Waals Complexes by Free Jet Absorption Millimeter Wave Spectroscopy: Pyridine-Argon. *Chemical Physics Letters* **1996**, *261* (3), 267–271. https://doi.org/10.1016/0009-2614(96)00977-3.

(11) Melandri, S.; Giuliano, B. M.; Maris, A.; Evangelisti, L.; Velino, B.; Caminati, W. Rotational Spectrum of the Mixed van der Waals Triad Pyridine–Ar–Ne. *ChemPhysChem* **2009**, *10* (14), 2503–2507. https://doi.org/10.1002/cphc.200900366.

(12) Maris, A.; Caminati, W.; Favero, P. G. Bond Energy of Complexes of Neon with Aromatic Molecules: Rotational Spectrum and Dynamics of Pyridine–Neon. *Chemical Communications* **1998**, *0* (23), 2625–2626. https://doi.org/10.1039/A807289B.

(13) Maris, A.; Caminati, W. Rotational Spectrum, Dynamics, and Bond Energy of the Floppy Dimethylether···neon van Der Waals Complex. *The Journal of Chemical Physics* **2003**, *118* (4), 1649–1652. https://doi.org/10.1063/1.1533012.

(14) Macario, A.; Blanco, S.; Alkorta, I.; López, J. C. Perfluorination of Aromatic Compounds Reinforce Their van Der Waals Interactions with Rare Gases: The Rotational Spectrum of Pentafluoropyridine-Ne. *Molecules* **2021**, *27* (1), 17. https://doi.org/10.3390/molecules27010017.

(15) Klots, T.; Emilsson, T.; Ruoff, R.; Gutowsky, H. Microwave Spectra of Noble Gas-Pyridine Dimers: Argon-Pyridine and Krypton-Pyridine. *The Journal of Physical Chemistry* **1989**, *93* (4), 1255–1261.

(16) Klots, T. D.; Emilsson, T.; Gutowsky, H. S. Rotational Spectra, Structure, Kr-83 Nuclear Quadrupole Coupling Constant, and the Dipole Moment of the Kr-Benzene Dimer. *The Journal of Chemical Physics* **1992**, *97* (8), 5335–5340. https://doi.org/10.1063/1.463793.

(17) Hillig, K. W.; LaBarge, M. S.; Taleb-Bendiab, A.; Kuczkowski, R. L. The Microwave Spectrum and Structure of the Neon-Phosphorus Trifluoride Complex.

Chemical Physics Letters **1990**, *171* (5–6), 542–546. https://doi.org/10.1016/0009-2614(90)85260-J.

(18) Dell'Erba, A.; Melandri, S.; Millemaggi, A.; Caminati, W.; Favero, P. G. Rotational Spectra and Dynamics of the van Der Waals Adducts of Neon and Argon with 1,1-Difluoroethylene. *The Journal of Chemical Physics* **2000**, *112* (5), 2204–2209. https://doi.org/10.1063/1.480786.

(19) Caminati, W.; Millemaggi, A.; Favero, P. G.; Makarewicz, J. Free Jet Absorption Millimeter Wave Spectrum and van Der Waals Potential Energy Surface of the Pyridazine−Argon Adduct. *J. Phys. Chem. A* **1997**, *101* (49), 9272–9275. https://doi.org/10.1021/jp972237w.

(20) Caminati, W.; Melandri, S.; Dell'Erba, A.; Favero, P. G. Bonding Energies of Rare Gases with Aromatic Molecules: Rotational Spectrum and Dynamics of Pyridazine?Neon. *PhysChemComm* **2000**, *3* (1), 1–4. https://doi.org/10.1039/A909649C.

(21) Caminati, W.; Favero, P. G.; Melandri, S.; Meyer, R. Free Jet Absorption Millimeter Wave Spectrum of the Pyrimidine—Argon Molecular Complex. *Chemical Physics Letters* **1997**, *268* (5), 393–400. https://doi.org/10.1016/S0009-2614(97)00198-X.

(22) Caminati, W.; Favero, P. G. Chemistry at Low Pressure and Low Temperature: Rotational Spectrum and Dynamics of Pyrimidine–Neon. *Chemistry – A European Journal* **1999**, *5* (2), 811–814. https://doi.org/10.1002/(SICI)1521-3765(19990201)5:2<811::AID-CHEM811>3.0.CO;2-1.

(23) Brupbacher, Th.; Makarewicz, J.; Bauder, A. Intermolecular Dynamics of Benzene–Rare Gas Complexes as Derived from Microwave Spectra. *The Journal of Chemical Physics* **1994**, *101* (11), 9736–9746. https://doi.org/10.1063/1.467939.

(24) Brupbacher, Th.; Bauder, A. Rotational Spectrum and Dipole Moment of the Benzene—Argon van Der Waals Complex. *Chemical Physics Letters* **1990**, *173* (5), 435–438. https://doi.org/10.1016/0009-2614(90)87230-O.

(25) BLANCO, S.; MARIS, A.; MELANDRI, S.; CAMINATI, W. Rotational Spectrum of Propylene Oxide-Neon. *Molecular Physics* **2002**, *100* (20), 3245–3249. https://doi.org/10.1080/00268970210157912.

(26) Arunan, E.; Emilsson, T.; Gutowsky, H. S. Rotational Spectra and Structures of Rg–C6H6–H2O Trimers and the Ne–C6H6 Dimer (Rg=Ne, Ar, or Kr). *The Journal of Chemical Physics* **1994**, *101* (2), 861–868. https://doi.org/10.1063/1.467738.

(27) Wilson, R. J.; Peebles, S. A.; Antolínez, S.; Sanz, M. E.; Kuczkowski, R. L. Aromatic-Rare Gas Complexes: The Microwave Spectrum and Structure of the Fluorobenzene-Neon Dimer. *Journal of Physical Chemistry A* **1998**, *102* (52), 10630–10635. https://doi.org/10.1021/jp9835519.

(28) Sun, M.; Kamaee, M.; van Wijngaarden, J. Microwave Spectroscopic Investigation and Structural Determination of the Ar–Difluoropyridine van Der Waals Complexes. *J. Phys. Chem. A* **2014**, *118* (38), 8730–8736. https://doi.org/10.1021/jp507018a.

(29) Zaleski, D. P.; Stephens, S. L.; Walker, N. R. A Perspective on Chemistry in Transient Plasma from Broadband Rotational Spectroscopy. *Phys. Chem. Chem. Phys.* **2014**, *16* (46), 25221–25228. https://doi.org/10.1039/C4CP04108A.

(30) Gaussian 09, Revision A.02, M. J. Frisch, G. W. Trucks, H. B. Schlegel, G. E. Scuseria, M. A. Robb, J. R. Cheeseman, G. Scalmani, V. Barone, G. A. Petersson, H. Nakatsuji, X. Li, M. Caricato, A. Marenich, J. Bloino, B. G. Janesko, R. Gomperts, B. Mennucci, H. P. Hratchian, J. V. Ortiz, A. F. Izmaylov, J. L. Sonnenberg, D. Williams-Young, F. Ding, F. Lipparini, F. Egidi, J. Goings, B. Peng, A. Petrone, T. Henderson, D. Ranasinghe, V. G. Zakrzewski, J. Gao, N. Rega, G. Zheng, W. Liang, M. Hada, M. Ehara, K. Toyota, R. Fukuda, J. Hasegawa, M. Ishida, T. Nakajima, Y. Honda, O. Kitao, H. Nakai, T. Vreven, K. Throssell, J. A. Montgomery, Jr., J. E. Peralta, F. Ogliaro, M. Bearpark, J. J. Heyd, E. Brothers, K. N. Kudin, V. N. Staroverov, T. Keith, R. Kobayashi, J. Normand, K. Raghavachari, A. Rendell, J. C. Burant, S. S. Iyengar, J. Tomasi, M. Cossi, J. M. Millam, M. Klene, C. Adamo, R. Cammi, J. W. Ochterski, R. L. Martin, K. Morokuma, O. Farkas, J. B. Foresman, and D. J. Fox, Gaussian, Inc., Wallingford CT, 2016.

(31) Miehlich, B.; Savin, A.; Stoll, H.; Preuss, H. Results Obtained with the Correlation Energy Density Functionals of Becke and Lee, Yang and Parr. *Chemical Physics Letters* **1989**, *157* (3), 200–206. https://doi.org/10.1016/0009-2614(89)87234-3.

(32) Vosko, S. H.; Wilk, L.; Nusair, M. Accurate Spin-Dependent Electron Liquid Correlation Energies for Local Spin Density Calculations: A Critical Analysis. *Can. J. Phys.* **1980**, *58* (8), 1200–1211. https://doi.org/10.1139/p80-159.

(33) Becke, A. D. Density-Functional Thermochemistry. I. The Effect of the Exchange-Only Gradient Correction. *The Journal of Chemical Physics* **1992**, *96* (3), 2155–2160. https://doi.org/10.1063/1.462066.

(34) Binkley, J. S.; Pople, J. A. Møller-Plesset Theory for Atomic Ground State Energies: MØLLER-PLESSET THEORY FOR ATOMIC GROUND STATE ENERGIES. *Int. J. Quantum Chem.* **1975**, *9* (2), 229–236. https://doi.org/10.1002/qua.560090204.

(35) Schäfer, A.; Huber, C.; Ahlrichs, R. Fully Optimized Contracted Gaussian Basis Sets of Triple Zeta Valence Quality for Atoms Li to Kr. *The Journal of Chemical Physics* **1994**, *100* (8), 5829–5835. https://doi.org/10.1063/1.467146.

(36) Bader, R. F. W. *Atoms in Molecules: A Quantum Theory*; The International series of monographs on chemistry; Clarendon Press ; Oxford University Press: Oxford [England] : New York, 1994.

(37) Western, C. M. PGOPHER: A Program for Simulating Rotational, Vibrational and Electronic Spectra. *Journal of Quantitative Spectroscopy and Radiative Transfer* **2017**, *186*, 221–242. https://doi.org/10.1016/j.jqsrt.2016.04.010.

(38) Atomic Weights and Isotopic Compositions with Relative Atomic Masses. *NIST* **2009**.

A.5 Supplementary Information:

Table A-5: Equilibrium geometry coordinates (Å) of 1FN···Ne complex for structure A in the abc principal axes system optimised at MP2/aug-cc-pVDZ level of theory.

Atoms	a	b	c
C_1	-2.334	-0.253	-0.364
C_2	-1.901	-1.592	-0.580
C_3	-1.381	0.741	-0.242
C_4	-0.546	-1.896	-0.668
C_5	0.435	-0.868	-0.539
C_6	0.016	0.495	-0.320
C_7	0.988	1.530	-0.186
H_8	0.655	2.558	-0.020
C_9	2.343	1.222	-0.265
C_{10}	2.769	-0.119	-0.481
C_{11}	1.834	-1.141	-0.616
H_{12}	-0.218	-2.927	-0.834
H_{13}	3.087	2.017	-0.161
H_{14}	3.838	-0.345	-0.541
H_{15}	2.162	-2.173	-0.782
H_{16}	-2.649	-2.385	-0.678
H_{17}	-3.394	0.001	-0.292
F_{18}	-1.789	2.031	-0.033
Ne_{19}	0.190	-0.636	2.759

Table A-6: Equilibrium geometry coordinates (Å) of 1FN···Ne complex for structure B in the abc principal axes system optimised at B3LYP-D3/aug-cc-pVDZ level of theory.

Atoms	a	b	c
C_1	2.212	-0.044	0.600
C_2	1.832	-1.378	0.897
C_3	1.232	0.864	0.288
C_4	0.506	-1.756	0.874
C_5	-0.510	-0.814	0.549
C_6	-0.146	0.539	0.246

C_7	-1.152	1.48	-0.083
H_8	-0.859	2.511	-0.311
C_9	-2.478	1.107	-0.112
C_{10}	-2.849	-0.229	0.186
C_{11}	-1.888	-1.165	0.509
H_{12}	0.220	-2.782	1.103
H_{13}	-3.248	1.836	-0.365
H_{14}	-3.901	-0.514	0.158
H_{15}	-2.174	-2.193	0.738
H_{16}	2.605	-2.105	1.146
H_{17}	3.254	0.268	0.614
F_{18}	1.588	2.147	0.001
Ne_{19}	0.643	-1.056	-2.531

Table A-7: Normal modes of vibrations for Structure A and Structure B of the 1FN···Ne complex calculated at MP2/aug-cc-pVDZ and B3LYP-D3/aug-cc-pVDZ level of theory.

Modes	**Frequency (cm^{-1})**	
	MP2/aug-cc-pVDZ	**B3LYP-D3/aug-cc-pVDZ**
1	6.4	20.0
2	19.1	25.2
3	43.1	54.8
4	142.6	144.7
5	175.9	179.9
6	263.6	267.5
7	264.2	274.1
8	417.3	428.7
9	454.9	468.3
10	458.3	475.1
11	465.6	483.9
12	525.7	535.6
13	563.8	574.6
14	564	582.3
15	600	643.4
16	679.7	718.4

17	707.7	744.7
18	749.7	786.1
19	788.6	796.3
20	790.1	824.5
21	844.8	879.9
22	866.9	890.1
23	878.4	909.5
24	929.8	968.7
25	938.4	982.4
26	942.1	1001.3
27	1030.4	1035.4
28	1044.2	1053.2
29	1084.1	1091.2
30	1151.5	1166.6
31	1162.8	1180.1
32	1169	1184.7
33	1234.1	1236.7
34	1258.4	1245.9
35	1265.3	1280.3
36	1398.8	1385.5
37	1430.6	1413
38	1471.3	1418.5
39	1475	1467.4
40	1497.9	1484.4
41	1543.8	1542.5
42	1607.7	1619.7
43	1622.5	1642.4
44	1678.2	1677.6
45	3194.7	3169.2
46	3200.8	3175.8
47	3208	3180.9
48	3220.8	3193.3
49	3221.8	3194.1
50	3233.8	3209.4
51	3237.6	3210.2

APPENDIX B

Preliminary Results of Microwave Spectroscopic Study on $Ar(H_2S)_2(H_2O)$ Complex

APPENDIX B | Preliminary Results of Microwave Spectroscopic Study on $Ar(H_2S)_2(H_2O)$ Complex |

B.1 Introduction:

The distinct structural disparities between the condensed phases of H_2O and H_2S are widely acknowledged. The water dimer has been extensively studied from both experimental and theoretical perspectives.[1–8] In the common form of solid water, which is ice, H_2O is surrounded by four other water molecules. Conversely, an individual molecule of H_2S is surrounded by twelve H_2S molecules in isomorphs of solid H_2S.[9] The microwave spectrum of $(H_2S)_2$ has also been the subject of study. The structures of both $(H_2O)_2$ and $(H_2S)_2$ exhibit similarities, and recently, it has been verified that $(H_2S)_2$ is hydrogen bonded.[10] In the realms of atmospheric and interstellar chemistry, the microsolvation of small molecules carries significant importance. The rotational spectra of Ar-H_2S, Ar_2-H_2S Ar_3-H_2S, $Ar(H_2S)_2$, and $Ar(H_2S)_2(H_2O)$ have been established.[11–15] This study focuses on analysing the microwave spectra of the $Ar(H_2S)_2(H_2O)$ complex, a four-body system.

B.2 Experimental and Computational Details:

The H_2S cylinder was procured from Sigma Aldrich for the purpose of the experiment. The spectrum was recorded using the chirped pulse Fourier transform microwave (CP-FTMW) spectrometer at Newcastle University.[16] Detailed information about the spectrometer can be found elsewhere. A small amount of H_2S gas was introduced into the sample tank, with the remaining portion filled with argon. The pressure was maintained at 5 bar throughout the experiment. As for water, a reservoir was employed, positioned after the nozzle. The reservoir contained a minute quantity of water, approximately 0.2 ml.

The optimisation of the $Ar(H_2S)_2(H_2O)$ structure was conducted using the Gaussian 09 software suite.[17] Both *ab-initio* and DFT methods were employed to obtain the optimised structures. MP2 and DFT method with B3LYP-D3 functional were utilised in conjunction with an aug-cc-pVDZ basis set.[18–22] Harmonic frequency calculations were also carried out for the optimized structure to ensure that it corresponds to the minimum on the potential energy hypersurface. The *freq=vibrot* keyword was implemented to calculate the distortion constants. In order to gain further insights into the nature of the interactions present, an Atoms in Molecules (AIM) analysis was performed.[23] The wave function for the AIM calculation was derived from the optimized geometry. The rotational transitions were fitted to the observed frequencies using the PGOPHER program.[24]

B.3 Preliminary Results:

B.3.1 Optimised Structures:

The structures of the $Ar(H_2S)_2(H_2O)$ complex were optimized using the B3LYP-D3 and MP2 level of theory with aug-cc-pVDZ basis sets. Two structures were obtained, which are illustrated in *Figure B-1*. The primary difference between the two structures lies in the position of the hydrogen atoms. In both structures A and B, H_2O and H_2S function as both hydrogen bond donors and acceptors. $(H_2S)_2(H_2O)$ forms cyclic structures, with Ar interacting from the top to create an overall cage-like structure. We expect there to be some cooperative effect in the hydrogen bonds present in this complex.

The rotational constants, centrifugal distortion constants, and dipole moment components for the optimized structures are provided in *Table B-1*. The binding energy suggests that structure A represents the global minimum, which is confirmed by both DFT and *ab-initio* calculations. However, the energy difference between the two structures is very less approximately 1-2 kJ/mol.

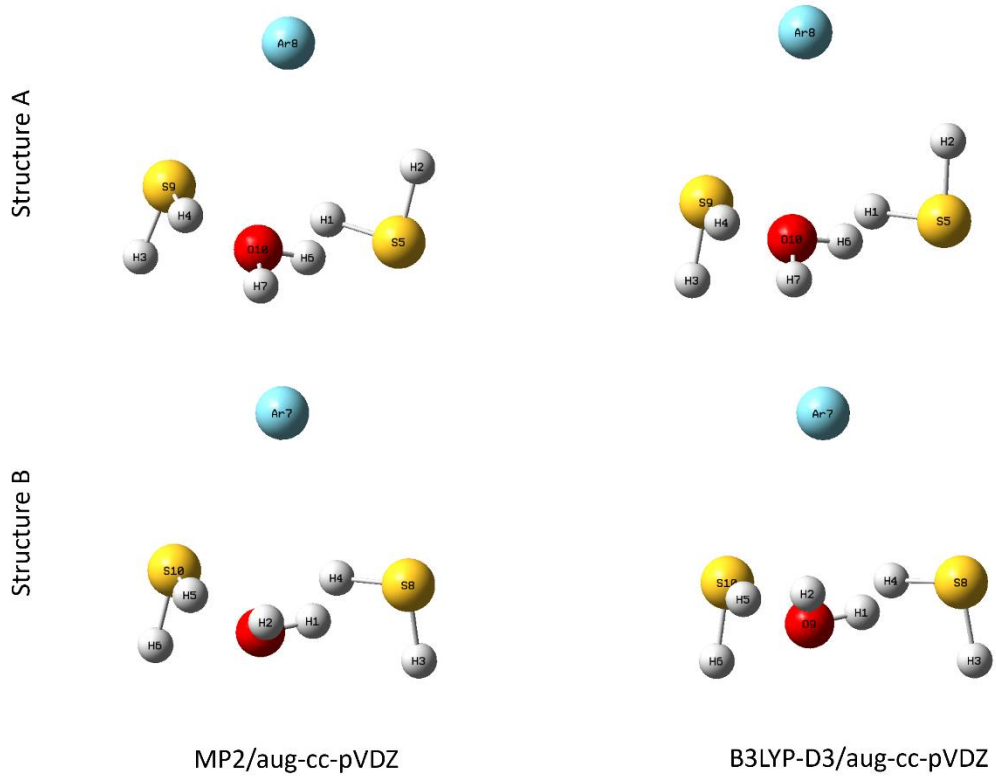

Figure B-1: Structures of the $Ar(H_2S)2(H_2O)$ complex optimised at B3LYP-D3/aug-cc-pVDZ and MP2/aug-cc-pVDZ level of theory.

Table B-1: Rotational Constants (MHz), Centrifugal Distortion Constants, Electric Dipole Moment (Debye), and the Binding Energy (ΔE) with BSSE Corrections (kJ/mol) for $Ar(H_2S)_2(H_2O)$ complex calculated at MP2/aug-cc-pVDZ and B3LYP-D3/aug-cc-pVDZ level of theories.

Constants	Structure A		Structure B	
	MP2/aug-cc-pVDZ	B3LYP-D3/aug-cc-pVDZ	MP2/aug-cc-pVDZ	B3LYP-D3/aug-cc-pVDZ
A_e	1407.9201	1371.8231	1335.6031	1341.0998
B_e	1204.3487	1250.4974	1310.1877	1317.8378
C_e	903.2758	914.7094	938.2469	938.9109
D_J	3.4412	3.3244	3.4878	2.9475
D_K	0.4739	-2.3579	-0.3239	-0.3973

D_{JK}	-2.8117	0.0454	-2.0382	-1.6503
d_1	-0.3948	-0.5938	0.6463	-0.5826
d_2	-0.4280	-0.0519	0.4360	0.3252
μ_a	1.0	-1.2	1.2	1.0
μ_b	-0.6	-0.3	0.5	0.3
μ_c	-1.1	0.9	0.9	0.6
ΔE	44.3	43.4	44.3	43.5
ΔE_{BSSE}	32.3	40.1	32.4	40.3

B.3.2 Rotational Spectrum and Preliminary Fit:

The fitted rotational constants are shown in the *Table B-2*. A total of 27 transitions were fitted within the experimental uncertainty. The broadband spectrum recorded at CP-FTMW spectrometer is shown in *Figure B-2*. All three rotational constants and five centrifugal distortion constants were fitted. The fitted rotational constants are in good agreement with the structure B calculated at the MP2/aug-cc-pVDZ level of theory. The obtained fit exhibits a standard deviation of 13.0 kHz, which falls within the range of experimental accuracy. The calculated distortion constants obtained from both the B3LYP-D3 and MP2 methods significantly differ from those derived experimentally. This discrepancy between the theory and experiment can be due to the large amplitude vibrations that are not treated accurately. A similar trend is observed in the case of the experimentally determined distortion constants for both $(H_2S)_2$ and $(H_2S)_2(H_2O)$.[10,15] In these complexes, the calculated distortion constants are considerably smaller than the experimentally obtained values. The fitted transition frequencies and their corresponding assignments can be found in *Table B-3*.

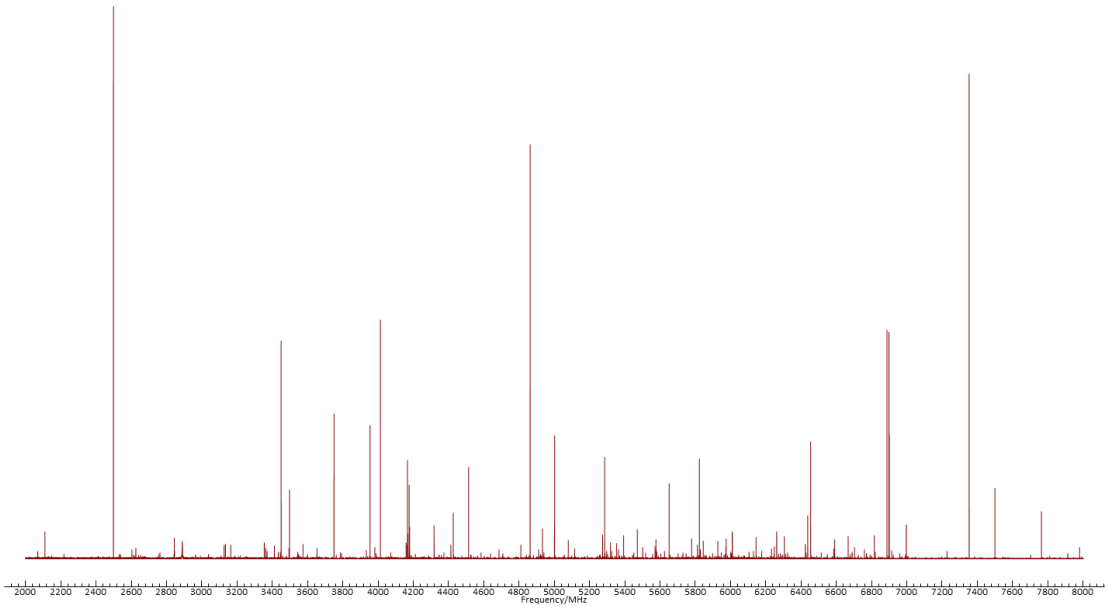

Figure B-2: The broadband spectrum recorded at CP-FTMW spectrometer.

Table B-2: Experimental rotational constants (MHz) and centrifugal distortion constants (kHz) of the Ar(H_2S)$_2$(H_2O) complex.

Constants	**Ar(H_2S)$_2$(H_2O)**
A_0	1336.398(5)
B_0	1309.554(6)
C_0	935.998(5)
D_J	80.2(4)
D_K	-203(2)
D_{JK}	-352(2)
d_1	-81.75(4)
d_2	-8.18(6)
N_{lines}	27
σ (kHz)	13.0

Table B-3: Experimentally observed rotational transition and their preliminary assignments for Ar(H2S)2(H2O) complex.

Transitions	Observed (MHz)	Calculated (MHz)	Obs-Cal (MHz)
$6_{2\,5} \rightarrow 6_{0\,6}$	4249.773	4249.771	0.002
$6_{1\,5} \rightarrow 6_{0\,6}$	4249.773	4249.7743	-0.0013
$6_{2\,5} \rightarrow 6_{1\,6}$	4249.773	4249.771	0.002
$6_{1\,5} \rightarrow 6_{1\,6}$	4249.773	4249.7743	-0.0013
$9_{3\,6} \rightarrow 9_{2\,7}$	4974.604	4974.5873	0.0167
$9_{3\,6} \rightarrow 9_{3\,7}$	4974.604	4974.5867	0.0173
$9_{4\,6} \rightarrow 9_{3\,7}$	4974.604	4974.6175	-0.0135
$9_{4\,6} \rightarrow 9_{2\,7}$	4974.604	4974.6181	-0.0141
$8_{2\,6} \rightarrow 8_{1\,7}$	5005.32	5005.3213	-0.0013
$8_{3\,6} \rightarrow 8_{1\,7}$	5005.32	5005.3244	-0.0044
$8_{2\,6} \rightarrow 8_{2\,7}$	5005.32	5005.3213	-0.0013
$8_{3\,6} \rightarrow 8_{2\,7}$	5005.32	5005.3244	-0.0044
$2_{1\,1} \rightarrow 1_{0\,1}$	5261.848	5261.8647	-0.0167
$2_{2\,0} \rightarrow 1_{1\,0}$	5296.293	5296.2561	0.0369
$2_{2\,1} \rightarrow 1_{1\,1}$	5326.809	5326.8292	-0.0202
$8_{1\,7} \rightarrow 8_{0\,8}$	5791.165	5791.1641	0.0009
$8_{2\,7} \rightarrow 8_{1\,8}$	5791.165	5791.164	0.001
$8_{1\,7} \rightarrow 8_{1\,8}$	5791.165	5791.1641	0.0009
$8_{2\,7} \rightarrow 8_{0\,8}$	5791.165	5791.164	0.001
$3_{1\,3} \rightarrow 2_{1\,2}$	6009.535	6009.5383	-0.0033
$3_{0\,3} \rightarrow 2_{1\,2}$	6009.536	6009.5338	0.0022
$3_{0\,3} \rightarrow 2_{0\,2}$	6010.802	6010.7992	0.0028
$3_{1\,3} \rightarrow 2_{0\,2}$	6010.802	6010.8037	-0.0017
$14_{5\,10} \rightarrow 14_{4\,11}$	7812.498	7812.5039	-0.0059
$14_{4\,10} \rightarrow 14_{3\,11}$	7812.498	7812.4923	0.0057
$14_{5\,10} \rightarrow 14_{3\,11}$	7812.498	7812.504	-0.006
$14_{4\,10} \rightarrow 14_{4\,11}$	7812.498	7812.4922	0.0058

B.3.3 Atoms in Molecules (AIM) Analysis:

The nature of intermolecular interactions present in the $Ar(H_2S)_2(H_2O)$ complex has been investigated using the Atoms in Molecules (AIM) topological study. Six intermolecular bond critical points (BCPs) were identified in both structures A and B. The electron density (ρ) and Laplacian of electron density ($\nabla^2\rho$) values are provided in *Table B-4*. It is important to note that the interactions between Ar and the two H_2S and H_2O molecules are weak in both structures, with electron densities ranging from 0.003 to 0.004 au. Apart from these weak interactions, the $Ar(H_2S)_2(H_2O)$ complex form three strong hydrogen bonds (S-H···O, O-H···S, and S-H···S). Since these six interactions are present in closed manner, it gives rise to the observation of four ring critical points (RCPs). The molecular graph illustrating the BCPs, and RCPs can be seen in *Figure B-3*.

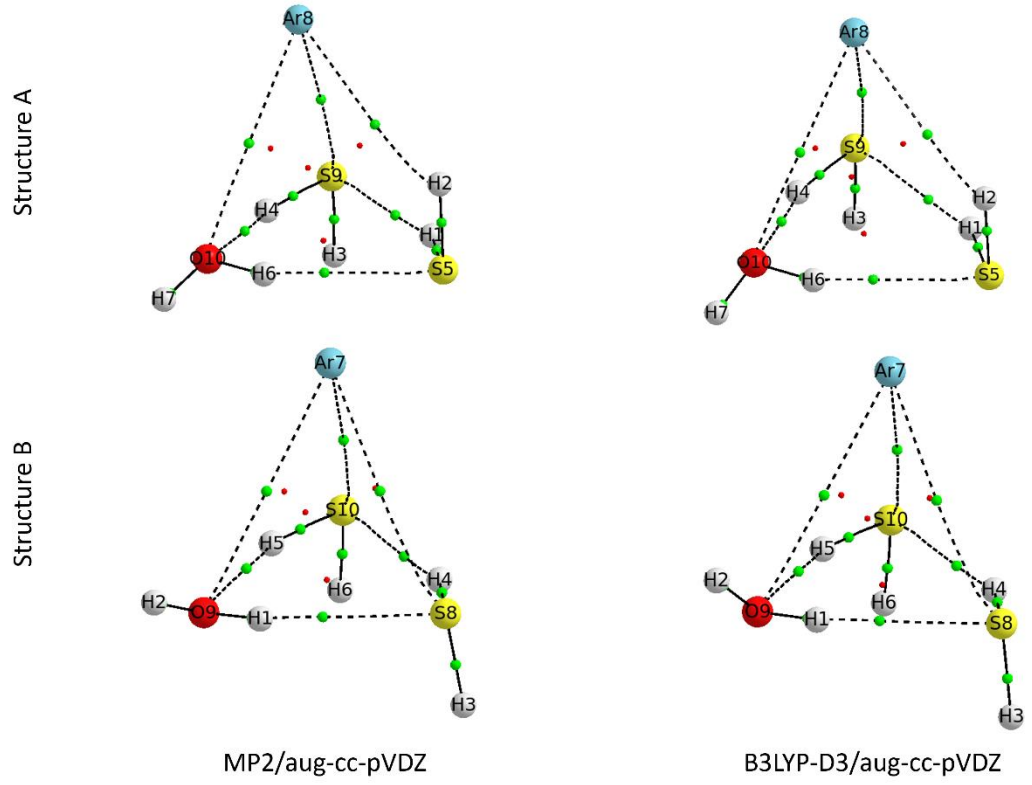

Figure B-3: Bond critical points (green) and ring critical points (red) of the $Ar(H_2S)_2(H_2O)$ complex calculated at B3LYP-D3/aug-cc-pVDZ and MP2/aug-cc-pVDZ level of theory.

Table B-4: Electron density (ρ) and the Laplacian of the electron density ($\nabla^2\rho$) of the Ar$(H_2S)_2(H_2O)$ complex, calculated at B3LYP-D3/aug-cc-pVDZ and MP2/aug-cc-pVDZ level of theories.

Interactions	Structure A				Interactions	Structure B			
	MP2/aug-cc-pVDZ		B3LYP-D3/aug-cc-pVDZ			MP2/aug-cc-pVDZ		B3LYP-D3/aug-cc-pVDZ	
	ρ (a.u)	$\nabla^2\rho$ (a.u)	ρ (a.u)	$\nabla^2\rho$ (a.u)		ρ (a.u)	$\nabla^2\rho$ (a.u)	ρ (a.u)	$\nabla^2\rho$ (a.u)
$O_{10}\cdots H_4$-S_9	0.017	+0.050	0.018	+0.048	$Ar_7\cdots O_9$-H_2	0.002	+0.009	0.003	+0.010
$Ar_8\cdots H_7$-O_{10}	0.003	+0.012	0.003	+0.010	O_9-$H_1\cdots S_8$	0.015	+0.036	0.016	+0.035
O_{10}-$H_6\cdots S_5$	0.015	+0.036	0.016	+0.035	S_{10}-$H_5\cdots O_9$	0.017	+0.051	0.019	+0.049
S_5-$H_1\cdots S_9$	0.011	+0.026	0.011	+0.024	S_8-$H_4\cdots S_{10}$	0.011	+0.026	0.011	+0.024
$Ar_8\cdots S_9$-H_3	0.004	+0.013	0.004	+0.012	$Ar_7\cdots S_{10}$-H_6	0.004	+0.013	0.004	+0.012
S_5-$H_2\cdots Ar_8$	0.003	+0.012	0.005	+0.015	$Ar_7\cdots S_8$-H_3	0.004	+0.013	0.004	+0.011

B.4 Conclusions and Future Directions:

The broadband rotational spectra of Ar$(H_2S)_2(H_2O)$ were measured in the frequency range of 2.0 to 8.0 GHz. The initial fitting of the complex suggests the presence of S-H···O, O-H···S, and S-H···S hydrogen bonded interactions, as well as three weak interactions with the Ar atom (two Ar···S and one Ar···O interactions). Additional experimental data for isotopologues is required to accurately assign the structure. Currently, this study is still in progress.

B.5 References:

(1) Rocher-Casterline, B. E.; Ch'ng, L. C.; Mollner, A. K.; Reisler, H. Communication: Determination of the Bond Dissociation Energy (*D*) of the Water Dimer, (H2O)2, by Velocity Map Imaging. *The Journal of Chemical Physics* **2011**, *134* (21), 211101. https://doi.org/10.1063/1.3598339.

(2) Mukhopadhyay, A.; Cole, W. T. S.; Saykally, R. J. The Water Dimer I: Experimental Characterization. *Chemical Physics Letters* **2015**, *633*, 13–26. https://doi.org/10.1016/j.cplett.2015.04.016.

(3) Mukhopadhyay, A.; Xantheas, S. S.; Saykally, R. J. The Water Dimer II: Theoretical Investigations. *Chemical Physics Letters* **2018**, *700*, 163–175. https://doi.org/10.1016/j.cplett.2018.03.057.

(4) Fraser, G. T.; Suenram, R. D.; Coudert, L. H.; Frye, R. S. Electric-Resonance Optothermal Spectrum of (H2O)2: Microwave Spectrum of the *K* = 1-0 Subband for the *E*2± States. *Journal of Molecular Spectroscopy* **1989**, *137* (1), 244–247. https://doi.org/10.1016/0022-2852(89)90284-1.

(5) Fraser, G. T.; Suenram, R. D.; Coudert, L. H. Microwave Electric-resonance Optothermal Spectroscopy of (H2O)2. *The Journal of Chemical Physics* **1989**, *90* (11), 6077–6085. https://doi.org/10.1063/1.456373.

(6) Fraser, G. T.; Suenram, R. D.; Coudert, L. H. Microwave Electric-Resonance Optothermal Spectroscopy of (H2O)2. *The Journal of Chemical Physics* **1989**, *90* (11), 6077–6085. https://doi.org/10.1063/1.456373.

(7) Dyke, T. R.; Muenter, J. S. Microwave Spectrum and Structure of Hydrogen Bonded Water Dimer. *The Journal of Chemical Physics* **1974**, *60* (7), 2929–2930. https://doi.org/10.1063/1.1681463.

(8) Dyke, T. R.; Mack, K. M.; Muenter, J. S. The Structure of Water Dimer from Molecular Beam Electric Resonance Spectroscopy. *The Journal of Chemical Physics* **1977**, *66* (2), 498–510. https://doi.org/10.1063/1.433969.

(9) Pauling, L. *The Nature of Chemical Bond*, 3rd ed.; Cornell University Press, 1960.

(10) Das, A.; Mandal, P. K.; Lovas, F. J.; Medcraft, C.; Walker, N. R.; Arunan, E. The H2S Dimer Is Hydrogen-Bonded: Direct Confirmation from Microwave Spectroscopy. *Angewandte Chemie - International Edition* **2018**, *57* (46), 15199–15203. https://doi.org/10.1002/ANIE.201808162.

(11) Gutowsky, H. S.; Emilsson, T.; Arunan, E. Rotational Spectra, Structure, and Internal Dynamics of Ar–H2S Isotopomers. *The Journal of Chemical Physics* **1997**, *106* (13), 5309–5315. https://doi.org/10.1063/1.473066.

(12) Bumgarner, R. E.; Pauley, D. J.; Kukolich, S. G. Microwave Measurements on Ar□H2S, Ar□HDS and Ar□D2S Complexes. *Journal of Molecular Structure* **1988**, *190*, 163–171. https://doi.org/10.1016/0022-2860(88)80281-3.

(13) Mandal, P. K.; Ramdass, D. J.; Arunan, E. Rotational Spectra and Structure of the Ar2–H2S Complex: Pulsed Nozzle Fourier Transform Microwave Spectroscopic and Ab Initio Studies. *Phys. Chem. Chem. Phys.* **2005**, *7* (14), 2740. https://doi.org/10.1039/b503640b.

(14) Arunan, E.; Emilsson, T.; Gutowsky, H. S.; Dykstra, C. E. Rotational Spectra and Structures of the Ar3–H2O and Ar3–H2S Symmetric Tops. *The Journal of Chemical Physics* **2001**, *114* (3), 1242–1248. https://doi.org/10.1063/1.1333707.

(15) Das, A. Microwave Rotation-Tunnelling Spectroscopic and Theoretical Studies on Weakly Bound Molecular Complexes: Intermolecular Bonding across the Periodic Table. Ph.D. Thesis, Indian Institute of Science, Bangalore, 2021.

(16) Zaleski, D. P.; Stephens, S. L.; Walker, N. R. A Perspective on Chemistry in Transient Plasma from Broadband Rotational Spectroscopy. *Phys. Chem. Chem. Phys.* **2014**, *16* (46), 25221–25228. https://doi.org/10.1039/C4CP04108A.

(17) Gaussian 09, Revision A.02, M. J. Frisch, G. W. Trucks, H. B. Schlegel, G. E. Scuseria, M. A. Robb, J. R. Cheeseman, G. Scalmani, V. Barone, G. A. Petersson, H. Nakatsuji, X. Li, M. Caricato, A. Marenich, J. Bloino, B. G. Janesko, R. Gomperts, B. Mennucci, H. P. Hratchian, J. V. Ortiz, A. F. Izmaylov, J. L. Sonnenberg, D. Williams-Young, F. Ding, F. Lipparini, F. Egidi, J. Goings, B. Peng, A. Petrone, T. Henderson, D. Ranasinghe, V. G. Zakrzewski, J. Gao, N. Rega, G. Zheng, W. Liang, M. Hada, M. Ehara, K. Toyota, R. Fukuda, J. Hasegawa, M. Ishida, T. Nakajima, Y. Honda, O. Kitao, H. Nakai, T. Vreven, K. Throssell, J. A. Montgomery, Jr., J. E. Peralta, F. Ogliaro, M. Bearpark, J. J. Heyd, E. Brothers, K. N. Kudin, V. N. Staroverov, T. Keith, R. Kobayashi, J. Normand, K. Raghavachari, A. Rendell, J. C. Burant, S. S. Iyengar, J. Tomasi, M. Cossi, J. M. Millam, M. Klene, C. Adamo, R. Cammi, J. W. Ochterski, R. L. Martin, K. Morokuma, O. Farkas, J. B. Foresman, and D. J. Fox, Gaussian, Inc., Wallingford CT, 2016.

(18) Miehlich, B.; Savin, A.; Stoll, H.; Preuss, H. Results Obtained with the Correlation Energy Density Functionals of Becke and Lee, Yang and Parr. *Chemical*

Physics Letters **1989**, *157* (3), 200–206. https://doi.org/10.1016/0009-2614(89)87234-3.

(19) Vosko, S. H.; Wilk, L.; Nusair, M. Accurate Spin-Dependent Electron Liquid Correlation Energies for Local Spin Density Calculations: A Critical Analysis. *Can. J. Phys.* **1980**, *58* (8), 1200–1211. https://doi.org/10.1139/p80-159.

(20) Becke, A. D. Density-Functional Thermochemistry. I. The Effect of the Exchange-Only Gradient Correction. *The Journal of Chemical Physics* **1992**, *96* (3), 2155–2160. https://doi.org/10.1063/1.462066.

(21) Binkley, J. S.; Pople, J. A. Møller-Plesset Theory for Atomic Ground State Energies: MØLLER-PLESSET THEORY FOR ATOMIC GROUND STATE ENERGIES. *Int. J. Quantum Chem.* **1975**, *9* (2), 229–236. https://doi.org/10.1002/qua.560090204.

(22) Schäfer, A.; Huber, C.; Ahlrichs, R. Fully Optimized Contracted Gaussian Basis Sets of Triple Zeta Valence Quality for Atoms Li to Kr. *The Journal of Chemical Physics* **1994**, *100* (8), 5829–5835. https://doi.org/10.1063/1.467146.

(23) Bader, R. F. W. *Atoms in Molecules: A Quantum Theory*; The International series of monographs on chemistry; Clarendon Press ; Oxford University Press: Oxford [England] : New York, 1994.

(24) Western, C. M. PGOPHER: A Program for Simulating Rotational, Vibrational and Electronic Spectra. *Journal of Quantitative Spectroscopy and Radiative Transfer* **2017**, *186*, 221–242. https://doi.org/10.1016/j.jqsrt.2016.04.010.

B.6 Supplementary Information:

Table B-5: Equilibrium geometry coordinates (Å) of Ar(H2S)2(H2O) complex for structure A in the abc principal axes system optimised at MP2/aug-cc-pVDZ level of theory.

Atoms	a	b	c
H1	1.469	0.134	0.876
H2	1.185	-1.799	0.833
H3	0.633	3.182	0.221
H4	-0.068	1.646	-0.779
S5	2.199	-0.959	0.538
H6	1.152	-0.331	-1.650
H7	0.839	0.030	-3.108
Ar8	-1.892	-1.117	0.185
S9	-0.255	2.191	0.448
O10	0.513	0.146	-2.207

Table B-6: Equilibrium geometry coordinates (Å) of Ar(H2S)2(H2O) complex for structure B in the abc principal axes system optimised at MP2/aug-cc-pVDZ level of theory.

Atoms	a	b	c
H1	1.243	0.152	1.606
H2	0.622	-0.041	2.996
H3	3.119	0.488	-0.661
H4	1.253	-0.016	-0.980
S5	-0.047	-1.738	0.675
H6	0.574	-3.181	-0.499
H7	-1.778	1.183	-0.013
Ar8	1.919	1.105	-0.606
S9	0.853	-0.521	2.190
O10	-0.336	-2.186	-0.573

Table B-7: Equilibrium geometry coordinates (Å) of $Ar(H_2S)_2(H_2O)$ complex for structure A in the abc principal axes system optimised at B3LYP-D3/aug-cc-pVDZ level of theory.

Atoms	a	b	c
H_1	-1.390	0.158	-0.932
H_2	-1.143	-1.780	-0.713
H_3	-0.507	3.200	-0.347
H_4	0.125	1.685	0.748
S_5	-2.166	-0.902	-0.563
H_6	-1.209	-0.192	1.610
H_7	-1.050	0.338	3.049
Ar_8	1.786	-1.230	-0.128
S_9	0.394	2.196	-0.487
O_{10}	-0.593	0.273	2.203

Table B-8: Equilibrium geometry coordinates (Å) of $Ar(H_2S)_2(H_2O)$ complex for structure B in the abc principal axes system optimised at B3LYP-D3/aug-cc-pVDZ level of theory.

Atoms	a	b	c
H_1	1.129	-0.317	1.600
H_2	0.266	0.009	2.833
H_3	3.028	-0.967	-0.519
H_4	1.147	-0.597	-0.971
S_5	-0.804	-1.485	0.696
H_6	-0.811	-3.132	-0.390
H_7	-1.072	1.827	-0.076
Ar_8	2.232	0.130	-0.579
S_9	0.478	-0.699	2.213
O_{10}	-1.255	-1.859	-0.536

Table B-9: Normal modes of vibrations (cm^{-1}) for Structure A and Structure B of the $Ar(H_2S)_2(H_2O)$ complex calculated at MP2/aug-cc-pVDZ and B3LYP-D3/aug-cc-pVDZ level of theory.

Modes	Structure A		Structure B	
	MP2/aug-cc-pVDZ	B3LYP-D3/aug-cc-pVDZ	MP2/aug-cc-pVDZ	B3LYP-D3/aug-cc-pVDZ
1	31.2	20.6	27.1	29.2
2	33.9	36.3	32.9	36.6
3	42.3	44.3	43.4	47.6
4	81.6	80.2	81.3	79.5
5	107.8	109.5	107.1	111.4
6	114.4	113.9	113.9	116.1
7	122.1	124.1	131.8	123.9
8	130.5	125.3	133.8	127.3
9	157.8	139.1	156.8	155.1
10	181.1	198.7	177.6	195.6
11	209	209	211.4	205
12	267.6	272.5	265.4	274.1
13	325.6	332.9	325.8	335.5
14	429.7	419.7	435.5	420.3
15	532.5	557	531.6	572.4
16	1197.2	1184.1	1198.2	1183.4
17	1201.8	1193.2	1200	1188.6
18	1626.7	1621.1	1626	1620.5
19	2682.5	2583.3	2682.1	2574.7
20	2696.8	2599.8	2694.2	2590.3
21	2761.2	2671.4	2760.7	2673.6
22	2764	2677	2764.6	2674.1
23	3702.8	3662.7	3703.9	3664.1
24	3893	3868	3892.5	3864.8

APPENDIX C

Preliminary Results of Microwave Spectroscopic Study on Hexafluorobenzene···Methanol Complexe

APPENDIX C | Preliminary Results of Microwave Spectroscopic Study on Hexafluorobenzene···Methanol Complex |

C.1 Introduction:

The substitution of any molecule with fluorine atoms drastically changes its properties. This is due to the inductive effect of fluorine, which causes a withdrawal of electron density and the generation of a region with reduced charge, resulting in the formation of a π-hole. The rotational spectra and structure of the hexafluorobenzene···H_2O complex have been well known.[1] In this structure, the presence of lone pair···π-hole interaction leads to a complete flipping of the water molecule, in comparison to benzene···H_2O, which has O-H···π hydrogen bonded structure. Similar trends were observed in the microwave spectroscopic study of pentafluoropyridine···H_2O, where one lone pair···π-hole interaction was observed.[2] The present investigation focuses on exploring the rotational spectra of the hexafluorobenzene···methanol complex.

C.2 Experimental and Computational Details:

To conduct the experiments, hexafluorobenzene (HFB) and methanol (MeOH) were obtained from Sigma Aldrich and used without any additional purification. Neon gas was used as the carrier gas, and the HFB was introduced into the neon flow at a backing pressure of 5 bar. Due to its low vapour pressure, the HFB was heated to 50°C. The broadband spectrum, covering a frequency range of 2.0 to 8.0 GHz, was recorded using the chirped pulse Fourier transform microwave (CP-FTMW) spectrometer at Newcastle University. More detailed information about the spectrometer can be found in other sources.[3]

To further investigate the structure of the HFB···MeOH complex, Gaussian 09 software suite was used to optimize its geometry.[4] *Ab-initio* and DFT methods were employed,

utilizing MP2 and B3LYP-D3 functionals with an aug-cc-pVDZ basis set.[5–9] Harmonic frequency calculations were also performed to ensure that the optimized structure represents the minimum in the potential energy hypersurface. Distortion constants were calculated using the freq=vibrot keyword. Additionally, Atoms in Molecules (AIM) analysis was conducted to gain insights into the nature of the interactions present.[10] The wavefunction for the AIM calculation was obtained from the optimized geometry. Finally, the rotational transitions were fitted to the observed frequencies using the PGOPHER program.[11]

C.3 Preliminary Results:

C.3.1 Optimised Structures:

The optimized structures obtained using the MP2 and B3LYP-D3 methods with the aug-cc-pVDZ basis set are presented in *Figure C-1*. The corresponding rotational constants and dipole moment components are provided in *Table C-1*. In these optimized structures, the methanol molecule interacts with the top of the HFB ring, and the complex is stabilized by lone pair···π-hole interaction. However, the position of MeOH differs among the optimized structures, as shown in *Figure C-1* and detailed in *Table C-1*.

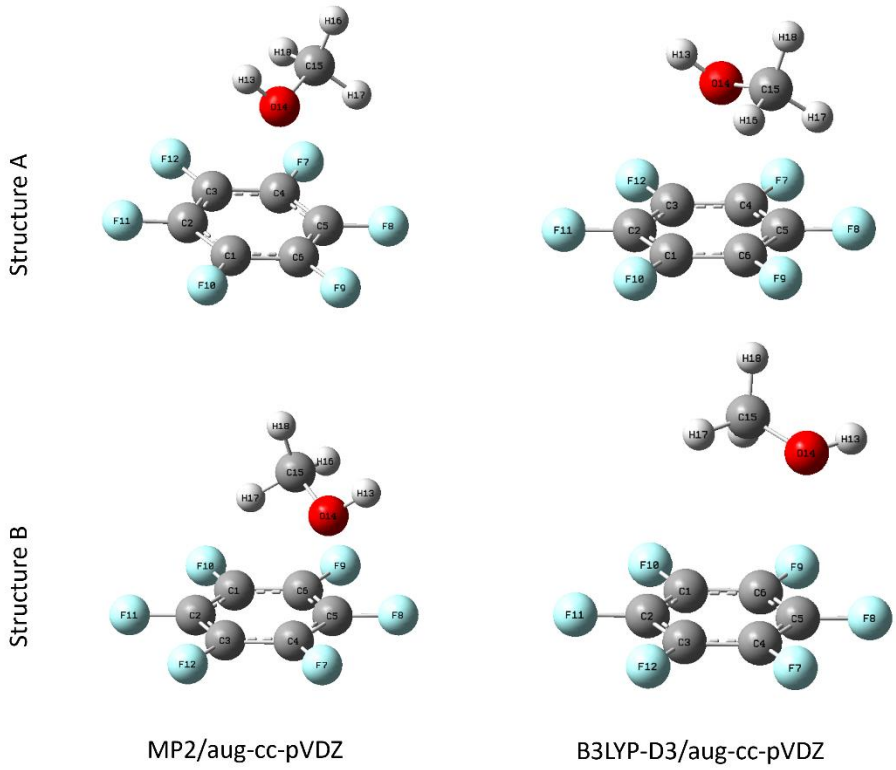

Figure C-1: Structures of the hexafluorobenzene···methanol complex optimised at B3LYP-D3/aug-cc-pVDZ and MP2/aug-cc-pVDZ level of theory.

Table C-1: Rotational Constants (MHz), Centrifugal Distortion Constants, Electric Dipole Moment (Debye), and the Binding Energy (ΔE) with BSSE Corrections (kJ/mol) for hexafluorobenzene···methanol complex calculated at MP2/aug-cc-pVDZ and B3LYP-D3/aug-cc-pVDZ level of theory.

Constants	**Structure A**		**Structure B**	
	MP2/aug-cc-pVDZ	**B3LYP-D3/aug-cc-pVDZ**	**MP2/aug-cc-pVDZ**	**B3LYP-D3/aug-cc-pVDZ**
A_e	679.1366	670.7647	699.7506	704.8726
B_e	642.2032	623.2923	630.2891	599.7635
C_e	482.1301	479.5108	462.6229	437.9702
D_J	0.0973	0.1351	0.1079	0.2858
D_K	-0.3744	-0.3465	-0.1762	-0.1781
D_{JK}	0.3071	0.2852	0.1035	0.0210

d_1	-0.0081	-0.0194	-0.0126	-0.0293
d_2	0.0144	0.0076	0.0181	0.0398
μ_a	0.9	1.0	-0.8	-1.7
μ_b	0.8	-0.8	1.0	-0.6
μ_c	1.5	1.5	-1.4	0.2
ΔE	29.5	19.2	29.7	18.8
ΔE_{BSSE}	13.9	15.5	12.8	15.4

C.3.3 Atoms in Molecules (AIM) Analysis:

To gain insights into the intermolecular interactions present in the complex, an Atoms in Molecules (AIM) analysis was performed. In all four structures, a bond critical point (BCP) was observed between the oxygen atom and one of the carbon atoms in the ring. Additional BCPs were formed between the hydrogen of the methyl group and the C/F atoms of the HFB ring. The molecular graph illustrating these BCPs is provided in *Figure C-2*. The electron density and Laplacian of electron density are presented in *Table C-2*.

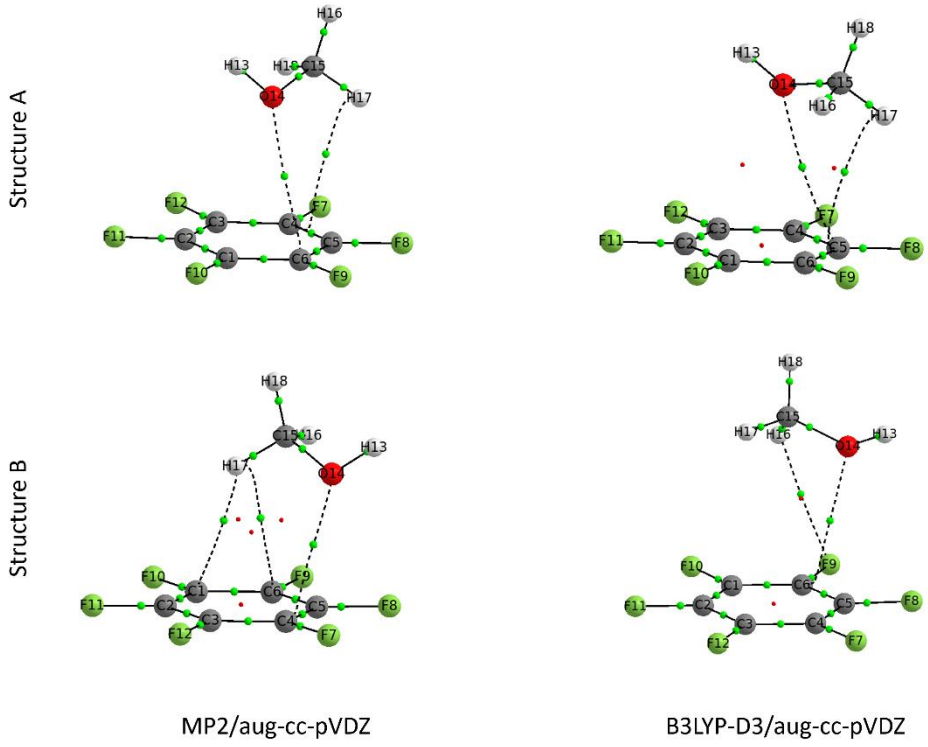

Figure C-2: Bond critical points (green) and ring critical points (red) of the hexafluorobenzene···methanol complex calculated at B3LYP-D3/aug-cc-pVDZ and MP2/aug-cc-pVDZ level of theory.

Table C-2: Electron density (ρ) and the Laplacian of the electron density (∇2ρ) of the hexafluorobenzene···methanol complex, calculated at B3LYP-D3/aug-cc-pVDZ and MP2/aug-cc-pVDZ level of theories.

Interactions	**Structure A**		**Interactions**	**Structure A**	
	MP2/aug-cc-pVDZ			**B3LYP-D3/aug-cc-pVDZ**	
	ρ (a.u)	**$\nabla^2\rho$ (a.u)**		**ρ (a.u)**	**$\nabla^2\rho$ (a.u)**
$O_{14}\cdots C_6$	0.008	+0.029	$O_{14}\cdots C_5$	0.007	+0.023
$H_{17}\cdots C_4$	0.007	+0.027	$H_{17}\cdots C_5$	0.005	+0.020

Interactions	**Structure B**		**Interactions**	**Structure B**	
	MP2/aug-cc-pVDZ			**B3LYP-D3/aug-cc-pVDZ**	
	ρ (a.u)	**$\nabla^2\rho$ (a.u)**		**ρ (a.u)**	**$\nabla^2\rho$ (a.u)**
$H_{17}\cdots C_1$	0.007	+0.022	$H_{16}\cdots F_9$	0.004	+0.022
$O_{14}\cdots C_4$	0.012	+0.044	$O_{14}\cdots C_6$	0.009	+0.031
$H_{17}\cdots C_6$	0.007	+0.023	---	---	---

C.3.2 Rotational Spectrum:

The rotational spectrum that was observed using the CP-FTMW spectrometer is depicted in *Figure C-3*. The spectrum remains unassigned, and it comprises a total of 258 transitions, the frequencies for which are listed in *Table C-3*.

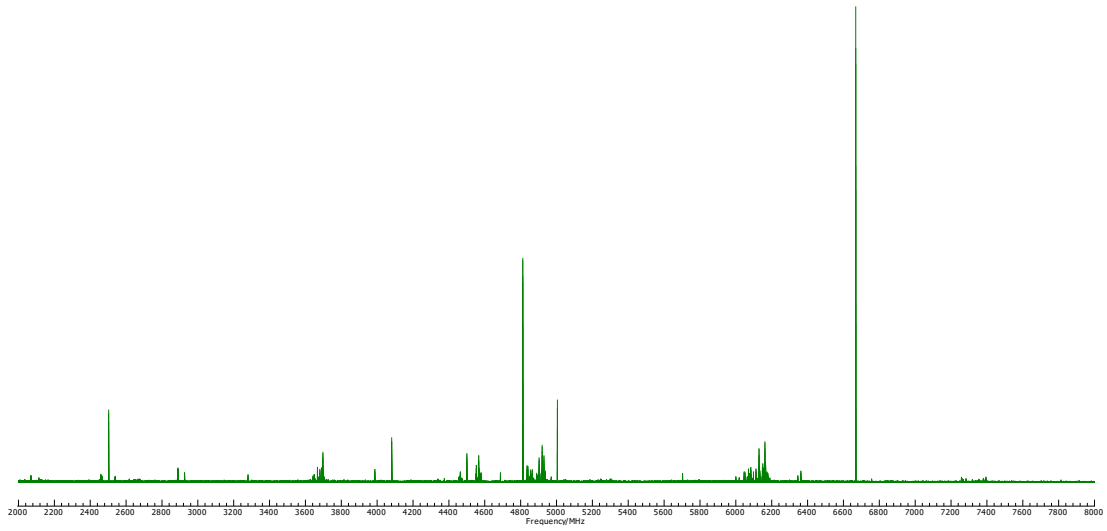

Figure C-3: The broadband spectrum of hexafluorobenzene···methanol complex recorded at CP-FTMW spectrometer.

Table C-3: Experimentally observed rotational transition recorded using hexafluorobenzene and methanol at CP-FTMW spectrometer.

Frequency (MHz)			
2008.22	4458.101	4873.669	6078.781
2034.881	4458.335	4873.8	6078.925
2113.372	4459.388	4875.105	6080.287
2926.027	4461.329	4881.175	6081.747
2931.206	4461.575	4883.378	6082.18
3279.964	4463.782	4883.696	6083.414
3282.281	4464.075	4889.651	6085.993
3639.022	4467.656	4895.106	6087.931
3642.352	4467.789	4903.172	6088.614
3648.315	4468.339	4907.179	6089.759
3648.432	4469.252	4918.66	6090.097
3648.606	4471.303	4920.07	6092.739
3649.132	4471.93	4921.673	6093.29
3649.42	4473.346	4923.553	6097.96
3651.319	4502.911	4923.744	6098.488
3651.736	4555.348	4923.272	6112.418

3653.495	4561.932	4924.582	6118.84
3653.703	4562.286	4926.449	6129.217
3654.687	4562.376	4928.002	6134.043
3667.065	4562.913	4929.894	6138.939
3671.362	4563.481	4930.843	6148.257
3680.344	4576.948	4931.171	6150.09
3680.509	4577.075	4932.594	6151.976
3683.327	4577.336	4933.13	6154.557
3689.024	4577.71	4933.525	6154.875
3690.043	4579.036	4936.44	6154.984
3692.534	4579.158	4936.575	6156.423
3692.703	4579.468	4936.951	6157.565
3692.864	4580.553	4937.226	6160.538
3693.472	4811.804	4938.149	6161.878
3695.064	4811.953	4941.415	6162.257
3695.735	4814.865	4942.913	6162.701
3697.47	4819.014	4945.819	6166.267
3698.525	4831.28	4949.028	6167.982
3699.498	4831.593	4965.238	6169.098
3699.658	4835.816	4969.381	6173.256
3699.902	4836.137	4970.787	6173.927
3701.728	4836.757	4921.023	6175.081
3703.034	4840.359	5185.852	6175.662
3703.199	4840.582	5244.949	6175.942
3705.595	4850.712	5249.996	6177.893
3708.873	4850.888	5278.561	6178.729
3715.57	4851.107	5278.875	6180.315
3716.775	4852.051	5279.013	6181.142
3721.195	4852.272	5631.93	6183.188
3722.427	4856.48	5641.46	6183.339
3724.346	4861.186	5731.518	6189.571
3728.282	4861.383	5795.116	6345.772
3728.594	4863.536	5997.082	6362.589
3750.788	4863.649	6000.068	7258.115
3759.425	4863.925	6013.71	7261.183

3987.016	4864.06	6019.25	7265.294
4080.65	4864.335	6025.1	7269.287
4080.8	4864.725	6028.05	7283.415
4188.02	4864.915	6044.255	7319.329
4338.06	4865.237	6046.181	7330.396
4338.52	4865.356	6046.45	7335.4
4341.67	4865.829	6050.698	7355.419
4344.061	4866.05	6054.127	7380.101
4345.556	4867.094	6063.892	7382.198
4455.23	4867.341	6065.065	7387.259
4455.464	4868.897	6070.604	7391.067
4456.148	4872.037	6075.805	7394.561
4456.378	4872.577	6076.389	
4457.51	4872.786	6077.236	

C.4 Conclusions and Future Directions:

We conducted *ab-initio* and DFT calculations to optimize the HFB···MeOH complex. In all of the optimized structures, MeOH interacts from the top of the ring and the oxygen atom points towards the π-cloud of the HFB ring. The rotational spectrum of HFB···MeOH was recorded using the CP-FTMW spectrometer within a frequency range of 2.0 to 8.0 GHz. The assignment of the spectrum is currently underway, and additional data on isotopologues are needed to determine the structure with certainty.

C.5 References:

(1) Evangelisti, L.; Brendel, K.; Mäder, H.; Caminati, W.; Melandri, S. Rotational Spectroscopy Probes Water Flipping by Full Fluorination of Benzene. *Angewandte Chemie* **2017**, *129* (44), 13887–13891. https://doi.org/10.1002/ange.201707155.

(2) Calabrese, C.; Gou, Q.; Maris, A.; Caminati, W.; Melandri, S. Probing the Lone Pair···π-Hole Interaction in Perfluorinated Heteroaromatic Rings: The Rotational Spectrum of Pentafluoropyridine·Water. *J. Phys. Chem. Lett.* **2016**, *7* (8), 1513–1517. https://doi.org/10.1021/acs.jpclett.6b00473.

(3) Zaleski, D. P.; Stephens, S. L.; Walker, N. R. A Perspective on Chemistry in Transient Plasma from Broadband Rotational Spectroscopy. *Phys. Chem. Chem. Phys.* **2014**, *16* (46), 25221–25228. https://doi.org/10.1039/C4CP04108A.

(4) Gaussian 09, Revision A.02, M. J. Frisch, G. W. Trucks, H. B. Schlegel, G. E. Scuseria, M. A. Robb, J. R. Cheeseman, G. Scalmani, V. Barone, G. A. Petersson, H. Nakatsuji, X. Li, M. Caricato, A. Marenich, J. Bloino, B. G. Janesko, R. Gomperts, B. Mennucci, H. P. Hratchian, J. V. Ortiz, A. F. Izmaylov, J. L. Sonnenberg, D. Williams-Young, F. Ding, F. Lipparini, F. Egidi, J. Goings, B. Peng, A. Petrone, T. Henderson, D. Ranasinghe, V. G. Zakrzewski, J. Gao, N. Rega, G. Zheng, W. Liang, M. Hada, M. Ehara, K. Toyota, R. Fukuda, J. Hasegawa, M. Ishida, T. Nakajima, Y. Honda, O. Kitao, H. Nakai, T. Vreven, K. Throssell, J. A. Montgomery, Jr., J. E. Peralta, F. Ogliaro, M. Bearpark, J. J. Heyd, E. Brothers, K. N. Kudin, V. N. Staroverov, T. Keith, R. Kobayashi, J. Normand, K. Raghavachari, A. Rendell, J. C. Burant, S. S. Iyengar, J. Tomasi, M. Cossi, J. M. Millam, M. Klene, C. Adamo, R. Cammi, J. W. Ochterski, R. L. Martin, K. Morokuma, O. Farkas, J. B. Foresman, and D. J. Fox, Gaussian, Inc., Wallingford CT, 2016.

(5) Miehlich, B.; Savin, A.; Stoll, H.; Preuss, H. Results Obtained with the Correlation Energy Density Functionals of Becke and Lee, Yang and Parr. *Chemical Physics Letters* **1989**, *157* (3), 200–206. https://doi.org/10.1016/0009-2614(89)87234-3.

(6) Vosko, S. H.; Wilk, L.; Nusair, M. Accurate Spin-Dependent Electron Liquid Correlation Energies for Local Spin Density Calculations: A Critical Analysis. *Can. J. Phys.* **1980**, *58* (8), 1200–1211. https://doi.org/10.1139/p80-159.

(7) Becke, A. D. Density-Functional Thermochemistry. I. The Effect of the Exchange-Only Gradient Correction. *The Journal of Chemical Physics* **1992**, *96* (3), 2155–2160. https://doi.org/10.1063/1.462066.

(8) Binkley, J. S.; Pople, J. A. Møller-Plesset Theory for Atomic Ground State Energies: MØLLER-PLESSET THEORY FOR ATOMIC GROUND STATE ENERGIES. *Int. J. Quantum Chem.* **1975**, *9* (2), 229–236. https://doi.org/10.1002/qua.560090204.

(9) Schäfer, A.; Huber, C.; Ahlrichs, R. Fully Optimized Contracted Gaussian Basis Sets of Triple Zeta Valence Quality for Atoms Li to Kr. *The Journal of Chemical Physics* **1994**, *100* (8), 5829–5835. https://doi.org/10.1063/1.467146.

(10) Bader, R. F. W. *Atoms in Molecules: A Quantum Theory*; The International series of monographs on chemistry; Clarendon Press ; Oxford University Press: Oxford [England] : New York, 1994.

(11) Western, C. M. PGOPHER: A Program for Simulating Rotational, Vibrational and Electronic Spectra. *Journal of Quantitative Spectroscopy and Radiative Transfer* **2017**, *186*, 221–242. https://doi.org/10.1016/j.jqsrt.2016.04.010.

C.6 Supplementary Information:

Table C-4: Equilibrium geometry coordinates (Å) of hexafluorobenzene···methanol complex for structure A in the abc principal axes system optimised at MP2/aug-cc-pVDZ level of theory.

Atoms	a	b	c
C_1	-1.517	-0.360	-0.155
C_2	-1.167	0.994	-0.212
C_3	0.155	1.366	-0.483
C_4	1.126	0.382	-0.702
C_5	0.776	-0.972	-0.643
C_6	-0.545	-1.344	-0.369
F_7	2.404	0.737	-0.945
F_8	1.720	-1.916	-0.828
F_9	-0.876	-2.647	-0.294
F_{10}	-2.786	-0.716	0.124
F_{11}	-2.100	1.941	0.014
F_{12}	0.498	2.670	-0.516
H_{13}	0.052	0.370	3.096
O_{14}	0.422	-0.170	2.385
C_{15}	1.848	0.009	2.396
H_{16}	2.276	-0.166	3.396
H_{17}	2.263	-0.737	1.706
H_{18}	2.134	1.016	2.047

Table C-5: Equilibrium geometry coordinates (Å) of hexafluorobenzene···methanol complex for structure B in the abc principal axes system optimised at MP2/aug-cc-pVDZ level of theory.

Atoms	a	b	c
C_1	1.441	0.727	0.078
C_2	1.486	-0.671	0.006
C_3	0.342	-1.426	0.304

C_4	-0.846	-0.785	0.676
C_5	-0.890	0.613	0.743
C_6	0.250	1.368	0.443
F_7	-1.940	-1.506	0.958
F_8	-2.037	1.235	1.072
F_9	0.196	2.715	0.485
F_{10}	2.538	1.455	-0.214
F_{11}	2.630	-1.292	-0.347
F_{12}	0.389	-2.770	0.229
H_{13}	-3.060	0.137	-2.076
O_{14}	-2.203	-0.185	-1.767
C_{15}	-1.176	0.500	-2.500
H_{16}	-1.154	1.578	-2.266
H_{17}	-0.224	0.049	-2.190
H_{18}	-1.289	0.366	-3.588

Table C-6: Equilibrium geometry coordinates (Å) of hexafluorobenzene···methanol complex for structure A in the abc principal axes system optimised at B3LYP-D3/aug-cc-pVDZ level of theory.

C_1	-0.055	-1.392	-0.459
C_2	-1.302	-0.871	-0.120
C_3	-1.495	0.509	-0.086
C_4	-0.441	1.368	-0.391
C_5	0.805	0.846	-0.731
C_6	0.998	-0.534	-0.766
F_7	-0.621	2.695	-0.342
F_8	1.828	1.671	-1.001
F_9	2.206	-1.034	-1.068
F_{10}	0.136	-2.720	-0.474
F_{11}	-2.314	-1.698	0.185
F_{12}	-2.692	1.010	0.252
H_{13}	0.376	-0.294	3.165
O_{14}	0.736	0.197	2.418
C_{15}	2.147	-0.026	2.355

H_{16}	2.387	-1.069	2.090
H_{17}	2.536	0.631	1.568
H_{18}	2.649	0.233	3.301

Table C-7: Equilibrium geometry coordinates (Å) of hexafluorobenzene···methanol complex for structure B in the abc principal axes system optimised at B3LYP-D3/aug-cc-pVDZ level of theory.

Atoms	**a**	**b**	**c**
C_1	-0.160	-1.252	-0.567
C_2	1.135	-1.157	-0.055
C_3	1.701	0.097	0.175
C_4	0.972	1.254	-0.104
C_5	-0.321	1.156	-0.615
C_6	-0.884	-0.096	-0.848
F_7	1.513	2.457	0.128
F_8	-1.032	2.264	-0.857
F_9	-2.140	-0.190	-1.309
F_{10}	-0.714	-2.457	-0.770
F_{11}	1.833	-2.270	0.214
F_{12}	2.946	0.190	0.663
H_{13}	-3.062	1.075	1.530
O_{14}	-2.217	0.676	1.768
C_{15}	-2.422	-0.711	2.049
H_{16}	-2.807	-1.257	1.173
H_{17}	-1.442	-1.123	2.317
H_{18}	-3.107	-0.862	2.898

Table C-8: Normal modes of vibrations for Structure A and Structure B of the hexafluorobenzene···methanol complex calculated at MP2/aug-cc-pVDZ and B3LYP-D3/aug-cc-pVDZ level of theory.

Modes	Frequecny (cm^{-1})			
	Structure A		Structure B	
	MP2/aug-cc-pVDZ	B3LYP-D3/aug-cc-pVDZ	MP2/aug-cc-pVDZ	B3LYP-D3/aug-cc-pVDZ
1	20	23.1	20.5	16.9
2	38.7	30.9	37.5	25.3
3	42.3	37.4	52.7	33
4	100.3	79.4	103.8	88.5
5	104	94.8	112.5	106.6
6	134.5	133.9	136.8	121.4
7	137.2	135.2	139.9	136.9
8	157	139	146	138.7
9	181.2	184.6	183.2	186.7
10	220.8	214.9	226.3	219.8
11	264.2	268.2	264.5	268.3
12	264.8	268.3	265.1	269
13	274.7	278.1	274.7	278.6
14	307.8	312.6	310.3	313
15	311.5	312.9	312	313.4
16	312.1	318.9	315.6	325.5
17	370.2	367.2	373.1	366.2
18	373.6	370.3	378.8	372.2
19	438	438.9	438.7	439.5
20	438.6	439.1	439	439.6
21	553.2	559.4	553.3	559.5
22	566.2	575.3	562	575.9
23	609.1	647.3	609.2	647
24	622.9	649.6	625.2	649.1
25	625.2	722.2	627.6	712.4
26	779.8	779.2	779.4	779.6
27	993.9	996.8	995.1	997.8
28	994.9	998.4	996.5	998.6

29	1036.4	1034.8	1039.9	1036.1
30	1074	1074.7	1073.4	1072.6
31	1143.6	1146.6	1145.3	1147.9
32	1145.1	1148.5	1149.7	1149.9
33	1167.8	1161	1167.6	1160.5
34	1331.3	1267.5	1335.4	1270
35	1363.9	1329.1	1362.3	1327.2
36	1463.8	1358.8	1460.3	1358.2
37	1483.9	1455.3	1480.6	1450.9
38	1493.9	1473.1	1488.3	1470.4
39	1506	1484.8	1505.8	1487.2
40	1510.6	1501.2	1514	1502.3
41	1550.8	1541.2	1548	1540.7
42	1552.3	1542.8	1553.2	1542.6
43	1694.3	1676.1	1691	1674.7
44	1694.5	1676.4	1691.6	1675.7
45	3050.3	3001.3	3047.6	3002.6
46	3133.5	3063.4	3130.8	3062.9
47	3181.5	3122.6	3176.4	3117.7
48	3826.2	3827.1	3827.2	3824.3

ORAL/POSTER PRESENTATIONS

1. **Ammonia@Crown Ether: Hydrogen bonds, inversion and tunnelling**; Surabhi Gupta, Sarvesh K. Pandey and Elangannan Arunan. *24th International Conference on Horizons in Hydrogen Bond Research (HBOND2022), Bilbao, Spain*. 12th-15th September 2022. (Oral Presentation)

2. **Phenylacetylene···Methanol Complex: Does it have a global minimum similar to Phenylacetylene···Water or not?**; Surabhi Gupta and Elangannan Arunan. *Spectroscopy and Dynamics Group Meeting (SDGM 2023), Durham University, United Kingdom*. 3rd-5th January 2023. (Oral Presentation)

3. **Microwave Spectrum and Structure of Phenylacetylene···Methanol Complex**; Surabhi Gupta, Charlotte N. Cummings, Nicholas R. Walker and Elangannan Arunan. *76th International Symposium on Molecular Spectroscopy (ISMS 2023), University of Illinois, at Urbana-Champaign, USA*. 19th-23rd June 2023. (Oral Presentation)

4. **Microwave Spectrum and Structure of 1-Fluoronaphthalene and its Water Complexes;** Surabhi Gupta, Charlotte N. Cummings, Nicholas R. Walker and Elangannan Arunan. *Virtual International Microwave Seminar, 13th December 2023*. (Oral Presentation)

5. **Microwave Spectroscopic and Computational Studies on 1-Fluoronaphthalene···$(H_2O)_{1-2}$ Complexes**; Surabhi Gupta, Charlotte N. Cummings, Nicholas R. Walker and Elangannan Arunan. *Spectroscopy and Dynamics of Molecules and Clusters (SDMC2024). Kaziranga, Assam, India.* 22nd-25th February 2024. (Poster Presentation)

6. **Microwave Spectrum and Structure of 1-Fluoronaphthalene and its Water Complexes;** Surabhi Gupta, Charlotte N. Cummings, Nicholas R. Walker and Elangannan Arunan. *77th International Symposium on Molecular Spectroscopy (ISMS 2024), University of Illinois, at Urbana-Champaign, USA*. 17th-21st June 2024. (*To be presented*) (Oral Presentation)

PUBLICATIONS

1. Gupta, S., Cummings, C. N., Walker, N. R., Arunan, E. Insights into intermolecular interactions: Microwave spectroscopic and computational analysis of the Phenylacetylene···Methanol complex. (*Manuscript under preparation*)

2. Gupta, S., Cummings, C. N., Walker, N. R., Arunan, E. Revisiting the microwave spectrum and molecular structure of 1-fluoronaphthalene. (*Manuscript under preparation*)

3. Gupta, S., Cummings, C. N., Walker, N. R., Arunan, E. Microwave spectrum and structure of 1-fluoronaphthalene···$(H_2O)_{1\text{-}2}$ complexes. (*Manuscript under preparation*)

4. Gupta, S., Pandey, S, K., Arunan, E. Ammonia@Crown Ether: Hydrogen bonding, inversion and tunnelling. (*Manuscript under preparation*)